GENERAL ATOMIC™

GA-A13804
UC-77

HTGR FUELS AND CORE DEVELOPMENT PROGRAM

QUARTERLY PROGRESS REPORT FOR THE PERIOD ENDING FEBRUARY 29, 1976

Prepared under
Contract E(04-3)-167
Project Agreement No. 17
for the San Francisco Operations Office
U.S. Energy Research and Development Administration

DATE PUBLISHED: MARCH 31, 1976

Printed in the United States of America
Available from
National Technical Information Service
U.S. Department of Commerce
5285 Port Royal Road
Springfield, Virginia 22161
Price: Printed Copy $8.00 Microfiche $2.25

DISCLAIMER

GENERAL ATOMIC

GA-A13804
UC-77

HTGR FUELS AND CORE DEVELOPMENT PROGRAM

QUARTERLY PROGRESS REPORT FOR THE PERIOD ENDING FEBRUARY 29, 1976

Prepared under
Contract E(04-3)-167
Project Agreement No. 17
for the San Francisco Operations Office
U.S. Energy Research and Development Administration

GENERAL ATOMIC PROJECT 3224 DATE PUBLISHED: MARCH 31, 1976

QUARTERLY REPORT SERIES

GA-4072-December, 1962, through February, 1963
GA-4350-March, 1963, through May, 1963
GA-4569-June, 1963, through August, 1963
GA-4937-September, 1963, through November, 1963
GA-5104-December, 1963, through February, 1964
GA-5366-March, 1964, through May, 1964
GA-5618-June, 1964, through August, 1964
GA-5866-September, 1964, through November, 1964
GA-6113-December, 1964, through February, 1965
GA-6418-March, 1965, through May, 1965
GA-6671-June, 1965, through August, 1965
GA-6869-September, 1965, through November, 1965
GA-7010-December, 1965, through February, 1966
GA-7181-March, 1966, through May, 1966
GA-7396-June, 1966, through August, 1966
GA-7553-September, 1966, through November, 1966
GA-7801-December, 1966, through February, 1967
GA-7981-March, 1967, through May, 1967
GA-8200-June, 1967, through August, 1967
GA-8356-September, 1967, through November, 1967
GA-8530-December, 1967, through February, 1968
GA-8662-March, 1968, through May, 1968
GA-8860-June, 1968, through August, 1968
GA-9090-September, 1968, through November, 1968
GA-9227-December, 1968, through February, 1969
GA-9372-March, 1969, through May, 1969
GA-9660-June, 1969, through August, 1969
GA-9815-September, 1969, through November, 1969
GA-9944-December, 1969, through February, 1970
GA-10088-March, 1970, through May, 1970
GA-10288-June, 1970, through August, 1970
GA-10399-September, 1970, through November, 1970
GA-10501-December, 1970, through February, 1971
GA-10661-March, 1971, through May, 1971
Gulf-GA-A10784-June, 1971, through August, 1971
Gulf-GA-A10930-September, 1971, through November, 1971
Gulf-GA-A10999-December, 1971, through February, 1972
Gulf-GA-A12150-March, 1972, through May, 1972
Gulf-GA-A12222-June, 1972, through August, 1972
Gulf-GA-A12422-September, 1972, through November, 1972
Gulf-GA-A12515-December, 1972, through February, 1973
Gulf-GA-12599-March, 1973, through May, 1973
Gulf-GA-A12725-June, 1973, through August, 1973
Gulf-GA-A12818-September, 1973, through November, 1973
GA-A12916-December, 1973, through February, 1974
GA-A13030-March, 1974, through May, 1974
GA-A13126-June, 1974, through August, 1974
GA-A13253-September, 1974, through November, 1974
GA-A13353-December, 1974, through February, 1975
GA-A13444-March, 1975, through May, 1975
GA-A13592-June, 1975, through August, 1975
GA-A13737-September, 1975, through November, 1975

ABSTRACT

This publication continues the quarterly report series on the HTGR Fuels and Core Development Program. The Program covers items of the base technology of the High-Temperature Gas-Cooled Reactor (HTGR) system. The development of the HTGR system will, in part, meet the greater national objective of more effective and efficient utilization of our national resources. The work reported here includes studies of reactions between core materials and coolant impurities, basic fission product transport mechanisms, core graphite development and testing, the development and testing of recyclable fuel systems, and physics and fuel management studies. Materials studies include irradiation capsule tests of both fuel and graphite. Experimental procedures and results are discussed and, where appropriate, the data are presented in tables, graphs, and photographs. More detailed descriptions of experimental work are presented in topical reports; these are listed at the end of the report.

INTRODUCTION

This report covers the work performed by the General Atomic Company under U.S. Energy Research and Development Administration Contract E(04-3)-167, Project Agreement No. 17. This Project Agreement calls for support of basic technology associated with the fuels and core of the gas-cooled, nuclear power reactor systems. The program is based on the concept of the High-Temperature Gas-Cooled Reactor (HTGR) developed by the General Atomic Company.

The 330-MW(e) prototype Fort St. Vrain reactor will be placed in operation in 1976. Characteristics of advanced large HTGR designs include:

1. A single-phase gas coolant allowing generation of high-temperature, high-pressure steam with consequent high-efficiency energy conversion and low thermal discharge.

2. A prestressed concrete reactor vessel (PCRV) offering advantages in field construction, primary system integrity, and stressed member inspectability.

3. Graphite core material assuring high-temperature structural strength, large temperature safety margins, and good neutron economy.

4. Thorium fuel cycle leading to U-233 fuel which allows good utilization of nuclear resources and minimum demands on separative work.

CONTENTS

FIGURES

FIGURES (Continued)

FIGURES (Continued)

TABLES

TABLES (Continued)

Dual units, SI followed by common usage units, appear in the text whereas common usage units are used in many cases in tables and figures. A considerable amount of the data in this report resulted from computer output and other tabulated data and figures obtained prior to the ERDA January 5, 1976 deadline for converting to SI units. The additional effort to convert the individual data points in the tables and figures was judged to be not warranted for this report. SI conversion factors are being added to the computer codes and future reports will contain SI or dual units as directed.

4. HTGR FISSION PRODUCT MECHANISMS
189a NO. SU001

TASK 100: FISSION PRODUCT TRANSPORT

Subtask 120: Fission Metal Release

In-Pile Cesium Retention in P13R and P13S Samples

Introduction and Summary. Selected loose particles from capsules P13R and P13S have been gamma scanned to establish the in-pile cesium retention of near-reference fissile and fertile particles (Ref. 4-1). Comparison of the predicted and observed fission product inventories revealed no cesium release within the experimental uncertainties of the measurement. These results are in accord with predicted fission product release behavior.

Experimental Method. Evaluation of cesium retention in near-reference fissile and fertile particles was carried out by comparing the predicted and measured CS-137/Zr-95 ratio present in intact particles. Individual particles which had been irradiated in the loose particle beds of capsules P13R and P13S were microscopically examined, and representative intact examples were selected for gamma counting.* These particles were subsequently gathered in groups ranging in size from one to nine particles, and fission product inventories were determined from gamma counting measurements. From these data, a mean Cs-137/Zr-95 ratio and accompanying standard deviation were established for each particle batch. Concurrently, the predicted Cs-137/Zr-95 ratio was established by modeling the particle

---

*The original intent of this subtask was to examine particle samples irradiated in the P13Q capsule. These samples were unavailable at the time of counting because the fuel rods in P13Q had not been mechanically deconsolidated (P13Q contained no loose particle beds).

irradiation environments with the FISS-PROD code. This GA code is used to predict fission product inventories in fuel materials following input of appropriate power history, uranium and thorium loading, fission yield, etc. The results of these studies are summarized in Table 4-1. Examination of predicted and observed Cs-137/Zr-95 ratios and associated uncertainties reveals that no measurable cesium escape occurred in any of the particle batches. This is true not only of the near-reference TRISO fissile fuel batch No. 2, but also of the near-reference BISO fertile particles in batch No. 5 and nonreference TRISO particles in batch Nos. 1, 3, 4, and 6.

This result is in accord with predicted behavior. No release is predicted from intact reference TRISO particles because the SiC coating layer is a very effective barrier to Cs release. The release of Cs from intact BISO fertile particles was calculated using curves of predicted cesium release generated by the FIPER code (Ref. 4-2) and the input data presented in Table 4-1 and Ref. 4-1. The results indicate that the predicted cesium release at the indicated temperature of 900°C is significantly less than the limits of detection of the experimental method.

TASK 200: FISSION PRODUCT TRANSPORT CODES

Subtask 210: Fission Product Transport Code Development

Advanced FIPER Code Alternatives

Alternative methods for improving the accuracy and usefulness of the FIPER code have been studied. In summary, this study led to the conclusions that (1) development of a new advanced code should await results of the Code Validation Program (Ref. 4-3) and (2) certain features, such as the particle release model COPAR which was recently developed, should be incorporated into the existing FIPER code (FIPER Q).

TABLE 4-1
GAMMA SCAN RESULTS OF SELECTED LOOSE PARTICLE BATCHES
IN CAPSULES P13R AND P13S[a]

Particle Type	Sample No.	Irradiation Temp (°C)	No. of Particles in Each Count[b]	Mean Measured Cs-137/Zr-95 Ratio	Mean Predicted Cs-137/Zr-95 Ratio[c]
UC_2 TRISO (nonreference: high coating density)	P13R-C4P10 6151-09-025-1	1070	3	0.038 ± 0.0009[d]	0.042 ± 0.004
UC_2 TRISO (near reference)	P13S-C4P10 6151-00-035-4	1090	3	0.037 ± 0.001	0.038 ± 0.004
UC_2 TRISO (nonreference: high coating density)	P13R-C4P8 6151-09-015-2	1010	3	0.038 ± 0.001	0.039 ± 0.004
UC_2 TRISO (nonreference: faceted particles)	P13R-C3P10 6151-00-046-1	1075	1-3	0.041 ± 0.002	0.045 ± 0.004
ThO_2 BISO (near reference)	P13S-C4P3 4252-02-010-2	900	1-9	0.016 ± 0.0003	0.016 ± 0.0002
ThO_2 TRISO (nonreference)	P13S-C3P12 6252-00-025-2	925	3	0.016 ± 0.0004	0.016 ± 0.0002

[a] Capsule irradiation time = 2.23×10^7 sec.

[b] Number of particle batches counted per particle type = 24.

[c] Using FISS-PROD code.

[d] From counting statistics.

For the past several years, fission product code development has concentrated upon developing fast-running design-oriented codes (such as TRAFIC) for use in calculating fission product release from whole cores. During this period, the FIPER Q code, which is the more general fission metal release code and has more flexibility than TRAFIC in such areas as modeling geometry and boundary conditions, has remained unchanged.

The FIPER Q code is very important for use as a standard in testing the accuracy of the design-oriented codes. In addition, it is the principal code used in the code validation work for evaluating results of release from fuel elements in capsule, loop, reactor, and laboratory experiments. In order to improve the accuracy and usefulness of the code, modeling improvements of the past several years need to be incorporated. An alternative is to develop a new, advanced code.

The need for an advanced FIPER code and the scope of such a code has been studied. One problem in designing such a code is the need to satisfy conflicting requirements. The model on which the code is based should be reasonably rigorous and should have geometrical flexibility. This points toward a two-dimensional code. On the other hand, the model should include complicated, nonlinear physical processes, and the code should also be reasonable in cost, both for development and routine application. On this basis, a one-dimensional code, such as FIPER Q, is preferable. While this conflict cannot be completely resolved by a single code, this study has converged on a concept that appears to satisfy both requirements. The first advanced FIPER concept would probably have the following characteristics:

1. The first advanced FIPER would be a one-dimensional code. There are no basic physical phenomena involved that require two dimensions to model. In view of other sources of uncertainty, the additional accuracy obtainable with a two-dimensional analysis is not presently worth the cost of the development or the application.

2. Adequate geometrical flexibility can be obtained by a hybrid one-dimensional code. This would consist of an arbitrary network of one-dimensional models coupled to one another through consistent, nonlinear boundary conditions. A spherical geometry model could be used for particles; a cylindrical geometry model could be used for the fuel rod; slab or cylindrical models could be used for structural graphite. All these could be considered simultaneously in one run.

3. The most suitable numerical solution method would be an implicit method. This involves solving a set of simultaneous linearized equations and iterating to account for nonlinear effects.

4. A substructured solution logic would be well suited for a one-dimensional network model. The logic of a substructured solution would proceed as follows:

   a. Assemble an independent system of equations for each branch of the network.

   b. Eliminate all interior unknowns within the branch by Cholesky factoring, deriving a reduced branch system containing only branch boundary conditions as unknowns.

   c. Assemble the reduced branch equations to form a global system of equations.

   d. Solve the global system by Cholesky factoring.

   e. Extract boundary unknowns for each branch in turn.

   f. Back substitute in the previously factored branch equations to solve for the interior unknowns.

5. It would be advisable to develop two different but closely related network programs. One would employ a rigorous, nonlinear numerical solution. The other would employ faster-running analytic solutions to eliminate the interior unknowns. The latter would be more useful for design analyses and parametric studies. The former would be used for experimental verification and calibration. Both of these network programs could use the same global solution method and the same input/output sections.

6. In addition to the existing capabilities of FIPER Q and TRAFIC, the advanced FIPER should have the following features:

   a. New particle release model. (A new particle release model called COPAR (Coated PArticle Release) has recently been developed. This model employs a reasonably rigorous analytic formulation of a multilayer diffusion problem in spherical geometry and accounts for all physical effects of known importance.)

   b. Nonlinear diffusion coefficients.

   c. Vapor pressure dependent on fast neutron dose.

   d. Temperature- and concentration-dependent sorption ratio.

   e. Readsorption in the coolant channel.

   f. Transport by thermal gradient diffusion.

   g. Two-phase non-Fickian diffusion model.

   h. Transverse flow.

i. Precursor contribution.

j. Automatic time steps.

The conclusions of this study are summarized as follows:

1. It is feasible and it would be desirable to develop an advanced FIPER code along the lines suggested above. The present FIPER Q code has many inherent limitations, and it cannot be modified to account for all the above effects.

2. It is premature to begin this development now. This should wait until the current Code Validation Program is complete. This will provide valuable information about the relative importance of various effects.

3. As an interim measure, and to provide improved capability for the Code Validation Program, the present FIPER Q code should be updated to include as many of the above effects as possible. This would include adding the COPAR particle release model and several other minor changes. It would exclude non-Fickian effects and geometrical flexibility.

Subtask 220: Validation of Codes and Input Data

Temperature Distribution in Heat Exchanger - Recuperator During the CPL-2/1 Experiment

Introduction and Summary. A thermal-fluid flow analysis has been performed to establish the temperature distribution which existed on the walls of the tubes in the heat exchanger - recuperator during the French Cadarache Pegase Loop CPL-2/1 experiment. A description of the loop and of the heat exchanger - recuperator is given in Ref. 4-4. The CPL-2/1 heat exchanger - recuperator was operated within the range of temperatures where

the level of plateout is limited by the sorptivity of the plateout species, such as Cs-137 and I-131; therefore, a strong effort was made to determine the temperature distribution as accurately as possible. The resulting temperature distribution will be utilized in the Plateout Activity Distribution (PAD) code to calculate the plateout distribution of various species in the heat exchanger - recuperator. The calculated plateout distribution will be compared with the observed distribution as a step toward verifying the accuracy of the PAD code.

A preliminary (earlier) estimate of the temperature distribution (illustrated in Fig. 4-10 of Ref. 4-4) was based on the assumption that the tube wall temperature was midway between the tube-side and shell-side gas temperature and that the distribution of the wall temperatures was linear.

Wall temperature distributions calculated from the results of the thermal-fluid flow analysis differ significantly from a linear distribution. Figure 4-1 compares the calculated and linear tube wall temperature distributions for a tube located midway between the center and the periphery of the tube bundle.

It is concluded that a temperature distribution based on a linear interpolation of measured gas temperatures is not an adequate representation of the temperature distribution in the heat exchanger - recuperator. The results of this work will be checked at CEA before being finalized.

Discussion. The difference between the linear and calculated distributions is due in most part to shell-side flow patterns. It was found in the analysis that the pressure drop across the shell side of the heat exchanger - recuperator induced a significant amount of flow moving across, or transverse to, the tube bundle. In the upper region of the heat exchanger - recuperator (tube-side outlet - shell-side inlet) cool gas moved from the periphery toward the center, whereas in the lower region

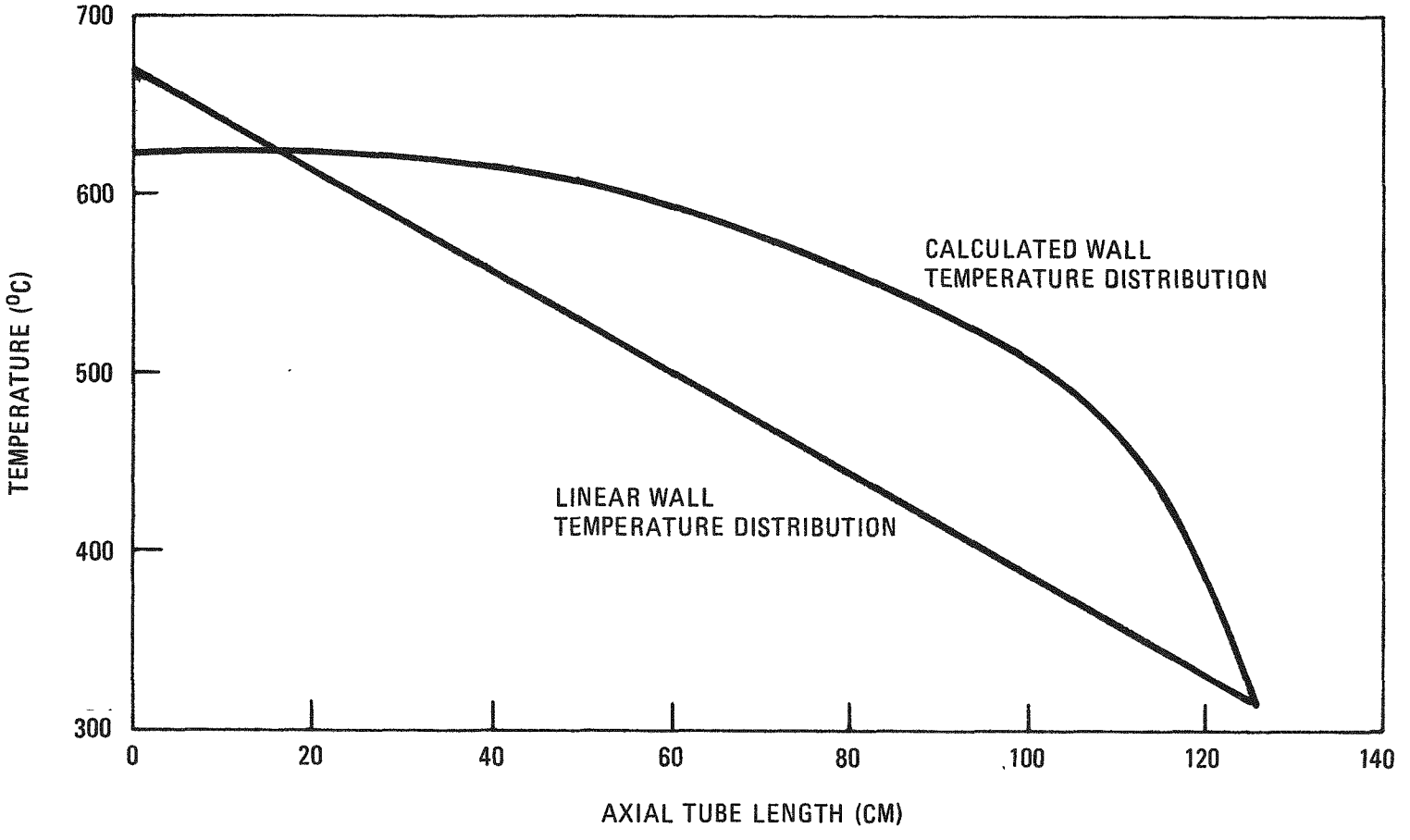

Fig. 4-1. Comparison of tube wall temperature distributions

(tube-side inlet - shell-side outlet) hot gas flow was induced from the center to the periphery. Thus, the outside of each tube (with the exception of the central tube which experienced flow stagnation) experienced a high degree of fluid turbulence due to the mixing of the cross flow with the flow moving axially along the tube. Conversely, the flow through the tube side of the heat exchanger - recuperator was found to be predominantly transitional, between laminar and turbulent, in nature. These results show that the heat transfer coefficient on the outside of the tube was, on the average, approximately two times greater than the heat transfer coefficient on the inside of the tube. A description of the procedure used in the thermal-fluid flow analysis follows.

Analysis Procedure. Figure 4-2 shows a schematic of the network used to analyze the shell-side flow distribution. Boxes indicate connecting nodes and resistances indicate flow branches. Flow branches 1 and 42 serve as the constant loss entrance and exit resistances, respectively. Branches 2 through 9 and 13 through 20 represent the frictional losses experienced by the flow as it moves across each successive row of tubes toward the center (2 through 9) and toward the periphery (13 through 20). The vertical flow branches 10, 11, 12, and 21 through 41 represent the axial flow down the channels formed by two adjacent tube rows. Finally, these axial flow branches were interconnected by branches 43 through 56 to allow "communication" between adjacent channels. This was necessary in order to permit the equilibration of pressure drops across each axial flow channel.

The tube side of the heat exchanger - recuperator was modeled in two halves to account for the azimuthal asymmetry of the measured tube-side gas outlet temperatures. Figure 4-3 shows a cross section of the heat exchanger - recuperator and illustrates the division of each ring of tubes into two sections. One section represents the half that was closest to the reactor core (designated "reactor side") and the other section the half that was farthest from the core (designated "water side").

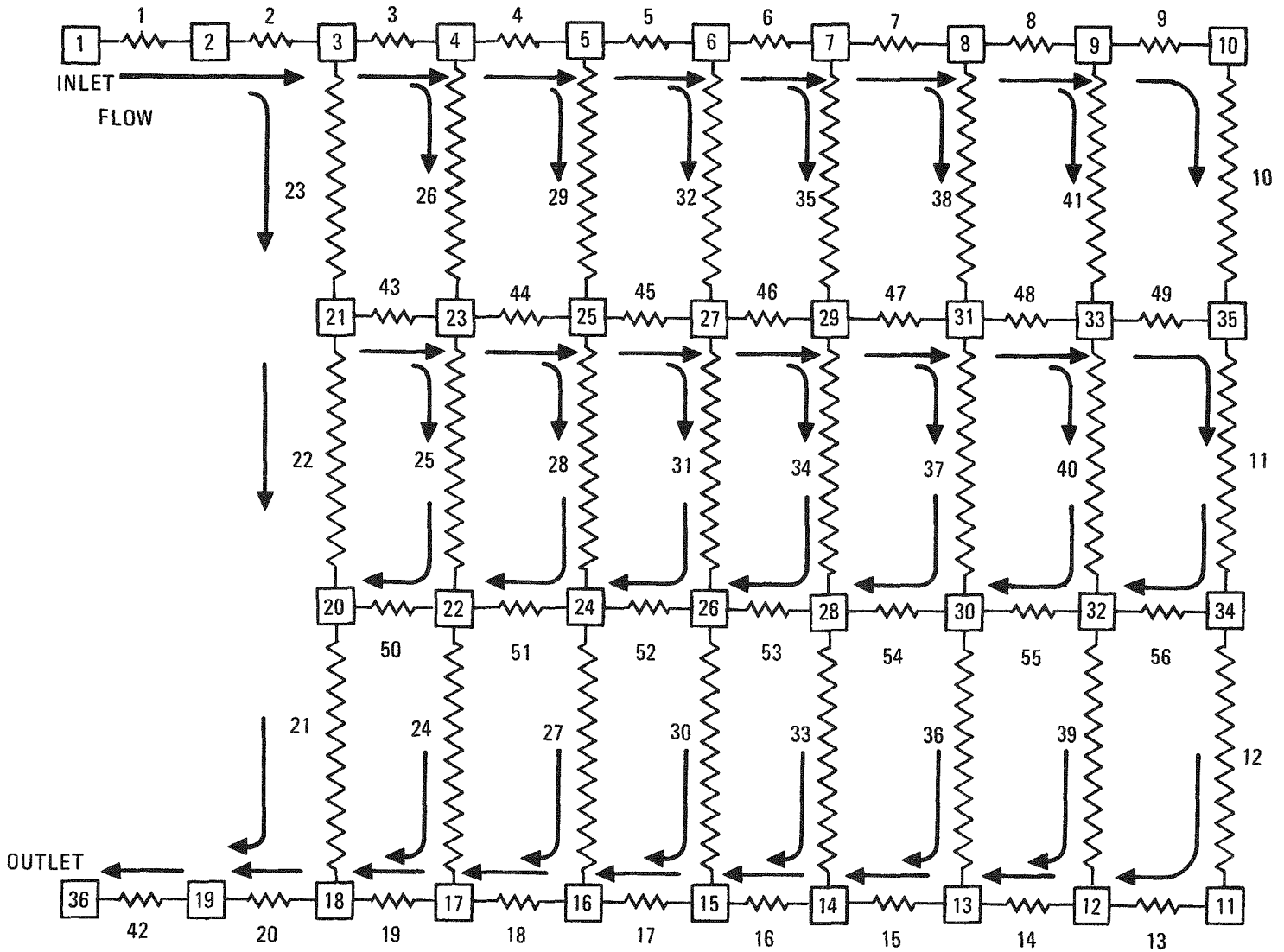

Fig. 4-2. Shell-side flow network

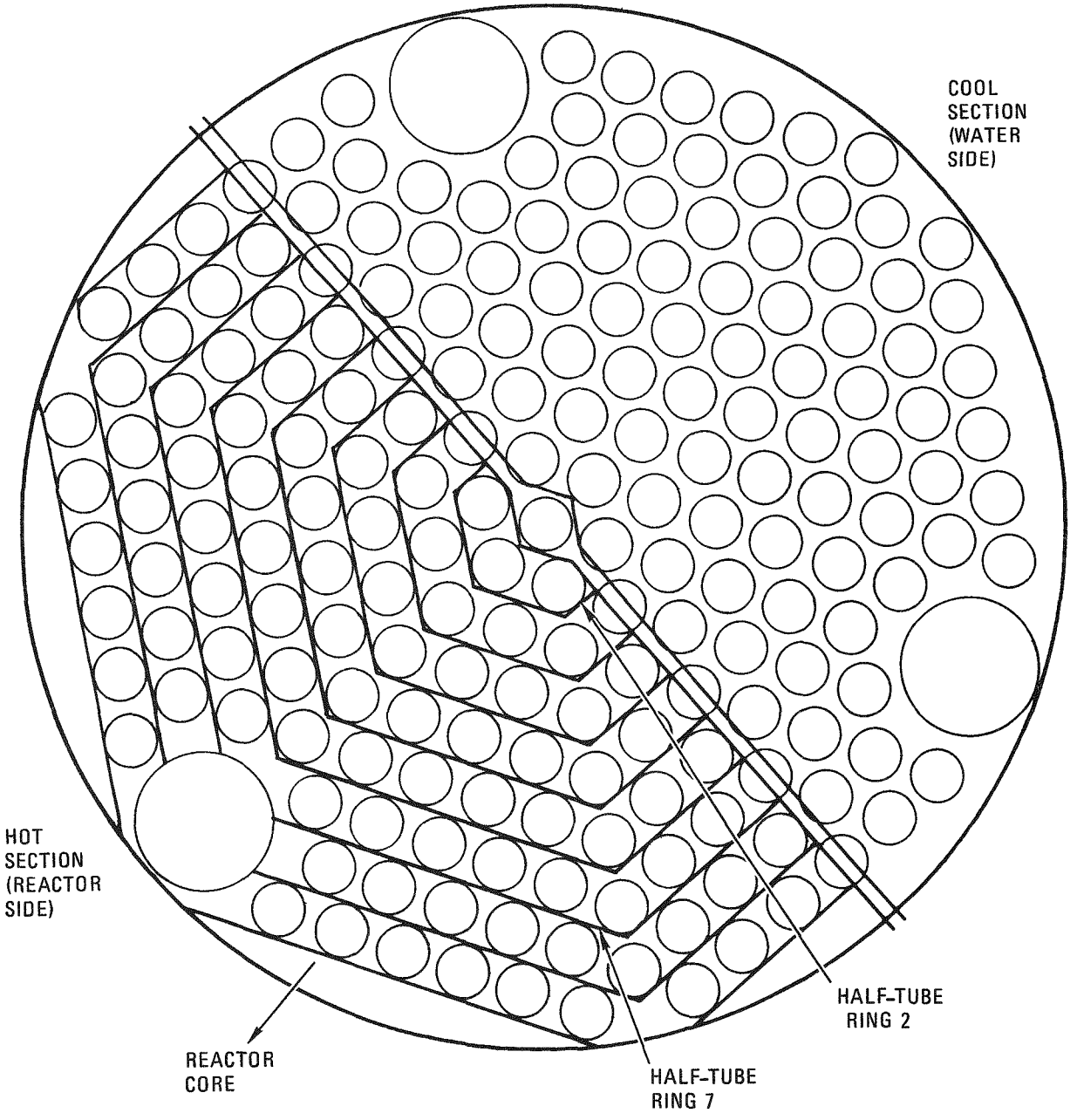

Fig. 4-3. Cross section of heat exchanger - recuperator showing half-tube rings

A schematic of the tube-side flow network is shown in Fig. 4-4. Nodes 1 and 19 function as the common inlet and outlet plenums, respectively. Branches 1 through 17 represent the frictional losses experienced by the fluid flowing through the tubes, where branch 1 is the central tube, 9 is the peripheral half-tube ring on the water side, and 10 is the peripheral half-tube ring on the reactor side. Nodes 2 through 18 function as the outlet of each half ring of tubes. The gas temperatures calculated at these nodes are compared to the measured values to determine when convergence has been attained. However, in order to join all the parallel flow branches to a common outlet plenum for computational efficiency, branches 18 through 34 were added to branches 1 through 17, respectively. These additional branches were modeled as the constant loss at the exit of each half-tube ring. These branches offer resistance to flow which is at most an order of magnitude less than the resistances in branches 1 through 17. Therefore, although the network does not model the actual configuration exactly, the results should reflect the distribution of flow into the tube side, without the influence of geometrical effects, quite accurately.

Table 4-2 gives the calculated Reynolds number through each branch of the tube-side flow network to illustrate the transitional nature of the tube-side flow. Figure 4-5 shows the calculated tube-side gas outlet temperature distribution and also the value and location of the measured temperatures.

The flow analysis results show that because of the high degree of fluid turbulence on the outside of the tube compared to the flow through the inside of the tube, the wall temperatures for a significant portion of the tube were closer to the shell-side gas temperatures. In addition, the distribution was found to be quite different from the linear approximation.

In confirmation of the flow analysis results, heat balances using calculated wall temperatures were performed. The temperature distributions of the gas on both the tube and shell side were calculated, and an energy

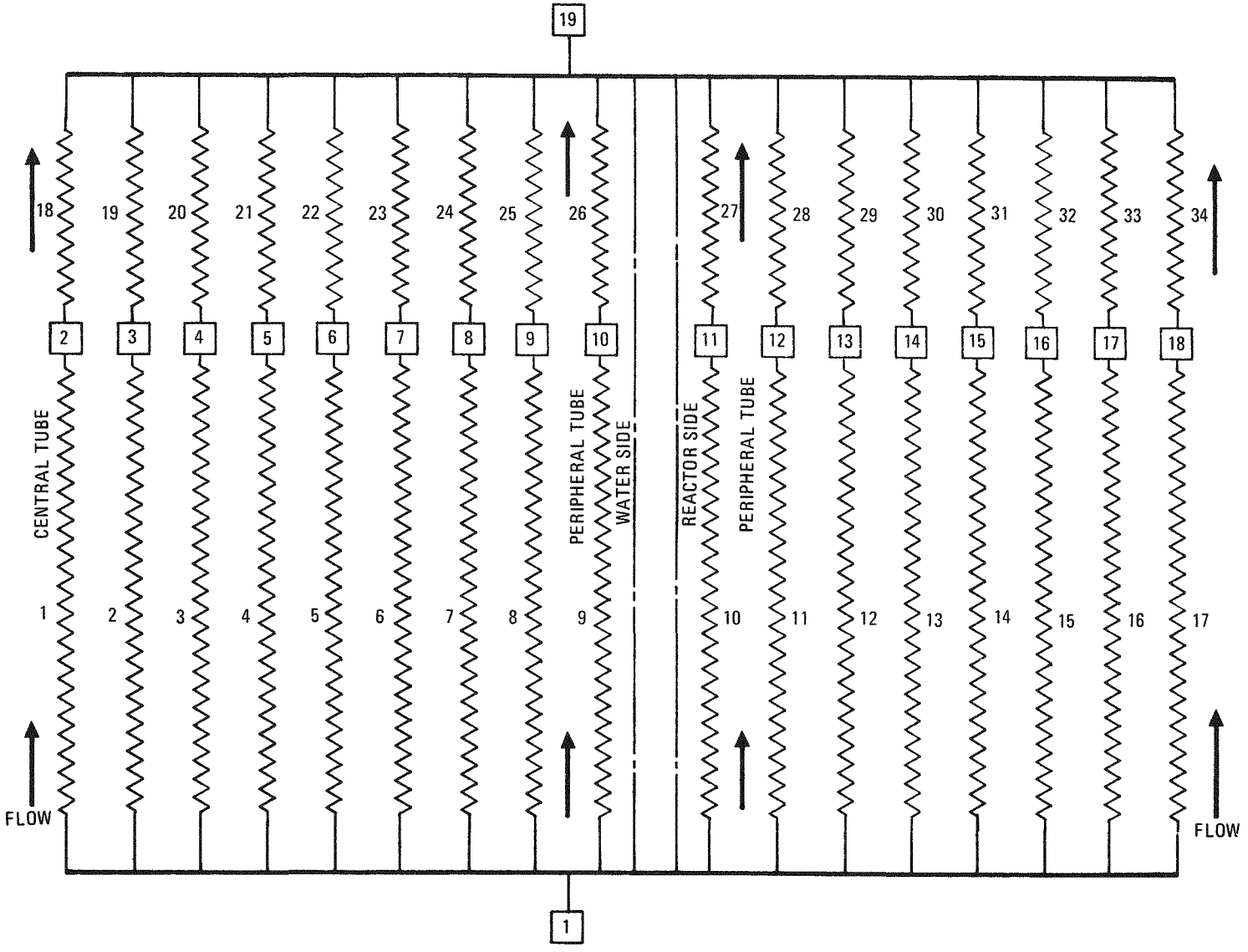

Fig. 4-4. Tube-side flow network

TABLE 4-2
HALF-TUBE RING FLOW RATES AND REYNOLDS NUMBERS

Flow Branch No.	Reynolds Number
Central tube	
1, 18	3377
2, 19	3383
3, 20	3387
4, 21	3394
5, 22	3402
6, 23	3409
7, 24	3417
8, 25	3421
Peripheral tube	
9, 26 (water side)	3431
10, 27 (reactor side)	3405
11, 28	3401
12, 29	3398
13, 30	3395
14, 31	3391
15, 32	3387
16, 33	3383
17, 34	3380

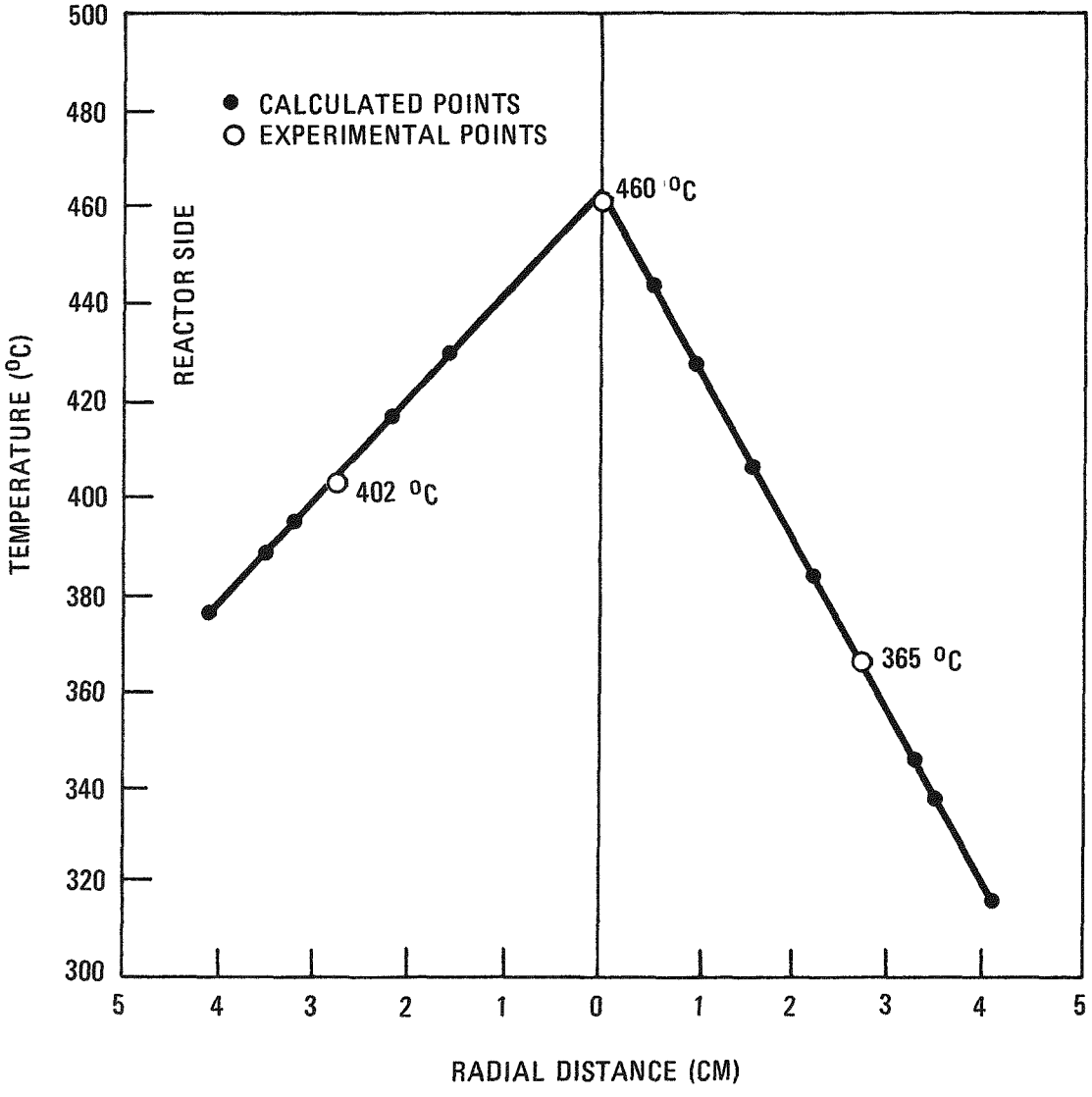

Fig. 4-5. Tube-side gas outlet temperatures

balance was performed for each row of tubes. This was done to confirm that the quantity of heat removed from the tube-side gas flow was equal to the heat accepted by the shell-side gas flow using the calculated temperature profiles. Results show that the gas temperature distributions, and therefore the wall temperature distributions, satisfy the heat transfer balance.

FIPER Validation Utilizing Data From the SSL-1 In-Pile Loop Test

An analysis of the release of Cs-137 from the fuel element of the Commissariat a L'Energie Atomique (CEA) Saclay Spitfire Loop (SSL-1) (Ref. 4-4) has been performed. This is a step toward validation of (i.e., checking the accuracy of) design methods (FIPER and TRAFIC codes) (Ref. 4-5) used to predict fission product metal release from HTGR fuel elements. This work is a part of the Fission Product Transport Code Validation Program (Ref. 4-3). The provisional results of this work are summarized in Table 4-3.

TABLE 4-3
MEASURED AND PREDICTED QUANTITIES OF Cs-137 AND ASSOCIATED UNCERTAINTIES DERIVED FROM THE SSL-1 LOOP TEST

Property Evaluated	Measured Values		Predicted Values	
	Nominal	Uncertainty (1σ)	Nominal	Uncertainty (1σ)
Total Cs-137 release	28 μCi	±18 μCi	15 μCi	+430 μCi -14.5 μCi
Sorption ratio at rod layer	1	+500% -80%	3	+500% -80%

The nominal predicted and measured releases (15 and 28 μCi, respectively) agree within a factor of two, which is considered to be good agreement in view of the complexity of the analysis and the uncertainties involved. The magnitude of the uncertainties is included in Table 4-3.

The calculated release was especially sensitive to the uncertainty in the diffusion coefficient for Cs in graphite, reflecting the need for additional work to reduce this uncertainty.

A value of the sorption ratio, which is the ratio of the concentration of cesium in matrix to that in graphite, was measured to be 1.0 (+500%, -80%) at rod layer 4. From the reference design data used in FIPER calculations, a value of 3.0 (+500%, -80%) would be predicted. These two values agree within the uncertainty of the data, which is a satisfactory result.

The sequence of steps followed in comparing predicted and measured results is:

1. Prediction of nominal end-of-life cesium release using preirradiation, operational, and postirradiation examination (PIE) data.

2. Determination of total cesium release observed during irradiation.

3. Comparison of predicted and observed cesium release (to supply calibration of FIPER).

4. Comparison of predicted and observed differential quantities (cesium profile in graphite, sorption ratio, etc.) to provide validation of individual FIPER modeling assumptions.

5. Estimation of uncertainties and calculation of sensitivity plots for each input parameter.

6. Assignment of uncertainties to the total release and differential quantities using the propagation-of-errors analysis (Ref. 4-6).

Although the results shown represent provisional conclusions, they exhibit satisfactory agreement and provide initial validation of fission metal transport methods. A detailed draft of this analysis has been completed and is in review (Ref. 4-7).

TASK 600: COOLANT IMPURITY/CORE MATERIAL INTERACTION

Subtask 620: Effect of Oxidation on the Mechanical Properties of Graphite

Introduction and Summary

An experimental program to measure the effect of steam oxidation on the mechanical properties of H-451 graphite is under way. The purpose of this work is to provide information for use in establishing the ability of the HTGR core to retain its structural integrity under conceivable conditions such as, for example, a seismic disturbance subsequent to exposure of the core to oxidizing impurities resulting from steam ingress. Analyses show that the burnoff (level of graphite oxidation) resulting from a slow, continuous steam leak is higher than that from a sudden massive leak. The latter is relatively unimportant because the reactor is rapidly and automatically shut down following detection of the leak.

In summary of the work to date, small cylindrical graphite samples, cored from selected locations in a log of H-451 graphite, were oxidized at 1073° and 1273°K in helium containing 3% water vapor and 5% H_2. After oxidation, the samples were mechanically tested with respect to ultimate tensile strength (UTS) and modulus of elasticity (E). The average rate of property change with burnoff at 1273°K for all burnoff ranges up to ∿20% was found to be quite low (average -3.6% UTS and -5.2% E per percent burnoff). However, when the strength data obtained for low burnoffs were subjected to statistical analysis (comparison of population means), no significant difference in UTS was found between nonoxidized controls and samples oxidized to up to approximately 2% burnoff.

Experimental Procedure

The following description of the experimental procedure is divided into three parts: (1) specimen preparation and sampling, (2) oxidation measurements, and (3) mechanical property testing.

Specimen Preparation and Sampling. Commercial graphite logs of the size used for fuel and reflector elements in HTGRs [0.43 m (17 in.) diameter by 0.86 m (34 in.) long] have been shown to have a nonuniform distribution of properties within a single log (Ref. 4-8). It has been observed, for example, that the tensile strength and elastic modulus of H-451 graphite are highest in the axial direction (parallel to extrusion), lowest at the midlength center (MLC) of a log, and increase from the center to the edges (Ref. 4-8). Samples for oxidation and mechanical property measurements were selected from quarter-length center (QLC) and quarter-length edge (QLE) positions of a single log (GA No. 6384-34) in order to determine the effect of oxidation on both the highest and lowest strength materials. Samples of both axial and radial orientations were selected as indicated in Figs. 4-6 through 4-9. A single quarter-length slab of H-451 graphite was taken from a representative H-451 log (Fig. 4-6). This slab was sectioned into two center sections and two edge sections, as shown in Fig. 4-7. Specimens, 7.93 mm (5/16 in.) in diameter and 63.4 mm (2.5 in.) long, were core drilled from each section, as shown in Figs. 4-8 and 4-9, and were finished (machined) to 6.34 mm (0.25 in.) diameter by centerless grinding.

Groups of samples were randomized and allocated for oxidation according to Table 4-4. Samples were oxidized in 63.4 mm (2.5 in.) lengths. After oxidation, approximately 0.6 mm (0.25 in.) was removed from each end of each oxidized sample (core). Each sample was then cut in half to provide two 6.34 mm (0.25 in.) diameter by $\sim$2.3 mm (0.9 in.) long mechanical property specimens.

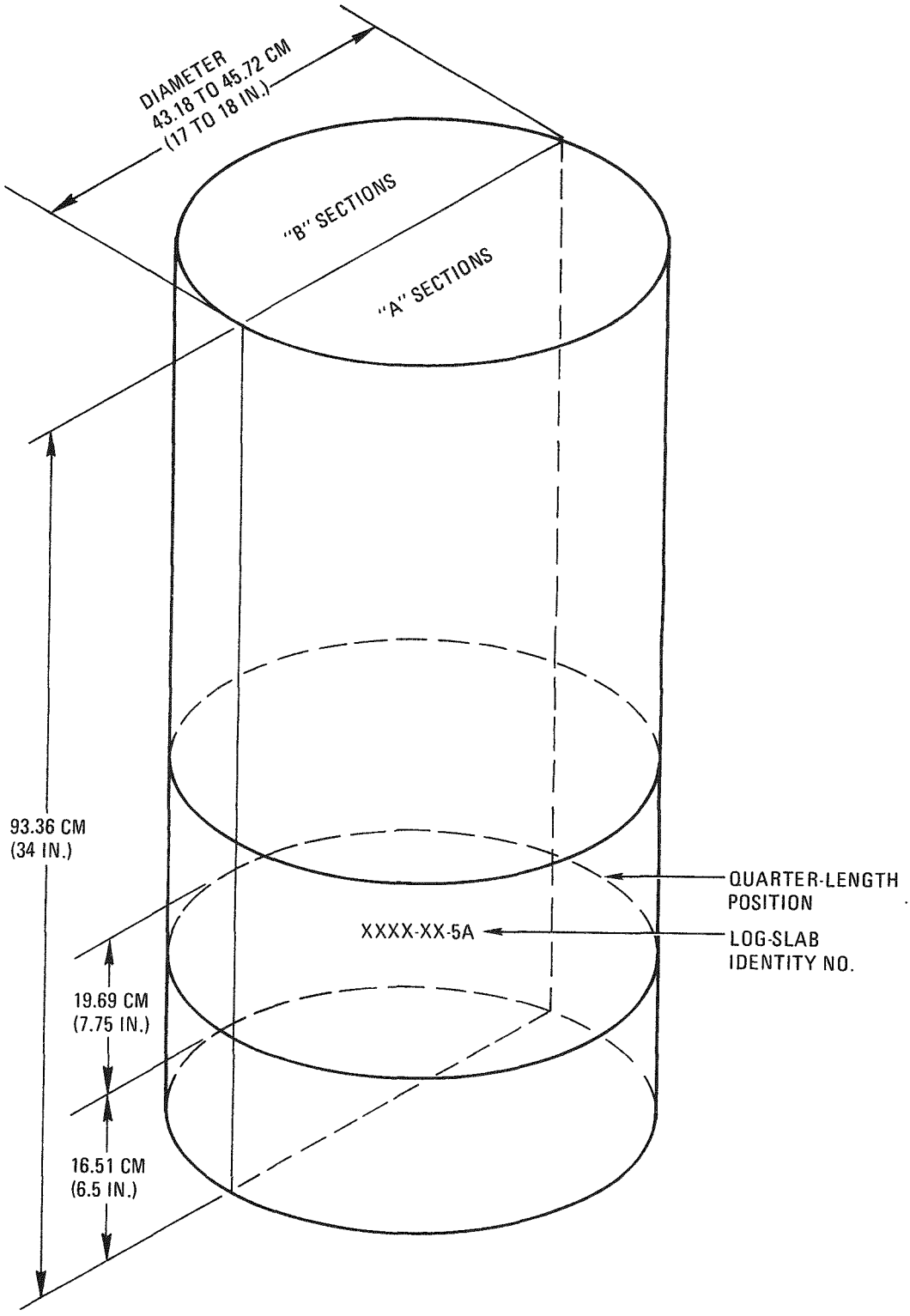

Fig. 4-6. Sampling plan of graphite log showing material (slab) designated for oxidation tests

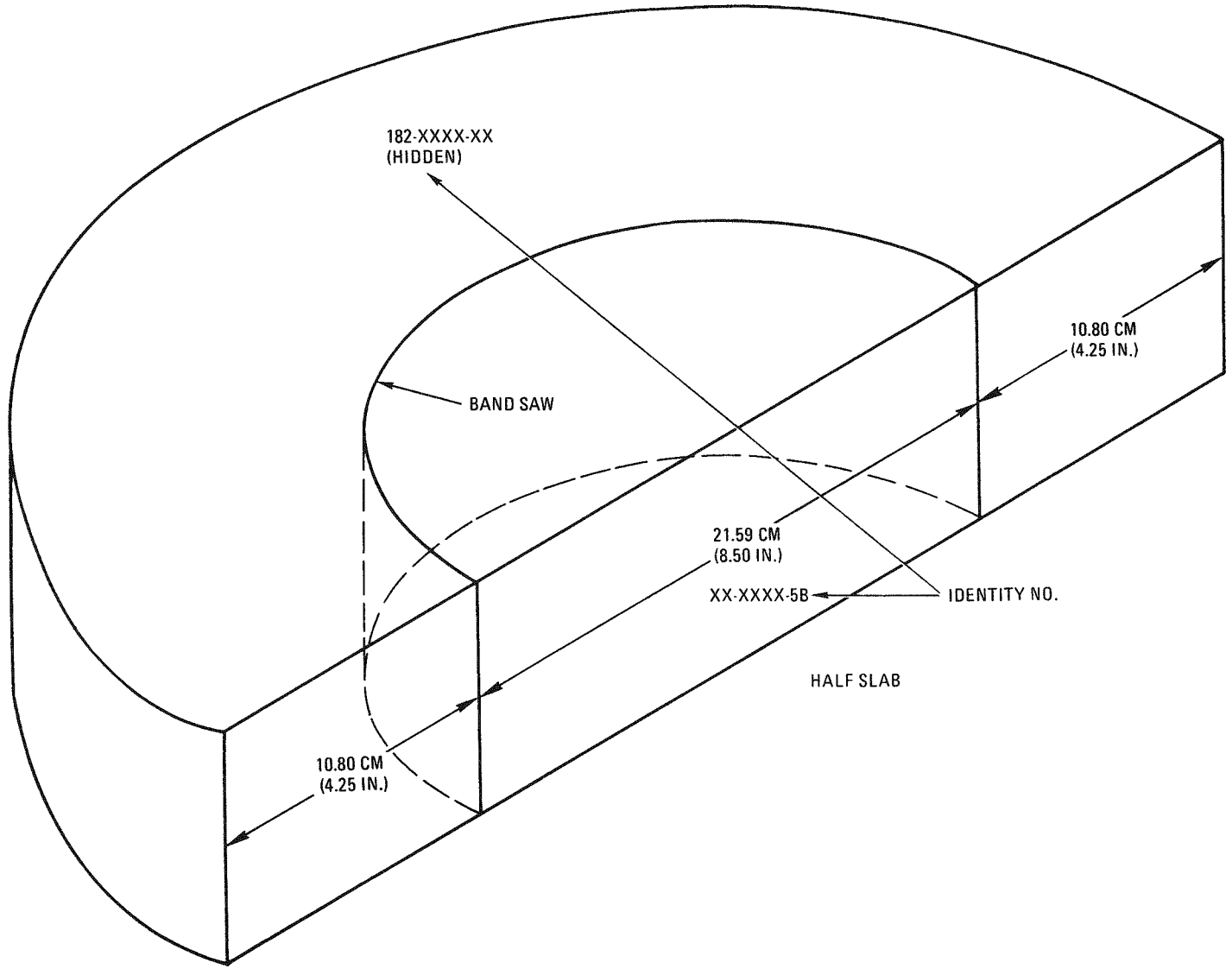

Fig. 4-7. Slab sectioning

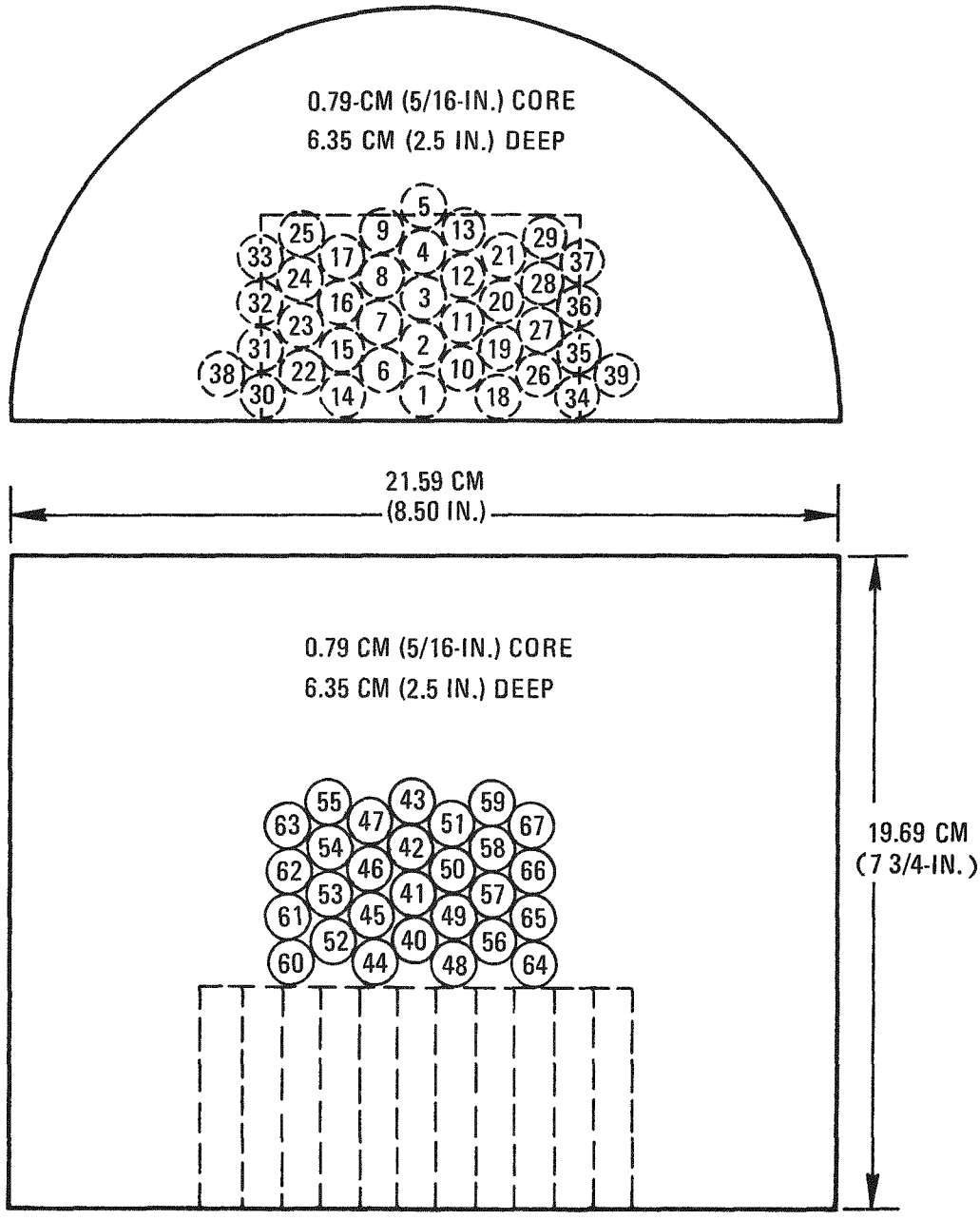

Fig. 4-8. Oxidation study core sampling plan - slab 5A/5B center

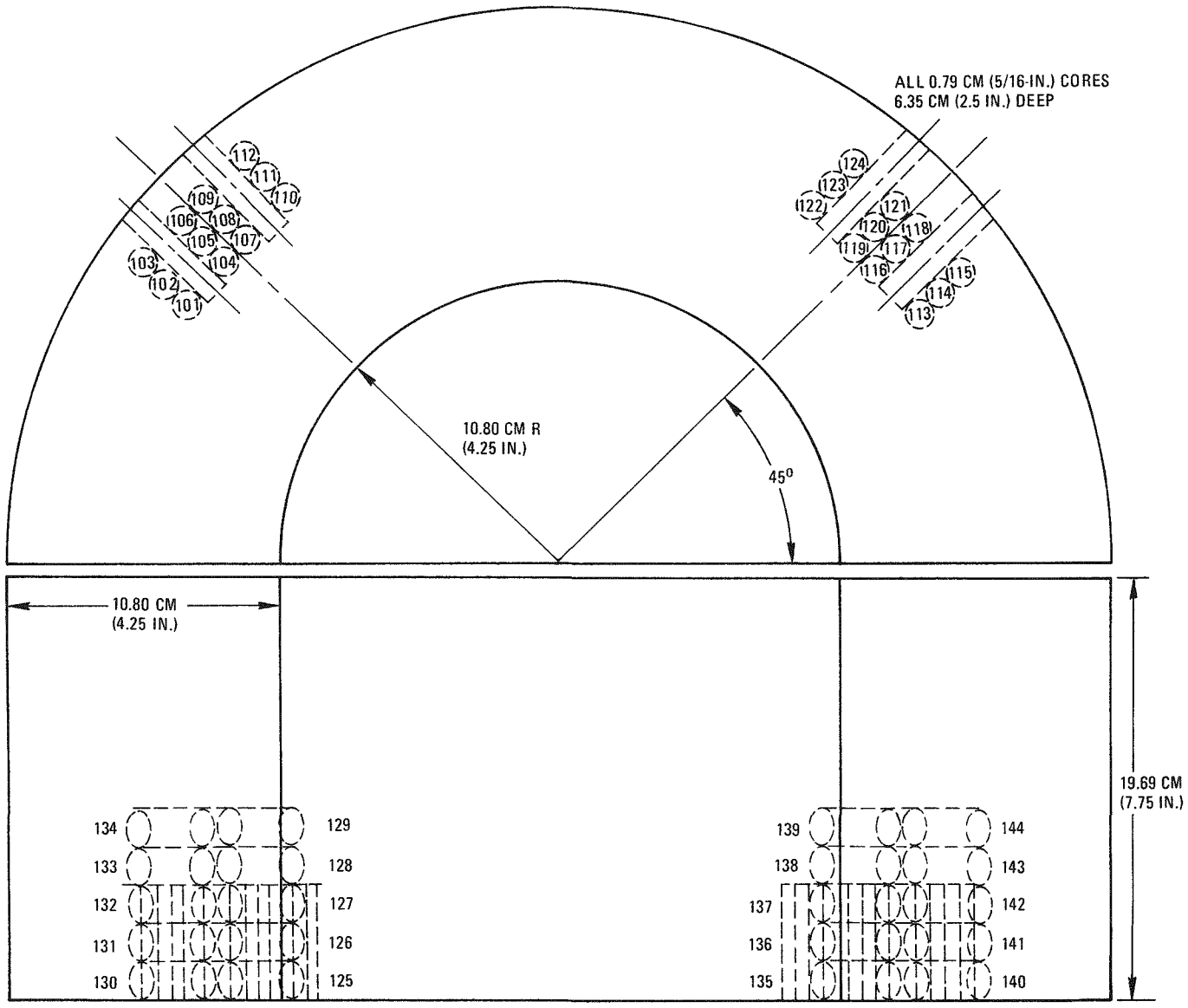

Fig. 4-9. Oxidation study core sampling plan - slab 5A/5B edge

TABLE 4-4
ALLOCATION OF GRAPHITE SAMPLES[a] FOR OXIDATION STUDIES

	Parallel (Axial) Orientation							Perpendicular (Radial) Orientation		
	Controls	1%[b] 1073°K	2% 1073°K	4% 1073°K	1% 1273°K	2% 1273°K	4% 1273°K	Controls	4% 1073°K	4% 1273°K
					QUARTER-LENGTH CENTER					
6484-34-5AC	1	2	3	4	8	10	7	43	42	40
	5	13	6	15	14	12	9	49	48	50
	16	17	18	25	19	22	11	54	52	56
	20	26	21	28	32	24	27	60	55	59
	33	31	23	34	35	29	30	64	62	61
	37		36	38			39	66	65	63
6484-34-5BC	11	1	4	3	2	8	5	40	41	45
	14	7	15	6	12	13	10	47	43	48
	21	9	29	17	25	18	16	52	44	51
	24	28	30	19	27	22	20	57	54	61
	26	33	32	23	31		35	59	58	65
	38		34	36		39	37	62	63	67
					QUARTER-LENGTH EDGE					
6484-34-5AE	101			103			102	128	126	129
	106			107			109	132	127	130
	111			112			110	134	133	131
	116			114			113	136	137	135
	121			118			117	138	141	143
	122			119			124	139	142	144
6484-34-5BE	103			102			101	129	126	125
	104			106			105	131	132	127
	112			108			111	122	134	128
	115			113			114	136	137	135
	117			116			120	141	138	139
	123			122			124	144	142	143

[a] Samples cored from H-451 graphite log 6484-34.

[b] Planned percent burnoff and temperature of oxidation.

Oxidation Measurements. A diagram of the apparatus used for the oxidation measurements is given in Fig. 4-10. Several of the cylindrical graphite samples were oxidized simultaneously in each experiment. The samples were supported by racks made from H-451 graphite and contained in inert quartz vessels. The quartz vessels were heated to 1073° or 1273°K in clamshell resistance furnaces. Temperatures were controlled to within ±10°K. During the oxidation phase, the vessels were purged with a gas mixture composed of 3% water vapor, 5% hydrogen, and the balance helium. The purge gas entered the vessels via a quartz tube which penetrated the length of the vessels along the bottom, under the graphite sample racks. Gas entered the vessels through holes drilled along the length of the entry tube. In this way the process gas contacted all samples in a relatively uniform manner. A flow of 16.67 cm^3/sec of process gas was maintained throughout the tests. During periods of heatup and cooldown, inert helium was purged through the reaction tubes.

To determine the extent of oxidation, the oxidation was interrupted periodically; the samples were allowed to cool and were then weighed on an analytical balance to ±0.1 mg accuracy. The burnoff (percent oxidation) was calculated from changes in sample weight.

It was anticipated that use of small diameter samples [6.34 mm (0.25 in.)] in a hydrogen-rich gas mixture would ensure that oxidation would be relatively uniform throughout the bulk of the samples. Uniformity of oxidation was checked by determining radial density profiles on a number of both oxidized and nonoxidized samples using a lathe technique.

The cylindrical samples were carefully weighed and dimensioned to determine the apparent average density. The samples were then reduced in radius by predetermined increments using a precision lathe. The shavings were collected with the use of a small vacuum-filter device attached directly to the cutting tool. After each incremental cut, the sample was reweighed and dimensioned and the density of the material removed was calculated from the weight difference of the sample and/or the weight of the collected shavings.

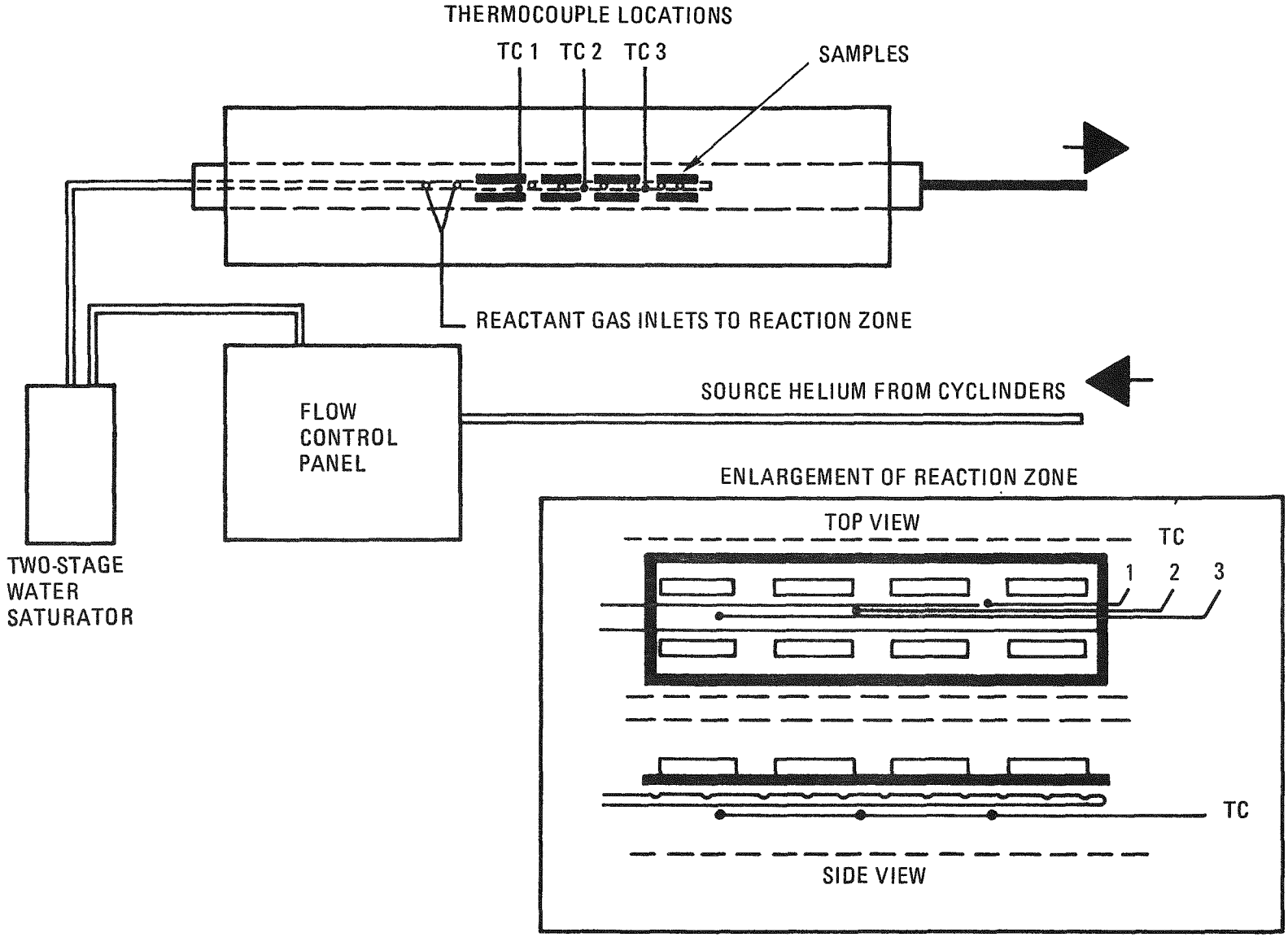

Fig. 4-10. Steam-graphite oxidation apparatus

Mechanical Property Testing. Tensile stress-strain curves were obtained in air at room temperature using an Instron tensile machine as described in Ref. 4-8. Tensile tests were conducted on 6.34 mm (6.25 in.) diameter by 23 mm (0.90 in.) long samples using a crosshead speed of 0.127 mm (0.005 in.)/min. Strains were measured using a 12.7 mm (0.5 in.) gage length nonaveraging clip-on extensometer. The samples were fixed to metal end pieces with high-strength epoxy cement, and the load was applied through roller-link chains to maintain uniaxial alignment during testing.

All samples were tested using a cyclic loading method. Each sample was loaded to 6.9×10^6 Pa (1000 psi) and the crosshead reversed. After unloading to approximately 6.9×10^5 Pa (100 psi), the crosshead was again reversed, and the sample was loaded until fracture occurred. A typical stress-strain curve obtained by this method is shown in Fig. 4-11.

Because of the inelastic component in the deformation of graphite, the unloading curve (dashed curve, Fig. 4-11) does not retrace the initial loading curve but reaches zero load with a positive "permanent set." The second loading curve generally superimposes on the unloading curve, and beyond the first strain reversal point it forms a continuation of the initial loading curve.

Samples tested for ultimate tensile strength only (no stress-strain curve) were loaded to failure without crosshead reversal. The tensile strength of all samples was calculated by dividing the load at fracture (stress corresponding to point q on the stress-strain curve, Fig. 4-11) by the original cross-sectional area of the specimen.

The modulus of elasticity of each specimen was calculated from its stress-strain curve as the slope of the chord (chord modulus) drawn between points on the second loading portion of the curve (chord rs, Fig. 4-11) corresponding to stresses of 6.9×10^5 Pa (100 psi) and 6.9×10^6 Pa (1000 psi). This chord modulus represents the effective modulus of a graphite component after its first stress excursion.

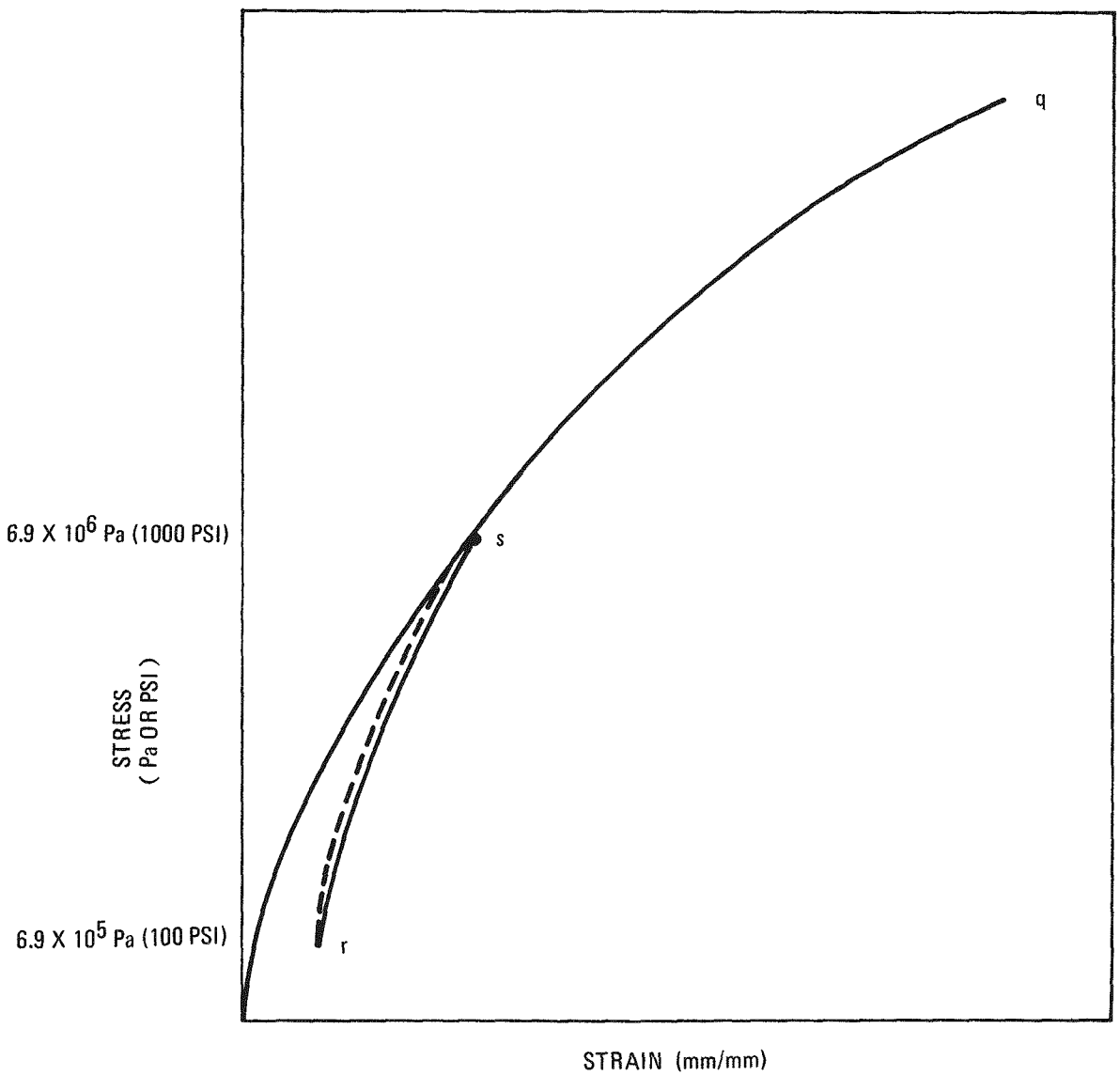

Fig. 4-11. Cyclic stress-strain curve for graphite

Results and Discussion

The results consist of (1) mechanical property (ultimate tensile strength and elastic modulus) data, and (2) density profile data.

Mechanical Property Data. The ultimate tensile strength (UTS) data are given in Figs. 4-12 and 4-13 and the elastic modulus (E) data are given in Figs. 4-14 and 4-15. The data are further summarized in Tables 4-5 and 4-6.

Statistical analyses were performed (1) to determine whether the distribution of UTS in this graphite log was Gaussian [using the chi-square analysis (Refs. 4-9,4-10)], (2) to compare population mean values of UTS and E for controls and oxidized samples [using the comparison of population means (CPM) test (Ref. 4-11)], and (3) to determine the maximum, minimum, and most probable (mean) rates of property change with burnoff for 95% confidence (using the CONFID computer code, derived from a technique given in Ref. 4-12).

The chi-square analysis verified that the distribution of UTS in this particular H-451 log was indeed Gaussian. This is in agreement with observations of Price and Cobb who studied statistical distributions of properties in other reactor graphites (Ref. 4-13). Verification of a Gaussian distribution is important since both the CPM test and the CONFID computer code assume Gaussian distributions.

The results of the CPM test are given in Table 4-5 and that of the CONFID analysis are shown in Table 4-6. In addition, the rates of property change as calculated by CONFID are presented graphically in Figs. 4-12 through 4-15, where the most probable rate changes are shown as linear regression fits of the data.

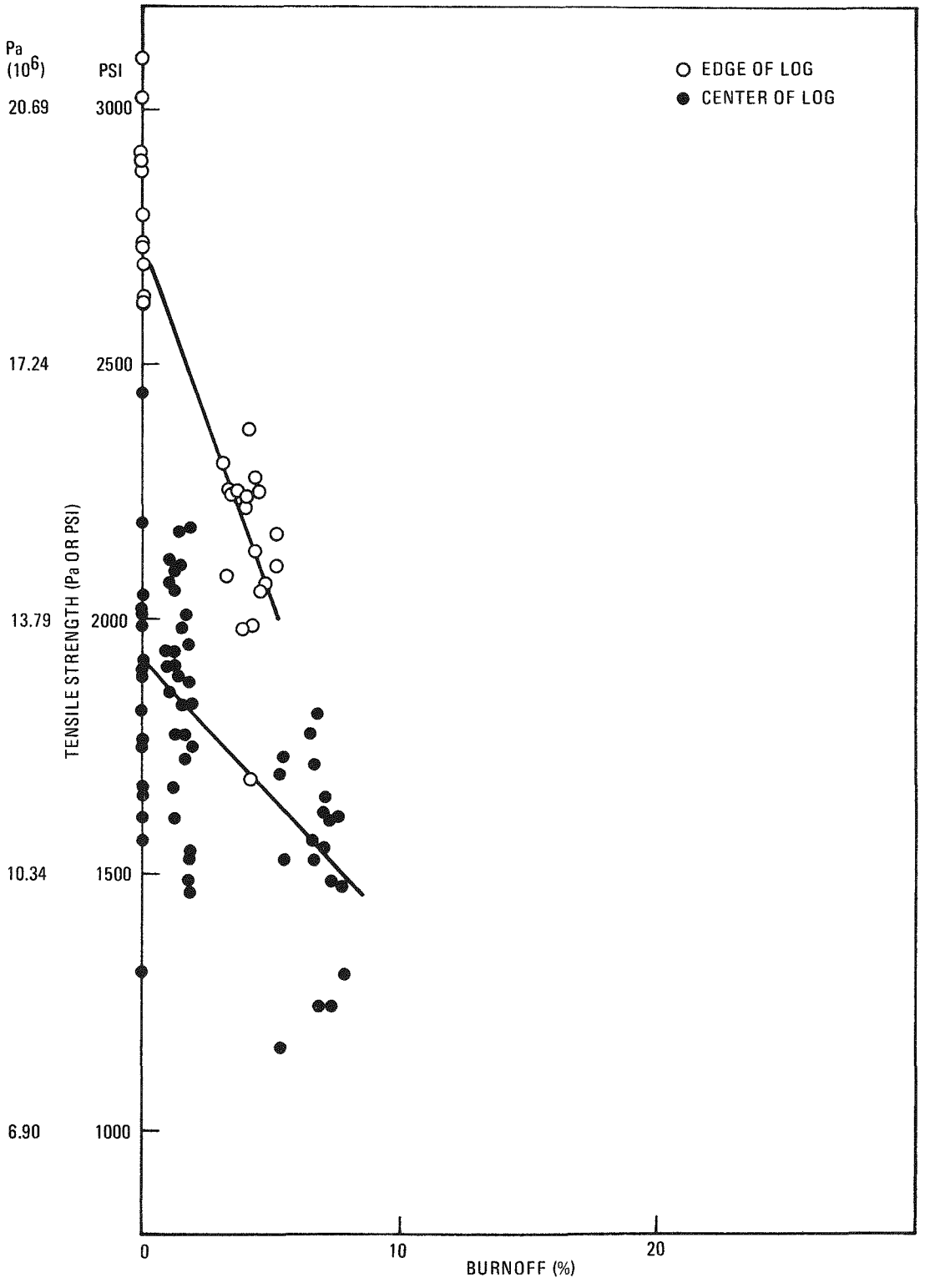

Fig. 4-12. Tensile strength versus burnoff for H-451 graphite, log 6484-34, oxidized at 1273°K: (a) quarter-length parallel samples

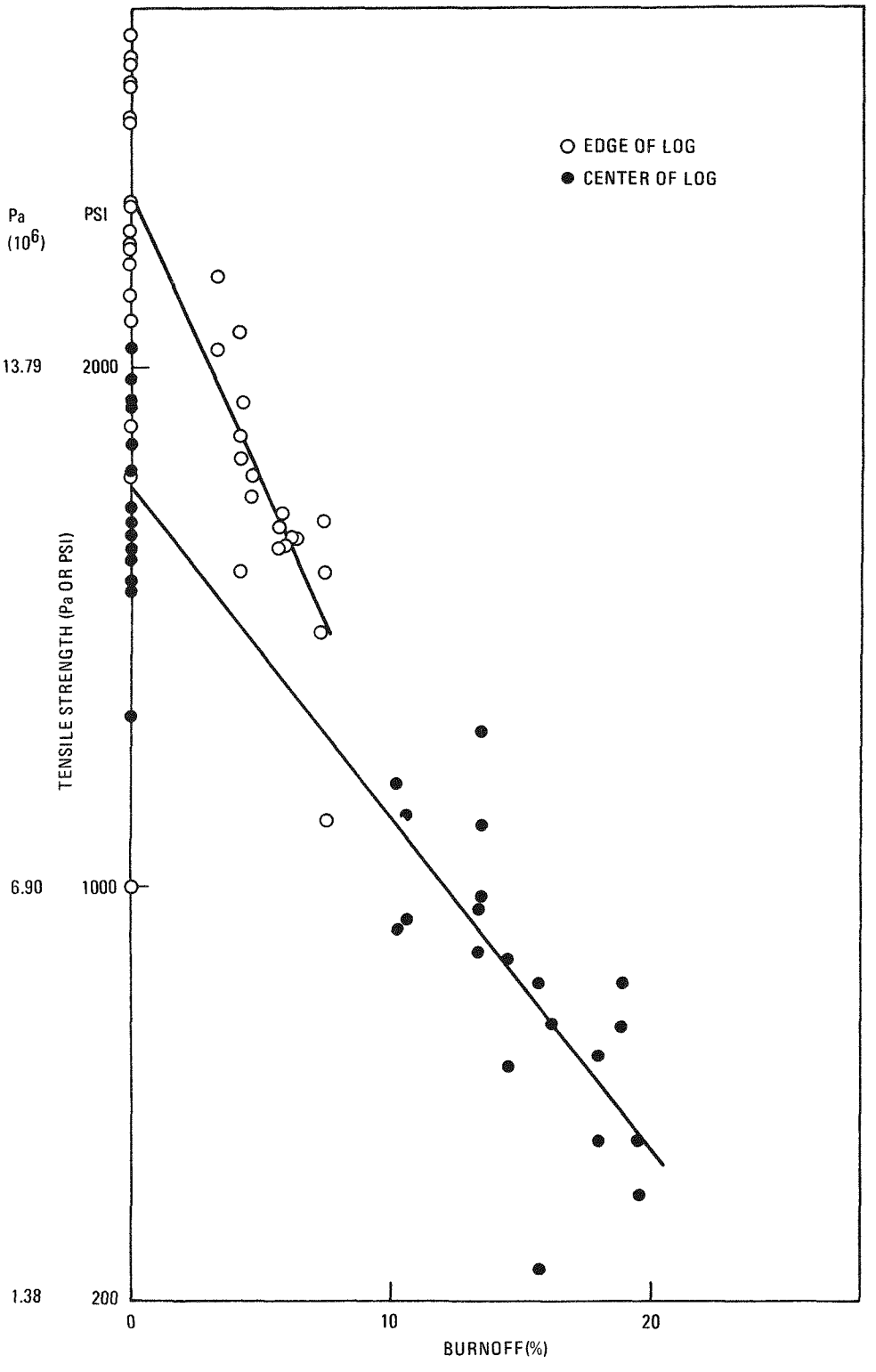

Fig. 4-12. Tensile strength versus burnoff for H-451 graphite, log 6484-34, oxidized at 1273°K: (b) quarter-length perpendicular samples

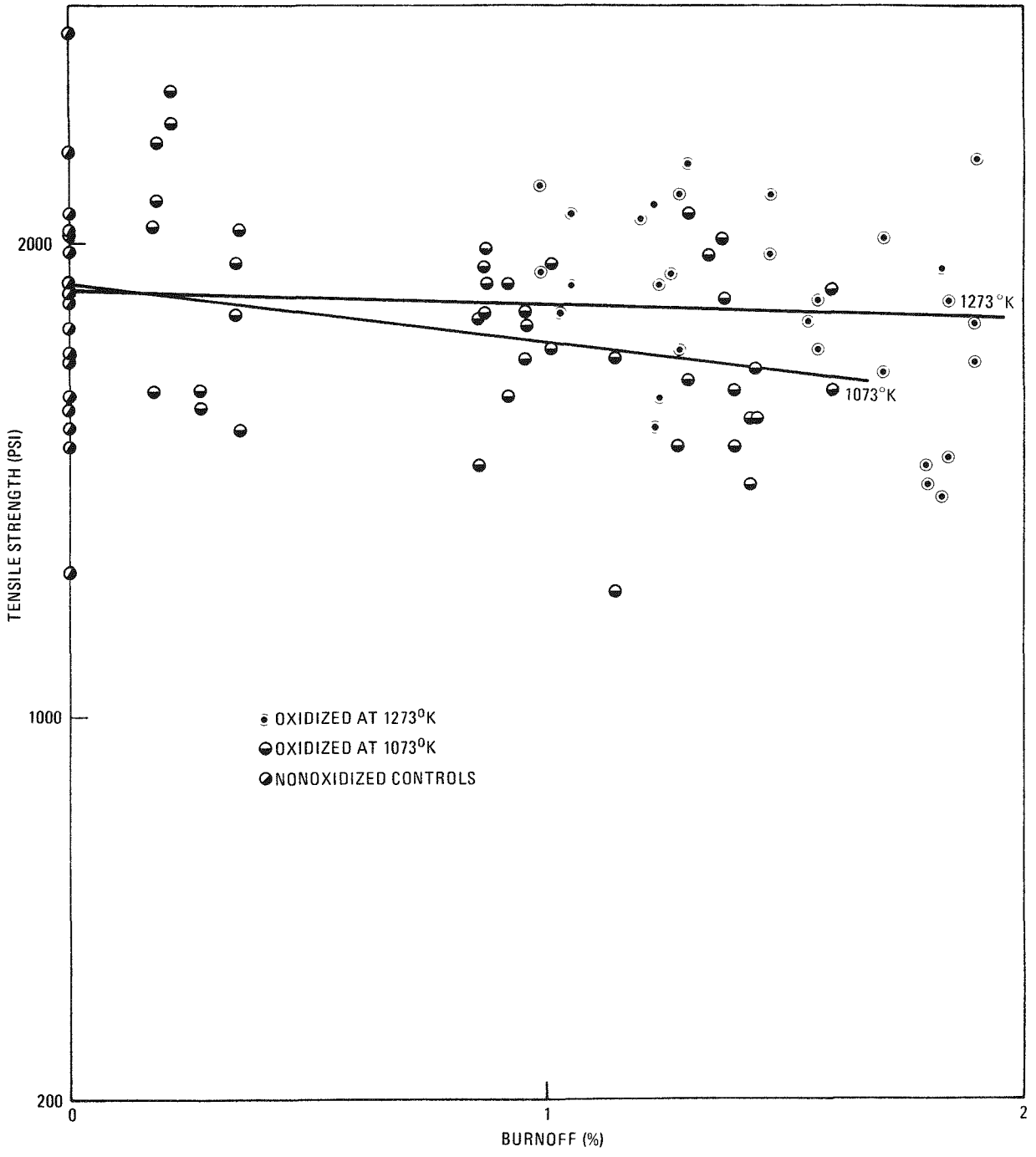

Fig. 4-13. Tensile strength versus burnoff for H-451 graphite, log 6484-34, quarter-length parallel center samples

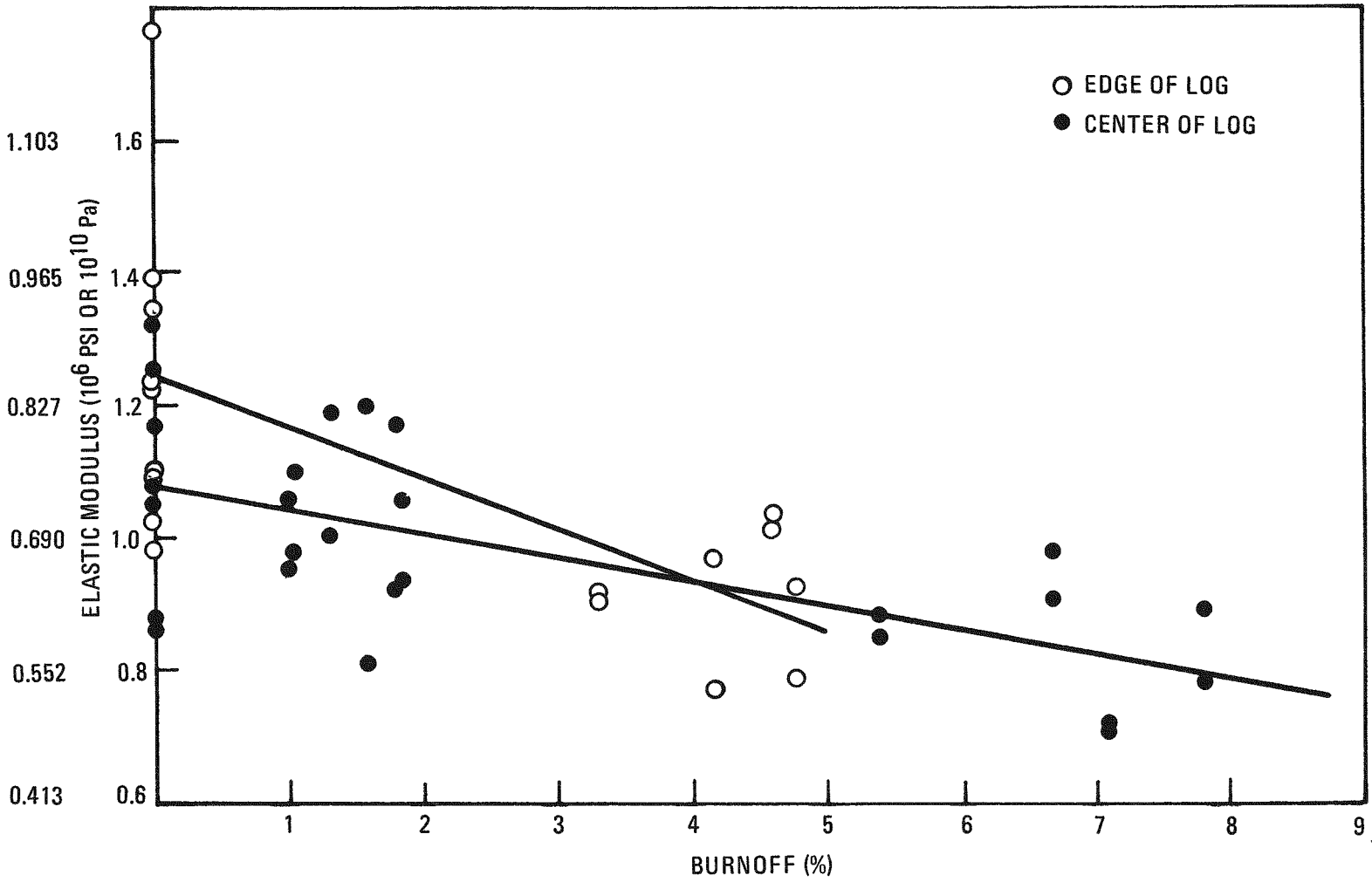

Fig. 4-14. Elastic modulus versus burnoff for H-451 graphite, log 6484-34, oxidized at 1273°K: (a) quarter-length parallel samples

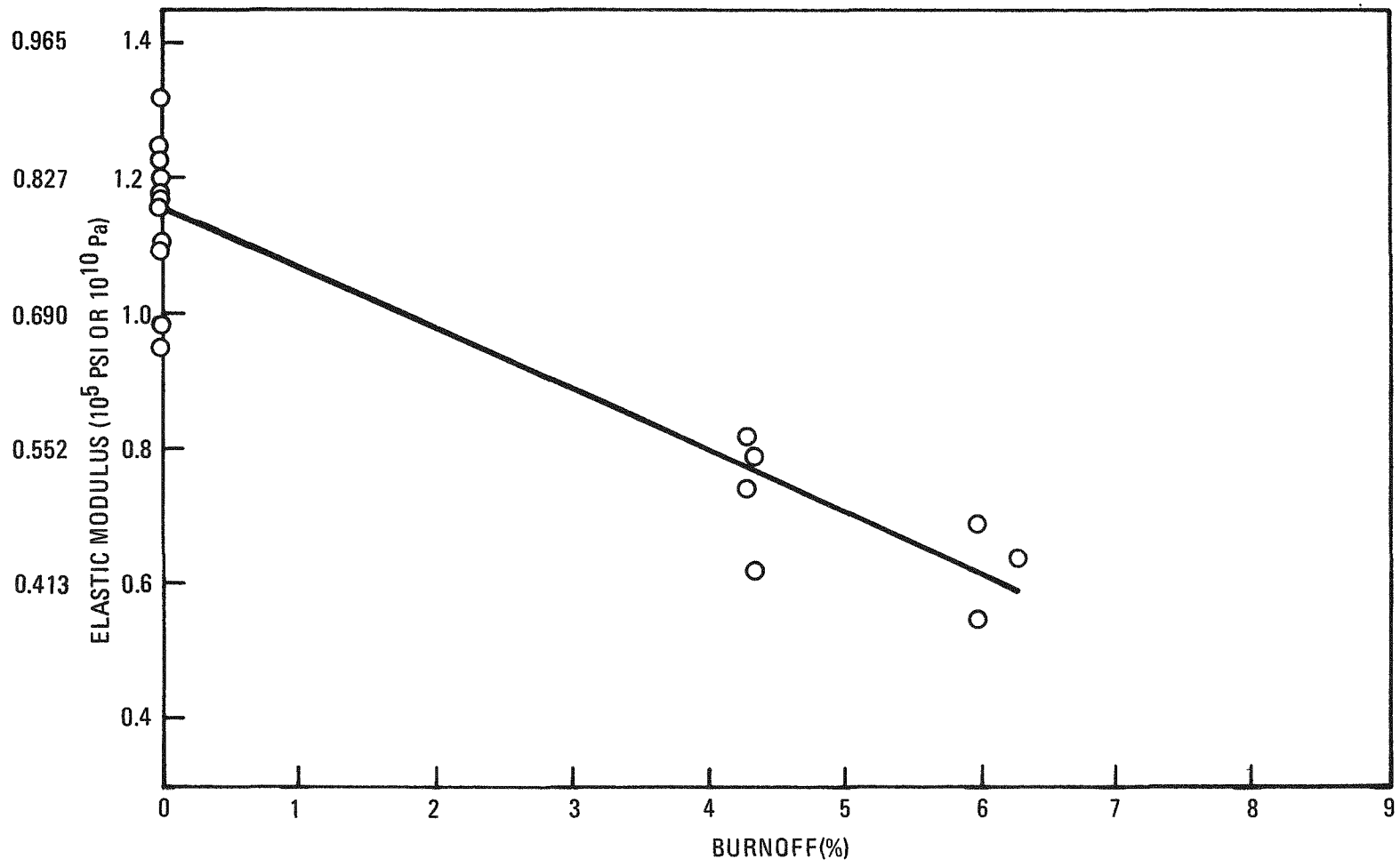

Fig. 4-14. Elastic modulus versus burnoff for H-451 graphite, log 6484-34, oxidized at 1273°K: (b) quarter-length perpendicular samples

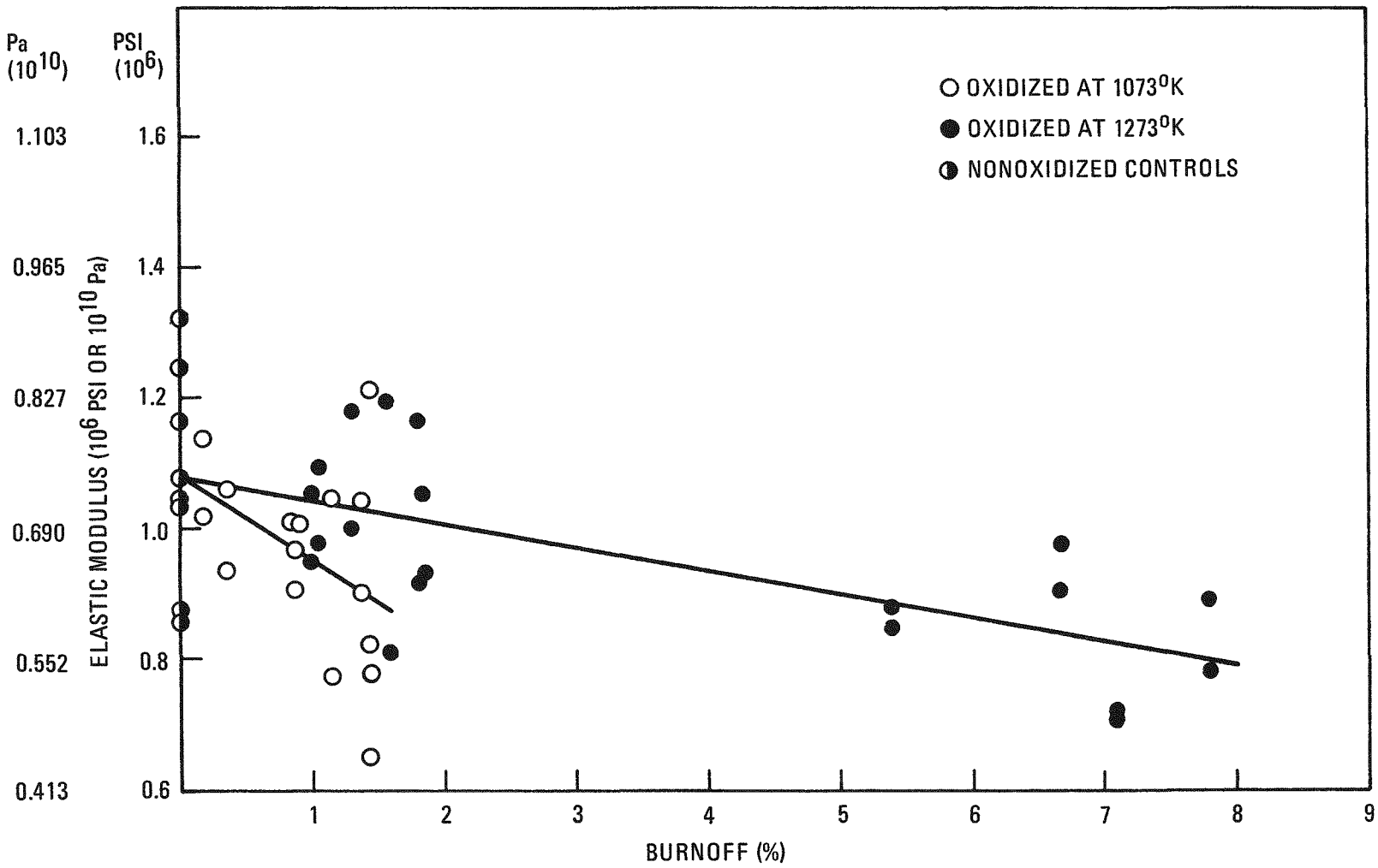

Fig. 4-15. Elastic modulus versus burnoff for H-451 graphite, log 6484-34, quarter-length parallel center samples

TABLE 4-5
SUMMARY OF MECHANICAL PROPERTIES AND COMPARISON OF POPULATION MEANS FOR QUARTER-LENGTH SAMPLES FROM H-451, LOG 6484-34

Location and Orientation[a]	Oxidation		Ultimate Tensile Strength						Elastic Modulus					
	Temp (°K)	Burnoff (%)	Mean (10^7 Pa)	Std. Dev.	Mean (psi)	Std. Dev.	No. of Data Points	CPM Test Results[b]	Mean (10^{10} Pa)	Std. Dev	Mean (10^6 psi)	Std. Dev.	No. of Data Points	CPM Test Results[b]
C (∥)	--	0	1.294	0.179	1877	260	19	--	0.7467	0.1120	1.083	0.162	8	--
C (∥)	1073	0.17- 0.36	1.338	0.168	1941	243	12	NSD	0.7164	0.0579	1.039	0.084	4	NSD
C (∥)	1073	0.86- 1.60	1.222	0.126	1772	183	29	NSD	0.6399	0.1041	0.928	0.151	12	SD
C (∥)	1273	0.99- 1.30	1.340	0.117	1943	169	14	NSD	0.7109	0.0572	1.031	0.083	8	NSD
C (∥)	1273	1.47- 1.90	1.247	0.149	1808	216	16	NSD	0.6950	0.1000	1.008	0.145	8	NSD
C (∥)	1273	5.38- 7.83	1.066	0.125	1546	182	20	SD	0.5792	0.0655	0.840	0.095	8	SD
C (⊥)	--	0	1.222	0.128	1773	186	20	--	0.6901	0.0586	1.001	0.085	9	--
C (⊥)	1273	10.2 -14.5	0.685	0.121	993	175	12	SD	--	--	--	--	--	--
C (⊥)	1273	15.7 -19.6	0.419	0.133	608	193	9	SD	--	--	--	--	--	--
E (∥)	--	0	1.893	0.174	2746	252	15	--	0.8563	0.1427	1.242	0.207	12	--
E (∥)	1273	3.3 - 5.2	1.480	0.107	2146	155	20	SD	0.6308	0.0655	0.915	0.095	8	SD
E (⊥)	--	0	1.614	0.183	2341	266	18	--	0.7956	0.0751	1.154	0.109	11	--
E (⊥)	1273	3.4 - 4.8	1.300	0.123	1886	178	9	SD	0.5109	0.0600	0.741	0.087	4	SD
E (⊥)	1273	5.8 - 7.6	1.094	0.125	1586	182	10	SD	0.4261	0.0407	0.618	0.059	4	SD
E (⊥)	1273	3.4 - 7.6	1.191	0.161	1728	233	19	SD	0.4688	0.0655	0.680	0.095	8	SD

[a] C (∥) means center samples, parallel (axial) direction.
E (⊥) means edge samples, perpendicular (radial) direction.

[b] NSD means there is no significant difference (95% confidence) between property averages of controls and oxidized samples.
SD means there is a significant difference (95% confidence) between property averages of controls and oxidized samples.

TABLE 4-6
REDUCTION IN ULTIMATE TENSILE STRENGTH AND ELASTIC MODULUS WITH OXIDATION

Location (Orientation)	Burnoff Temp (°K)	Burnoff Range (%)	% Reduction/1% Burnoff		
			Maximum (2.3% Probability)	Mean (Most Probable)	Minimum (2.3% Probability)
ULTIMATE TENSILE STRENGTH					
QLC (∥)	1073	0-2	11.92	6.38	0.0
QLC (∥)	1273	0-2	7.32	1.73	-4.32
QLC (∥)	1273	0-8	3.85	2.82	1.70
QLE (∥)	1273	0-6	6.48	5.14	3.74
QLC (⊥)	1273	0-20	3.92	3.59	3.18
QLE (⊥)	1273	0-8	5.93	4.79	3.72
Average (1273°K)			5.5	3.6	1.6
ELASTIC MODULUS					
QLC (∥)	1073	0-2	22.43	12.04	-0.33
QLC (∥)	1273	0-2	11.56	3.71	-5.51
QLC (∥)	1273	0-8	4.88	3.26	1.45
QLE (∥)	1273	0-5	9.53	6.10	1.96
QLE (⊥)	1273	0-6	9.31	7.83	6.11
Average (1273°K)			8.8	5.2	1.0

Ultimate tensile strength and elastic modulus values for nonoxidized control material were observed to be highest in the axial direction and increased from center to edge, as illustrated in Table 4-7. The obtained UTS and E values are in general agreement with other data obtained for this log (Ref. 4-8) and other logs of H-451 graphite.

TABLE 4-7
MEAN ULTIMATE TENSILE STRENGTH AND ELASTIC MODULUS FOR NONOXIDIZED CONTROL H-451 SAMPLES (LOG 6384-34)

	Axial (parallel)		Radial (perpendicular)	
Location	UTS (psi)	E x 10^6	UTS (psi)	E x 10^6
QLC	1877 ± 260	1.083 ± 0.162	1773 ± 186	1.001 ± 0.085
QLE	2746 ± 252	1.242 ± 0.207	2341 ± 266	1.154 ± 0.109

A comparison of UTS values obtained for oxidized and nonoxidized materials showed that strength decreases with oxidation. To arrive at an estimate of when UTS significantly changes with oxidation, the population means of the treated samples were compared with the controls. These results are summarized in Table 4-5, column 9. Briefly, the results of the CPM test indicate that at a 95% level of confidence no significant loss in UTS was observed in samples that were oxidized in the 0 to 2% burnoff range. Figure 4-13 graphically illustrates the probability that no significant loss of strength occurred in the 0 to 2% burnup range. Thus far, only QLC(11) samples were tested in this early burnoff interval. Statistically significant decreases in strength at higher degrees of oxidation were noted for all sample types.

Figure 4-12a compares the UTS losses of parallel samples oxidized at 1273°K. For both center and edge positions the strength decreased with burnoff, but the relative loss in strength was clearly greater for the stronger edge material. In fact, the rate of decrease in strength for edge

samples appears to be almost twice that observed for center material. This result, although interesting, is of little significance with respect to fuel element strength because (1) the design strength is always taken as a fraction of the minimum (or center) strength of the log, and (2) the strength of the oxidized edge material never is less than that of the center samples for the 0 to 2% burnoff range. As shown in Fig. 4-12b, strength versus oxidation was also examined with respect to radial (perpendicular to axis) orientation. A similar decrease in strength with burnoff was observed.

The effect of burnoff temperature on UTS versus oxidation was examined over a narrow burnoff range (0 to 2%). Figure 4-13, a plot of QLC(11) samples, summarizes all the data obtained for material oxidized at 1073° and 1273°K in the 0 to 2% range. It is of interest that the slope of the linear fit of the 1073°K oxidized samples is slightly greater than that of the samples oxidized at 1273°K.

Data on the effect of oxidation on elastic modulus are plotted in Figs. 4-14 and 4-15, with their respective linear regression fits. A comparison of the mean modulii shows a decrease with oxidation for both parallel and perpendicular orientations and both edge and center positons. A significant decrease in mean elastic modulus for 1073°K data was noted at the 1% burnoff level, whereas at 1273°K a decrease in mean modulus was not detected until 2% burnoff was exceeded (for example, see results of the CPM tests in Table 4-5, column 15). Decreases in modulii of edge material again exceeded those decreases observed for the center location.

The effect of burnoff temperature on elastic modulus is illustrated in Fig. 4-15. In this figure the 0 to 2% burnoff data obtained at 1073°K and 1273°K on parallel samples are compared. When superimposed, the linear lines indicate that the rate of decrease at 1073°K is about three times that obtained at 1273°K.

Table 4-6 summarizes all of the trends in both modulus and UTS by comparing the relative reduction in each property at 1% burnoff. These results were obtained with the computer code CONFID (see above) which at 95% confidence calculated the most probable or "mean" (50% probability) decrease in property and the maximum and minimum (2.3% probability) decrease in property. The 1073°K oxidations caused about twice the reduction in UTS and E as compared to the oxidations at 1273°K. Also, as noted previously, changes in mechanical properties were greater for the edge material as compared to center samples. This phenomenon was particularly obvious in modulus decrease, where at 1273°K the average decrease in edge sample modulus was twice that of center sample modulus.

Density Profile Data. Density profiles for an unoxidized control sample of H-451 and for three oxidized samples are given in Fig. 4-16. The large scatter in the data is due to difficulties in measuring small changes in weight and dimension on such a heterogeneous material as graphite. Also, even though care was taken to provide perfectly smooth and uniform cuts, the rather large grain size of H-451 graphite possibly contributed to some tearing out of graphite chunks, which would lead to inhomogeneity in sample weights from cut to cut. The scatter tended to average out, however, as many cuts were taken across a radial dimension of about 1.5 mm (total initial diameter of 6.3 mm). The final central core of the samples (diameter $\sim$3 mm) was used as the final data point and in all cases confirmed the apparent density trends of the smaller cuts near the outside of the samples.

The results of the oxidized samples show that in all cases at 1073° or 1273°K the oxidation profiles are quite uniform. It was anticipated that at 1273°K some preferential oxidation on the outer surface of the samples would occur; that is, the final sample radial density profile after oxidation should increase from outside to inside such as occurred in sample 124B (Fig. 4-16c). In some other cases, as shown in Fig. 4-16d, the 1273°K oxidation produced quite a uniform oxidation profile. This was generally

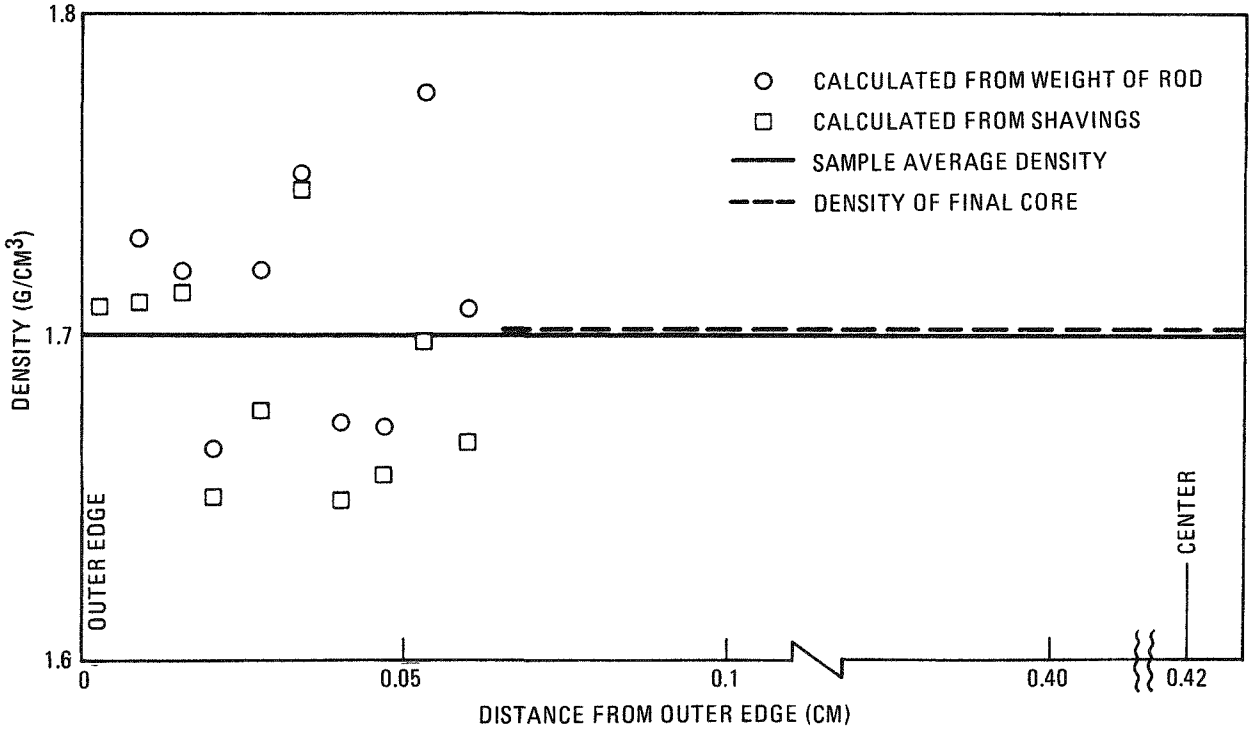

Fig. 4-16. Density profile for sample of H-451 graphite: (a) 0% burnoff

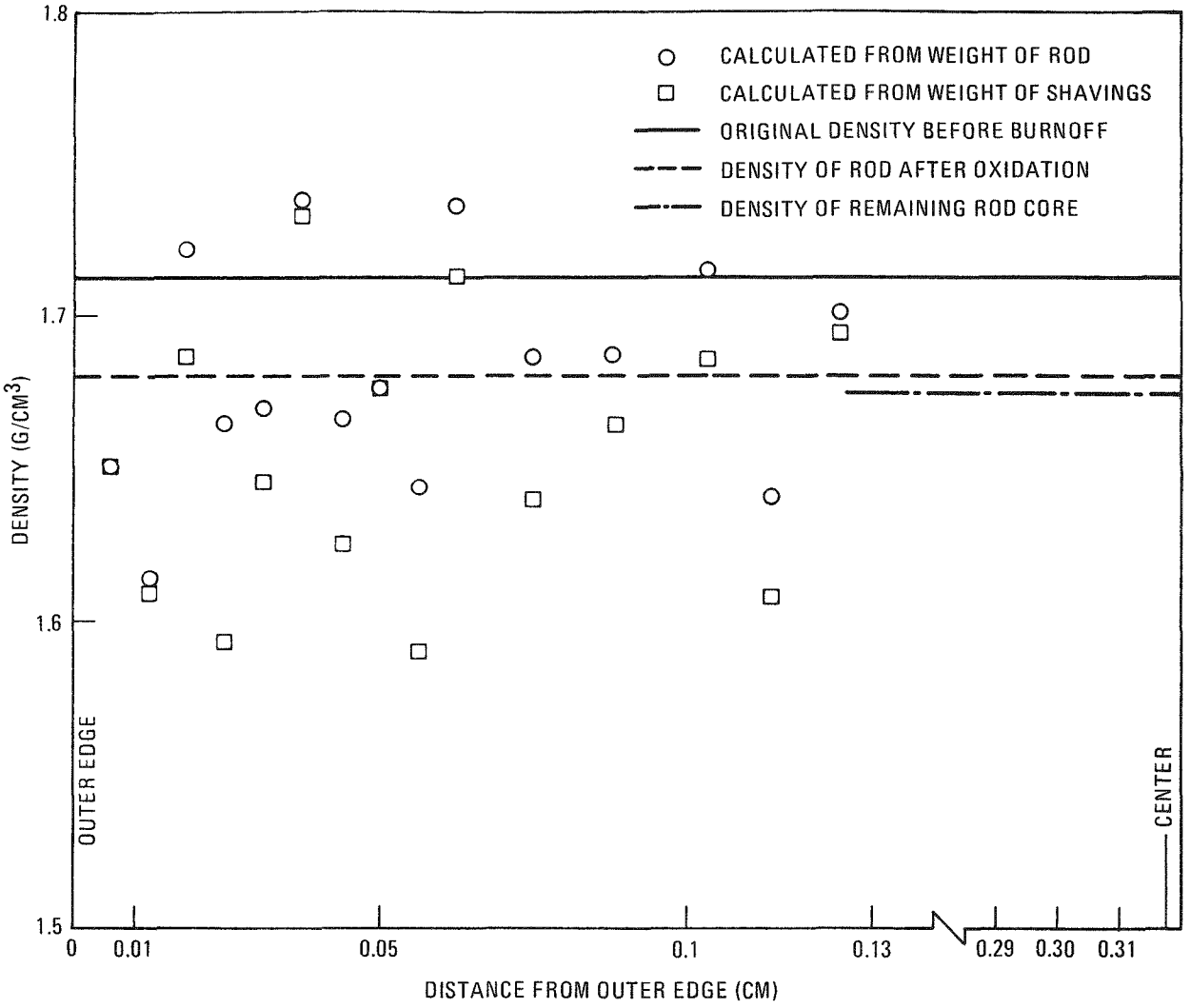

Fig. 4-16. Density profile for sample of H-451 graphite: (b) sample 6484-34-5B, quarter-length center parallel, oxidized at 1073°K to 0.96% burnoff

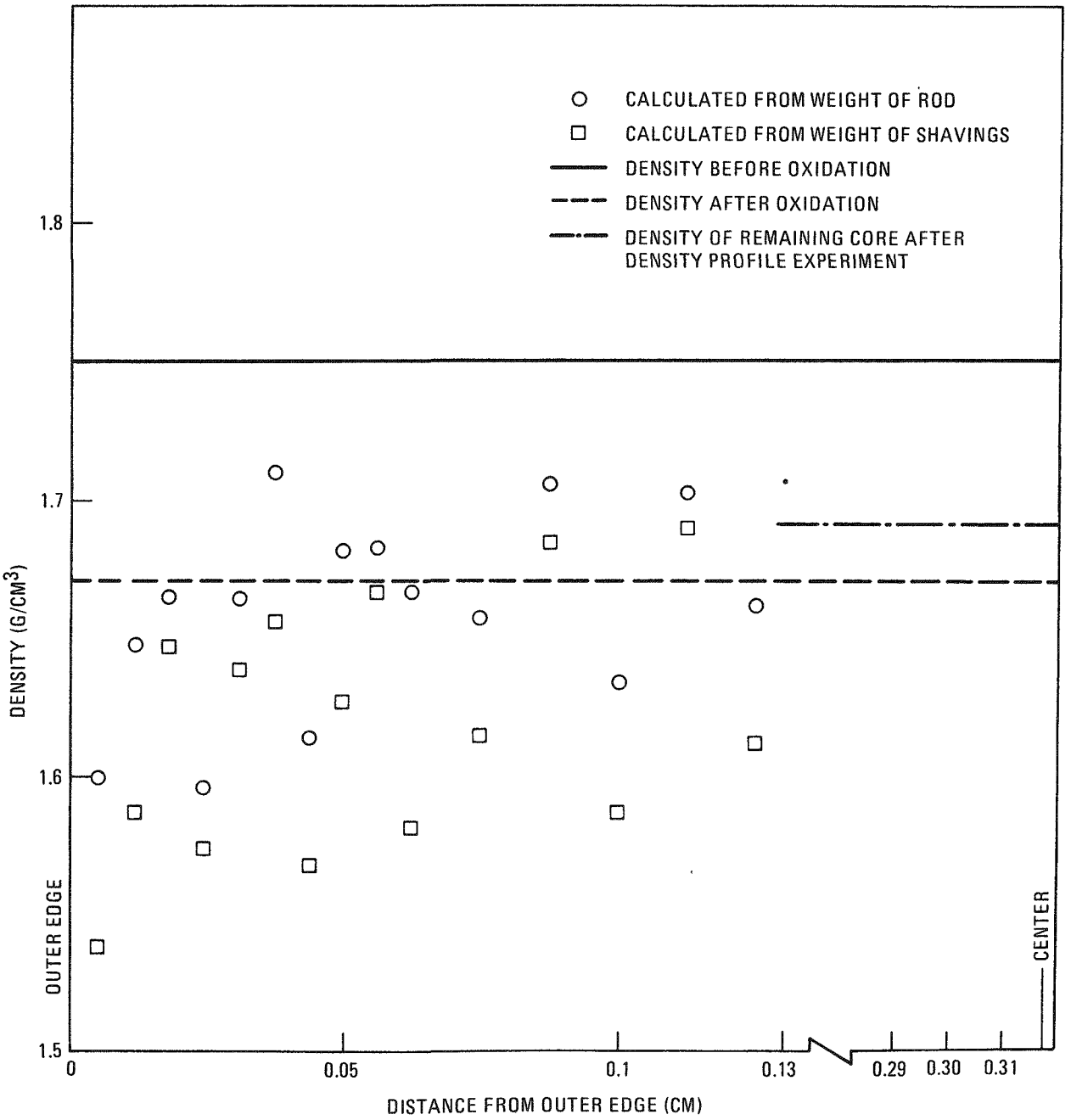

Fig. 4-16. Density profile for sample of H-451 graphite: (c) sample 6484-34-5B, quarter-length center parallel, oxidized at 1273°K to ∿4.3% burnoff

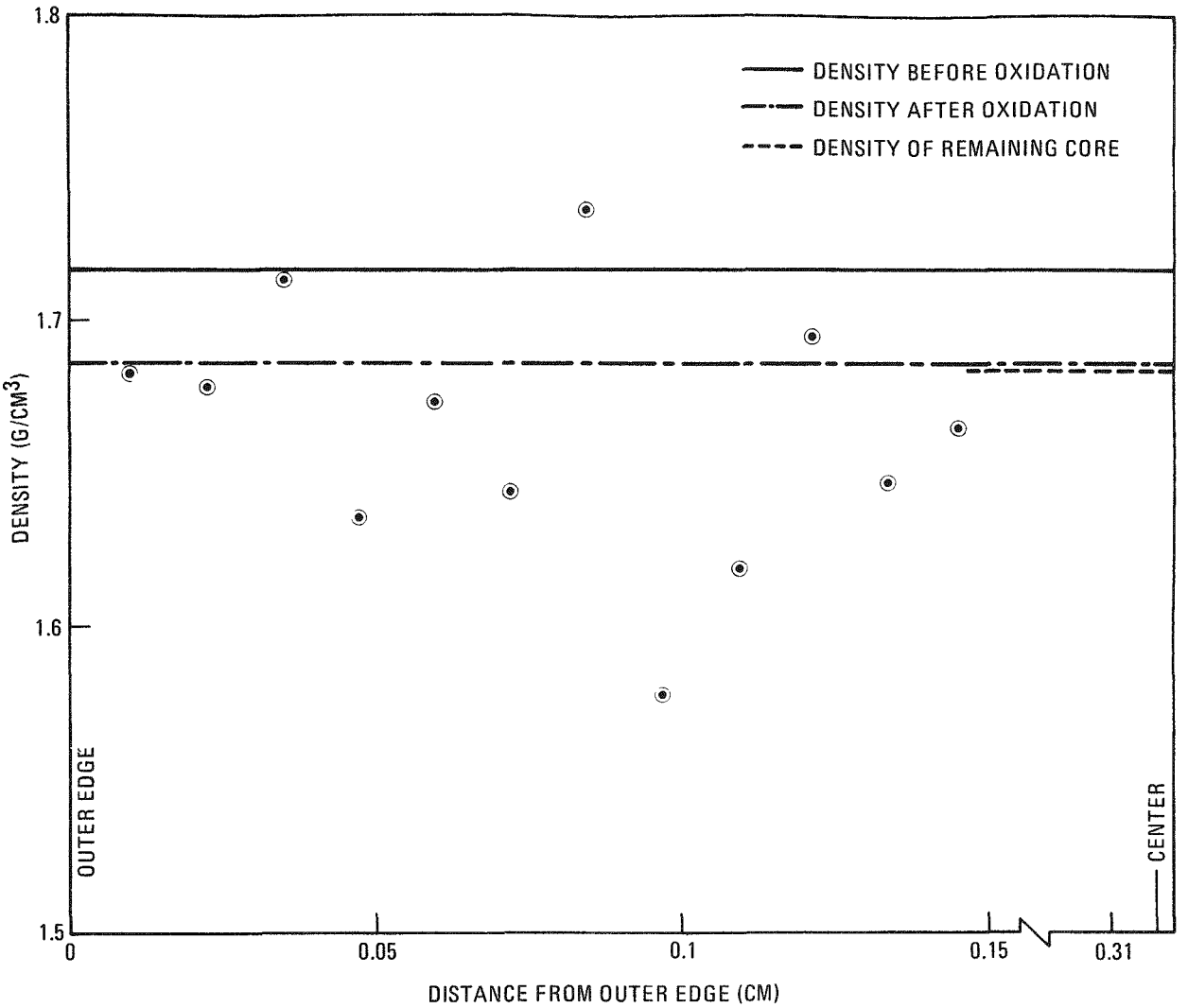

Fig. 4-16. Density profile for sample of H-451 graphite: (d) sample 6484-34-5A-29B, quarter-length center parallel, oxidized at 1273°K to 1.5% burnoff

the case in all other density profiles measured. It is sufficient to state that all of the profile measurements performed showed that these tensile samples were oxidized in a uniform manner.

Conclusions

Although this study has pointed to a need for larger numbers of samples to be tested, particularly in the low percent burnoff range, to improve on the statistical analysis, the conclusions of this preliminary phase of the work can be summarized as follows:

1. The elastic modulus and ultimate tensile strength are decreased by oxidation at 1273°K an average of -3.6% UTS and -5.2% E per percent burnoff. This result is obtained by averaging all 1273°K data, regardless of orientation, position, or burnoff.

2. No statistically significant reduction in ultimate tensile strength occurred in center parallel samples when oxidized to 1.9% at either 1073° or 1273°K; no statistically significant reduction in modulus occurred in these samples when oxidized to 1.9% at 1273°K. This result is of particular importance because the maximum localized burnoff in the HTGR core graphite is only 1%.

3. The rate of reduction of ultimate tensile strength and elastic modulus for center parallel specimens is greater at 1073°K compared to that at 1273°K, although this result is relatively unimportant for design considerations because the maximum burnoff in the core occurs at the highest temperature, approximately 1273°K. Core graphite burnoff at 1073°K would be only about 0.1 to 0.2%.

4. In general, the rate of elastic modulus reduction with burnoff was greater than that of ultimate tensile strength. This observation is of design importance because a lower modulus should decrease secondary stresses (i.e., thermal and irradiation) in the block.

5. The rate of reduction of ultimate tensile strength and elastic modulus for parallel specimens oxidized at 1273°K is greater at the edge than in the center of a log. For design considerations, this effect does not impose a limitation because the design strength of a fuel block is always taken as a fraction of the minimum (or center position) strength, and the strength of the oxidized edge material is never less than that of the center samples for 0 to 2% burnoff.

6. In general, radial (perpendicular) specimens experienced slightly sharper reductions in mechanical properties than did their axial (parallel) counterparts. This phenomenon could have a slight design impact because the seismic stress in the HTGR fuel element is in the radial direction. However, since the modulus change in the perpendicular samples was greater than the strength loss, the overall effect on seismic performance should be negligible.

REFERENCES

4-1. Scott, C. B., and D. P. Harmon, "Postirradiation Examination of Capsules P13R and P13S," ERDA Report GA-A13827, General Atomic Company, to be published.

4-2. "HTGR Base Program Quarterly Progress Report for the Period Ending November 30, 1973," USAEC Report Gulf-GA-A12818, Gulf General Atomic, December 28, 1973.

4-3. Jensen, D. D., et al., "Planning Guide for Validation of Fission Product Transport Codes," ERDA Report GA-A13386, General Atomic Company, April 15, 1975.

4-4. "HTGR Fuels and Core Development Program Quarterly Progress Report for the Period Ending August 31, 1975," ERDA Report GA-A13592, General Atomic Company, September 30, 1975.

4-5. Alberstein, D., P. D. Smith, and M. J. Haire, "Metallic Fission Product Release from the HTGR Core," General Atomic Report GA-A13258 (GA-LTR-20), May 15, 1975.

4-6. "HTGR Accident Initiation and Progression Analysis Status Report - Volume V. AIPA Fission Product Source Terms," ERDA Report GA-A13617, General Atomic Company, February 1976.

4-7. Jensen, D., and M. J. Haire, "Analysis of Cesium Release From the Saclay Spitfire Loop Experiment SSL-1," ERDA Report GA-A13839, General Atomic, to be published.

4-8. Johnson, W. R., and G. B. Engle, "Properties of Unirradiated Fuel Element Graphites H-451 and TS-1240," ERDA Report GA-A13752, General Atomic Company, January 31, 1976.

4-9. Bevington, P. R., Data Reduction and Error Analysis for the Physical Sciences, McGraw-Hill Book Company, 1969, p. 84.

4-10. Ibid., p. 314.

4-11. Johnson, N. L., and F. C. Leone, Statistics and Experimental Design, Vol. 1, John Wiley and Sons, 1964, p. 224.

4-12. Bevington, P. R., op. cit., p. 104.

4-13. Price, R. J., and H. R. W. Cobb, "Application of Weibull Statistical Theory to the Strength of Reactor Graphite," Gulf General Atomic Report GA-10257, August 6, 1970.

6. HTGR ALTERNATIVE FUEL SYSTEM STUDIES
189a NO. SU047

SUMMARY

The major efforts under Task 6 during this reporting period involved the preparation of the topical report (Ref. 6-1) on plutonium-fueled HTGRs and the preliminary evaluation of the nuclear and thermal design characteristics of a variety of potential fuel particle and fuel block designs for achieving high conversion ratio in the HTGR. These study results indicate that the development of silicon-alloyed BISO fertile particles with thinner coatings is the most promising means of achieving higher conversion ratios in the HTGR.

Analysis work has begun on determining the cost tradeoffs resulting from recycle strategies which lead to simplifications in the design of the reprocessing-refabrication plant. Recent dramatic increases in the cost of U_3O_8 and its projected future costs yield higher relative fuel cycle cost penalties for not recycling U-235.

The projections of higher rates of U_3O_8 cost escalations due to future scarcity of U_3O_8 has also significantly increased the economic incentives for higher conversion HTGR designs. If U_3O_8 costs increase by 6%/year due to resource scarcity, the minimum HTGR fuel cycle cost occurs at a conversion ratio of about 0.80 rather than 0.66. This design would be characterized by a 4-year cycle with annual refueling, a power density of 6.5 to 7.5 W/cm^3, and a C/Th ratio of 150.

EVALUATION OF ALTERNATE FUEL PARTICLE AND FUEL BLOCK DESIGNS

Preliminary investigations of nuclear and thermal designs of the high conversion ratio HTGR have been conducted. Two design approaches were taken. The first approach was to increase the conversion ratio by improvement of the fuel particle designs. The second approach was to investigate alternate fuel element designs. Results indicated that by using the thinner coating of the advanced Si-alloyed PyC material, the conversion ratio can be increased significantly (up to 0.81 for a reference HTGR at 8.4 W/cm^3). Modification of the block design and operating characteristics achieves a slightly lower conversion ratio increment. Concise descriptions of these designs are presented herein. Details of the computations and analysis will be shown in the final topical report on high conversion ratio.

Alternative Fuel Particle Designs

Central to the achievement of high conversion ratio is the success of packing large amounts of Th into a block. There are two ways to increase the Th load in a block. One is to design a block to maximize its fuel volume. The other is to design the fuel particles to maximize the Th nuclide for a fixed fuel volume. The former calls for alternative fuel elements and the latter alternative fuel particles.

Separate Particle (Fissile-Fertile) Systems

There have been serious efforts to design new fuel particles to improve (1) strength against pressure vessel rupture and (2) barrier against fission metal release, mainly Cs-137 and Sr-90. These efforts center around two methods, namely fuel kernel doping with silico-aluminate and Si-PyC alloy coating. Associated with these improvements is the possibility of achieving a fuel particle with thinner coatings and therefore higher Th load in a fuel rod. Table 6-1 shows the proposed particle parameters of the different designs. Note that the particles all have the same

TABLE 6-1
COATED PARTICLE PARAMETERS FOR DIFFERENT DESIGNS

	Present Design	Advanced Particle 1	Advanced Particle 2		Advanced Particle 3	
Fertile Particle						
	Present BISO ThO_2	BISO I ThO_2	BISO II ThO_2		BISO III ThO_2	
Kernel						
Diameter, μm	500	500	500		500	
Density, g/cm^3	9.5	9.5	9.5		9.5	
Buffer						
Thickness, μm	90	60	50		40	
Density, g/cm^3	1.10	1.0	1.0		1.0	
Outer PyC		Si-alloyed PyC	Si-alloyed PyC		Si-alloyed PyC	
Thickness, μm	70	65	50		35	
Density, g/cm^3	1.88	2.04	2.04		2.04	
Total diameter, μm	820	750	700		650	
Fissile Particle[a]						
	Present TRISO UC_2	Present TRISO UC_2	UC_2		UC_2	
Kernel						
Diameter, μm	310	310	310		310	
Density, g/cm^3	3.3	3.3	3.3		3.3	
			Present TRISO	TRISO I	Present TRISO	TRISO I
Buffer						
Thickness, μm	45	45	45	45	45	45
Density, g/cm^3	1.15	1.15	1.15	1.15	1.15	1.15
Inner PyC						
Thickness, μm	25	25	25	5	25	5
Density, g/cm^3	1.90	1.90	1.90	1.90	1.90	1.90
SiC				ZrC		ZrC
Thickness, μm	25	25	25	20	25	20
Density, g/cm^3	3.20	3.20	3.20	6.70	3.20	6.70
Outer PyC						
Thickness, μm	35	35	35	35	35	35
Density, g/cm^3	1.80	1.80	1.80	1.80	1.80	1.80
Particle metal density, g/cm^3	0.425	0.425	0.425	0.559	0.425	0.559
Total diameter, μm	570	570	570	520	570	520
Normalized Th load at 56% packing fraction[b]	1.0	1.27	1.47	1.55	1.70	1.87
Conversion ratio increment	0	+0.055	+0.075	+0.085	+0.010	+0.145

[a] Applies to recycle bred (U-233) and residual recycle (U-235) particles also.

[b] It is realized that as the particle size decreases, the packing fraction increases. In this table and in Fig. 6-1, the standard 56% packing fraction for the present design is applied to all particle systems for first approximation comparison.

kernel size but the advanced particles (BISO-I, -II, -III, and TRISO-I) have thinner coatings and therefore their particle total diameters are smaller. Consequently, a larger number of advanced particles can be accommodated in a fuel rod than with the present BISO-TRISO design. Table 6-2 illustrates this point; for the same power density, the improved particle can increase Th load, i.e., decrease the C/Th ratio. Specifically, at the nominal packing fraction limit of 56% and at 6 W/cm^3, the Th load can be increased 87% (from 12.89 kg/block to 24.12 kg/block) and the core average C/Th decreased from 192 to 102. Correspondingly, the conversion ratio changes from 0.76 to 0.905 by switching from the present TRISO-BISO particles to the TRISO I - BISO III design.

It should be pointed out that the improved fertile particles designated as BISO-I, -II, and -III all use the Si-alloyed PyC as coating instead of PyC. Their coating thicknesses (75 to 125 μm) are estimated to yield about the same (or less) fission product release as the present BISO design. Verification of the fission product retention of such particles under irradiation would be an integral part of their future development. Table 6-2 shows that only nominal loading increases result from utilizing the ZrC TRISO I fissile particle and its development is not essential to achieving higher conversion.

Figure 6-1 shows the effects of different particle designs on the Th loadings and the conversion ratios. The example used is for a high gain HTGR operated at 6 W/cm^3 and on a 4-yr annual refueling scheme. On the right-hand side of the figure, it is shown that the Th load is in direct proportion to the packing fraction. At the nominal packing fraction limit of 56%, the maximum Th load is about 0.053 MT/MW(e) for the present BISO-TRISO design. The corresponding C/Th is ∿190 (shown as point 1 in Fig. 6-1). Tracing point 1 horizontally to the left-hand side of the figure, a conversion ratio of 0.76 is found. Similarly, for a BISO I - present TRISO design, the maximum Th load is about 0.066 MT/MW(e) (C/Th = 150) (point 2 in Fig. 6-1). The corresponding conversion ratio (0.81) can be obtained

TABLE 6-2
THORIUM LOADINGS FOR DIFFERENT PARTICLE SYSTEMS
(6 W/cm^3, 4-yr Annual High Gain HTGR,
56% Packing Fraction)

Particle Type	Max. Th (kg/block)	Core Average Th (kg/block)	Core Average C/Th	Conversion Ratio
Present BISO-TRISO	12.89	10.65	192	0.760
BISO I - present TRISO	16.40	13.55	151	0.815
BISO II - present TRISO	18.96	15.68	131	0.835
BISO III - present TRISO	21.87	18.07	113	0.860
BISO II - TRISO I	19.93	16.47	124	0.845
BISO III - TRISO I	24.12	19.93	102	0.905

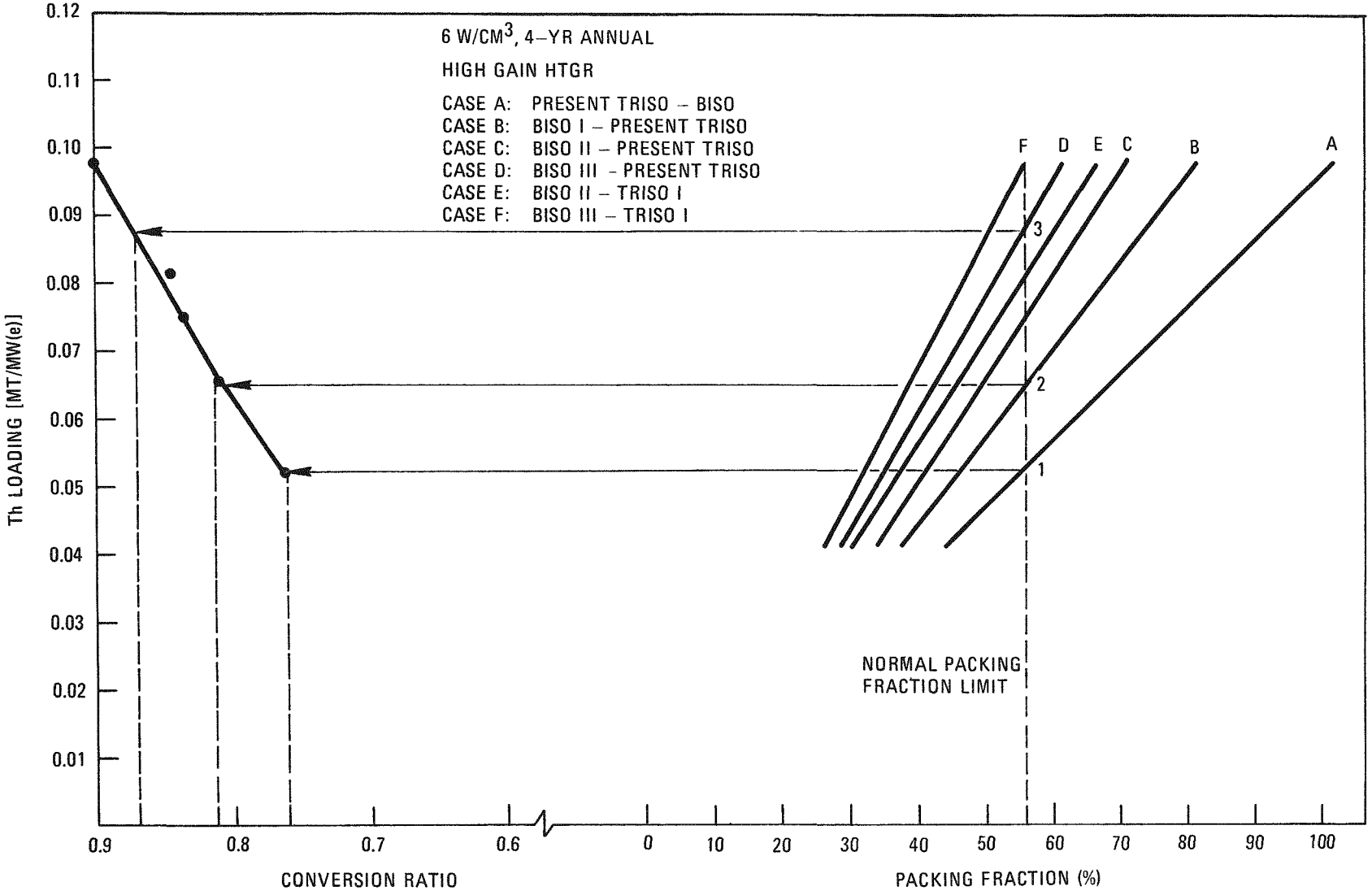

Fig. 6-1. Particle effect on conversion ratio

from the left-hand plot. Likewise, for the BISO III - present TRISO design, the Th loading is 0.088 MT/MW(e) (C/Th = 115) and the conversion ratio is ∿0.87. Surveying all the data points, it is observed that the improved particle systems can increase the Th loading from approximately 30 to 90%. The conversion ratio can increase as much as 0.15.

Single Particle (Mixed Fissile-Fertile) System

The previous section deals with the improvement of conversion ratio for a TRISO-BISO, i.e., separate fissile-fertile, particle system. This section deals with further increasing the conversion ratio by using the single particle mixed-oxide system. In particular, the impact of the Si-alloyed PyC coating on the advanced all-BISO system is examined.

A single particle design can be considered for higher conversion applications since the requirement to limit U-236 buildup decreases with increasing conversion ratio.

Four types of all-BISO single particle mixed-oxide systems have been considered: the reference BISO with a PyC coating and the advanced Si-alloyed coating BISO-I, -II, and -III systems. The dimensions of these BISO particles were assumed identical to those given in Table 6-1. Table 6-3 summarizes the expected characteristics for each system at nominal (8.4 W/cm^3) power density. The table shows that from the thorium loading viewpoint, the single particle mixed-oxide system is the most desirable. This is so because the BISO particle has a large kernel (500 μm) and a high particle volume fraction for the kernel. With a high particle volume fraction for the kernel (0.227 to 0.477 for BISO versus 0.161 for the reference TRISO), more Th can be loaded per unit fuel rod. Thus, for a fixed particle packing fraction, the replacement of the TRISO particle with the BISO particle in essence facilitates more kernel volume and less coating volume. Accordingly, the all-BISO systems display a C/Th range of 180 to 160, whereas that of the reference TRISO-BISO system is 190 to 210.

TABLE 6-3
ACHIEVABLE CONVERSION RATIO FOR DIFFERENT COATED PARTICLE MIXED-OXIDE SYSTEMS
[3000-MW(t) Standard HTGR]

Particle System	Power Density (W/cm^3)	Particle Parameters					Neutronic Penalty in ΔCR[b]			Fission Product Release Estimate[b]	Conversion Ratio[b]
		Kernel Diameter (μm)	Buffer Thickness (μm)	Outer Coating Thickness (μm)	Total Coating Thickness (μm)	Particle Volume Fraction of Kernel	C/Th Limit[a]	Si	U-236		
Reference TRISO-BISO	8.4	310 (TRISO) 500 (BISO)	70 90	60 70	130 160	0.161 0.227	190-210	-0.005	-0.026	Acceptable	0.68
Mixed Th/U, PyC BISO	8.4	500	90	70	160	0.227	160	-0.000	-0.040	Unacceptable	0.74
Mixed Th/U, advanced BISO-I	8.4	500	60	65 (Si-PyC)	125	0.274	130	-0.030	-0.040	Acceptable	0.75
Mixed Th/U, advanced BISO-II	8.4	500	50	50 (Si-PyC)	100	0.364	100	-0.020	-0.040	Acceptable	0.82
Mixed Th/U, advanced BISO-III	8.4	500	40	35 (Si-PyC)	75	0.477	80	-0.012	-0.040	Acceptable	0.87

[a] Based on a graphite density of 5.9×10^{-2} nuclides/barn-cm and a 56% nominal packing fraction.

[b] Estimation and inference deduced from existing data.

With a low coating thickness per unit kernel diameter (low T/D), the all-BISO systems face potential problems in fission product release. For example, the mixed Th/U PyC BISO system may yield too high a fission product release. There are two factors which work in favor of lowering fission product release in an advanced all-BISO system. First, for the high gain HTGR, the burnup is usually low (<5% FIMA) such that the fission density in a BISO kernel could be low enough for satisfactory fission product retention. Second, the advanced coating materials such as Si-alloy display higher strength and, hopefully, better fission product retention properties than PyC. With these two factors working together, the advanced all-BISO systems (i.e., BISO-I, -II, -III) may become a successful high-gain fuel particle design.

Another consideration in an all-BISO system is the neutronic penalty of the Si-alloy coating and the mixing of U-236 with the bred U-233. These are complex phenomena and the penalty depends on the burnup (i.e., the fluence) and the kernel and coating dimensions. A rough estimate of these neturonic penalties was made in units of ΔCR (columns 9 and 10 of Table 6-3). In all the single particle BISO cases, the neutronic penalty from Si and U-236 mixing does not exceed the reference case by more than 0.042. This is outweighed by the gain in conversion ratio (0.09 to 0.14) due to higher thorium loading. Consequently, despite the neutronic penalty due to Si-alloy coating and U-236 mixing, the conversion ratio of the all-BISO mixed kernel system shows a net increase of 0.04 to 0.13.

Figure 6-2 shows the conversion ratio of various particle systems at a power density of 8.4 W/cm^3. The figure indicates that the advanced all-BISO family is superior in achieving a higher conversion ratio.

Alternative Fuel Elements

For a given power density and particle design, the increase of conversion ratio is very much dependent on the fuel volume available in an element. Specifically, for the fuel volumes corresponding to the range of

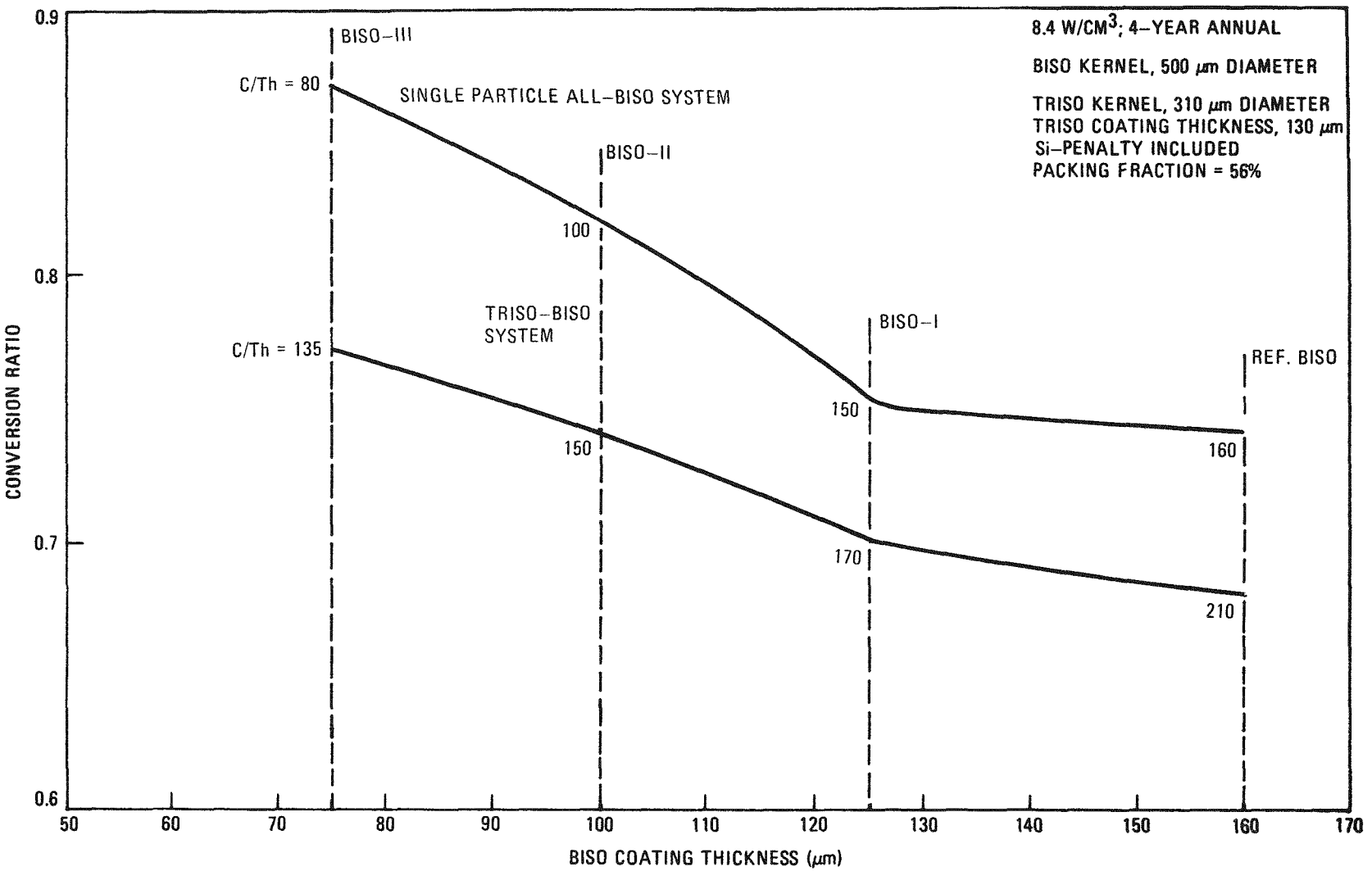

Fig. 6-2. BISO particle dimension versus conversion ratio

C/Th between ∞ and 160, it is found that the conversion ratio is directly proportional to the fuel volume. Beyond C/Th = 160, the rate of increments of conversion ratio starts to reduce.

In order to achieve significant conversion ratio increases, it is necessary that alternative block designs of higher fuel volume be utilized. Furthermore, the resonance integral of these blocks should be sufficiently high such that the effective thorium conversion is attractive.

Three categories of fuel elements have been investigated: (1) the eight-row block, (2) the ten-row block, and (3) the direct-cooled fuel element. The characteristics of these three fuel element types are listed in Table 6-4.

Fifteen cases were examined: six eight-row block designs, five ten-row block designs, and four direct-cooled ring designs. Table 6-4 summarizes the pertinent parameters and the results of these 15 cases. The GA standard LHTGR eight-row block (case A) is used as the basis for comparison and normalization.

Columns two through four in Table 6-4 deal with parameters that affect the effective resonance integral (RI). The last three columns show the condensed results. For the eight-row and ten-row blocks it is observed that despite the varying geometric configurations of these blocks, the effective thorium conversion, i.e., $VF_{fuel} \cdot RI$, is very much dependent on the fuel volume. Therefore, the effective C/Th limit is to a large extent determined by the available fuel volume.

Among the eight-row blocks (cases A through F), it is observed that nothing is gained by switching from 2:1 to 1:2 configurations. The 1:1 configuration (Fig. 6-2), however, offers a slight increase in conversion ratio (+0.01 to +0.03) and about a 10% decrease in core pressure drop. Also, the German type (Hobeg Company) monolithic block achieves a +0.07 increase in conversion ratio at the expense of a thinner graphite web and

TABLE 6-4
COMPARISON OF EFFECTIVE THORIUM CONVERSION OF THE MODIFIED FUEL ELEMENTS FOR HIGH GAIN HTGRs

Type	Case	Parameters Affecting Effective Th Absorption				Effective C/Th Limit[a]	Maximum RPF [Normalized Pressure Drop][b]
		Fuel Rod Diameter (cm) [No. of Fuel Rods]	Coolant Hole Diameter (cm) [No. of Coolant Holes]	Fuel Volume, V (cm^3) [VF_{fuel}]	Effective Th Conversion; Normalized VF_{fuel} • RI		
Eight-row block	A[c] (2:1)	1.560 [138]	2.077 [72]	20920 [0.2318]	1.00	190-210	1.51 [1.00]
	B (1:2)	2.077 [72]	1.585 [138]	19340 [0.2139]	0.92	228	1.55 [1.10]
	C*[d,e] (2:1) Hobeg	1.900 [138]	1.900 [72]	31025 [0.3432]	1.55	135	1.32 [1.21]
	D (1:1)	1.747 [105]	1.747 [105]	20920 [0.2318]	1.02	205	1.50 [1.11]
	E (1:1) Hobeg	1.875 [105]	1.800 [105]	22990 [0.2543]	1.13	185	1.46 [0.89]
	F* (1:1)	1.889 [105]	1.786 [105]	23335 [0.2581]	1.15	180	1.45 [0.91]
Ten-row block	G*[f] (2:1)	1.270 [210]	1.576 [108]	21100 [0.2334]	1.05	200	1.49 [1.72]
	H (1:2)	1.551 [108]	1.270 [210]	16177 [0.1790]	0.78	270	1.62 [1.57]
	I (1:1)	1.455 [160]	1.455 [158]	21100 [0.2334]	1.05	200	1.49 [1.19]
	K (1:1)	1.507 [160]	1.354 [158]	22622 [0.2502]	1.14	185	1.46 [1.64]
	L (1:1)	1.331 [160]	1.517 [158]	17656 [0.1953]	0.87	240	1.57 [1.08]
Direct-cooled ring design	M*[g]	1.740[h] [19]	4.544 [19]	26400 [0.292]	1.23	170	1.42 [0.26]
	N	0.711 [90]	2.240 [90]	20722 [0.2296]	1.10	190	1.47 [0.41]
	O	1.252 [90]	1.280 [90]	26870 [0.2977]	1.40	150	1.38 [5.68]
	P*	0.9448 [90]	1.900 [90]	25128 [0.2784]	1.32	160	1.40 [0.85]

[a] Assuming a graphite atom density of 5.9×10^{-2}/barn-cm for all blocks, three-particle with 56% nominal packing fraction limit.

[b] Pressure drop across a block calculated by $\Delta P = \frac{1}{2\rho}\left(\frac{\dot{m}}{A}\right)^2 \left(\frac{4fL}{D}\right)\left(\frac{\bar{T}}{Ti}\right)$ with RPF taken into account.

[c] GA eight-row block for large HTGR.

[d] HRB monolithic block with uniform hole size.

[e] Asterisk indicates alternate designs selected for more detailed performance evaluations.

[f] GA ten-row block for FSV design.

[g] Nineteen-hole direct-cooled fuel element; GA preliminary ring design.

[h] Equivalent fuel rod diameter $\frac{4V_f}{S}$, where S is the inside and outside annular surface.

increased core pressure drop (+21%). The 1:1 design and the Hobeg block, therefore, should be further studied from the stress and temperature viewpoint for potential application as high gain fuel elements.

Within the class of ten-row blocks (cases G through L), it is observed that the performance of these blocks in conversion ratio and pressure drop is in general less attractive than that for the eight-row blocks. However, the comparison does not include stress and fuel temperature, for which the ten-row blocks probably have a lower value.

Among the ten-row blocks, it is concluded that switching from 2:1 to 1:2 designs shows little, if any, improvement. One specific 1:1 design (case K) offers a slight increase (+0.02) in conversion ratio but a substantially higher pressure drop (+64%). Unless there is overwhelming impetus to attain lower fuel temperature, the use of ten-row blocks in a high gain HTGR is not strongly recommended.

In general, the direct-cooled fuel element offers higher conversion ratio and lower pressure drop. These designs assume some form of advanced technology, either in high-strength graphite matrix or improved particle coating for higher fission product retention. Nonetheless, in cases M and P, these direct-cooled fuel elements show an increased conversion ratio (+0.04 to +0.05) and lower pressure drop (-15% to -74%). Their stress and temperature behavior should be further studied for evaluation as potential high gain fuel elements.

Finally, it should be pointed out that the 2:1 GA eight-row and ten-row blocks are presently available. The 1:1 eight-row block requires short-term research and development. The Hobeg monolithic block and the direct-cooled ring design require long-term developmental efforts.

Accordingly, cases C, F, G, M, and P were chosen for further detail performance analysis. These cases are designated by an asterisk* in Table 6-4.

Comparison of Particle Effect and Fuel Element Effect

It is appropriate at this point to put into perspective the particle effect and the fuel element effect. From Fig. 6-2 and Table 6-4, it is seen that the particle effect is equal to or greater than the effect for increased fuel volume of the alternative fuel element. Specifically, by using the most advanced particle system (BISO III - TRISO I), the gain in conversion ratio is slightly higher than that when using the most advanced alternative fuel element. Using a more conservative advanced particle system (BISO I - present TRISO), the conversion ratio gain is roughly equivalent to that of using a direct-cooled fuel element. Using an all-BISO single particle system yields a conversion ratio higher than those of the alternative fuel element designs. It is therefore concluded that from the high conversion ratio viewpoint, improvement in fuel particle yields better results than that of alternative fuel elements. Research and development in fuel particles should therefore be pursued with priority. In addition, since the fuel particle design has significant implications on block fuel volume and fuel element thermal hydraulics, the research on fuel particle improvements should be conducted in close coordination with the design and optimization of alternative fuel elements.

PERFORMANCE IMPROVEMENTS OF HIGH CONVERSION RATIO HTGRS

Due to the heavy thorium loading (C/Th around 120 to 170 versus the reference 190 to 210) of the high conversion ratio HTGR, the associated region peaking factor (RPF) is lowered by around 20%. Consequently, the core pressure drop is lower and the plant efficiency is higher (Fig. 6-3). With a lower C/Th ratio, the RPF and hence the core pressure drop decrease. Specifically, at a C/Th of 150, the core pressure drop reduction is about 20% (or roughly 2.3 psi). The net result is a higher plant efficiency.

Another way of achieving a high conversion ratio is by increasing the fuel rod diameter at the expense of decreasing the coolant hole diameter (while maintaining the same fuel to coolant hole graphite web thickness).

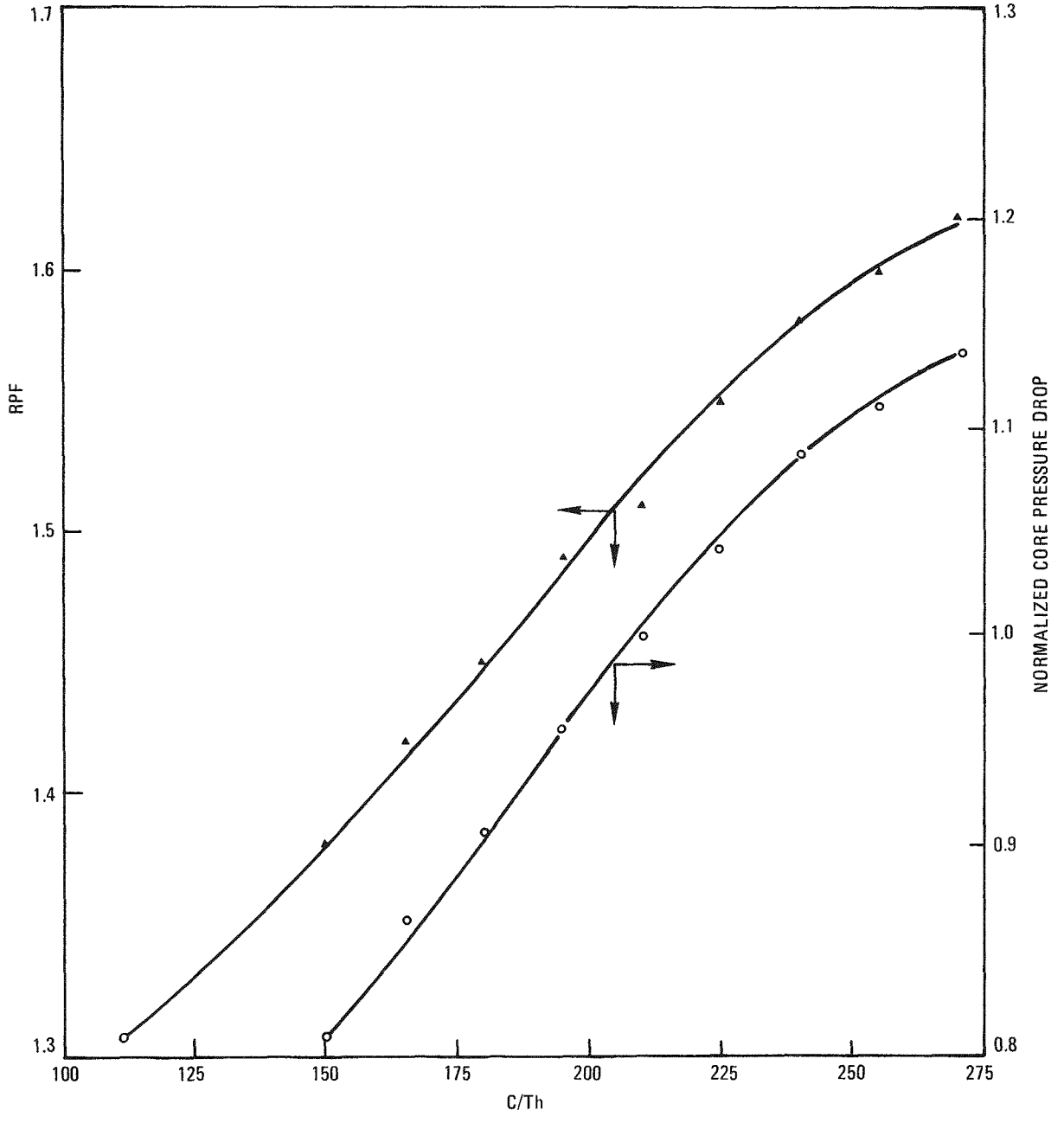

Fig. 6-3. RPF and normalized core pressure drop versus C/Th (core power density = 8.4 W/cm^3)

With a smaller coolant hole (and hence larger fuel rod), heavier thorium loadings can be achieved. This is shown by curve A in Fig. 6-4. The heavy thorium loading is attained at the expense of higher pressure drop, as shown by curves B and C in Fig. 6-4. For the nominal power density of 8.4 W/cm^3, to achieve a C/Th of 150 would incur ∿75% increase in pressure drop due to the smaller coolant hole. This ∿75% ΔP increase is prohibitively high. However, by switching to a lower power density of 6 W/cm^3 and accepting the same nominal core pressure drop (i.e., point 1 on curve C), a C/Th of about 135 can be achieved. This operating point seems particularly attractive for two reasons. First, no advanced technology development is required either in fuel particle designs or in graphite block fabrication. Second, the lower power density reduces the fuel performance requirements and possibly would allow higher gas outlet temperatures. The only penalty is a larger PCRV for the same total core power. Additional performance calculations are planned for this concept of achieving higher conversion ratio.

EVALUATION OF ALTERNATE STRATEGIES FOR U-235 RECYCLE

A search is currently under way to find the optimum strategy for recycle of U-235 in the HTGR fuel cycle. The objectives include minimization of:

1. Resource requirements.
2. Recycle plant design and cost.
3. Total fuel cycle cost.

In searching for the optimum strategy, the following features of the fuel cycle and its evaluation are being allowed to vary:

1. Fuel cycle design.
2. Economic projection and assumption.

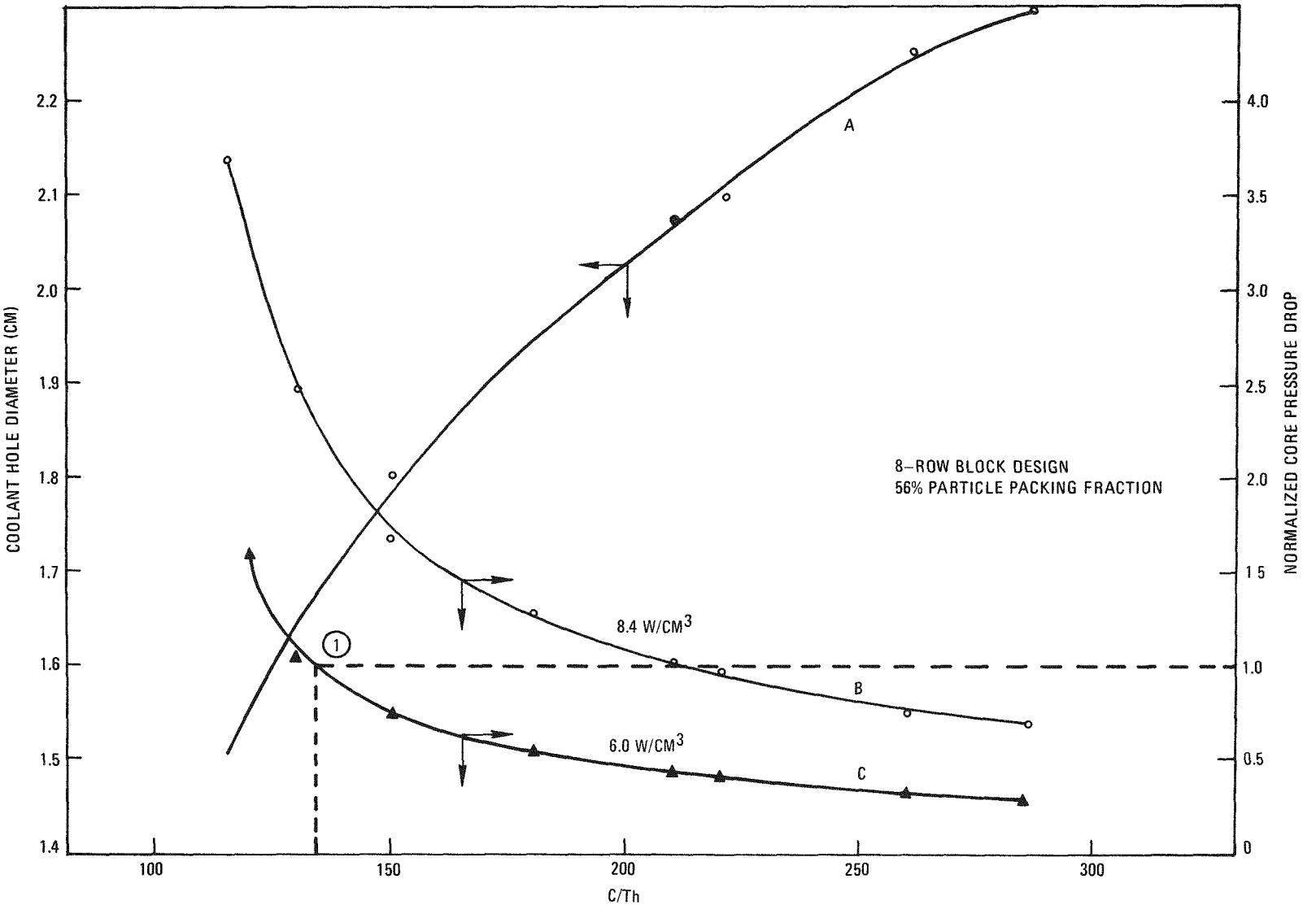

Fig. 6-4. Variable hole sizes, pressure drop, and C/Th

A portion of the results will be applied in a detailed study of the recycle plant being done under the Thorium Utilization Program.

Basically the procedure is to calculate fuel cycle costs, including depletion costs representing resource utilization, for various HTGR fuel cycle designs and to determine the difference relative to the reference fuel cycle design, which includes U-235 recycle in specially dedicated fuel elements. Besides the changes in depletion costs and in distribution between fabrication and refabrication, the changes in reprocessing and refabrication prices are also reflected in the fuel cycle cost calculation. These price changes in turn result from capital and operating cost changes within the recycle plant as a result of the modifications in the fuel cycle design regarding U-235 recycle. All of these comparisons are done for various sets of economic ground rules and assumptions. In particular, costs are computed both with and without general escalation and for various assumptions on U_3O_8 ore scarcity.

The uniqueness of the current evaluation of U-235 recycle relative to past studies lies in (1) the inclusion of the fuel cycle cost effect of the attendent modification in the detailed design of the recycle plant, and (2) the approximate effect on fuel cycle cost of changes in the waste disposal requirements.

For this early preliminary report, results will be quoted only for three of the fuel cycle designs under study. Furthermore, the detailed effects of waste handling have not been included in these early results. The three cycles are as follows:

1. Reference fuel cycle - all U-235 is recycled once in specially dedicated fuel elements prior to retirement at zero value.

2. No U-235 recycle - no U-235 is recycled; all U-235 is retired at zero value upon discharge after one residence period in the reactor.

3. Partial U-235 recycle - same as case 2 except U-235 discharged from segments 1 and 2 is recycled once in specially dedicated fuel elements, along with the U-233 from those segments, prior to retirement at zero value.

Table 6-5 reflects the fuel cycle cost changes that would result from shifting to cycles 2 or 3 above from cycle 1, the current reference cycle. Table 6-5 includes identified cost changes in the projected commercial HTGR recycle facility (Table 6-6). Table 6-5 omits the effects of refabrication price changes that might be required to offset the loss of revenue from the elimination of U-235 recycle. The rationale for ignoring this effect rests in the preliminary determination that there would be a price adjustment in the fresh fuel manufacture which would largely compensate for the refabrication price change.

Table 6-5 includes results for three sets of economic evaluation conditions. The first two are unescalated, i.e., without inflation, but include a "scarcity-escalation" of U_3O_8 ore price to reflect a projection of excess demand for this basic resource. In the primary case, this "escalation" is 6% per year to 2000 A.D., followed by 3% per year thereafter. In the alternative case, it is 3% per year to 2000 A.D., with a constant U_3O_8 price thereafter. For these unescalated cases, the working capital and discount rates are 9.1 and 4.3%, respectively. The third set of economic conditions includes escalation provisions for all prices contributing to fuel cycle costs (resource as well as handling). In this case working capital and discount rates are 15.6 and 7.4%, respectively.

EFFECT OF U_3O_8 COSTS ON OPTIMUM CONVERSION RATIO

The price of U_3O_8 has increased by about 40% in the last 7 months. Current values are about \$77/kg U_3O_8 (\$35/lb). Estimates of the future increase in U_3O_8 marginal costs of recovery vary significantly, depending primarily on the total rate of consumption (electrical demand) and on various estimates of likely reserves. Typical scarcity-related cost increases of 5 to 6% per year are not uncommon. Recently completed fuel

TABLE 6-5
COMPARISON OF FUEL CYCLE COSTS FOR ALTERNATIVE U-235 RECYCLE PLANS

Evaluation Condition and Cost Components	Level (0 to 30 year) Fuel Cycle Cost Changes [m/kW/-hr(e)]		
	Reference (Cycle 1)	No U-235 Recycle (Cycle 2)	Partial U-235 Recycle (Cycle 3)
No general escalation but 6 to 3% ore scarcity			
Depletion	--	+0.25	+0.17
Handling	--	-0.07	-0.07
Total	--	+0.18	+0.10
No general escalation but 3 to 0% ore scarcity			
Depletion	--	+0.15	+0.09
Handling	--	-0.07	-0.07
Total	--	+0.08	+0.02
General escalation			
Depletion	--	+0.54	+0.37
Handling	--	-0.26	-0.26
Total	--	+0.28	+0.11

TABLE 6-6
PROJECTED COST CHANGES FOR RECYCLE FACILITY

	Cost Change (1975 $)	
	Capital (10^6)	Operating (10^6/yr)
Reference cycle (cycle 1)	--	--
No U-235 recycle (cycle 2)	-26	-14
Partial U-235 recycle (cycle 3)	-26	-14

cycle cost calculations for many potential high gain HTGR designs show that the optimum conversion ratio is a strong function of the assumed rate of U_3O_8 cost increase due to scarcity.

Results for various HTGR designs, as well as for a typical PWR, have been calculated for scarcity-cost increases of 2%/yr and 6%/yr. The 1976 cost of fuel was conservatively based on \$57/kg U_3O_8 (\$26/lb) and \$100/SWU for enrichment. This enrichment cost is consistent with current estimates of private enrichment costs.

The calculations were based on 30-year levelized fuel cycle costs and included the assumption of an overall inflation rate of 6% on all cost components. A working capital rate of 15.6% was assumed.

The relative escalated fuel cycle costs for the two assumed rates of U_3O_8 scarcity are shown in Fig. 6-5 for 1985 plant startups. Note that the optimum HTGR cycle at a 2% U_3O_8 scarcity rate is nearly the same as the previously marketed HTGR design except for a slightly higher thorium loading. This optimum occurs at C/Th of $\sim$200 and a power density of 8 W/cm^3. The optimum cycle is 1 m/kW-hr cheaper than a PWR.

The situation is dramatically changed for U_3O_8 scarcity cost increases of 6%/yr. For this assumption, the optimum HTGR conversion ratio is about 0.80, and the escalated cost advantage of the HTGR is 4.8 m/kW-hr relative to the PWR. The optimum cycle is then characterized by a C/Th of 150 and a power density of about 7 W/cm^3.

The results shown include only fuel cycle costs, and a constant thermal efficiency of 38.7% for all HTGR designs was assumed. Thermal efficiency improvement would accrue due to the increased thorium loading and reduced core power density since both changes reduce the core pressure drop. This effect would further reduce the optimum design fuel cycle costs by about 0.25 m/kW-hr. This credit, as well as the plant cost increase due to a larger plant, will be evaluated to determine the overall power cost optimum.

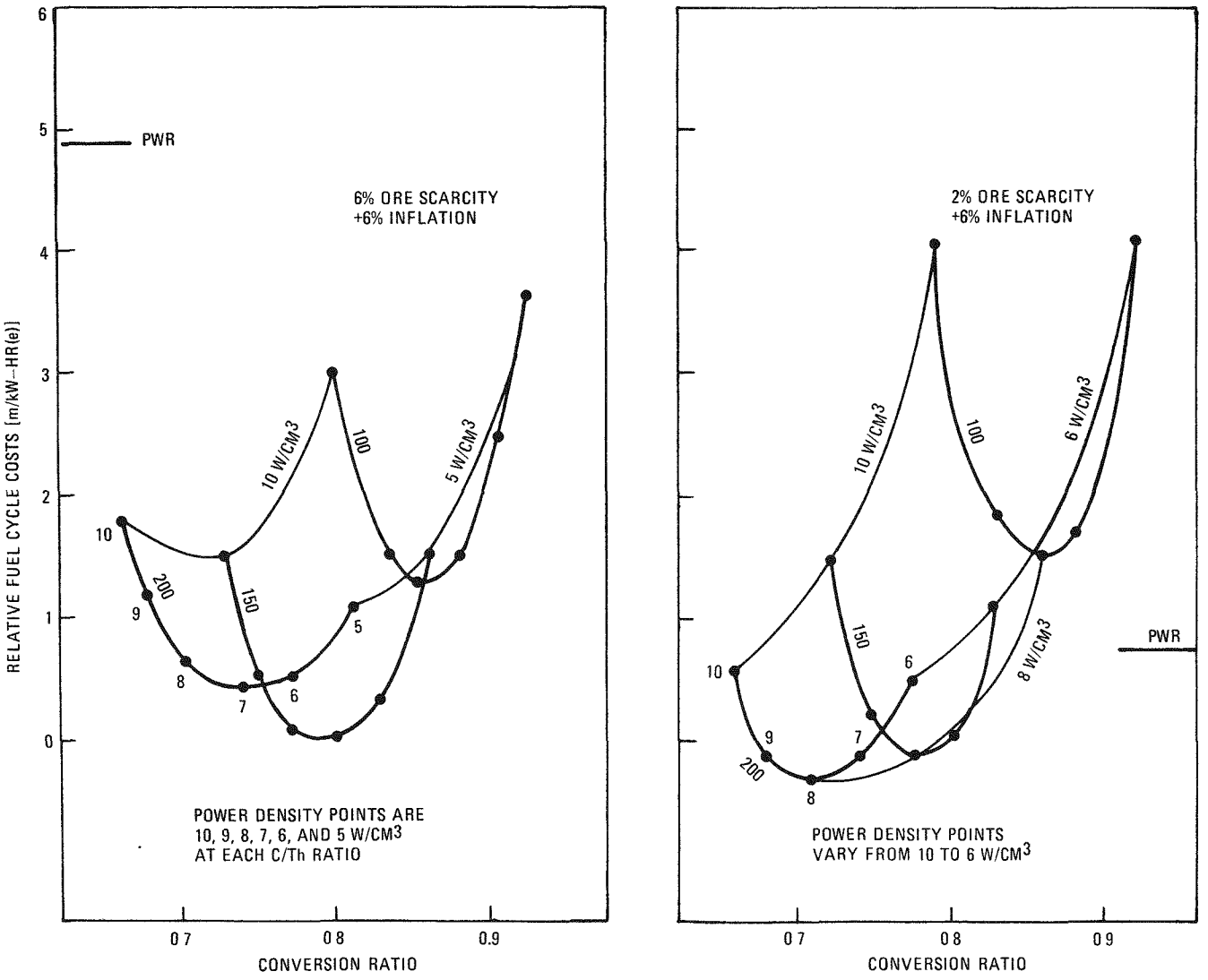

Fig. 6-5. Relative fuel cycle costs versus conversion ratio, 4-year annual refueling, 6% inflation

REFERENCE

6-1. Karin, S., et al., "Utilization of Plutonium in the HTGR and Its Actinide Production," ERDA Report GA-A13786, General Atomic Company, to be published.

8. HTGR PHYSICS
189a NO. SU002

XENON STABILITY STUDY

During this quarter a study was performed to assess the sensitivity of the xenon stability characteristics predicted for HTGRs to uncertainties in the data used to calculate these characteristics. The essence of this work was the determination of coefficients which quantify the sensitivity of the results of a linear stability analysis to the various parameters in the linear stability equation. Sensitivity coefficients for parameters which do not affect the initial flux distribution, e.g., decay constants and fission yields, were calculated analytically; coefficients for parameters that do affect the flux distribution were calculated numerically. These coefficients are suitable for use in a statistical analysis, e.g., the propagation of errors technique, of the uncertainty associated with the prediction of xenon stability in a specific HTGR.

Complete documentation will be included in the final report of this study to be written in the coming quarter.

MULTIDIMENSIONAL REACTOR KINETICS

A thorough review of the literature available in the field of multi-dimensional reactor kinetics has been completed. As a result of this survey it appears that the most efficient way to acquire the capability to perform this type of calculation at GA is to obtain and convert a computer code, TRIMHEX (Ref. 8-1), which has been developed at the Savannah River Laboratory. Detailed discussions with Savannah River Laboratory personnel to verify this tentative conclusion are planned for the near future.

REFERENCE

8-1. Buckner, M. R., and J. W. Stewart, "Multidimensional Space-Time Kinetics Studies - Part I - Theoretical," Nucl. Sci. Eng. 59 (1976), to be published.

9. HTGR FUEL DEVELOPMENT AND ENGINEERING
189a NO. SU003

TASK 200: ACCELERATED IRRADIATION TESTS

Subtask 210: Fresh Fuel Qualification

Summary and Conclusions

Postirradiation analysis of capsules P13Q, P13R, and P13S is in progress.

Capsule P13T has now reached a fast neutron exposure of 4.6×10^{21} n/cm^2 $(E > 0.18 \text{ MeV})_{HTGR}$. The fission gas release from the two cells remains low (R/B Kr-85m $< 5 \times 10^{-6}$).

Assembly of capsules P13U and P13V has been completed; the capsules will be inserted into the GETR on February 27, 1976.

Capsules P13R and P13S

Capsules P13R and P13S are the seventh and eighth in a series of irradiation tests to demonstrate the integrity of reference and alternate LHTGR fuels over a wide range of irradiation conditions. The capsules were discharged from the GETR on October 31, 1974 and the disassembly and postirradiation examination commenced at the GA hot cell facility on December 5, 1974.

The thermal analysis for these two capsules was completed during this reporting period. These data are currently being factored into the post-irradiation analysis of the fuel. A detailed discussion of the capsule thermal analysis will appear in a topical report to be issued later this year.

Capsule P13T

Capsule P13T is the ninth in a GA series of LHTGR fuel irradiation tests conducted under the HTGR Fuels and Core Development Program. P13T is a large-diameter capsule containing two cells. Cell 1 is a qualification test of reference fresh fuel [TRISO UC_2 (VSM) and BISO ThO_2 particles] irradiated at 1300°C. Cell 2 is an evaluation test of reference fresh fuel and recycle fissile fuel [TRISO UC_xO_y (WAR) particles] irradiated at 1100°C. The capsule was inserted in the ORR reactor in May 1975 and will be irradiated to a peak fast fluence of 8.5×10^{21} n/cm^2 $(E > 0.18 \text{ MeV})_{HTGR}$. A detailed description of the capsule is given in Ref. 9-1.

The capsule has reached an estimated peak fast fluence of 4.6×10^{21} n/cm^2 $(E > 0.18 \text{ MeV})_{HTGR}$. The latest fission gas release of the fuel is still low: 5.2×10^{-6} and 1.1×10^{-6} (R/B Kr-85m) for cells 1 and 2, respectively. The irradiation conditions as a function of time for the two cells are presented in Figs. 9-1 and 9-2.*

Since early in the operation of the capsule, eight tungsten/rhenium (W/R) thermocouples have failed at different times. These failures have become significant in cell 1 because seven of the nine W/R thermocouples, including the three measuring fuel rod centerline temperatures, have become inoperative. This problem, however, has not appreciably affected the ability to maintain design temperature in the cell since it has been controlled by a chromel-alumel thermocouple from the beginning of the irradiation.

An analysis of the fuel performance was made on cells 1 and 2 of capsule P13T (Ref. 9-1). The projected fission gas release (Kr-85m) for cells 1 and 2 is shown in Figs. 9-1 through 9-3.

The release values for the cells were based on current fuel particle performance models and the preirradiation contamination level as described below:

*Figures appear at the end of Section 9.

$$(R/B) = \left[(R/B)_U \cdot f_{fissile} + (R/B)_f \cdot D_{fertile} \cdot f_{fertile}\right]_{\text{(contamination contribution)}}$$

$$+ \left[(R/B)_f \cdot D_{fissile} \cdot F'_{fissile} \cdot f_{fissile}\right]_{\text{(fissile particles with defective SiC coatings)}}$$

$$+ \left[(R/B)_f \cdot F_{fissile} \cdot f_{fissile}\right.$$

$$\left. + (R/B)_f \cdot F_{fertile} \cdot f_{fertile}\right]_{\text{(in-pile failure)}}$$

where $(R/B)_U$ = ratio of rate of release (R) to the rate of birth (B) for exposed fissile fuel at beginning of life; experimentally determined by TRIGA activation on fired fuel rods; $(R/B)_U$ temperature corrected to volume average temperatures for cell 1 (1230°C) and cell 2 (1020°C). This value accounts for uranium contamination.

$(R/B)_f$ = fractional release from contamination and failed particles in fuel rods; the values were corrected for temperature:

	Fractional Release $(R/B)_f$	
	Cell 1	Cell 2
Fissile and fertile contamination	0.50	0.21
Fissile particle failure	0.008	0.008*
Fertile particle failure	0.008	0.0035

*Cells 1 and 2 have the same $(R/B)_f$ inspite of the temperature difference because of the higher $(R/B)_f$ assumed for WAR TRISO in the lower temperature cell 2. Fissile particles in cell 2 are 1/3 WAR TRISO and 2/3 VSM UC_2 TRISO. The $(R/B)_f$ of WAR at 1020°C is assumed to be 0.0175 and VSM $(R/B)_f$ is assumed to be 0.0035. The fissile fuel in cell 1 is all VSM UC_2 TRISO.

$F_{fissile,fertile}$ = failure fraction of fissile or fertile fuel as a function of fluence:

Fluence (10^{21} n/cm^2) (E > 0.18 MeV)$_{HTGR}$	0	2	4	6	8	9
$F_{fissile}$ (x 10^{-2})	0	0	0.14	0.40	0.50	0.53
$F_{fertile}$ (x 10^{-2})	0	0.13	0.25	0.38	0.50	0.56

$F'_{fissile}$ = failure fraction of defective SiC coated particles; determined by dividing burnup by 78% FIMA.

$f_{fissile,fertile}$ = fraction of fissions occurring in fissile or fertile fuel as a function of fluence. The fission power distributions in the two cells are:

Fluence (10^{21} n/cm^2) (E > 0.18 MeV)$_{HTGR}$		0	2	4	6	8	9
$f_{fissile}$	Cell 1	1.0	0.78	0.52	0.38	0.34	0.34
	Cell 2	1.0	0.87	0.68	0.55	0.47	0.46

$$f_{fertile} = 1 - f_{fissile}$$

$D_{fertile}$ = thorium contamination at beginning-of-life; since fuel rod fabrication did not appear to cause additional contamination, the exposed heavy metal (thorium hydrolysis) values for the particle batches were used.

$D_{fissile}$ = the fraction of fissile particles with defective SiC coatings at the beginning-of-life; values measured by the burn-leach method on the individual particle batches.

Capsules P13U and P13V

Capsules P13V and P13V will test TRISO WAR UC_xO_y and BISO ThO_2 coated particles under normal and thermal cycling conditions to peak LHTGR temperatures and fluences. Each capsule will be 31.75 mm in diameter and similar

in design to capsules P13R and P13S. Five fuel rod cells and one unbonded particle cell will be tested in each irradiation test vehicle. A detailed description of the capsules is given in Ref. 9-2.

The construction of the two capsules is on schedule. The date for insertion of P13U and P13V into the GETR is February 27, 1976.

TASK 300: INTEGRAL FUEL SYSTEM TESTING

Subtask 310: Peach Bottom Fuel Test Elements

Summary of FTE-4 Gamma Scanning Results

Fuel rods, fuel bodies, and spine samples from FTE-4 were gamma-scanned using a Ge(Li) spectrometer with a 6.3% efficiency. All the samples were traversed past a 1066.8-mm (42-in.) collimator at slow speeds using a specially built rig (Fig. 9-4). The size and the shape of the collimator cross section were changed for varying activities and shapes of the specimens being scanned. All data were analyzed by the Sigma II computer facility, which was directly interfaced with the Ge(Li) detector.

Several general conclusions were reached from the gamma scanning results:

1. The measured isotopic inventory agreed well with independent ORNL measurements.

2. The Cs-137 inventory in the fuel rods agreed with the predicted thermal fluence profile.

3. Total FIMA measured from the Cs-137 fuel rod inventories was consistent with predicted and chemistry measured values.

4. All fuel rods had homogeneous axial fuel loadings except for rods in holes 7 and 8. The homogeneity was determined from single-channel gamma scan plots of the fuel rods.

Gamma-Scans of FTE-4 Fuel Rods

Representative fuel rods from all three fuel bodies were gamma scanned using a 22.2 by 0.6 mm (0.875 by 0.023 in.) collimator. The rods were passed by the collimator so that the long axis of the collimator was perpendicular to the length of the rod. This counting geometry was calibrated with a standard rod from capsule P13R, which allowed the quantitative calculation of all the fuel rod inventories. The data are presented in Table 9-1. Because these fuel rods were counted almost 2 years after being taken out of the Peach Bottom reactor, many of the short-lived isotopes had decayed away. Also the count rates of most of the isotopes were low, which gave substantial counting errors as shown in Table 9-1.

The results of the fuel rod inventories were substantiated by the analysis of several similar rods at both GA and ORNL (Ref. 9-3). The results of this comparison are shown in Table 9-2. Comparisons of the results at the two facilities show good agreement for all isotopes except Zr-95. In the case of Zr-95, the low count rates resulted in high counting errors.

The Cs-137 inventory measured in fuel rods from stack 3 is plotted against core location in Fig. 9-5. Because the Cs-137 isotope has such a long half-life (30.2 yr), it is easily correlated to both the time-averaged burnup and the time-averaged thermal fluence. A normalized time-averaged thermal fluence curve overlayed on the data in Fig. 9-5 shows good agreement between the calculated thermal fluence and the measured Cs-137 inventory.

From the end-of-life Cs-137 inventory, an approximate burnup can also be calculated. The calculation proceeds as follows:

$$\begin{pmatrix}\text{Fission per initial heavy metal atom}\end{pmatrix}\begin{pmatrix}\text{total}\\ \text{FIMA}\end{pmatrix} = \frac{\text{Number of Cs-137 atoms produced}}{\begin{pmatrix}\text{Fission yield}\\ \text{of Cs-137}\\ \text{from U-235}\end{pmatrix}\begin{pmatrix}\text{Number of}\\ \text{initial}\\ \text{U-235 atoms}\end{pmatrix} + \begin{pmatrix}\text{Number of}\\ \text{initial}\\ \text{Th-232 atoms}\end{pmatrix}} \quad ,(9\text{-}1)$$

TABLE 9-1
SUMMARY OF GAMMA SPECTROSCOPY RESULTS OF FTE-4 FUEL RODS
[Curies/Fuel Stick (Decayed to 9/14/73)]

Isotope (% 2σ Counting Error)[a]	1-3-5[b]	1-3-6	1-3-7	1-5-5	1-5-6	1-5-7	1-7-7	2-3-3	2-3-4	2-3-5	2-3-6	2-3-7	2-3-10	2-4-6	2-4-7	2-4-8	2-4-9	2-4-10	2-5-5
Ru-106 (14%)	0.562	0.561	0.610	0.495	0.425	0.636	0.623	0.823	0.934	0.847	0.855	0.882	0.841	0.894	0.896	0.903	0.872	0.859	0.881
Cs-134 (3%)	0.258	0.300	0.349	0.262	0.228	0.367	0.346	0.672	0.720	0.717	0.638	0.691	0.713	0.711	0.701	0.736	0.698	0.689	0.708
Cs-137 (2%)	0.476	0.506	0.549	0.460	0.419	0.565	0.550	0.772	0.839	0.830	0.726	0.796	0.890	0.824	0.832	0.839	0.789	0.791	0.819
Ce-144 (15%)	6.920	7.820	8.410	6.870	6.600	8.680	9.220	12.00	12.50	13.80	11.90	11.10	12.50	13.00	12.70	10.20	11.90	12.20	11.60
Zr-95 (55%)	22.10	39.20	28.80	--	17.90	31.90	26.40	52.30	38.10	46.20	40.30	42.30	48.10	51.40	38.20	47.00	33.20	42.30	35.40
	2-5-6[b]	2-5-8	2-6-8	2-7-6	2-7-7	2-7-8	2-7-9	2-8-6	2-8-8	2-8-9	2-8-10	2-8-1	3-3-5	3-3-6	3-3-7	3-3-8	3-5-5	3-7-7	3-7-8
Ru-106 (14%)	0.862	0.876	0.899	0.779	0.695	0.755	0.818	0.875	0.871	0.851	0.775	0.820	0.706	0.669	0.644	0.611	0.69	0.57	0.59
Cs-134 (3%)	0.672	0.708	0.712	0.641	0.624	0.664	0.638	0.711	0.683	0.721	0.721	0.669	0.446	0.443	0.382	0.331	0.42	0.34	0.32
Cs-137 (2%)	0.772	0.816	0.802	0.714	0.699	0.727	0.714	0.725	0.743	0.795	0.797	0.726	0.603	0.649	0.592	0.546	0.62	0.49	0.50
Ce-144 (15%)	11.30	11.60	11.20	11.20	11.60	11.10	11.40	12.30	11.30	12.60	12.10	13.60	9.35	10.40	9.84	8.50	10.10	7.91	7.87
Zr-95 (55%)	51.50	38.90	45.10	46.50	65.10	49.20	49.70	54.50	43.30	38.20	36.40	31.10	--	34.10	--	--	33.20	--	--

(a)

$$\%\ 2\sigma\ \text{error} = \frac{2\ [CNT + (1 - CH/2)^2] \cdot [(LC - RC)/\sqrt{PTS}]^{1/2}}{PEAK} \times 100$$

where PEAK = counts in the peak,
CNT = total counts in peak (peak + background),
CH = number of channels in peak,
LC = counts in lowest energy channel,
RC = counts in highest energy channel,
PTS = number of smoothing points.

(b) Fuel rod identification: fuel body 1, hole 3, position 5.

TABLE 9-2
COMPARISON OF GA AND ORNL GAMMA SPECTROSCOPY RESULTS FOR ISOTOPIC INVENTORIES

Isotope	2σ Counting Error at GA[a] (%)	Curies per Fuel Rod			
		3-5-5[b] GA	3-5-6 ORNL	3-5-7 ORNL	3-5-8 ORNL
Zr-95	55	3.30	16.58	18.60	16.85
Ru-106	14	0.69	0.59	0.65	0.59
Cs-134	3	0.42	0.34	0.39	0.33
Cs-137	2	0.62	0.52	0.56	0.51
Ce-144	15	10.10	8.87	8.87	8.32

(a)

$$\%\ 2\sigma\ \text{error} = \frac{2[CNT + (1 - CH/2)^2] \cdot [(LC - RC)/\sqrt{PTS}]^{-1/2}}{PEAK} \times 100$$

where PEAK = counts in the peak,
CNT = total counts in peak (peak + background),
CH = number of channels in peak,
LC = counts in lowest energy channel,
RC = counts in highest energy channel,
PTS = number of smoothing points.

(b) Fuel rod identification number.

where Fission yield of Cs-137 from U-235 = 6.27 (assume all uranium is U-235 on initial loading),

$$\text{Number of Cs-137 atoms produced} = \frac{\text{Disintegrations/minute (DPM)}}{\lambda \text{ Cs-137 } (0.4407 \times 10^{-7}/\text{min})},$$

$$\text{Number of initial U-235 atoms} = \frac{\text{Grams of initial uranium}}{235 \text{ g/mole}} \times 6.02 \times 10^{23} \text{ atoms/mole},$$

$$\text{Number of initial Th-232 atoms} = \frac{\text{Grams of initial thorium}}{232 \text{ g/mole}} \times 6.02 \times 10^{23} \text{ atoms/mole}.$$

Figures 9-6a through 9-6c compare the total FIMAs calculated by the GAUGE computer code and measured by wet chemistry and gamma spectroscopy for fuel rods with similar fuel blends. In all three cases the data showed a consistent trend:

1. The FIMA values measured by gamma spectroscopy and calculated by the GAUGE code for the bottom section of the active core (i.e., body 1) were nearly equal.

2. In the middle and top sections of the active core (i.e., bodies 2 and 3), the FIMAs measured by gamma spectroscopy were consistently higher than the GAUGE-calculated values by up to 20%.

3. The one FIMA value measured by wet chemistry was consistent with the values measured by gamma spectroscopy.

To substantiate these data, samples are being prepared for isotope dilution mass spectroscopy, which offers an extremely accurate measurement of fissile burnup.

The 2σ error limits placed on the FIMAs measured by gamma spectroscopy were determined by a simple error analysis, which proceeds as follows:

$$\text{FIMA} \approx K_1 \frac{\text{No. of Curies}}{\text{g Th + U}}, \qquad (9\text{-}2)$$

where

$$\text{Curie} \approx K_2 \frac{\text{CPM (counts/minute)}}{\text{CE (detector counting efficiency)}} \quad . \tag{9-3}$$

First, determining the error in Eq. 9-3,

$$(\Delta\text{Curie})^2 = \left[\frac{\partial(\text{Curie})}{\partial(\text{CPM})}\right]^2 [\Delta(\text{CPM})]^2 + \left[\frac{\partial(\text{Curie})}{\partial(\text{CE})}\right]^2 [\Delta(\text{CE})]^2 \quad .$$

Then, solving and reducing,

$$(\Delta\text{Curie})^2 = \text{Curie}^2 \left\{\frac{[\Delta(\text{CPM})]^2}{\Delta(\text{CPM})^2} + \frac{[\Delta(\text{CE})]^2}{\Delta(\text{CE})^2}\right\} \quad . \tag{9-4}$$

Substituting some typical values for Cs in Eq. 9-4:

$$\text{Curie} = 0.7$$

$$\text{CPM} = 700 \qquad \text{CPM} = 14 \ (2\sigma)$$

$$\text{CE} = 1 \times 10^{-8} \qquad \text{CE} = 2 \times 10^{-8} \ (2\sigma)$$

$$\Delta\text{Curie} = 0.140 \ (2\sigma \text{ error})$$

Using this value in the analysis of Δ(FIMA) with Eq. 9-2,

$$[\Delta(\text{FIMA})]^2 = \left[\frac{\partial(\text{FIMA})}{\partial(\text{Curie})}\right]^2 [\Delta(\text{Curie})]^2 + \left[\frac{\partial(\text{FIMA})}{\partial(\text{g Th + U})}\right]^2 [\Delta(\text{g Th + U})]^2 \quad ,$$

and solving and reducing,

$$(\Delta\text{FIMA})^2 = (\text{FIMA})^2 \left\{\frac{[\Delta(\text{Curie})]^2}{(\text{Curie})^2} + \frac{[\Delta(\text{g Th + U})]^2}{(\text{g Th + U})^2}\right\} \quad . \tag{9-5}$$

Substituting some typical values in Eq. 9-5,

FIMA = 8%

Curie = 0.7 $\quad\quad$ ΔCurie = 0.140

(g Th + U) = 3 g $\quad\quad$ Δ(g Th + U) = 0.15

ΔFIMA = 1.65 (2σ error)

This is the value reported in Fig. 9-6.

In addition to the multichannel analysis of the fuel rods, single channel scans of Cs-137 were plotted to determine the relative axial homogeneity of the fuel rods. To date only representative rods from holes 3, 4, 5, 6, 7, and 8 have been examined. An empirical examination of the data shows that fuel rods loaded in holes 3 through 6 were fairly homogeneous and the fuel rods loaded in holes 7 and 8 were nonhomogeneous. Representative fuel rods from holes 5 and 8 (Fig. 9-7) show this difference.

Gamma Scans of FTE-4 Radial Graphite Web

Fuel body 2, which had been sectioned near its center, was scanned across several radial planes to determine fission product release in various fuel holes (Fig. 9-8). The 3.0 by 3.0 mm (0.12 by 0.12 in.) collimator was used with a slow traversing speed. Because this geometry is not calibrated for quantitative results, a comparison of the counts per minute of the volatile Cs-134 and Cs-137 isotopes gave a qualitative release of these fission products in various regions of the cross section of the fuel body (Table 9-3). The gamma scanning shows insignificant cesium release near holes 3, 6, and 7 and relatively high release near hole 2. This is verified by the autoradiography of a thin section of body 2 in Fig. 9-24 of Ref. 9-4.

Plots of the Cs-137 and Cs-134 activities across hole 2 are shown in Figs. 9-9 and 9-10. These data have not been corrected for the collimator effect, which tends to smear the data at the edges of the graphite. The purpose of the plots is only to give a qualitative picture of the cesium

TABLE 9-3
RADIAL GRAPHITE GAMMA SPECTROSCOPY SCAN SUMMARY

Hole 7-3[a]					Hole 2-6[c]				
		Isotope Relative Activity (cpm)					Isotope Relative Activity (cpm)		
Scan Number	Radial Location[b] (in.)	Cs-137 (661 keV)	Cs-134 (604 keV)	Cs-134 (795 keV)	Scan Number	Radial Location[b] (in.)	Cs-137 (661 keV)	Cs-134 (604 keV)	Cs-134 (795 keV)
2229	0.0555 to 0.0115	6	0	0	2116	0 to 0.063	14	22	12
2230	to 0.081	5	0	0	2117	to 0.125	30	27	25
2231	to 0.151	6	0	0	2118	to 0.188	64	65	44
2232	to 0.221	8	0	0	2119	to 0.250	77	100	59
2233	to 0.292	7	0	0	2120	to 0.313	60	91	70
2234	to 0.363	8	0	7	2121	to 0.375	37	75	45
2235	to 0.436	4	18	7	2122	to 0.438	14	33	28
2236	to 0.508	5	0	0	2123	to 0.500	8	21	12
2237	to 0.581	6	0	0	2124	to 0.563	8	16	14
2238	to 0.655	5	10	0	2125	to 0.625	11	15	16
2239	to 0.729	5	12	11	2126	to 0.688	19	24	23
2240	to 0.803	11	14	0	2127	to 0.750	23	42	23
2241	to 0.877	6	11	9	2128	to 0.813	23	133	91
2242	to 0.952	7	32	8	2129	to 0.875	22	150	98
2243	to 1.027	7	34	26	2130	to 0.938	13	99	57
2244	to 1.102	6	6	6	2131	to 1.000	6	15	14
2245	to 1.177	7	0	0	2132	to 1.063	5	0	7
2246	to 1.243	5	0	6	2133	to 1.125	7	0	0
2247	to 1.328	6	0	0	2134	to 1.188	6	0	0
2248	to 1.404	8	0	0	2135	to 1.250	10	0	0
2249	to 1.480	4	0	0	2136	to 1.313	0	0	0
2250	to 1.556	0	0	0	2137	to 1.375	3	0	0
2251	to 1.632	6	0	0	2138	to 1.438	5	0	0
2252	to 1.708	0	0	0	2139	to 1.500	5	0	0
2253	to 1.784	8	0	0	2140	to 1.563	0	0	0
2254	to 1.861	9	19	18	2141	to 1.625	5	0	0
2255	to 1.936	8	25	18	2142	to 1.688	5	0	0
2256	to 2.006	10	0	6	2143	to 1.750	7	0	0
2257	to 1.082	7	0	9	2144	to 1.813	5	0	0
2258	to 2.158	8	0	8	2145	to 1.875	7	0	0
2259	to 2.234	7	10	8	2146	to 1.938	7	0	8
2260	to 2.310	7	0	0	2147	to 2.000	5	0	0
2261	to 2.386	8	0	7	2148	to 2.063	5	0	0
2262	to 2.462	9	0	0	2149	to 2.125	0	0	0
2263	to 2.538	0	0	0	2150	to 2.188	0	0	0
2264	to 2.614	6	0	0	2151	to 2,250	6	0	0
2265	to 2.690	10	0	0	2152	to 2.313	7	0	7
2266	to 2.766	8	0	0	2153	to 2.375	6	0	0
2267	to 2.842	4	0	0	2154	to 2,438	5	0	0
					2155	to 2,500	5	0	0
					2156	to 2.563	5	0	0
					2157	to 2,625	5	0	7
					2158	to 2,688	9	14	0
					2159	to 2.750	5	8	5
					2160	to 2.813	0	0	0
2σ counting error[d] (%)		30-60%	30-80%	30-80%					

(a)

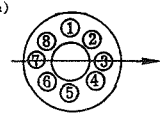

(b) See Fig. 9-8.

(c)

(d) See Table 9-1, footnote a for definition.

profile in the graphite web. The shape of the Cs-134 and Cs-137 profile from the outside edge of the fuel body to the fuel hole is similar to that found by a core drilling method. The space between the fuel hole and the surface of the spine hole shows a lower Cs-137 activity and a significantly higher Cs-134 activity.

Gamma Scans of FTE-4 Spine Samples

Several spine samples from each fuel body were gamma scanned using the 3.0 by 3.0 mm (0.12 by 0.12 in.) collimator. Plots for Cs-137, Cs-134, and Cs-144 along the length of each of the spine samples are shown in Figs. 9-11a through 9-11c for fuel bodies 1, 2, and 3. Because this counting geometry is not calibrated for quantitative results, the scans give only relative activity differences in the various samples. The scans show that the spine samples containing no fuel had no volatile cesium plateout.

TASK 400: OUT-OF-PILE PARTICLE TESTING AND EVALUATION

Subtask 420: Thermal Gradient Postirradiation Heating

Summary and Conclusions

The results of tests designed to study the kinetics of migration of irradiated ThO_2, UC_2, and $UC_{4.3}O_{1.3}$ fuel kernels and the kinetics of fission product - SiC reactions in TRISO UC_2 and WAR $UC_{4.3}O_{1.3}$ fissile fuel particles are reported. The conclusions drawn from the test results are itemized below by fuel particle type.

The test results for BISO ThO_2 fuel are summarized as follows:

1. Migration of ThO_2 fuel kernels up a thermal gradient occurs during postirradiation thermal gradient heating.

2. Redeposited graphite was observed on the cool side of migrating ThO_2 kernels. The appearance of the graphite layer was identical

to that observed on migrating carbide kernels, suggesting that carbon diffusion from the hot side to the cool side of ThO_2 kernels is related to kernel migration.

3. The migration of ThO_2 kernels was shown to be caused more by kernel elongation toward the hot side than by uniform kernel displacement, suggesting that heavy metal migration up the thermal gradient contributes significantly to the measured ThO_2 kernel migration.

4. Migration of ThO_2 is characterized by a period of slow migration followed by a period of more rapid migration. The period of slow migration (incubation period) decreases with increasing kernel burnup and temperature. The incubation period is significant relative to LHTGR core operating conditions for kernel burnups less than 1.5% FIMA and therefore will be important when estimating the impact of ThO_2 kernel migration in LHTGR fuel performance. Definition of the cause of and characterization of the length of the incubation period will however aid in complete understanding of the mechanism for ThO_2 kernel migration.

5. A least-squares analysis of available data showed that

$$KMC^* \ (cm^2\text{-}^\circ K/sec) = 1.36 \times 10^5 \exp(-83{,}419/RT) \qquad (9\text{-}6)$$

for R having units of cal/mole-°K or

$$KMC \ (m^2\text{-}^\circ K/sec) = 13.6 \exp(-3.4906 \times 10^5/RT) \qquad (9\text{-}7)$$

for an R value of 8.314 J/mole-°K.

6. Tests of kernels from two different ThO_2 production batches showed that ThO_2 KMC does not vary significantly from production batch to production batch.

*KMC = kernel migration coefficient.

7. Kernel migration coefficients for ThO_2 are less than KMC values assumed for ThC_2 during Fort St. Vrain (FSV) core design studies. Use of ThO_2 particles in planned FSV test elements will therefore provide an increased performance margin relative to FSV core 1 fuel.

The test results for TRISO UC_2 fuel are summarized as follows:

1. Kernel migration rates for irradiated UC_2 kernels are less than or equal to those for unirradiated UC_2 kernels.

2. Kernel migration coefficients for UC_2 are less than KMC values assumed during FSV core design studies. Use of UC_2 particles in planned FSV test elements will therefore provide an increased performance margin relative to FSV core 1 fuel.

3. Electron microprobe studies of TRISO UC_2 particles irradiated at less than 700°C to a kernel burnup of 63% FIMA and fast neutron exposure of 2.1×10^{21} n/cm^2 ($E > 0.18$ MeV) showed:

   a. Cesium is released from UC_2 kernels during irradiation at less than 700°C.

   b. Released Cs is concentrated in the buffer layer at the buffer-kernel interface.

   c. Barium is also released from these UC_2 kernels and concentrated in the buffer at the buffer-kernel interface.

   d. Lanthanide fission products are not released from UC_2 kernels during irradiation at 700°C or less.

4. Out-of-pile, thermal gradient testing can be used to duplicate the physical and chemical characteristics observed for SiC - fission product attack from in-pile testing as well as rates of reaction.

5. Electron microprobe evaluations of fission product distributions in TRISO UC_2 fuel after postirradiation thermal gradient heating at ∿1525°C showed that:

   a. Ce and Ba are uniformly distributed within the buffer layer.

   b. Lanthanide fission products are concentrated at the cool side inner PyC - SiC layer interface adjacent to the SiC - fission product reaction zone.

   c. No Cs, Ba, or lanthanide fission products remained in the UC_2 kernels after 188 hr of heating at ∿1525°C.

6. Rates of SiC - fission product reaction observed at ∿1525°C are independent of kernel burnup or fission product concentration when particles are heated in a thermal gradient. The variation in rate of reaction defined as rate of SiC thinning (t) was shown to be

$$t(\mu m/hr) = 9.74 \times 10^{8} \exp(90{,}094/RT) \qquad (9\text{-}8)$$

   for R having units of cal/mole-°K or

$$t(\mu m/sec) = 2.706 \times 10^{5} \exp(-3.7699 \times 10^{5}/RT) \qquad (9\text{-}9)$$

   for a R value of 8.314 J/mole-°K.

The test results for TRISO WAR UC_xO_y fuel are summarized as follows:

1. No conventional kernel migration has been observed in irradiated or unirradiated WAR UC_xO_y fuel kernels having O/U values of 1.3 and 0.7.

2. Since no kernel migration is observed in WAR fuel kernels, use of TRISO WAR fuel in proposed FSV test elements will provide an increased performance margin relative to FSV core 1 fuel.

3. Electron microprobe studies of TRISO WAR $UC_{4.3}O_{1.3}$ and $UC_{3.0}O_{0.7}$ particles irradiated at less than 700°C to kernel burnups of 63% FIMA at a fast neutron exposure of 2.1×10^{21} n/cm^2 $(E > 0.18 \text{ MeV})_{HTGR}$ showed that essentially no release of Cs, Ba, or lanthanide fission products occurs during low-temperature irradiations.

4. Postirradiation thermal gradient heating of TRISO $UC_{4.3}O_{1.3}$ fuel particles irradiated to 63% FIMA indicated very little metallic fission product release from the fuel kernels under conditions where 100% release of Cs, Ba, and lanthanides was observed from irradiated UC_2 kernels. No fission product - SiC reactions were observed in these same WAR particles under conditions where SiC layers in irradiated TRISO UC_2 fuels were thinned as much as 15 μm by SiC - fission product reactions.

5. The data presented show conclusively that TRISO WAR fuel particles will perform better than TRISO UC_2 fuel particles under irradiation conditions expected to cause kernel migration or SiC - fission product reactions in TRISO UC_2 fuel.

Introduction

The performance of LHTGR fissile and fertile fuel particles at high temperatures appears to be controlled by migration of fissile and fertile kernels toward the hot side of particle coatings when in a thermal gradient (kernel migration) or by fission product - coating reactions in fissile fuel. Fission product - coating reactions could lead to failure if the reactions allow some fission products to penetrate structural coating layers. Fission product - coating reactions are not observed in BISO coated ThO_2 fertile fuel. Reactions between certain metallic fission products and the SiC layer of TRISO UC_2 fuel have however been observed after irradiation in the temperature range 1300° to 1900°C (Refs. 9-5, 9-6). The fission products reacting at 1350°C have been shown to be lanthanides (Ref. 9-5). Conclusions drawn from observations of attack during irradiation are

(1) the rate of reaction increases with temperature and (2) the reaction rate increases with the density of fission products within particle coatings (Ref. 9-5). These conclusions led to a series of tests designed to define the kinetics of SiC - fission product reactions in TRISO UC_2 fuel by out-of-pile, postirradiation heating. The results of this test series are described in this section. TRISO coated WAR UC_xO_y fissile fuel is being evaluated as a possible alternate for TRISO UC_2 fuel. Available results on SiC - fission product reactions in irradiated TRISO WAR UC_xO_y are also summarized.

Kernel migration could lead to failure of HTGR fuel coatings if migrating kernels penetrate the structural layers of these coatings. Migration of UC_2 and ThO_2 fuel kernels has been discussed elsewhere (Refs. 9-2 and 9-7 through 9-9). Additional data describing UC_2 and ThO_2 migration, as well as the behavior of WAR UC_xO_y fuel kernels, are provided here.

Description of Experiments

Low-Temperature Irradiation Tests. A series of low-temperature, privately sponsored irradiation capsules (HB-1, -3, and -5) was undertaken during CY-75. A small number of ERDA-sponsored fuel particles was included in these tests to provide a set of samples for postirradiation heating studies (Ref. 9-10). Following irradiation to 2.1×10^{21} n/cm^2 $(E > 0.18 \text{ MeV})_{HTGR}$ and 63% FIMA at temperatures less than 700°C, samples of TRISO UC_2, WAR $UC_{4.3}O_{1.3}$, and $UC_{3.0}O_{0.7}$ batches irradiated in the HB-tests were prepared metallographically and subjected to electron microprobe evaluation. The microprobe study was conducted to evaluate as-irradiated fission product distributions of samples to be used in future postirradiation heating studies. Preirradiation coating and kernel properties for the samples examined are summarized in Table 9-4.

Postirradiation Thermal Gradient Heating. Postirradiation thermal gradient heating is used to study both kernel migration and SiC - fission product reaction rates. Precise definitions of the kinetics of these

TABLE 9-4
LOW IRRADIATION TEMPERATURE FISSILE PARTICLE SAMPLES USED FOR FISSION PRODUCT DISTRIBUTION STUDIES[a]

Particle Batch Data Retrieval Number	Kernel			Coatings													Total Coated Particle				
					Buffer[d]			Inner Isotropic PyC			SiC		Outer Isotropic PyC								
	Type	Mean Diameter (μm)	Density[b] (g/cm³)	Coating Type[c]	Thickness (μm)	Density[b] (g/cm³)	Seal Coat[b] (μm)	Thickness (μm)	Density[b] (g/cm³)	OPTAF[b,e]	Thickness (μm)	Density[b] (g/cm³)	Thickness (μm)	Density[b] (g/cm³)	Coating Rate[b] (μm/min)	OPTAF[b,e]	Diameter (μm)	Density[f] (g/cm³)	Th,U[b] Ratio	Uranium[f,g] (wt %)	Thorium[f] (wt %)
6151-00-035-001[h]	UC_2	202(11.9)	10.99	TRISO	91(8 6)	1.07	--	33(3 5)	1.92	1 22	29(3.7)	3.20	36(4.0)	1.85	3.96	1.17	572(39.6)	2.33	0	18 1	--
OR-1694-11[i]	$U{\cdot}C_{4.37}{\cdot}O_{0.41}$	326(50.8)	3.36	TRISO	48(9.3)	1.2	5.0	20(2.1)	2.01	<1.2	22(2.1)	3.24	39(3.7)	1.91	NA[j]	NA	580(63.5)	2.24	0	20.0[k]	--
6157-02-016[l]	$U{\cdot}C_{3.0}{\cdot}O_{0.68}$	291(27.3)	3.45	TRISO	35(8.2)	1.09	--	32(4.1)	1.96	1.15	38(2.4)	3.22	30(2.7)	1.89	3.57	1.17	558(43.8)	2.39	0	16.7[m]	--

[a] Standard deviations given in parentheses.
[b] Parent batch values.
[c] TRISO denotes a coating design with an SiC layer.
[d] For TRISO particles, buffer = (buffer + IPyC) - IPyC (for parent batch), the standard deviation is for the measured buffer + IPyC value.
[e] Optical Anisotropy Factor, relative units.
[f] Computed value based on the particle dimensions and densities for each batch.
[g] Weight percent of U in kernel.
[h] Parent batch 6151-00-035, thorium-doped kernels, Th/U = 0.0096.
[i] Parent batch OR-1694.
[j] NA = not available.
[k] 76.48 wt % U in kernel.
[l] Parent batch 6157-02-010.
[m] 83.03 wt % U in kernel.

phenomena are required in order to evaluate their impact on fuel performance during LHTGR core operation. Although both phenomena have been observed during irradiation testing (Refs. 9-5, 9-8, 9-9), it is difficult to extract kinetics data as the irradiation temperatures, kernel burnups, and fission product concentrations vary with time. Postirradiation heating provides a source for data generated at constant burnup under a well defined thermal environment that can be used to evaluate the effects of irradiation exposure, temperature, and temperature gradient on kernel migration rate and the rate of SiC - fission product reactions.

The methods used for preparation of samples and the techniques used for thermal gradient heating of irradiated particles are described in detail in Ref. 9-2. Briefly, one to seven irradiated fuel particles are loaded in a slotted graphite slab. Four graphite slabs are then placed near a resistance-heated graphite element to establish an operating temperature and temperature gradient across the coated particles. Contact x-radiographs of the particles in the graphite slabs are prepared at the beginning of each test. Thermal gradient heating is also interrupted periodically for x-ray examination to allow measurements of kernel migration distances and SiC thinning, which is caused by SiC - fission product reactions, as a function of time. Kernel migration is defined as the advance of the hot side of a kernel. When examining TRISO coated fuels, movement of the hot side of a kernel is detected by measuring the change in distance between the kernel buffer interface and the SiC layer on the hot side of coated particles. It is generally not possible to define a reference point in BISO coated particles for measurement of advance of the hot side of a kernel. As discussed in Ref. 9-2, kernel migration in BISO fuels is determined by measuring the change in distance from the cold side of a kernel or the interface between a rejected graphite layer and the buffer layer and the hot side buffer-kernel interface.

Postirradiation thermal gradient heating was also utilized to measure the extent of SiC - fission product reaction in TRISO fissile fuel as a function of time, temperature, burnup, and kernel type. Contact x-radiographs showed that a concentration of fission products developed on

the cool side of TRISO UC_2 particles during thermal gradient heating. The extent of fission product - SiC reactions was monitored by measuring the decrease in SiC thickness with time as shown in contact x-radiographs.

Fission product release measurements are also made during thermal gradient heating. The tests are conducted in a He atmosphere that is purged periodically through a liquid nitrogen cold trap, which is counted to detect Kr-85 release. Release of metallic fission products is monitored by gamma counting loaded graphite slabs before thermal gradient heating and each time a test is interrupted for kernel migration or SiC - fission product reaction measurements.

Sample Description. All fuel particles heated in this test series were irradiated. Average kernel and coating properties and general irradiation conditions for the particles tested are given in Table 9-5. The overall irradiation behavior of these samples is described in Refs. 9-5, 9-6, and 9-11. Following postirradiation examination (PIE), all fuel particles were gamma counted and x-rayed. Contact x-radiographs were examined to ensure macroscopic coating integrity and to determine diameters of particles heated in the thermal gradient tests. The Cs/Ru and Cs/Zr ratios determined by gamma counting were evaluated to ensure that no particle used in postirradiation heating had released Cs during irradiation.

Kernel Migration Results

TRISO UC_2 Fuel. Kernel migration of TRISO UC_2 fuel is related to diffusion of C from the hot side of a kernel to the cool side in a thermal gradient (Ref. 9-7). The carbon is rejected at the cool side buffer kernel interface as graphite, which causes translation of the kernel toward the hot side of a particle. The rate of kernel migration is characterized by the KMC, which is given by (Ref. 9-7)

$$KMC = (dx/dt)\ (T_2)\ (dT/dx)^{-1} \quad , \qquad (9\text{-}10)$$

TABLE 9-5
GENERAL KERNEL AND COATING PROPERTIES AND GENERAL IRRADIATION CONDITIONS FOR FUEL PARTICLES USED IN POSTIRRADIATION ISOTHERMAL AND THERMAL GRADIENT HEATING STUDIES

	Kernel		Coatings								Irradiation Conditions				
			Buffer		IPyC		SiC		OPyC						
Data Retrieval No.	Type	Diameter (μm)	Thickness (μm)	Density (g/cm^3)	Thickness (μm)	Density (g/cm^3)	Thickness (μm)	Density (g/cm^3)	Thickness (μm)	Density (g/cm^3)	Capsule and Location	Fast Neutron Exposure[a] ($10^{21}n/cm^2$)	Kernel Burnup (% FIMA)	Time Average Temp[b] (°C)	Time (hr)
4161-01-030	UC_2[c]	203	87	1.26	28	1.91	29	3.20	32	1.80	FTE-14, TS3-6	1.1	<30	1000	7608
4161-01-032-2	UC_2[c]	233	87	1.26	28	1.91	25	3.20	35	1.80	P13P, C1-P4	5.3	61	1350	4456
OR1694	$UC_{4.3}O_{1.3}$[d]	314	46	1.20	20	2.01	23	3.24	37	1.91	P13P, 1D-28	5.8	60	1050	4456
5466-149	ThO_2	481	63	1.11					76	2.02	FTE-14, TS6-1	1.2	0.9	1250	7608
4252-02-015-5	ThO_2	505	85	1.08					76	1.84	HT-12, 40	2.8	1.5	900	ND
4413-75T	ThO_2	576	69	ND[e]					85	1.89	P13L, C4T6	5.7	4.7	1325	6552
4252-02-015-6	ThO_2	508	84	1.08					75	1.84	HT-13, 40	6.1	5.8	900	ND
4252-02-015-7	ThO_2	509	88	1.08					68	1.84	HT-14, 40	9.8	11.4	900	ND

[a] Equivalent HTGR graphite damage fluence for E > 0.18 MeV.
[b] Design temperature.
[c] Dense melted kernels fabricated by the VSM process.
[d] Low-density kernels fabricated by the weak acid resin (WAR) process.
[e] ND = not determined.

where dx/dt = migration rate (cm/sec),

T = temperature (°K),

dT/dx = thermal gradient (°K/cm).

The variation in KMC with temperature (°K) is given by

$$KMC = \beta\, e^{-\Delta H/RT} \tag{9-11}$$

where β = pre-exponential constant (cm^2-°K/sec),

ΔH = apparent activation energy for kernel migration (cal/mole),

R = gas constant (cal/mole-°K),

T = temperature (°K).

Evaluation of UC_2 kernel migration during HTGR operation is made by estimating migration as a function of time using temperature and temperature gradient histories determined during HTGR core design studies and KMC values measured on unirradiated UC_2 kernels. This design approach is conservative given the assumption that kernel migration rates for irradiated UC_2 kernels are less than or equal to those for unirradiated UC_2 kernels.

Migration of UC_2 kernels from irradiated particle samples 4161-01-032-2 and 4161-01-030 was evaluated during postirradiation heating at nominal temperatures and temperature gradients of 1550°C and 450°C/cm, respectively, in experiment 6804 (Ref. 9-12). Particle properties and irradiation conditions are summarized in Table 9-5. Seven particles of each sample were prepared for testing. Prior to thermal gradient testing, particles were fired in their graphite thermal gradient crucibles to provide a good bond between the particles, graphite slab, and a graphitic "binder" material. During firing, two of the seven particles from 4161-01-032-2 failed. Failure was detected by monitoring both Cs and Kr-85 release. Failure of this type is attributed to shrinkage of the binder which provides a strong bond between the outer PyC layer of the coated particles and the graphite crucible. It should be noted here that the resin binder used is not the reference binder used for HTGR fuel rod fabrication.

The kernel migration results from the five remaining particles from 4161-01-032-2 and seven particles from 4161-01-030 are summarized in Table 9-6. The KMC values calculated using Eq. 9-10 are included in Table 9-6 for particles exhibiting kernel migration. When no kernel migration was observed, the KMC values were calculated assuming the minimum detectable migration distance for the measurement method used, which is 3 μm. The range for KMC at the 90% confidence level is also shown in Table 9-6 for unirradiated UC_2. KMC values from 4161-01-032-2 are consistent with unirradiated UC_2 data even though the fuel kernels experienced 61% FIMA during irradiation. Six of the seven particles from 4161-01-030 did not migrate. The fuel kernels in these six particles appeared to sinter slightly. The lack of migration and possible sintering were expected since photomicrographs of particles taken during PIE showed the kernels to be porous after irradiation (Ref. 9-11). The KMC value for the kernel from 4161-01-030 that did migrate is consistent with KMC values measured from unirradiated UC_2.

All available irradiated UC_2 KMC data are plotted versus inverse temperature in Fig. 9-12. The data summarized in Table 9-6 are included, as well as results obtained from thermal gradient heating of particles irradiated in capsule P13L and in-pile results from capsule P13N. In order to include the data, KMC values calculated assuming 3 μm of migration are plotted for particles from 4161-01-030. For comparison, Fig. 9-12 also shows the range for UC_2 KMC at the 90% confidence level determined on unirradiated fuel kernels. It is clear from Fig. 9-12 that rates for migration of irradiated UC_2 kernels are less than or equal to the unirradiated UC_2 kernel migration rates that are used to evaluate HTGR core designs. This justifies the HTGR core design approach that is used to evaluate UC_2 kernel migration.

TRISO WAR $UC_{4.3}O_{1.3}$ Fuel. The migration behavior of samples of TRISO coated $UC_{4.3}O_{1.3}$ kernels that were fabricated at ORNL using a weak acid resin (WAR) process was also studied in experiment 6804 (Ref. 9-12). The particles used were irradiated in fuel rod 1D-28 of capsule P13P and were

TABLE 9-6
KERNEL MIGRATION DATA FROM IRRADIATED TRISO COATED UC_2 FUEL PARTICLES HEATED AT ~1550°C

Sample Data Retrieval No.	Particle No.	Postirradiation Heating Results					KMC for Unirradiated UC_2[b] (cm^2-°K/sec)
		Temp (°C)	Temp Gradient (°C/cm)	Time (hr)	Kernel Migration Distance[a] (μm)	KMC Value (cm^2-°K/sec)	
4161-01-030	1	1552	541	476	12	4.3×10^{-6}	$2.7 \times 10^{-6} - 2.2 \times 10^{-5}$
	2	1552	541	476	-2	$<1.1 \times 10^{-6}$[c]	$2.7 \times 10^{-6} - 2.2 \times 10^{-5}$
	3	1552	476	617	-3	$<1.1 \times 10^{-6}$[c]	$2.7 \times 10^{-6} - 2.2 \times 10^{-5}$
	4	1552	476	617	-4	$<1.1 \times 10^{-6}$[c]	$2.7 \times 10^{-6} - 2.2 \times 10^{-5}$
	5	1552	541	476	-4	$<1.1 \times 10^{-6}$[c]	$2.7 \times 10^{-6} - 2.2 \times 10^{-5}$
	6	1552	541	476	2	$<1.1 \times 10^{-6}$[c]	$2.7 \times 10^{-6} - 2.2 \times 10^{-5}$
	7	1552	476	617	-3	$<1.1 \times 10^{-6}$[c]	$2.7 \times 10^{-6} - 2.2 \times 10^{-5}$
4161-01-032-2	1	1523	442	476	10	4.3×10^{-6}	$1.9 \times 10^{-6} - 1.6 \times 10^{-5}$
	2	1523	442	476	16	6.8×10^{-6}	$1.9 \times 10^{-6} - 1.6 \times 10^{-5}$
	3	1523	442	476	16	6.8×10^{-6}	$1.9 \times 10^{-6} - 1.6 \times 10^{-5}$
	4	1523	442	476	1	$<1.3 \times 10^{-6}$[c]	$1.9 \times 10^{-6} - 1.6 \times 10^{-5}$
	5	1523	(d)				
	6	1523	(d)				
	7	1523	442	476	11	4.7×10^{-6}	$1.9 \times 10^{-6} - 1.6 \times 10^{-5}$

[a] Negative numbers imply sintering of the kernel; positive numbers imply kernel migration.
[b] Range for KMC at the 90% confidence level determined from unirradiated UC_2 fuel particles.
[c] Calculated assuming a minimum detectable migration distance of 3 μm.
[d] Particle failed prior to thermal gradient heating.

recovered from the rod by burning in air and leaching. The particles tested in experiment 6804 therefore did not have outer PyC layers. During firing of the thermal gradient samples to ensure good thermal contact between particles and the graphite slab, one of seven particles failed. This was attributed to a combination of the missing outer PyC layer and binder-SiC interactions.

WAR kernels are low density and porous. The kernel porosity should tend to reduce the kernel migration rate relative to UC_2. The effect of the oxygen in WAR kernels or kernel migration is unknown. Results presented in Ref. 9-2 showed that kernel migration is not observed in unirradiated WAR kernels.* The kernels were shown to sinter during thermal gradient heating. Limited heavy metal migration was observed to take place up the temperature gradient; however, the rate of conventional UC_2 kernel migration was 5 to 6 times greater than the observed metal migration in WAR particles.

The results of thermal gradient heating of irradiated TRISO WAR $UC_{4.3}O_{1.3}$ fuel particles are summarized in Table 9-7. The hot side of one kernel advanced toward the SiC layer. The remaining kernels either remained motionless or decreased in diameter during thermal gradient heating. The KMC values calculated from the resin data using Eq. 9-10 are shown in Table 9-7 along with the range for KMC at the 90% confidence level estimated from unirradiated UC_2 data. The KMC value estimated for the one kernel that appears to have migrated is less than KMC values expected for UC_2 kernels. KMC values for kernels showing no migration were estimated assuming 3 μm of migration, which is the minimum migration distance that can be detected with the techniques employed. Even with this very conservative assumption, the apparent KMC for the irradiated resin kernels is about a factor of 10 less than KMC values expected for UC_2 kernels.

The data from both irradiated and unirradiated WAR fuel particles continue to support the conclusion that kernel migration like that observed in

*The chemical composition of WAR particle batch OR-1694 was erroneously reported as $UC_{4.4}O_{0.4}$ in Ref. 9-2.

TABLE 9-7

KERNEL MIGRATION DATA FROM IRRADIATED TRISO COATED WAR $UC_{4.3}O_{1.3}$ PARTICLES HEATED AT ~1530°C

Sample Data Retrieval No.[a]	Particle No.	Postirradiation Heating Results					KMC For Unirradiated UC_2[c] (cm^2-°K/sec)
		Temp (°C)	Temp Gradient (°C/cm)	Time (hr)	Kernel Migration Distance[b] (μm)	KMC Value (cm^2-°K/sec)	
OR1694	1	(d)					
OR1694	2	1530	515	667.5	0	$<5.7 \times 10^{-7}$[e]	$2.1 \times 10^{-6} - 1.7 \times 10^{-5}$
OR1694	3	1532	723	331	-7	$<1.1 \times 10^{-6}$[e]	$2.1 \times 10^{-6} - 1.7 \times 10^{-5}$
OR1694	4	1530	515	667.5	-3	$<5.7 \times 10^{-7}$[e]	$2.1 \times 10^{-6} - 1.7 \times 10^{-5}$
OR1694	5	1530	515	667.5	1	$<5.7 \times 10^{-7}$[e]	$2.1 \times 10^{-6} - 1.7 \times 10^{-5}$
OR1694	6	1530	515	667.5	-10	$<5.7 \times 10^{-7}$[e]	$2.1 \times 10^{-6} - 1.7 \times 10^{-5}$
OR1694	7	1530	515	667.5	5	9.5×10^{-7}[e]	$2.1 \times 10^{-6} - 1.7 \times 10^{-5}$

[a] Particles are from capsule P13P, fuel rod ID-28.

[b] Negative numbers imply sintering of the kernel; positive numbers imply kernel migration.

[c] Range for KMC at the 90% confidence level determined from unirradiated UC_2 fuel kernels.

[d] Particle failed prior to thermal gradient heating.

[e] Calculated assuming a minimum detectable migration distance of 3 μm.

UC_2 does not occur in WAR UC_xO_y fuel kernels. Substitution of WAR fissile fuel kernels for the UC_2 kernels planned for LHTGRs will therefore increase the performance margin of HTGR fuel. Testing is continuing to broaden the data base needed to support the conclusion that no kernel migration will take place in WAR UC_xO_y fuel kernels.

BISO ThO_2 Fuel. A discussion of kernel migration of irradiated BISO ThO_2 fuel was presented in Ref. 9-2. Based primarily upon results of postirradiation thermal gradient heating at 1500° to 1550°C, the following major conclusions were drawn:

1. ThO_2 kernels migrate up a thermal gradient during postirradiation thermal gradient heating.

2. The observation that graphite precipitates at grain boundaries on the cool side of migrating kernels suggested that ThO_2 kernel migration is related to solid-state diffusion of carbon in ThO_2. This implies that the rate controlling step in the migration process is the same for ThO_2, ThC_2, and UC_2.

3. At ∿1500°C, ThO_2 kernel migration was only observed after an incubation period (delay time) that increased with decreasing burnup. Once the delay time was exceeded, observed migration rates were burnup independent.

4. Kernel migration appears to stop after coating failure, suggesting that the presence of fission products released during coating failure or CO/CO_2 are needed for ThO_2 kernel migration.

ThO_2 kernel migration data accumulated since Ref. 9-10 was issued are summarized below and combined with results in Ref. 9-2 to provide a more complete description of ThO_2 migration.

The experiments conducted were an extension of those described in Ref. 9-2. The experimental procedures and the analytical techniques and interpretations are the same as those described in Ref. 9-2. A summary of the

experiments conducted to evaluate ThO_2 kernel migration is provided in Table 9-8. The burnups of the ThO_2 particles heated range from 0.9 to 11.4% FIMA, which exceeds the range expected for LHTGR fuel. Three separate batches of fuel kernels are also represented, which will show to some degree the variability in migration behavior that can be expected from batch to batch.

Release of Kr-85 and Cs-137 was monitored as a function of time for all tests summarized in Table 9-8. Earlier results from experiment 6532 (Ref. 9-2) suggested that at 1548°C essentially 100% Kr-85 and Cs-137 release occurred within 50 to 100 hr of failure of a coating on irradiated BISO ThO_2 fuel (Ref. 9-2). The experiments outlined in Table 9-8 each contained samples from four irradiation experiments. Since Kr-85 release was monitored by sampling furnace atmospheres during testing, the gaseous release data from these experiments represent an average release from the four samples in each test. Cesium release was monitored by gamma counting individual heating crucibles whenever tests were interrupted for kernel migration measurements.

Fission product loss data for Kr-85 and Cs-137 are shown as a function of time in Fig. 9-13 for the test conducted at ∿1500°C (experiment 6617). Approximately 50% of the Kr-85 inventory of the particles in the test (24 particles total) was released ∿100 hr after test initiation. Gamma counting of individual crucibles during test interruptions showed high Cs loss for samples from 4252-02-015-7 very early in the test and very slow diffusive release of Cs from the other three samples. Based on the observations of Cs and Kr loss made on particles that failed in experiment 6532 (Ref. 9-2), it appears that particles from batch 6542-02-015-7 failed in experiment 6617, while the other particles being tested survived. This is supported by the fact that the quantity of Kr-85 lost during the test is 112% of the expected inventory in particles from batch 6542-02-015-7.

Similar results were obtained from the other tests in the series being described. Particles from batch 4252-02-015-7 always failed early in each

TABLE 9-8

SUMMARY DESCRIPTION OF OUT-OF-PILE HEATING EXPERIMENTS CONDUCTED TO EVALUATE IRRADIATED ThO_2 KERNEL MIGRATION

Out-Of-Pile Experiment No.	Particle Batch No.	Kernel Burnup (% FIMA)	Number Of Particles Per Test	Total Heating Time (hr)	Average Temp (°C)	Average Temp Gradient (°C/cm)	Range Of Migration Distances Observed (μm)
6613	5466-149	0.9	7	4709	1335	408	0-2
	4252-02-015-5	1.5	7	4709	1319	413	3-14
	4252-02-015-6	5.8	7	4709	1322	309	10-16
	4252-02-015-7	11.4	3	1405	1336	741	1-5
7011	5466-149	0.9	7	676	1419	360	0-1
	4252-02-015-5	1.5	7	676	1449	447	0-20
	4252-02-015-6	5.8	7	676	1454	513	3-14
	4252-02-015-7	11.4	5	676	1449	385	2-11
6617	5466-149	0.9	7	606	1510	699	2-7
	4252-02-015-5	1.5	7	606	1559	705	2-47
	4252-02-015-6	5.8	7	606	1521	405	21-31
	4252-02-015-7	11.4	3	512	1494	539	15-22
6532	4413-759	3.0	7	348	1548	588	17-33
7015	5466-149	0.9	7	12.5	1662	904	0
	4252-02-015-5	1.5	7	12.5	1686	838	0-2
	4252-02-015-6	5.8	7	12.5	1681	1053	0-22
	4252-02-015-7	11.4	5	12.5	1664	852	1-3

test, while no failure was detected in the other samples tested. As can be seen in Table 9-5, batch 4252-02-015-7 received the most severe irradiation exposure of the ThO_2 samples tested. The exposure far exceeded maximum exposures expected in a LHTGR. The failure that was observed in the out-of-pile tests was due to the combination of high irradiation exposure and interactions that take place between particle coatings and the carbonaceous resin binder used in thermal gradient tests. In order to avoid possible confusion by introducing ThO_2 kernel migration data from failed fuel particles, data from tests conducted on 4252-02-015-7 are not treated in the discussion that follows.

Metallographic and microprobe examinations of irradiated ThO_2 particles heated for 348 hr at 1548°C under a thermal gradient of 588°C/cm were described in Ref. 9-2. It was shown that C diffusion from the hot side to the cool side of irradiated ThO_2 kernels in conjunction with C precipitation in ThO_2 grain boundaries is related to ThO_2 kernel migration. The microstructures observed were similar to those observed in ThO_2 kernels irradiated under conditions severe enough to cause in-pile migration (Ref. 9-13).

Metallographic examinations have also been completed on particles from batches 4252-02-015-5, 4252-02-015-6, and 4252-02-015-7 after thermal gradient heating at ∿1520°C (experiment 6617). The appearance of a particle from batch 4252-02-015-5 is shown in Figs. 9-14 and 9-15. The kernel was spherical and centered in the particle before thermal gradient heating. The hot side of the kernel has clearly advanced and there is a deposited layer on the cool side of the kernel that is optically responsive under polarized light (Fig. 9-14). The optically responsive layer is identical in appearance to the redeposited graphite layer found during kernel migration of UC_2 and ThC_2 kernels, which supports earlier conclusions that carbon diffusion from the hot side of the kernel to the cool side of the kernel is related to migration of irradiated ThO_2 fuel kernels. A higher magnification micrograph of the redeposited layer is shown in Fig. 9-15.

One description of kernel migration (Ref. 9-7) suggests that kernels are pushed up a thermal gradient as the redeposited graphite layer grows on the cool side of a kernel. This implies no kernel shape change and suggests that the cool and hot sides of the kernel migrate at the same rate. Assuming that the original kernel-buffer interface on the cool side of the kernel in Fig. 9-14 is the buffer-redeposited graphite layer, the hot side of the kernel clearly advanced toward the high-temperature side of the particle more rapidly than the cool side. Similar observations were made from examination of particles irradiated to fast neutron exposures and kernel burnups higher than those experienced by 4252-02-015-5. The only change noted as the irradiation exposure of particles tested increased was that the hot side buffer-kernel interface became more regular with increasing exposure. This is illustrated in Fig. 9-16 which shows photomicrographs taken after thermal gradient testing of particles irradiated to 1.5% FIMA at 2.8×10^{21} n/cm^2 (E > 0.18 MeV)$_{HTGR}$ (4252-02-015-5) and 5.8% FIMA at 6.1×10^{21} n/cm^2 (E > 0.18 MeV)$_{HTGR}$ (4252-02-015-6).

The kernel elongation that is observed could occur if gas phase C transport caused movement of enough C from the buffer on the hot side of the particle to produce a void and fission gases trapped within the kernel caused the kernel to extrude into the void. This type of behavior should however produce "flow" lines in the kernel. No metallographic examinations to date show the presence of any flow patterns within migrating ThO_2 fuel kernels (see Figs. 9-14 through 9-16), which suggests that the elongation is not due to any form of extrusion. A possible explanation is that the elongation is related to migration of Th up the thermal gradient across the kernel. This potential mechanism will be treated further in future discussions of ThO_2 kernel migration.

The primary purpose for this test series was to define kernel migration rates for irradiated ThO_2 kernels as a function of temperature and irradiation exposure (fast neutron fluence and kernel burnup). Testing in the temperature range 1500° to 1550°C is complete. Testing at nominal temperatures of 1300°, 1400°, and 1700°C is continuing. Results provided

for these tests must therefore be considered as preliminary; however, no significant changes are expected.

Initial heating tests (Ref. 9-2) showed that the diameter of irradiated ThO_2 kernels may increase slightly during out-of-pile thermal gradient heating. Kernel swelling measurements are summarized in Table 9-9. Swelling was detected by determining the change in kernel diameter perpendicular to the thermal gradient as a function of time at temperature. Based on the change in diameter observed as a function of time during the tests, no additional swelling is expected at nominal test temperatures of 1300° or 1500°C. Continued testing should however cause additional kernel swelling in particles heated at ∿1400° or ∿1700°C. Results obtained during heating of particles from batch 4413-75T suggest that swelling is related to the presence of C dissolution in the ThO_2 kernels. Final interpretation of the data must await completion of the 1400° and 1700°C tests.

Measurements of kernel migration were made periodically during each heating experiment by determining the change in diameter of kernels parallel to the thermal gradient from contact x-radiographs (Ref. 9-2). A typical set of such measurements is shown in Fig. 9-17 for particles heated at 1559°C under a thermal gradient of 705°C/cm after irradiation to a kernel burnup of 1.5% FIMA (batch 4252-02-015-5). One characteristic apparent in Fig. 9-17 is that there is a period of slow migration followed by a period of rapid migration. The period of slow migration has been termed an incubation period. The incubation period is even more noticeable if kernel swelling perpendicular to the thermal gradient is subtracted from the kernel migration distance. The incubation period for batch 4252-02-015-5 is in the range 100 to 400 hr at 1559°C. It also appears that the migration rates of the various particles shown in Fig. 9-17 are approximately the same after the incubation period is exceeded. Incubation periods were observed in the other samples heated in this test series and are summarized in Table 9-10. The data suggest that the incubation period decreases with increasing kernel burnup and test temperature.

TABLE 9-9
KERNEL SWELLING OBSERVED DURING OUT-OF-PILE THERMAL GRADIENT HEATING OF BISO ThO_2 FUEL PARTICLES

Particle Batch No.	Kernel Burnup (% FIMA)	Out-of-Pile Heating Condition			Kernel Swelling (μm)
		Time (hr)	Average Temp (°C)	Average Temp Gradient (°C/cm)	
5466-149	0.9	4709	1335	408	0.4 (±1.0)[a]
		676	1419	360	-0.4 (±0.5)
		606	1510	699	1.6 (±1.0)
		12.5	1662	904	1.4 (±1.0)
4252-02-015-5	1.5	4709	1319	413	0.1 (±1.6)
		676	1449	447	1.3 (±1.1)
		606	1559	705	4.0 (±1.2)
		12.5	1686	838	0.9 (±2.0)
4413-75T	3.0	348	1548	588	8.6 (±2.4)
4252-02-015-6	5.8	4709	1322	309	0.1 (±1.1)
		676	1454	513	-0.4 (±1.1)
		606	1521	405	3.7 (±1.0)
		12.5	1681	1053	1.3 (±2.4)

[a] Values in parentheses are standard deviations.

TABLE 9-10
INCUBATION PERIOD REQUIRED BEFORE SIGNIFICANT ThO_2 KERNEL MIGRATION IS OBSERVED

Particle Batch No.	Kernel Burnup (% FIMA)	Out-of-Pile Heating Conditions		Incubation Period (hr)
		Average Temp (°C)	Average Temp Gradient (°C/cm)	
5466-149	0.9	1335	408	>4709[(a)]
		1419	360	>676
		1510	699	>606
		1662	904	>12.5
4252-02-015-5	1.5	1319	413	2500->4709
		1449	447	360->676
		1559	705	100-400
		1686	838	>12.5
4413-75T	4.7	1548	588	25-110
4252-02-015-6	5.8	1322	309	<1000
		1454	513	<360
		1521	405	0-30
		1681	1053	<12.5

[(a)] Implies incubation period has not been exceeded.

Quantifying and understanding the incubation period will be an important part of understanding ThO_2 kernel migration. The incubation period will also be a necessary consideration when predicting ThO_2 kernel migration behavior during LHTGR operation. Although it appears that the incubation period will have only a minor impact on the migration of kernels with burnups exceeding 1.5% FIMA, it is significant when discussing the behavior of fuel having burnups of less than 1.5% FIMA.

Based on the observations of C diffusion in migrating ThO_2 kernels, kernel migration coefficients were calculated for ThO_2 using Eq. 9-10. The incubation period and kernel swelling perpendicular to the thermal gradient were ignored. The variation in KMC with kernel burnup is shown in Figs. 9-18 and 9-19 for testing at 1510° to 1559°C and 1319° to 1335°C, respectively. Both sets of data suggest that ThO_2 KMC values increase by approximately an order of magnitude as ThO_2 kernel burnups increase from $\sim$1 to 2% FIMA and that KMC values, within the scatter of available data, do not vary with kernel burnup for burnups in excess of 1.5% FIMA. There may be a real difference in ThO_2 KMC values for particles having kernel burnups greater than or less than 1.5% FIMA. This might be expected if the U-233 that builds up in the kernels during irradiation is related to kernel migration. This type of argument is consistent with in-pile results that show more rapid migration for mixed Th/UO_2 kernels than for ThO_2 kernels (Ref. 9-9) and will be evaluated at a later date by predicting U contents for irradiated ThO_2 kernels in the various samples tested in this series. Another possible explanation for the increase in apparent KMC at $\sim$1.5% FIMA is that the incubation period has not been exceeded in the low burnup samples (<1.5% FIMA), while the incubation time is insignificant relative to total test time for the high burnup samples. This possibility can only be evaluated through continued testing.

The variation in KMC with inverse temperature is shown in Fig. 9-20 for data obtained in the temperature range 1300° to 1700°C. Data were accepted for this figure only if the incubation period for a particular kernel was short relative to the test being conducted. Migration distances

and times used to calculate KMC values included kernel swelling and the incubation time. Figure 9-20 supports the conclusion that KMC values are independent of ThO_2 kernel burnup for test times that are long relative to the incubation period.

The data plotted in Fig. 9-20 were collected from particles having kernels from two different kernel batches. Kernels in particles irradiated to 1.5 and 5.8% FIMA were fabricated in late 1972, while kernels irradiated to 4.7% FIMA were fabricated in late 1968. The similarity in KMC values for kernels from these two distinct fabrication batches suggests that little variation in ThO_2 KMC should be expected from batch to batch. A least-squares analysis of the ThO_2 KMC data assuming the variation with temperature indicated by Eq. 9-11 yielded

$$\text{KMC } (\text{cm}^2\text{-}^\circ\text{K/sec}) = 1.36 \times 10^{-5}\, e^{-83{,}419/RT} \quad . \qquad (9\text{-}12)$$

The range for KMC at the 90% confidence level is also shown in Fig. 9-20.

The variation in ThO_2 KMC with temperature given in Eq. 9-12 can be used to evaluate the impact of ThO_2 kernel migration on LHTGR fuel performance. Coupled with the assumption that ThO_2 kernel migration is independent of kernel burnup, Eq. 9-12 will yield a conservative estimate of behavior.

Fission Product Distributions During Low-Temperature Irradiation

TRISO UC_2 Fuel. TRISO UC_2 fuel particles from batch 6151-00-035-001 were prepared metallographically and examined by electron microprobe at ORNL after irradiation at less than 700°C to 63% FIMA and 2.1×10^{21} n/cm^2 $(E > 0.18 \text{ MeV})_{HTGR}$. Representative photomicrographs are shown in Fig. 9-21. Excellent performance was noted for the inner PyC, SiC, and outer PyC layers of all particles examined. Metallographic examination suggested that the inner PyC layer actually shrank away from the SiC layer during irradiation. The kernels were quite porous, showing very large bubbles

that were formed by gaseous fission products trapped within the kernels during irradiation.

Results of electron microprobe analyses of these same fuel particles are shown in Fig. 9-22. Distributions of U, Si, Cs, and lanthanide fission products were evaluated. The U is concentrated in the kernel and Si is concentrated in the SiC layer. Evaluations of samples irradiated at higher temperatures (1100°C) generally show Cs distributed in the buffer layer while lanthanides are concentrated at the SiC - inner PyC interface on the cool side of a particle (Ref. 9-5). Barium is generally associated with Cs. Figure 9-22 shows that Cs is at the buffer-kernel interface after irradiation at less than 700°C. A simultaneous scan for Cs and U showed that Cs was located in the buffer layer at the buffer-kernel interface, implying that Cs is released from the UC_2 kernel at temperatures less than 700°C. As is the case in higher temperature irradiations, Cs and Ba were correlated. The lanthanides formed during this low-temperature irradiation remained within the kernel. Neodynium is shown in Fig. 9-22e as an example. Comparison of this result with those obtained from samples irradiated at temperatures greater than 1100°C shows that lanthanide fission products are released from UC_2 kernels in the temperature range 700° to 1100°C.

The behavior of fission products in this sample will be evaluated during out-of-pile heating studies conducted at higher temperatures in order to determine the effect of temperature on fission product release from UC_2 kernels and fission product redistribution in TRISO UC_2 fuels.

TRISO WAR $UC_{x-y}O$ Fuel. Metallographic and microprobe examinations were also made on samples from the two TRISO coated WAR UC_xO_y batches identified in Table 9-4. Typical results obtained by examining particles from batch 6157-02-016 ($UC_{3.0}O_{0.7}$ kernel) are included in Fig. 9-23. Coating performance was excellent. No failures were observed. The inner PyC layer shrank away from the SiC layer during irradiation. Large bubbles were observed in the kernels and the kernels appeared to have sintered during irradiation.

The sintering is suggested by the large quantity of void within the original kernel cavity (Fig. 9-23a). On closer inspection (Fig. 9-23b), the kernel appears to have separated into two distinct phases. No microprobe work sensitive enough to identify the chemical constituents of each phase was done; however, it seems reasonable to assume that one phase is C rich while the other is O rich. Attempts will be made to distinguish between the two phases in future studies.

Distributions of U, Si, Cs, and lanthanide fission products were evaluated by microprobe examination. Uranium (Fig. 9-23c) was found to be concentrated in the kernels and Si was concentrated in the SiC layer. Essentially all of the Cs formed during irradiation of TRISO UC_2 particles at 700°C or less was released into the buffer layer (Fig. 9-22). The majority of the Cs appears to have been retained by the WAR kernels (Fig. 9-23d). Comparison of the size of the U and Cs images in Fig. 9-23c and 9-23d shows however that some Cs was released from the WAR kernel into the buffer. As with UC_2, Ba and Cs appear correlated in these WAR particles. All lanthanides examined behaved similarly; neodynium is shown in Fig. 9-23e as an example. The central portion of the Nd image is dense. Comparison of this dense portion with the U image indicates that the dense portion represents Nd that is contained within the kernel. The lower density Nd halo surrounding the kernel suggests release of small quantities of Nd. It is not known whether this release occurred as a result of diffusive release from the kernel or from decay of recoil fission fragments. Similar release of lanthanide fission products could also have occurred from the TRISO coated UC_2 kernels; however, the available data are not sensitive enough to distinguish between lanthanides in the buffer and lanthanides in the UC_2 kernel.

Observations made during examination of samples from OR-1694-11 ($UC_{4.3}O_{1.3}$ kernel) are similar to those described above, indicating that the O content of WAR kernels has little impact on Cs, Ba, and lanthanide fission product distributions at 700°C or less. Microprobe analyses of samples of OR-1694 have also been done after irradiation at 1085° and

1320°C (Ref. 9-5). Fission product distributions observed after these higher temperature irradiations are the same as those observed after irradiation at 700°C or less. Fission product distributions in $UC_{4.3}O_{1.3}$ kernels therefore seem independent of temperature for temperatures less than 1320°C.

The samples of TRISO WAR fuels discussed above will be used in high-temperature out-of-pile heating studies to evaluate effects of temperature on fission product distributions in TRISO WAR fuel particles.

SiC - Fission Product Reactions

TRISO UC_2 Fuel. During irradiation at temperatures in excess of 1100°C, certain metallic fission products are released from UC_2 kernels into the buffer layer of TRISO coatings. At temperatures in excess of ∿1300°C, the lanthanide fission products have been shown to concentrate at the inner PyC - SiC interface of TRISO UC_2 fuel and to react slowly with the SiC layer (Ref. 9-5). A series of out-of-pile thermal gradient tests is now under way to provide data that will define the kinetics of fission product - SiC reactions in TRISO UC_2 fuel as a function of kernel burnup, temperature, and temperature gradient. A summary of the tests that have been completed to date is given in Table 9-11.

The results were obtained from tests conducted primarily to observe kernel migration rates in irradiated TRISO UC_2 fuel. Particles were heated in the configuration described earlier for thermal gradient (kernel migration) testing. Test samples were radiographed periodically during each test. Radiographs taken before thermal gradient heating and after 93 and 476 hr at temperature are shown in Figs. 9-24 and 9-25 for particles from samples 4161-01-030 and 4161-01-032-2, respectively. Sample 4161-01-030 had been irradiated to 30% FIMA and 1.1×10^{21} n/cm^2 $(E > 0.18\ MeV)_{HTGR}$ at about 1100°C. Zero-hour radiographs (Fig. 9-24a) indicated little or no fission product release from the kernels during irradiation. Radiographs taken after 93 hr at 1552°C (Fig. 9-24b) showed a white region near the

TABLE 9-11
SUMMARY OF POSTIRRADIATION THERMAL GRADIENT HEATING TESTS PROVIDING INPUT TO A DESCRIPTION OF SiC - FISSION PRODUCT REACTION RATES IN TRISO UC_2 FUEL

Out-of-Pile Experiment No.	Particle Batch No.	Kernel Burnup (% FIMA)	Number of Particles Per Test	Total Heating Time (hr)	Average Temp (°C)	Average Temp Gradient (°C/cm)	Reduction in SiC Thickness Caused by SiC - Fission Product Reactions (μm)
6804	4161-01-030	30	7	617	1552	476	11-15
6804	4161-01-032-2	61	5	331	1523	442	5-9
5217-5	4413-5	73	6	600-2566	1460	260	3-9
5217-5	4413-5	73	12	6868	1383	260	3-13
5217-5	4413-5	73	8	6868	1306	260	3-6

cool side inner PyC - SiC interface. As will be seen later, electron microprobe results showed this to be lanthanide fission products. The rapid appearance of these fission products on the cool side of the test particles suggests that the rate of release from the kernel is quite high at 1552°C and that fission product mobility in the coatings must also be high. There is no evidence of a large increase in fission product concentration with longer times at temperature (Fig. 9-24c). Close examination of the SiC layer on the cool side of the particle in Figs. 9-24a, b, and c shows that the SiC is being thinned by the reaction with the fission products. The variation in cool side SiC thickness with time was measured from higher magnification images of radiographs like those in Fig. 9-24 to obtain SiC - fission product reaction rate data, which will be discussed later.

A similar series of radiographs is shown in Fig. 9-25 for particles heated in a thermal gradient at 1523°C after irradiation to 61% FIMA and a fast neutron exposure of 5.3×10^{21} n/cm^2 $(E > 0.18\ MeV)_{HTGR}$ at approximately 1350°C (batch 4161-01-032-2). The conclusions drawn from Fig. 9-25 are the same as those from Fig. 9-24. One interesting difference is that the conditions under which batch 4161-01-032-2 was irradiated resulted in release of metallic fission products from the kernel during irradiation. The fission products also concentrated in one specific region of the particle during irradiation. After only 93 hr at 1523°C these fission products relocated to the cool side of the particle in the out-of-pile heating test. This confirms the conclusion of high fission product mobility made in the discussion of Fig. 9-24 and suggests that the driving force for lanthanide fission product concentration at the cool side inner PyC - Sic layer interface in TRISO UC_2 fuel is the thermal gradient. Another difference in Figs. 9-24 and 9-25 is that the quantity of fission products on the cool side of particles in Fig. 9-25 appears larger than the quantity noted in Fig. 9-24. This is not surprising since the kernel burnup, and therefore the quantity of fission products, is higher for batch 4161-01-032-2 than for batch 4161-01-030.

One set of particles from batch 4161-01-030 was removed from experiment 6804 after 188 hr at temperature for metallographic and electron microprobe analysis. Radiographs of these particles were essentially identical to the radiographs shown in Fig. 9-24. Bright field and polarized light photomicrographs of a typical particle are shown in Fig. 9-26. The UC_2 kernels in these particles were quite porous following irradiation. The hot side of the particle shows no visible effects of irradiation or postirradiation thermal gradient heating. There is considerable evidence of SiC - fission product reaction on the cool side, however. Comparison of the SiC thickness at the cool side with SiC thickness measured at other points in the particle shows clearly that the coating was thinned during out-of-pile heating. Some of the reaction products are shown in the enlargement of the reaction zone (Fig. 9-27). The whitish phase that penetrates the SiC layer and is scattered within the inner PyC layer is clearly visible. Figures 9-26 and 9-27 also suggest that the inner PyC layer was pushed away from the SiC layer. The makeup of the gray phase between the SiC and inner PyC on the particle cool side is unknown. Another observation is that the inner PyC has become optically responsive on the particle cool side (Fig. 9-26b). This is generally attributed to graphitization of the PyC layer. These characteristics are identical to those described by both GA and workers at ORNL when SiC - fission product reactions are observed during postirradiation examination of TRISO UC_2 fuel.

The particle shown in Figs. 9-26 and 9-27 was also subjected to electron microprobe analysis. The results are shown in Fig. 9-28. Figure 9-28a is a specimen current image that shows a heavy metal concentration on the cool side of the particle. The uranium trace (Fig. 9-28b) showed no uranium redistribution except for a minor amount of dispersed metal in the buffer adjacent to the kernel hot side. No redistribution of Si (Fig. 9-28c) was noted. Silicon has been found in UC_2 kernels in the past in some particles showing extensive SiC - fission product attack. The lack of Si redistribution (Fig. 9-28c) suggests that some form of Si transport is not a necessary component of the attack mechanism. There is no explanation

for the Si activity seen midway between the hot and cool sides of the particle. Cesium (Fig. 9-28d) was found to be uniformly distributed throughout the buffer layer. Barium was also distributed throughout the buffer layer. All lanthanide fission products were concentrated near the reaction zone on the cool side. Neodynium (Fig. 9-28e) is included as an example. No detectable Cs, Ba, or lanthanide fission products were found in the kernel, implying 100% release of these fission products from UC_2 fuel kernels at 1552°C.

The microprobe data described above are identical to results obtained from irradiation data (Ref. 9-5), which leads to the conclusion that fission product redistribution and fission product - SiC reaction kinetics can be studied under well defined thermal conditions using out-of-pile heating techniques.

The degree of SiC - fission product reaction was monitored by measuring the change in SiC thickness from enlargements of radiographs like those shown in Figs. 9-24 and 9-25. The change in SiC thickness measured as a function of time at 1520° to 1550°C is shown in Fig. 9-29 for TRISO UC_2 particles irradiated to 30% FIMA or 60% FIMA. A least-squares fit to the data for each particle type, assuming a linear decrease in SiC thickness with time, is also shown. The fact that the intercept is not zero is not surprising since the zero hour SiC thickness was the hardest to measure. Silicon carbide thinning in the particles that had been irradiated to 30% FIMA was more rapid than in particles irradiated to 60% FIMA. This is consistent with the test temperatures for these samples. It is however surprising in view of the difference in the number of fission products in each sample. Prior to conducting these tests, the decrease in SiC thickness was expected to vary with the concentration of the reacting fission products. The burnup of one sample tested was twice that of the other. A more important measure of expected reaction rate might have been the fission density, which is defined as the number of fissions per unit volume inside the SiC layer. This quantity is proportional to the quantity of any single fission product contained within the SiC layer. The ratio of fission densities for the two samples is 2.62, which implies that fission

product - SiC reactions might have proceeded much more rapidly in the high burnup sample than in the low burnup sample. The fact that the apparent reaction rates are independent of fission density and kernel burnup implies that the concentrating effect of the thermal gradient saturates the reaction zone with fission products. As a result, the kinetics of the phenomenon are dependent only on temperature. This conclusion will be tested by heating particles from the samples discussed here in the absence of a thermal gradient to determine if the rate of reaction is fission density sensitive in the absence of a thermal gradient.

Rates of SiC thinning due to SiC fission product reactions were determined for the test samples outlined in Table 9-11. Rates were estimated assuming the observed decrease in SiC thickness increased linearly with time (Fig. 9-29). No explicit model that describes the phenomenon and provides a theoretical description of the kinetics of the phenomenon has as yet been developed. It was assumed for discussion purposes that a rate expression for SiC thinning would be of the form

$$t = Ae^{-Q/RT} \quad , \tag{9-13}$$

where t = rate of SiC thinning (μm/hr),
A = pre-exponential constant (μm/hr),
Q = apparent activation energy (cal/mole),
R = gas constant (cal/mole-°K),
T = temperature (°K).

The rate of SiC thinning is shown in Fig. 9-30 as a function of inverse temperature. A least-squares fit to the data assuming a rate expression of the form given by Eq. 9-13 is included.

The tests conducted to determine rates of SiC thinning due to SiC - fission product reactions were conducted to the point that as much as one half of the SiC layer on some particles was removed. A very important observation relative to overall coating integrity is that coating failure

resulting in fission gas release was not detected even after this amount of SiC thinning. This is further support for the conservatism incorporated into the pressure vessel design of HTGR fuel particles.

As data similar to those shown in Fig. 9-30 evolve to the point that they can be used to estimate fuel performance in an operating HTGR, their relationship to in-pile observations must be explored. A summary of in-pile observations of SiC - fission product reactions was provided in Ref. 9-5. Reference 9-5 includes statements of the fractions of test samples in which some reaction was observed and the fractions of test samples in which one-half of the SiC layer was penetrated by SiC - fission product reactions. Reaction rates were estimated from these data using the time-average operating temperature and total test time plus the assumptions that the observation of some reaction implied less than 5 μm of reaction depth while 50% penetration implied a 15-μm reaction depth. Additional data were taken from PIE results from FTE-14 and -15 and RTE-2 and -4 (Ref. 9-12). Maximum SiC thinning rates estimated from the in-pile data were superimposed in a duplicate of Fig. 9-30 and are presented in Fig. 9-31. Given the uncertainties and assumptions used to treat the in-pile data, the in-pile and out-of-pile data are generally consistent. The out-of-pile tests therefore duplicate not only the physical and chemical characteristics of SiC - fission product attack in TRISO UC_2 fuel but also yield rates of reaction similar to those determined from in-pile studies.

TRISO WAR $UC_{4.3}O_{1.3}$ Fuel. TRISO coated WAR UC_xO_y fissile fuel particles have been chosen as the reference recycle fissile fuel and are being evaluated for use as fresh fissile fuel. One advantage of the WAR kernels is that they do not migrate in a thermal gradient. Use of WAR fuel kernels also offers the potential for eliminating SiC - fission product reactions in TRISO fissile fuel. Theoretically, the excess oxygen will combine with lanthanide fission products. The efficiency of lanthanide oxide formation will depend on both the oxygen content and burnup of the kernels. Formation of oxides will limit lanthanide release from WAR fuel kernels and therefore limit or possibly eliminate SiC - fission product

reactions. This has been confirmed by qualitative observations made from irradiation testing at ORNL and GA.

Out-of-pile thermal gradient experiment 6804 contained seven particles from TRISO WAR $UC_{4.3}O_{1.3}$ batch OR-1694. Kernel and coating properties measured during preirradiation evaluation of this batch of fuel particles are summarized in Table 9-5. The particles heated in experiment 6804 were irradiated in capsule P13P, fuel rod 1S-28. They were separated from the rod after irradiation by burn leaching and therefore have no outer PyC layer. The particles were heated for a total of 617 hr at 1530°C under a thermal gradient of 575°C/cm. Contact x-radiographs of one particle as loaded (0 hr) and after 93 hr and 476 hr at 1530°C are shown in Fig. 9-32. No indication of release during irradiation of large quantities of fission products from the kernel into the buffer or inner PyC is visible in the 0 hr radiograph. Radiographs taken periodically as the test progressed indicated very slow release of some metallic fission products from the kernel. Small concentrations of the metallic fission products are visible on the cool side of the particle in Figs. 9-32b and c. The TRISO WAR and TRISO UC_2 particles heated in experiment 6804 were gamma counted prior to postirradiation heating to ensure that no detectable Cs or lanthanide fission products were lost during irradiation. The Cs and lanthanide inventories of the UC_2 and WAR samples are similar. Comparison of Figs. 9-24, 9-25, and 9-32 suggests that very few metallic fission products were released from the WAR $UC_{4.3}O_{1.3}$ kernels even during heating at 1530°C. This is consistent with expected performance and will be verified by metallographic and electron microprobe examination.

The change in SiC thickness in the TRISO $UC_{4.3}O_{1.3}$ particles was measured as a function of time at 1530°C using the same methods described earlier for the TRISO UC_2 fuel. One of the WAR particles failed earlier in the test. The average value for the decrease in SiC thickness measured for the WAR samples after 617 hr at 1530°C was 0.7 μm, which is less than the limit of detectability (2 to 3 μm) for the methods used. The decrease in SiC thickness with time at 1620° to 1550°C and 440° to 540°C/cm is compared

in Fig. 9-33 for the UC_2 and $UC_{4.3}O_{1.3}$ samples heated in experiment 6804. The rate of SiC thinning in the $UC_{4.3}O_{1.3}$ sample is clearly much less than in the UC_2 samples. This is the first quantitative comparison of this aspect of the behavior of TRISO WAR and UC_2 fuel particles and proves that TRISO WAR fuel particles offer large potential performance advantages relative to TRISO UC_2 fuel.

TASK 500: FUEL ROD TEST AND EVALUATION

Summary

Final assembly and out-of-hot-cell calibration of equipment for measuring thermal expansivity (CTE) of unirradiated and irradiated LHTGR fuel rods is nearing completion. Fabrication of a glove-box-housed cutoff machine for preparing fuel rod mechanical property specimens has been completed.

Discussion

One of the objectives of the fuel rod testing and evaluation program is to provide reliable data for HTGR core design by measuring the thermal and mechanical properties of fuel rods under HTGR conditions. The initial phase of this program was completed during the last reporting period (Ref. 9-14). Nineteen types of prototype LHTGR fuel rods (see Table 9-20 of Ref. 9-14) were fabricated for thermal and mechanical property measurements.

During the current quarter work has been concentrated on completing the final assembly of equipment for (1) measurement of the CTE of unirradiated and irradiated LHTGR fuel rods and (2) preparation of fuel rods for mechanical property testing.

Final assembly is nearly complete on equipment for measuring the CTE of unirradiated (laboratory unit 1) and irradiated (hot cell unit 2) fuel rods. Calibration runs with a platinum standard on unit 1 have indicated

that very slow heating rates (∿1°C/min) may be required for accurate fuel rod CTE measurements. A special furnace programmer is now being assembled to provide this function.

Fabrication has been completed on a glove-box-housed cutoff machine for preparing unirradiated fuel rods for mechanical property measurements. The construction of this device has been necessitated because a number of prototype HTGR fuel rods (Ref. 9-14) were broken during removal from their curing crucibles. The cutoff machine will be used to remove the fractured ends from these rods and will allow these rods to be used for mechanical property tests. Additional whole rods will be sectioned with the device in order to provide several test specimens from each rod.

REFERENCES

9-1. Young, C. A., and D. P. Harmon, "Preirradiation Report of Fuel Materials for P13T Irradiation Capsule," General Atomic Report GA-A13343, to be published.

9-2. "HTGR Fuels and Core Development Program Quarterly Progress Report for the Period Ending May 31, 1975," ERDA Report GA-A13444, General Atomic, June 30, 1975.

9-3. Vaughen, V. C. P., F. F. Dyer, and K. A. Valentine, "Determination of Fission Product Inventories in FTE-4 Fuel Rods by Gamma Scanning," Oak Ridge National Laboratory unpublished data, October 25, 1975.

9-4. "HTGR Fuels and Core Development Program Quarterly Progress Report for the Period Ending February 28, 1975," ERDA Report GA-A13353, General Atomic, March 31, 1975.

9-5. Harmon, D. P., and C. B. Scott, "Development and Irradiation Performance of LHTGR Fuel," ERDA Report GA-A13173, General Atomic, October 31, 1975.

9-6. "HTGR Base Program Quarterly Progress Report for the Period Ending May 31, 1973," USAEC Report GA-A12599, Gulf General Atomic, June 29, 1973.

9-7. Gulden, T. D., "Carbon Thermal Diffusion in the UC_2-C System," J. Am. Cer. Soc. 55, 14 (1972).

9-8. Stansfield, O. M., et al., "Kernel Migration in Coated Carbide Fuel Particles," Nucl. Tech. 25, 517 (1975).

9-9. Lindemer, T. B., and R. A. Olstad, "HTGR Kernel Migration Data for the Th-U-C-O System as of April 1, 1974," USAEC Report ORNL-TM-4493, Oak Ridge National Laboratory, June 1974.

9-10. Sims, J. R., Jr., "Preirradiation Description of Fuel Materials Branch Samples Contained in Capsules HB-1, HB-3, and HB-5," ERDA Report GA-A13310, General Atomic, February 1, 1975.

9-11. "HTGR Fuels and Core Development Program Quarterly Progress Report for the Period Ending November 30, 1974," ERDA Report GA-A13253, General Atomic, January 31, 1975.

9-12. General Atomic Company unpublished data.

9-13. Olstad, R. A., et al., "An Irradiation Test of Candidate HTGR Recycle Fuels in the H-1 and H-2 Capsules," USAEC Report ORNL-TM-4397, Oak Ridge National Laboratory, July 1974.

9-14. "HTGR Fuels and Core Development Program Quarterly Progress Report for the Period Ending November 30, 1975," ERDA Report GA-A13737, General Atomic, December 31, 1975.

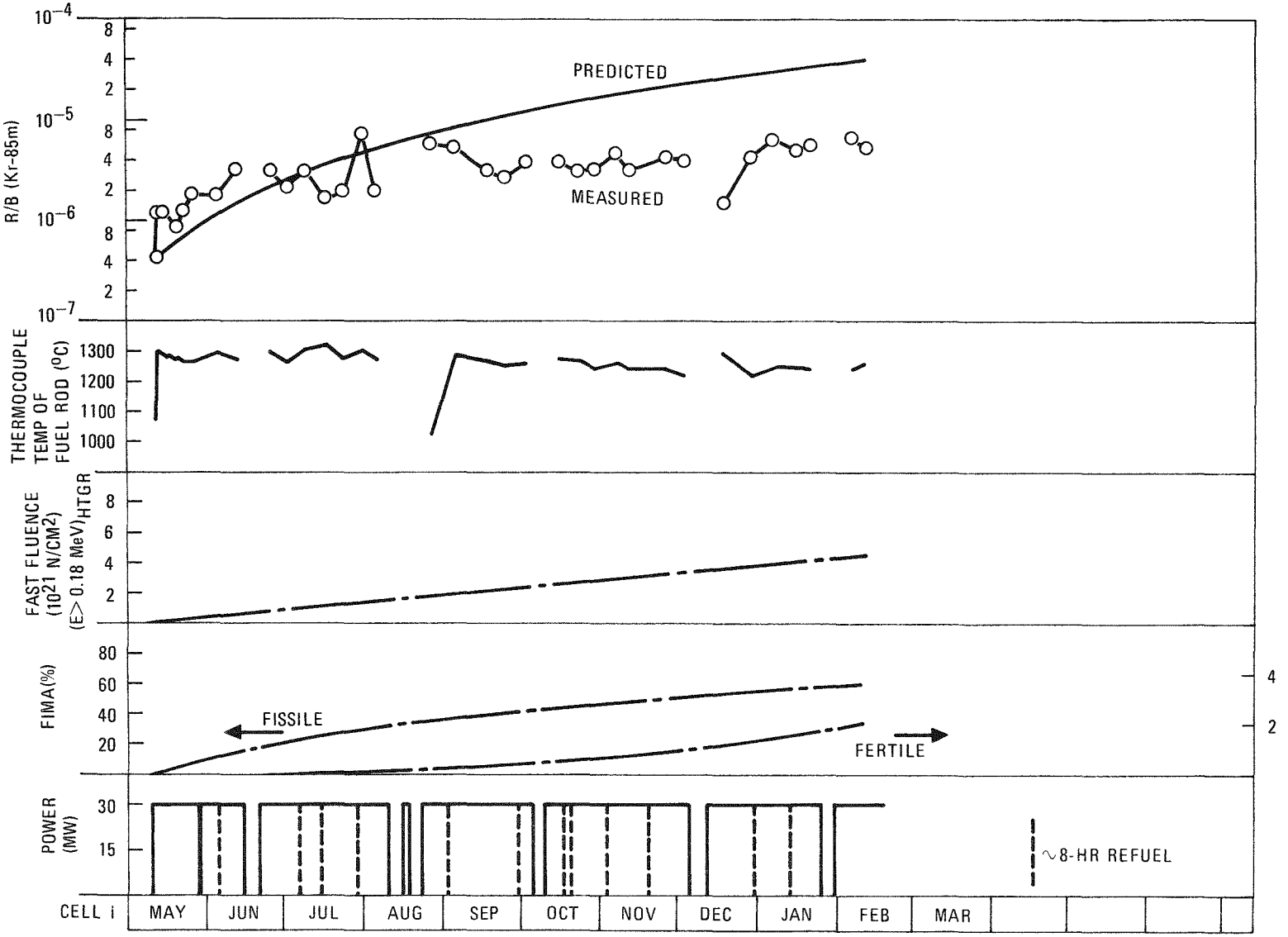

Fig. 9-1. Operating history of cell 1 of P13T capsule containing UC_2 (VSM) TRISO and ThO_2 BISO coated particles

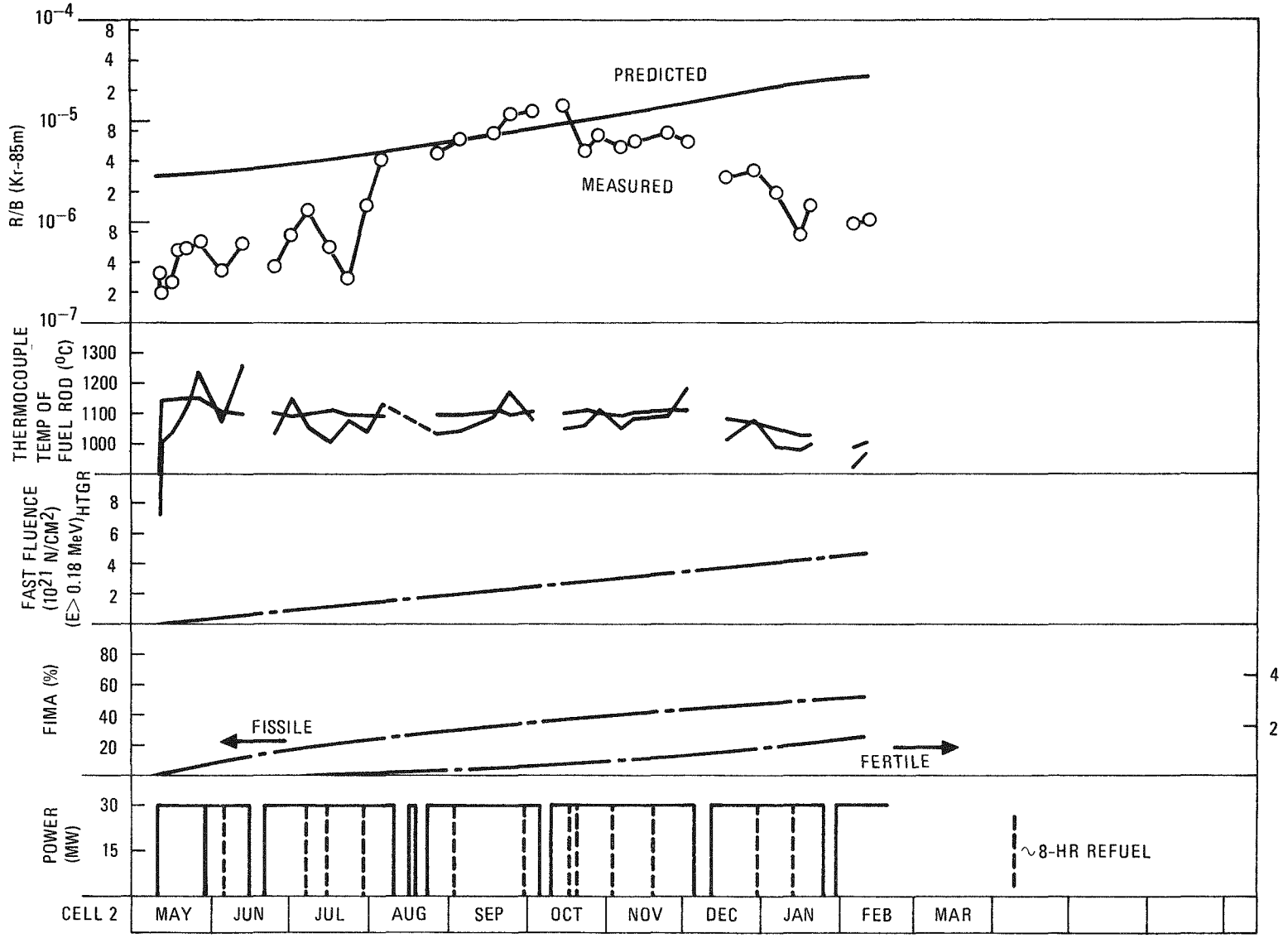

Fig. 9-2. Operating history of cell 2 of P13T capsule containing UC_2 (VSM) and UC_xO_y (WAR) TRISO and ThO_2 BISO coated particles

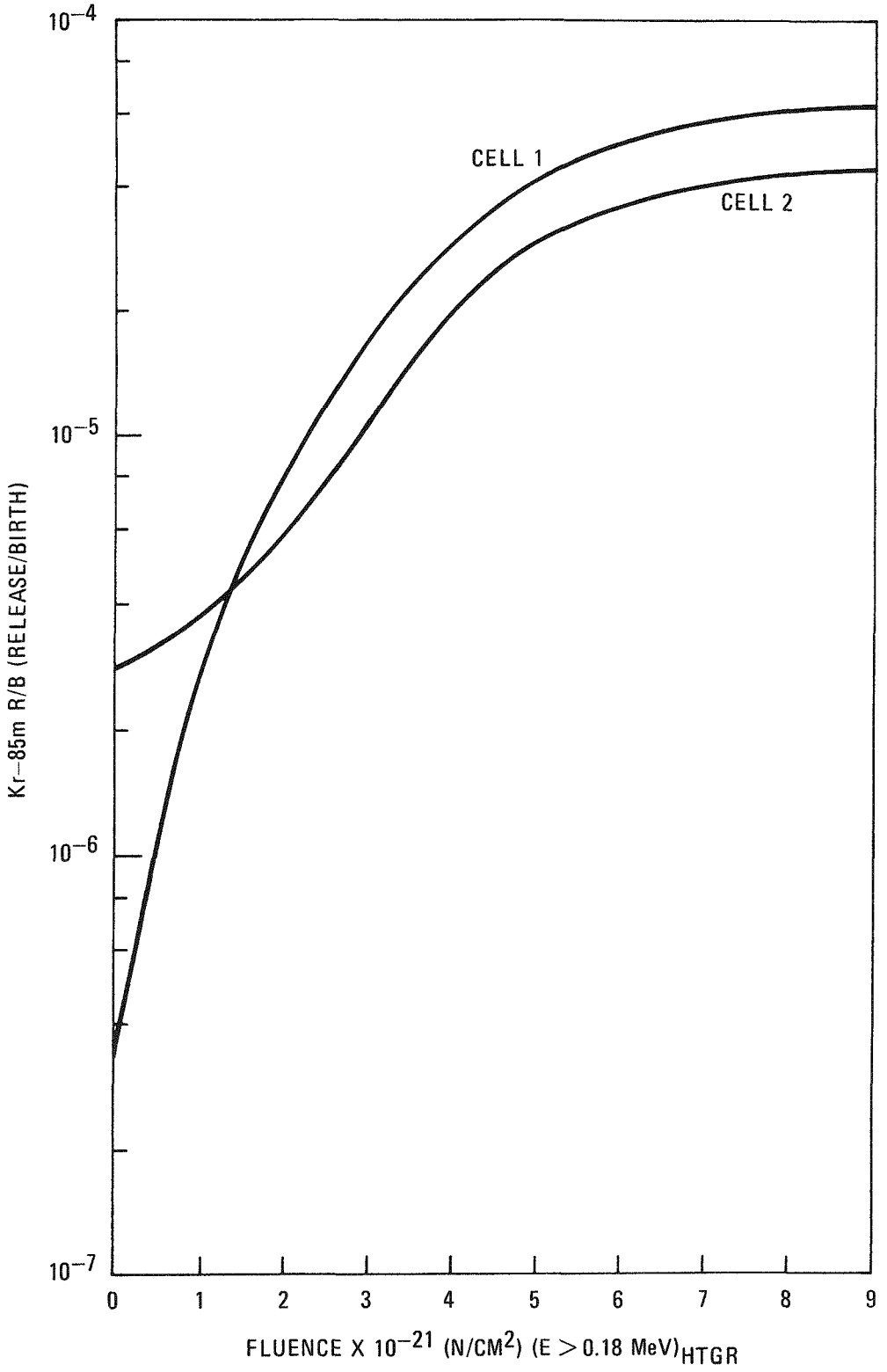

Fig. 9-3. Predicted Kr-85m release based on fuel failure consistent with design criteria and measured preirradiation contamination levels for cells 1 and 2 of P13T capsule

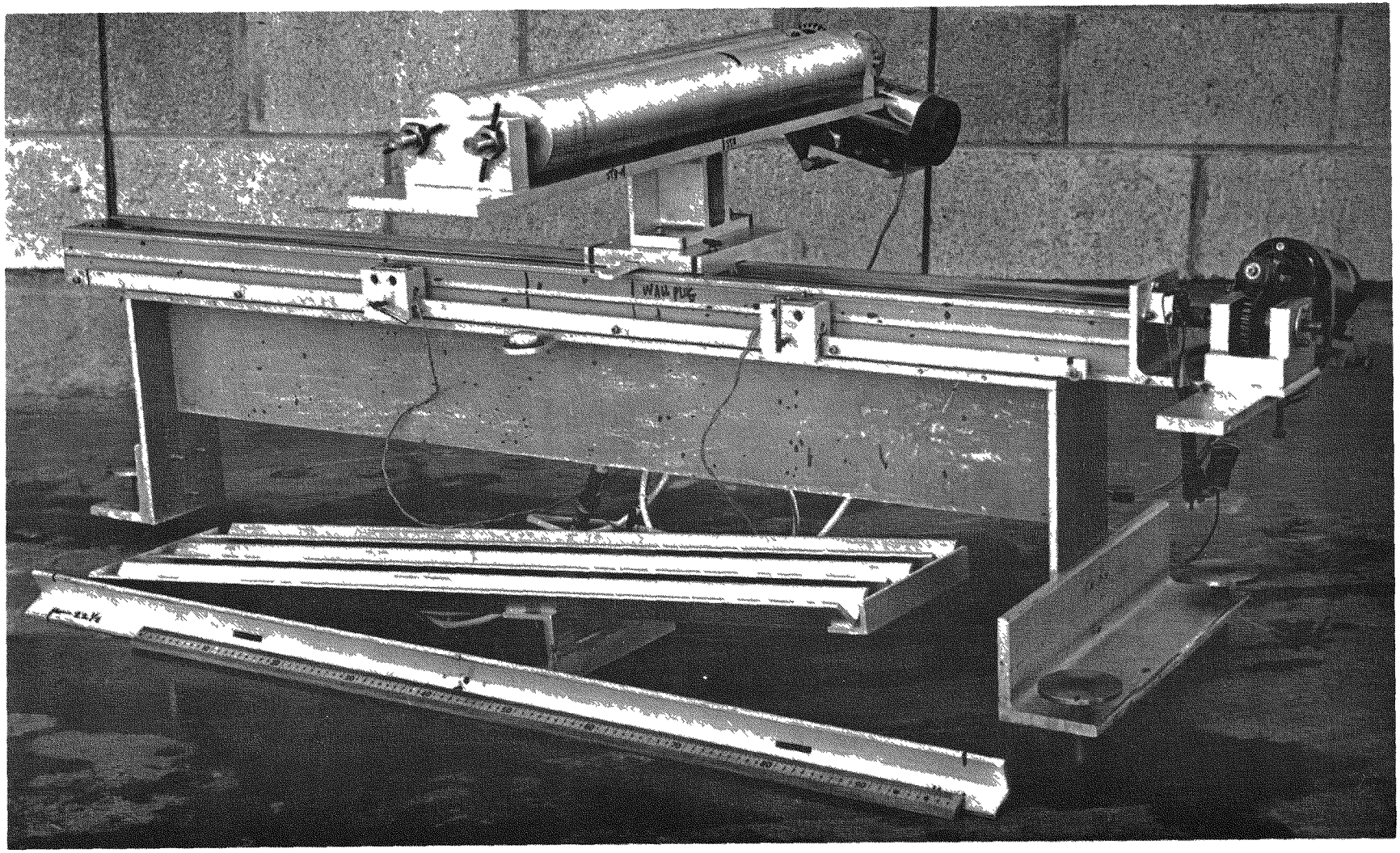

Fig. 9-4. Axial gamma scanning rig in the hot cell

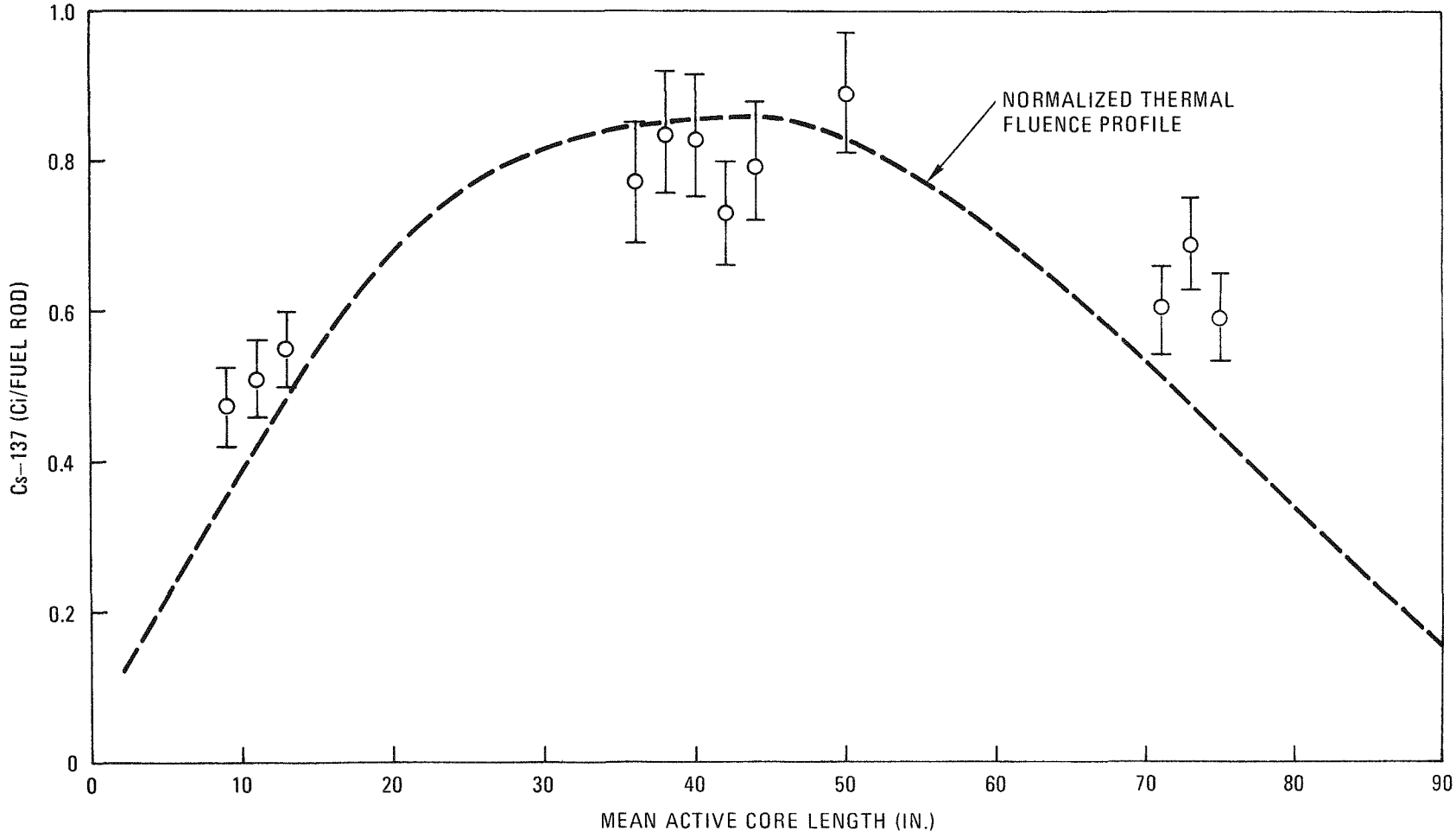

Fig. 9-5. Comparison of Cs-137 inventory in stack 3 fuel rods and the calculated thermal fluence in FTE-4

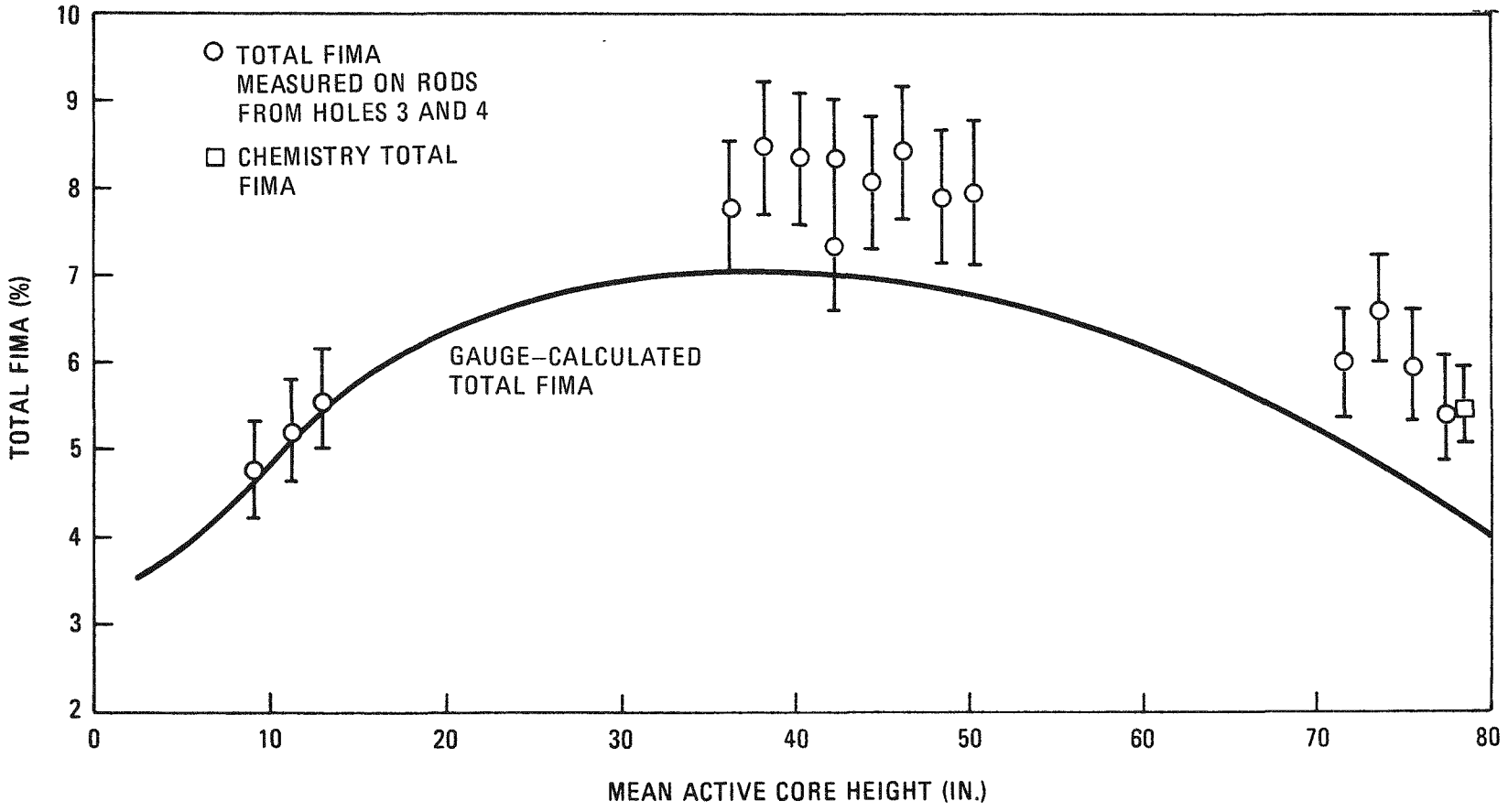

Fig. 9-6. Comparison of calculated and measured total FIMA: (a) rods from stacks 3 and 4

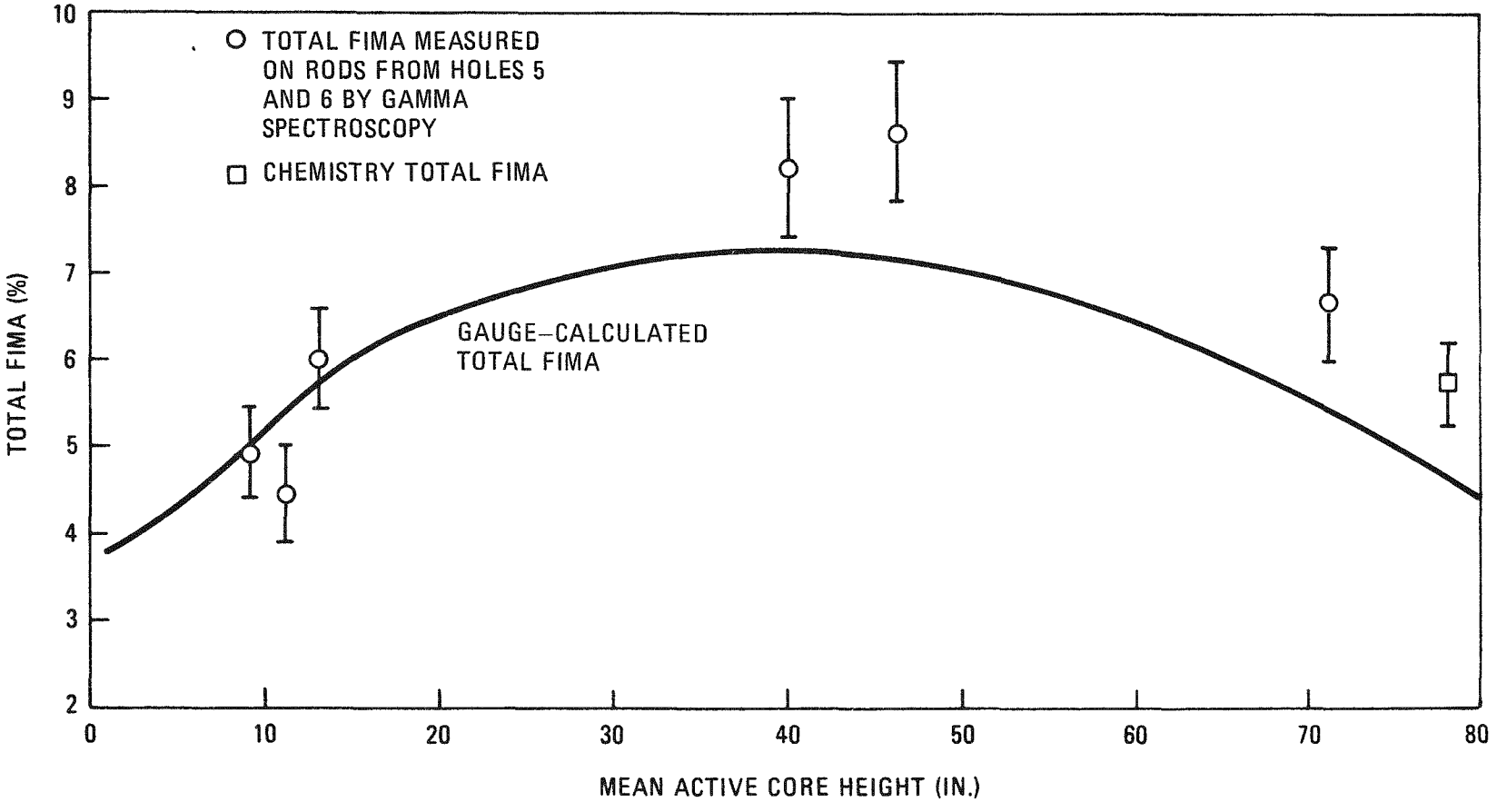

Fig. 9-6. Comparison of calculated and measured total FIMA: (b) rods from stacks 5 and 6

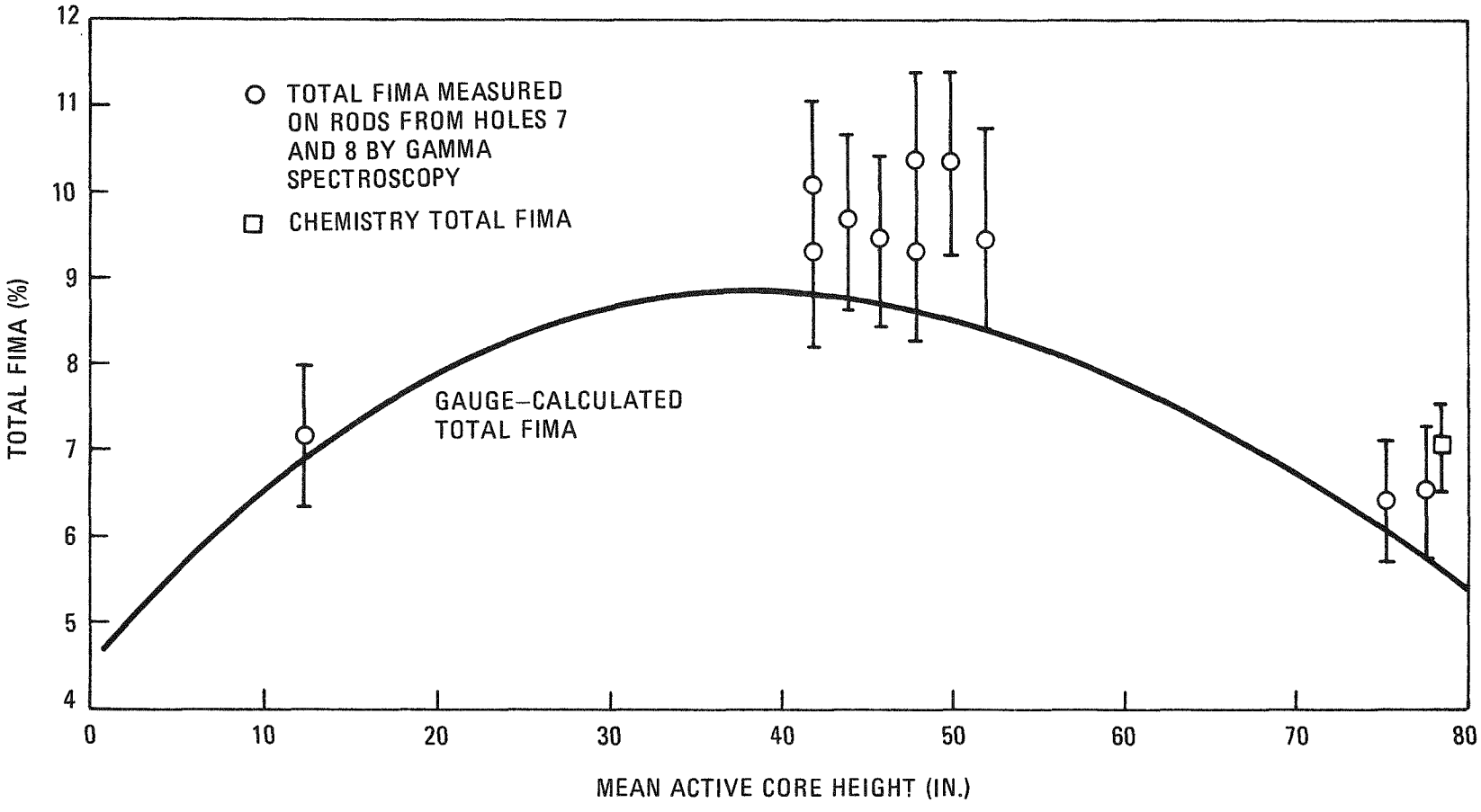

Fig. 9-6. Comparison of calculated and measured total FIMA: (c) rods from stacks 7 and 8

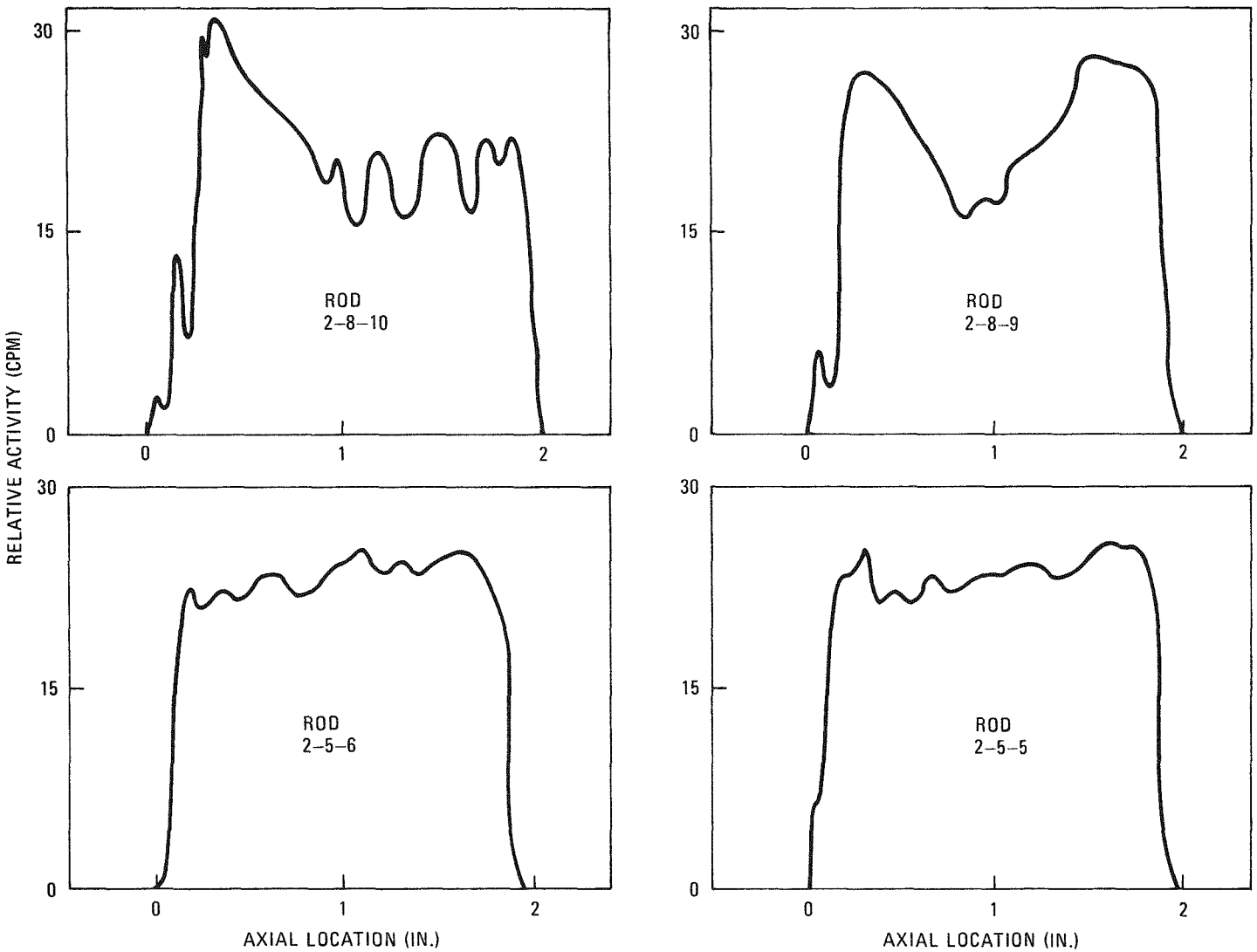

Fig. 9-7. Representative single channel gamma spectroscopy scans of Cs-137

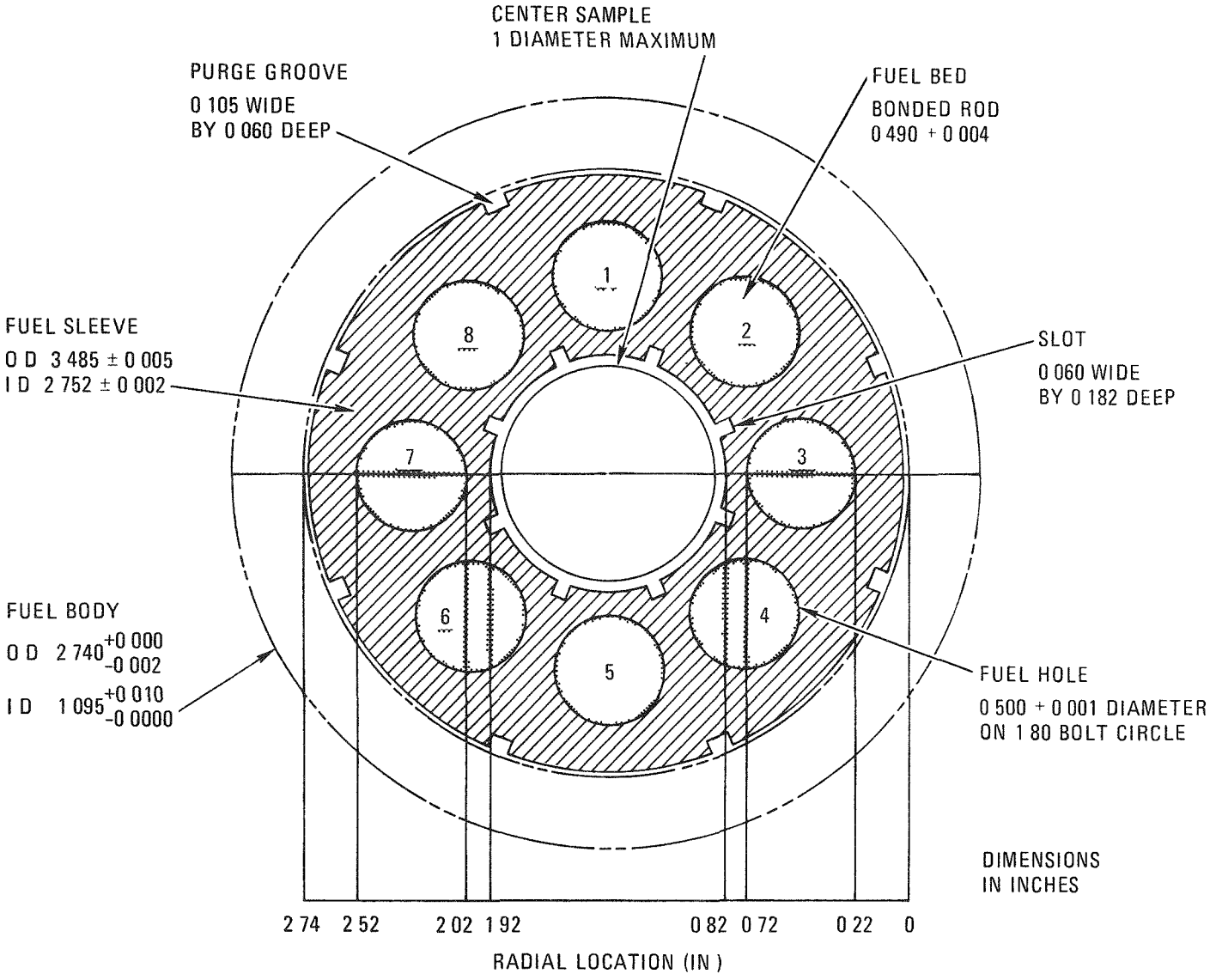

Fig. 9-8. Diagram of graphite web gamma scanning geometry

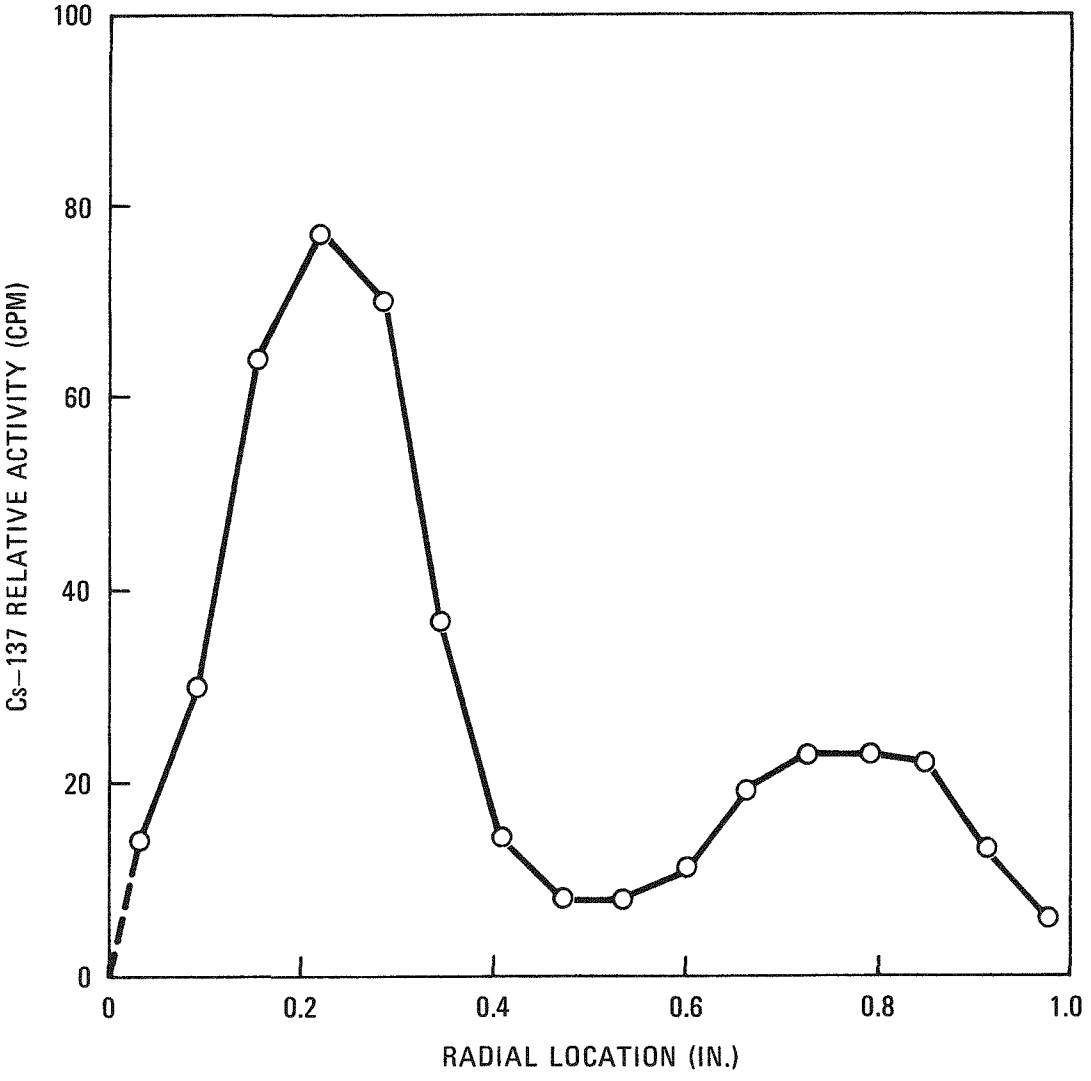

Fig. 9-9. Cs-137 profile across hole 2 of body 2 in FTE-4

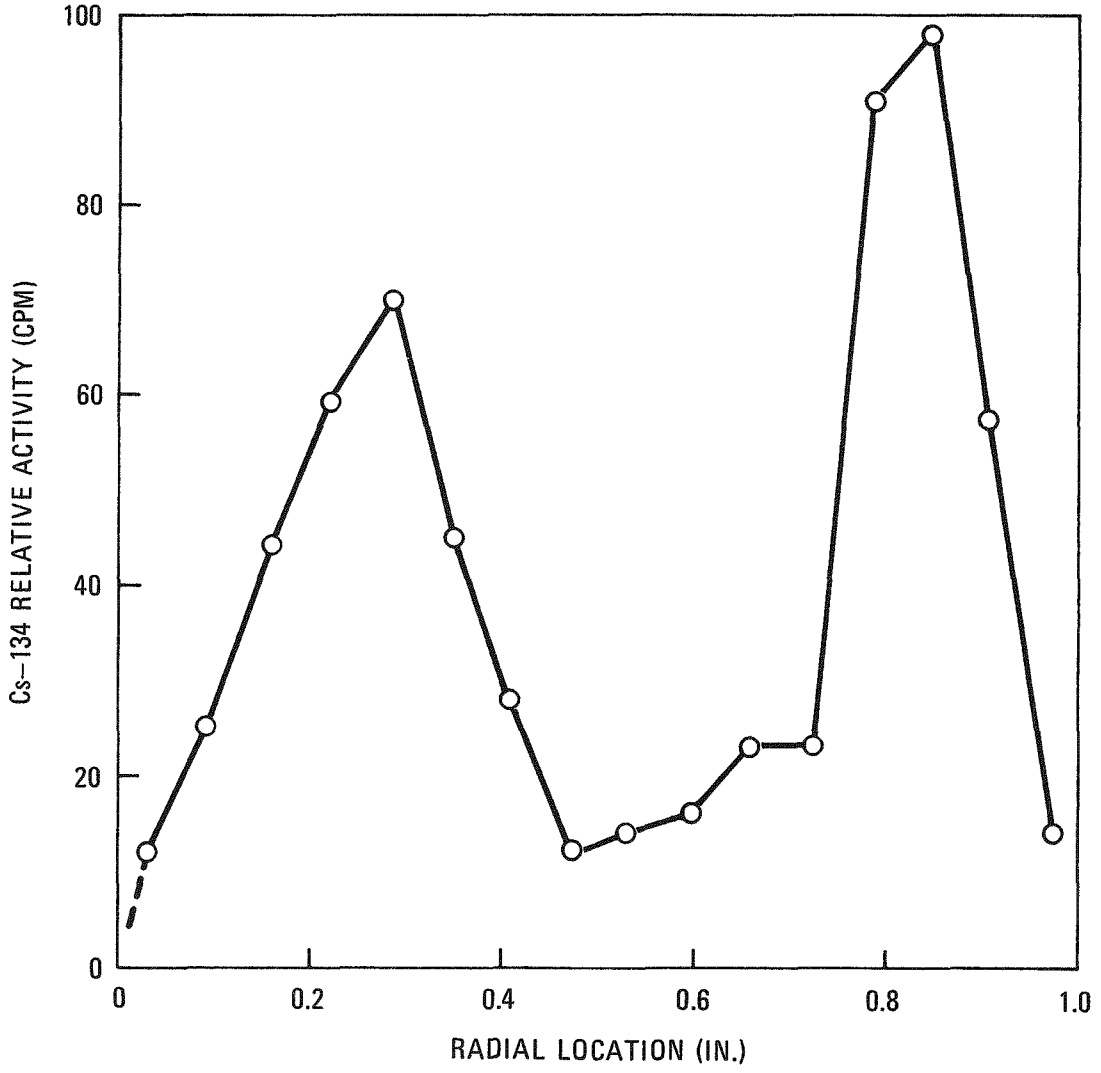

Fig. 9-10. Cs-134 profile across hole 2 of body 2 in FTE-4

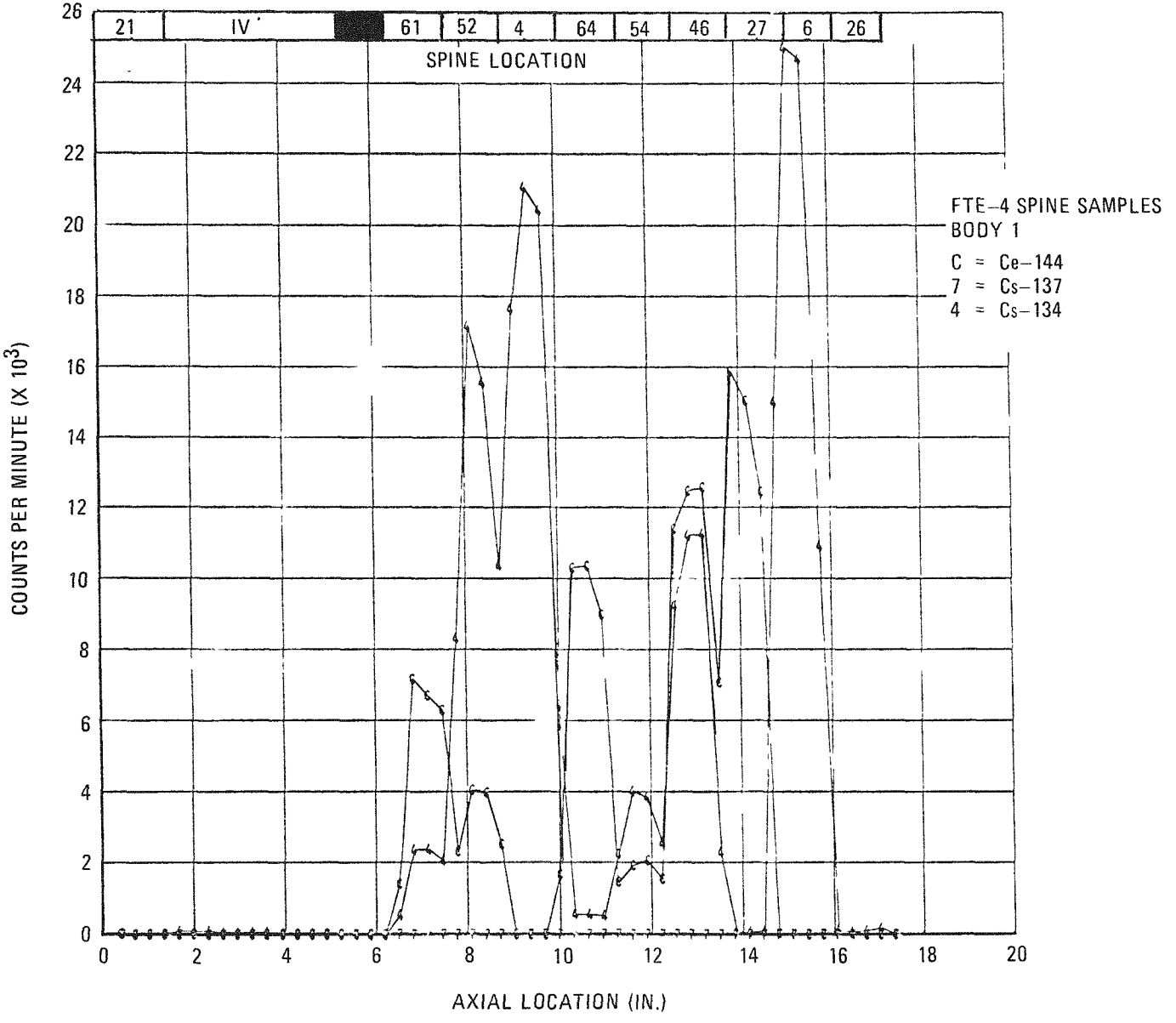

Fig. 9-11. Hot cell gamma scan of FTE-4 spine samples: (a) body 1

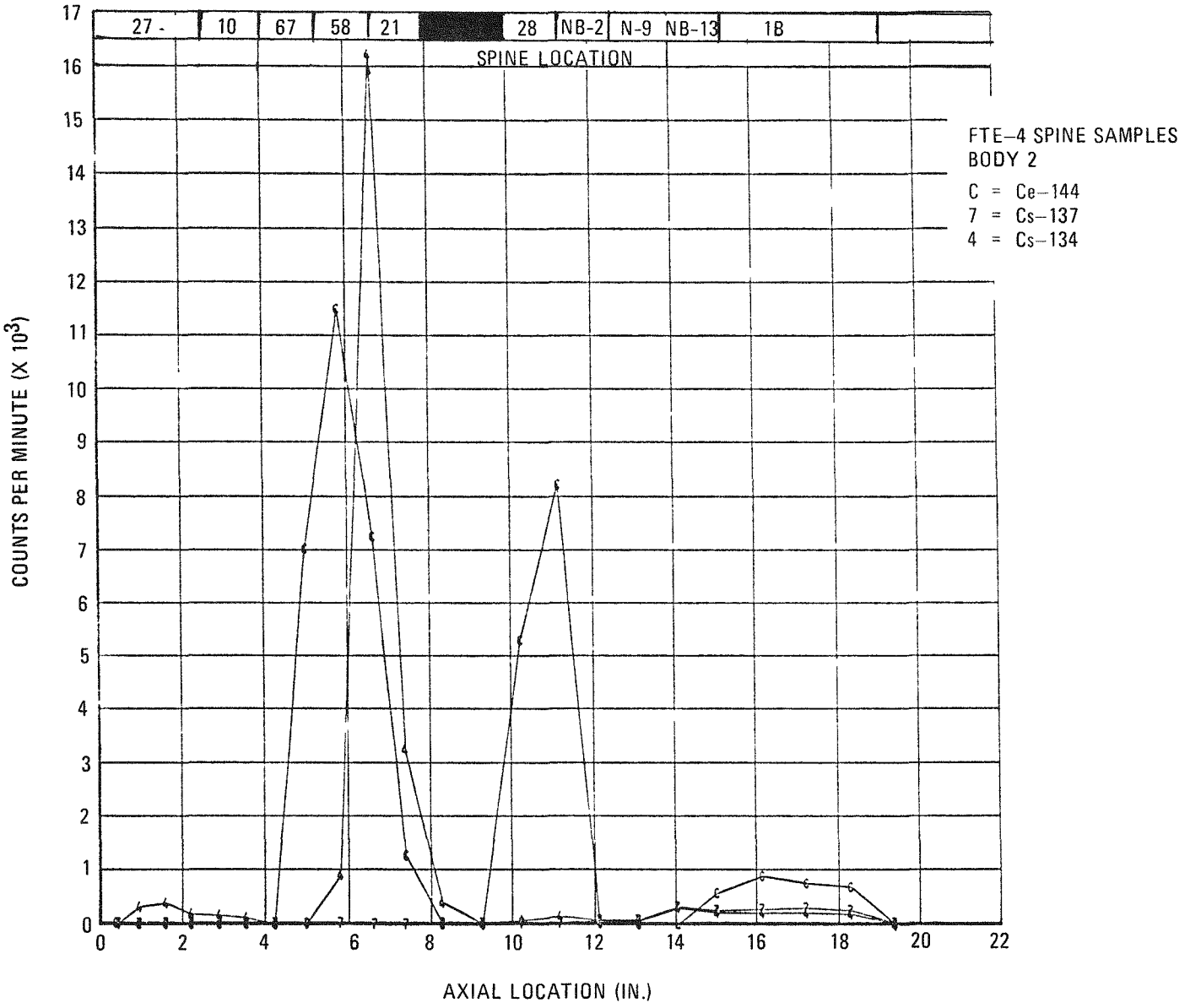

Fig. 9-11. Hot cell gamma scan of FTE-4 spine samples: (b) body 2

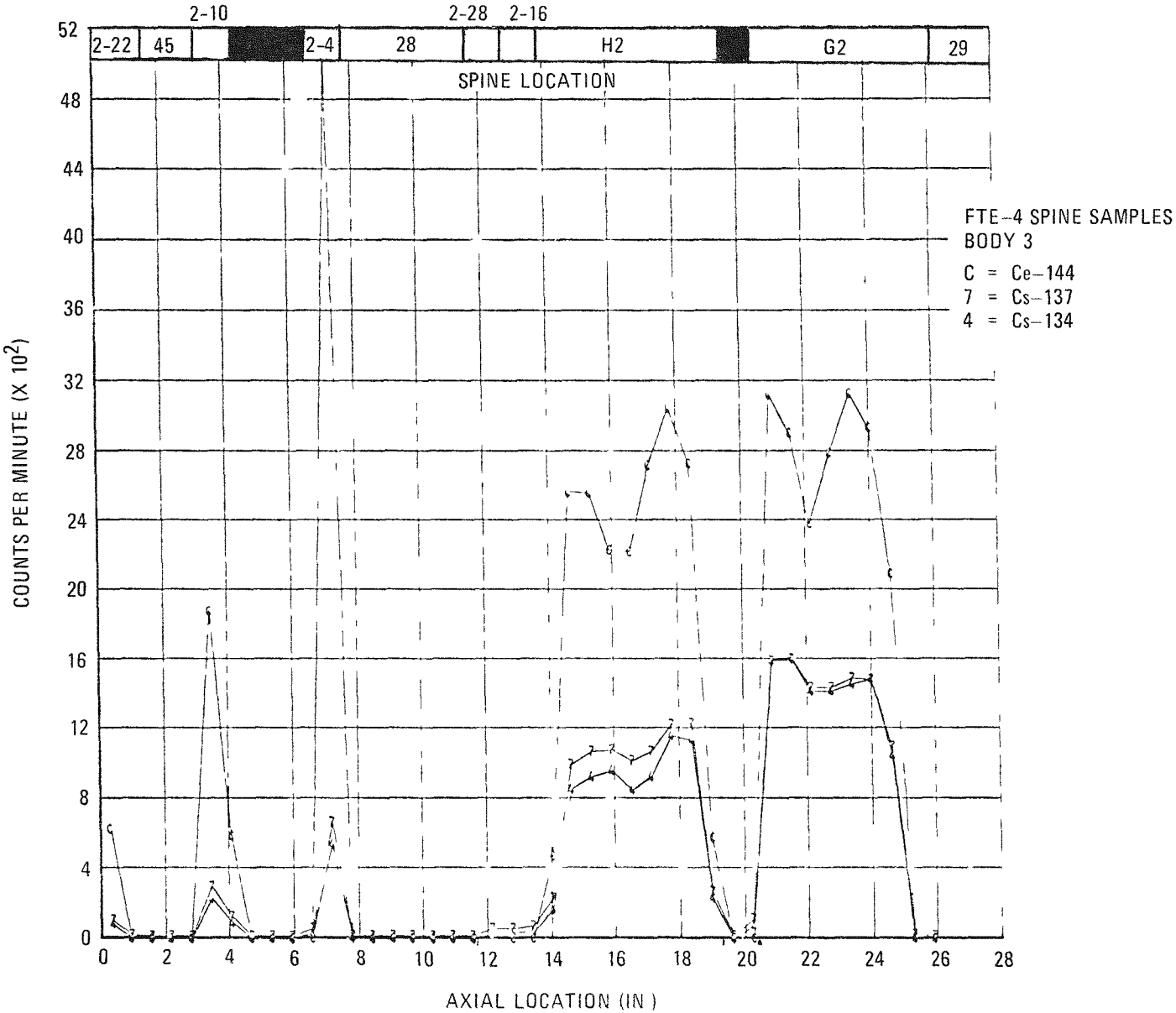

Fig. 9-11. Hot cell gamma scan of FTE-4 spine samples: (c) body 3

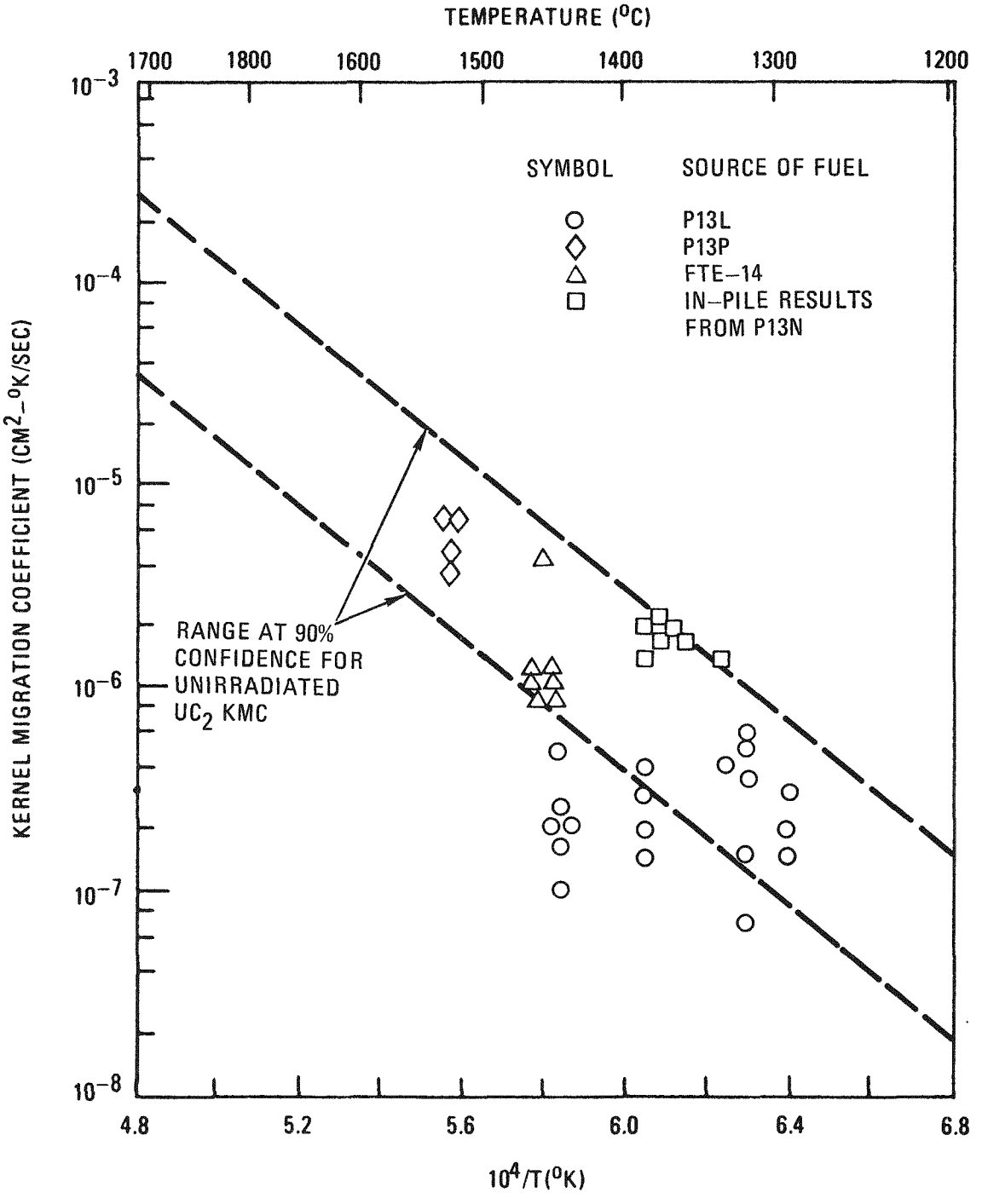

Fig. 9-12. Comparison of UC_2 KMC values determined for irradiated kernels with the range of UC_2 KMC values determined at the 90% confidence level for unirradiated UC_2 kernels

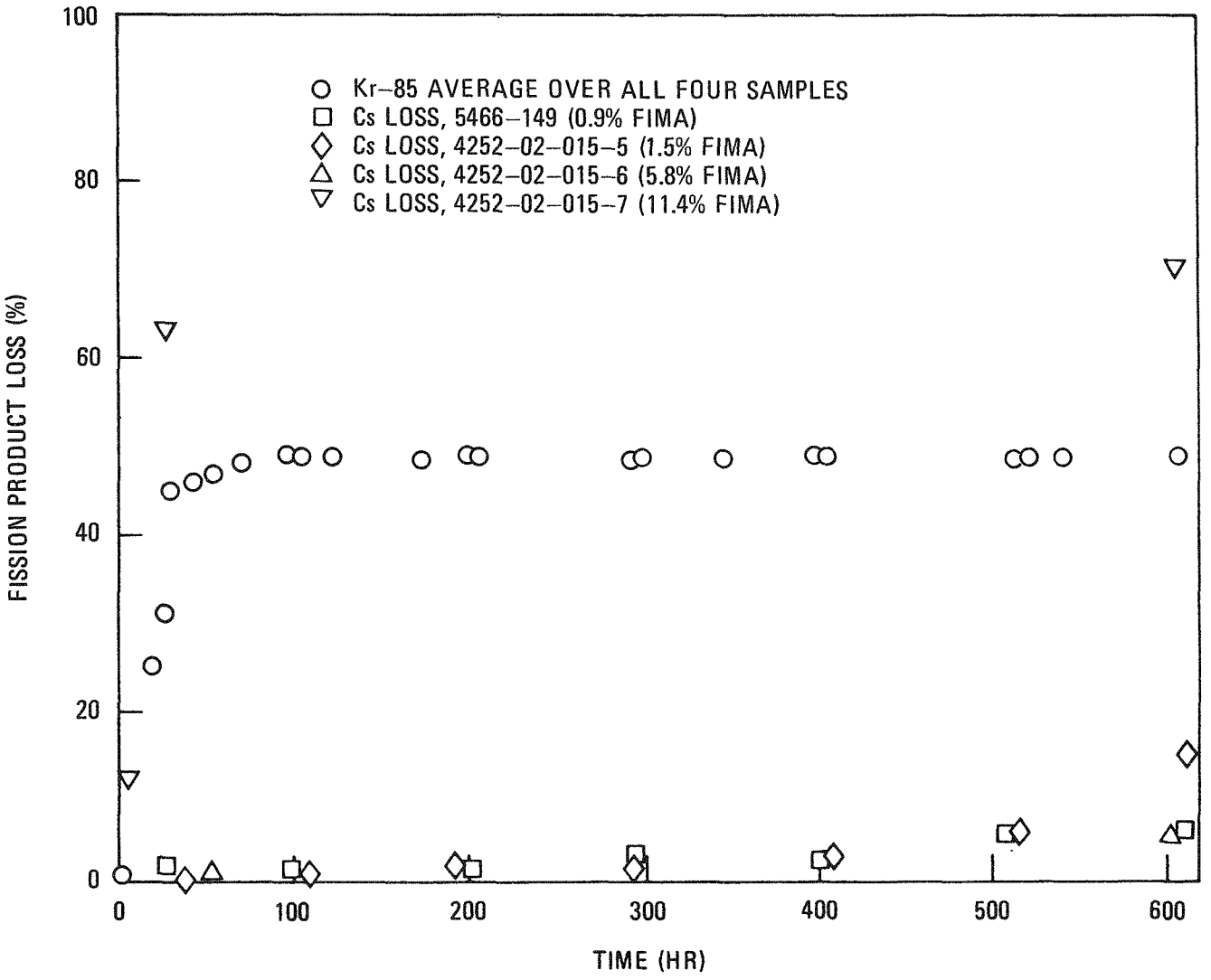

Fig. 9-13. Fission product release (Kr-85 and Cs-137) versus time for irradiated ThO_2 particles heated at 1494° to 1559°C in thermal gradient experiment 6617

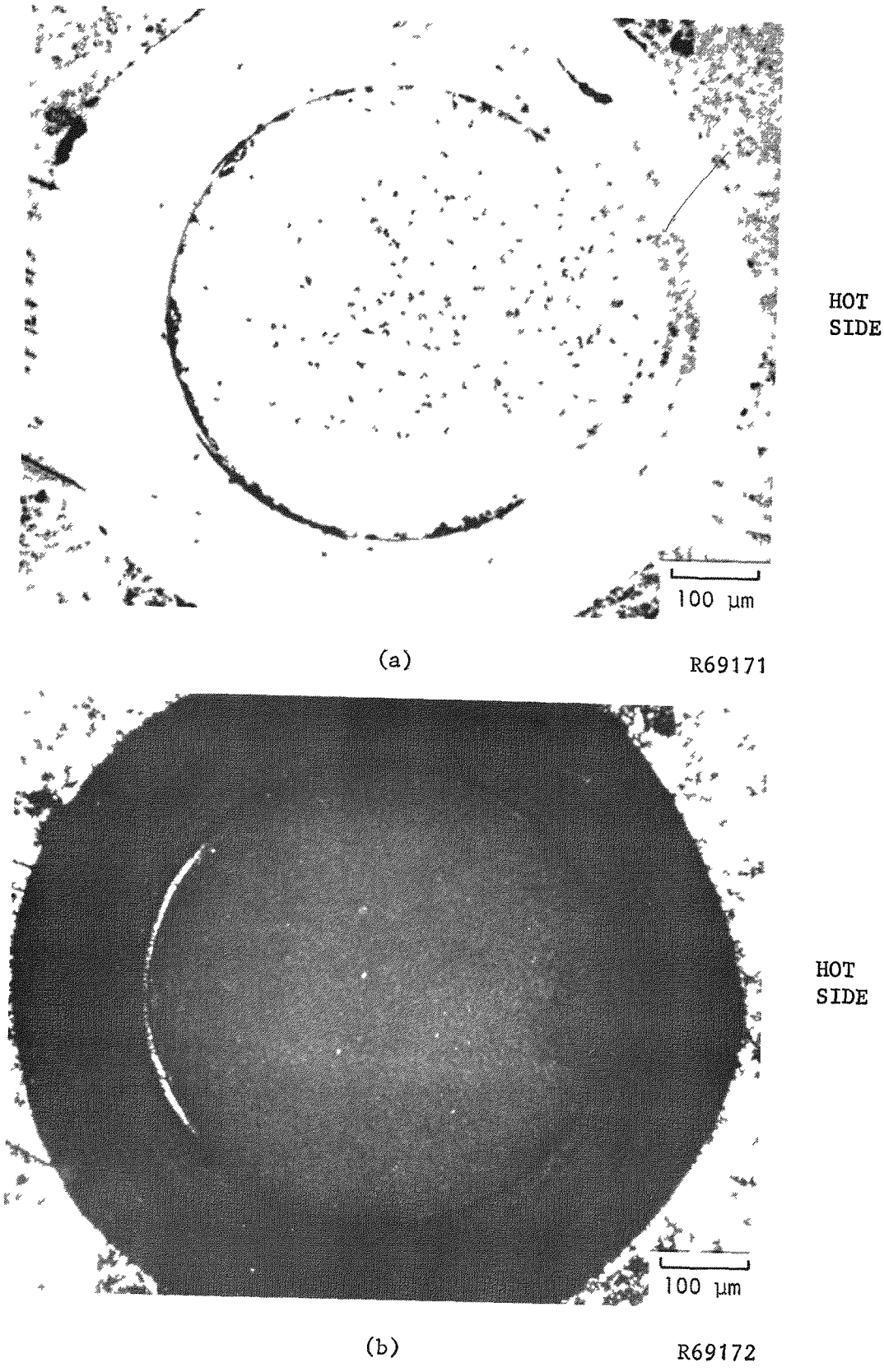

Fig. 9-14. Photomicrographs of BISO coated ThO_2 fuel particle 3 (batch 4252-02-015-5) irradiated in capsule HT-12-40 to 1.5% FIMA and then heated at 1559°C in a thermal gradient of 705°C/cm for 606 hr): (a) bright field and (b) polarized light

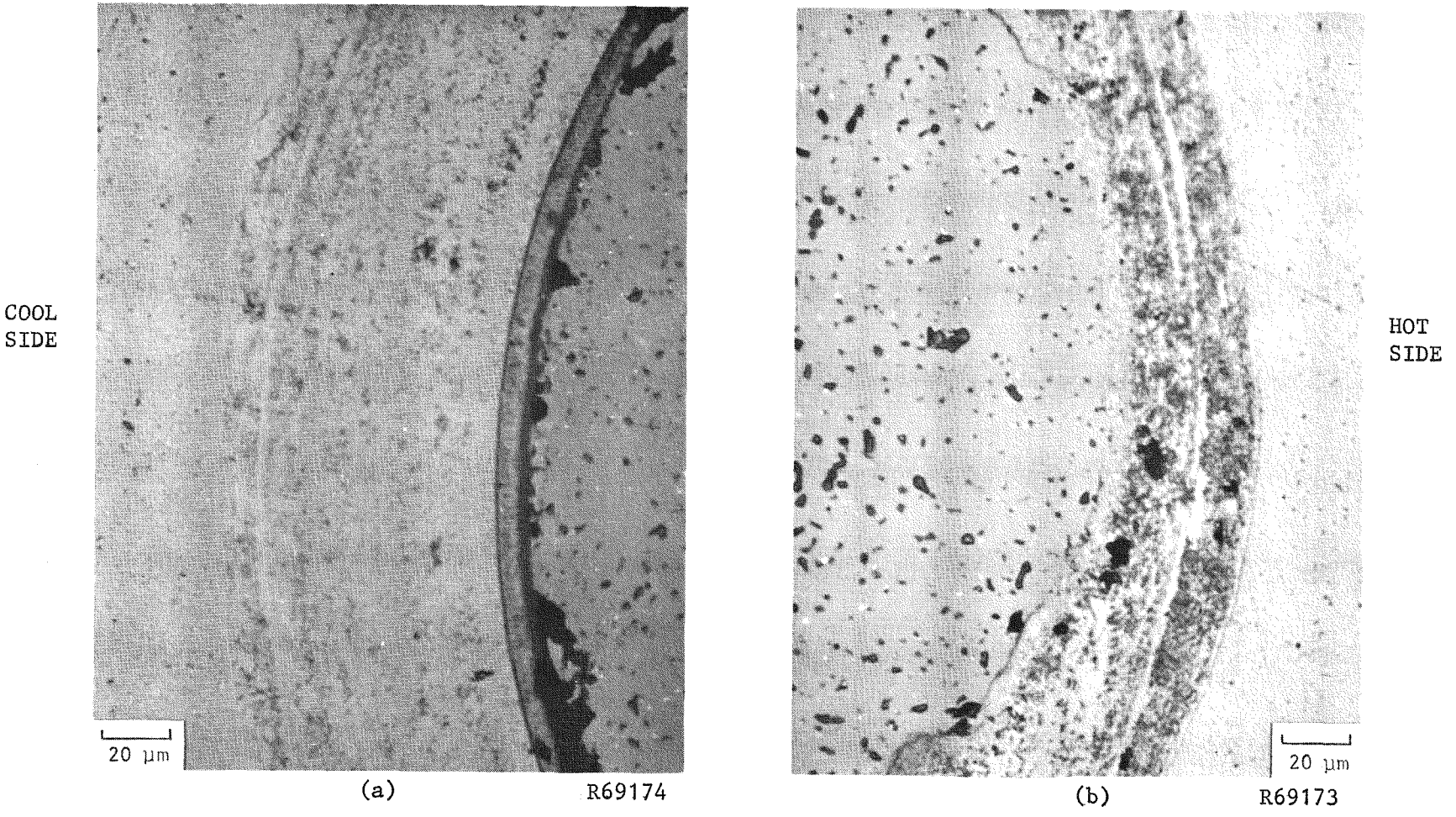

Fig. 9-15. Photomicrographs of a ThO_2 kernel irradiated in capsule HT-12-40 to 1.5% FIMA and then heated at 1559°C in a thermal gradient of 705°C/cm for 606 hr: (a) cool side and (b) hot side

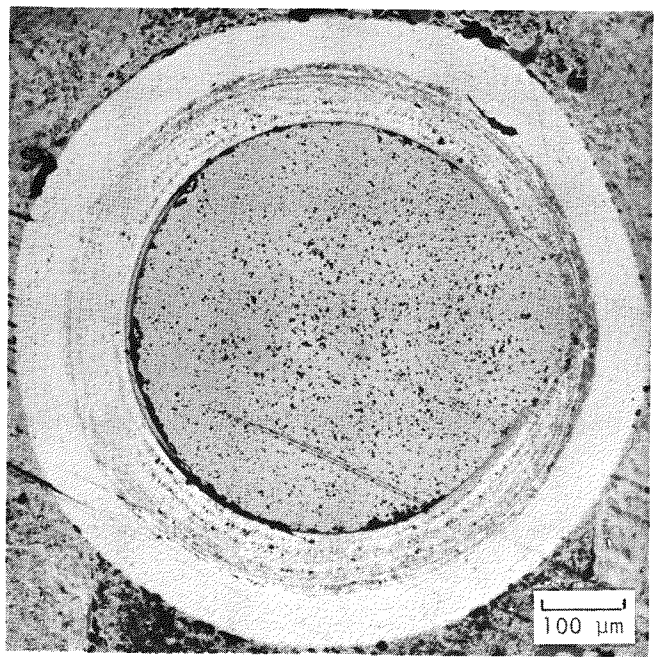

HOT
SIDE

(a) R69171

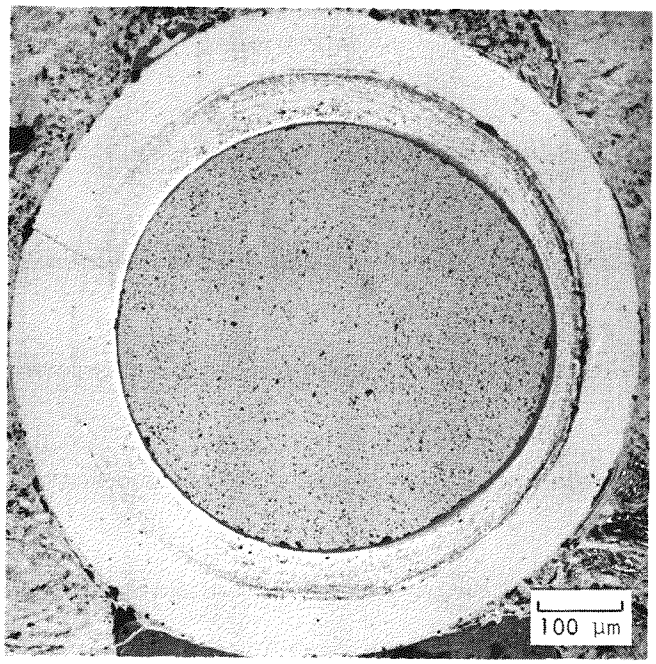

HOT
SIDE

(b) R69162

Fig. 9-16. Photomicrographs of particles heated for 606 hr at: (a) 1559°C and 705°C/cm after irradiation to 1.5% FIMA and 2.8 x 10^{21} n/cm^2 $(E \geq 0.18\ MeV)_{HTGR}$ and (b) 1521°C and 405°C/cm after irradiation to 5.8% FIMA and 6.1 x 10^{21} n/cm^2 $(E \geq 0.18\ MeV)_{HTGR}$

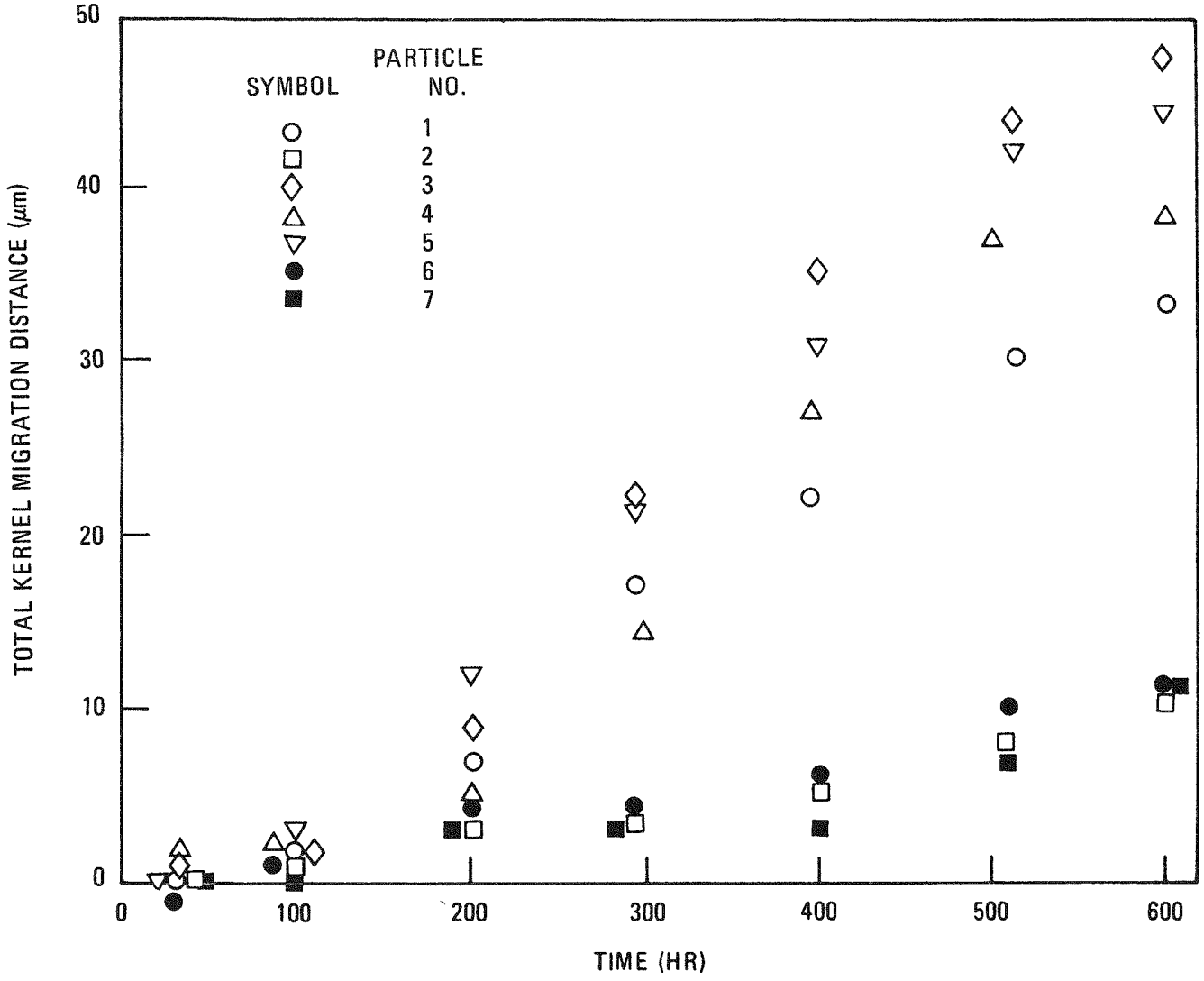

Fig. 9-17. Kernel migration distance (μm) versus time (hr) for particles heated at 1559°C under a thermal gradient of 705°C/cm after irradiation to a kernel burnup of 1.5% FIMA and fast neutron exposure of 2.8×10^{21} n/cm^2 $(E \geq 0.18 \text{ MeV})_{HTGR}$ (batch 4252-02-015-5)

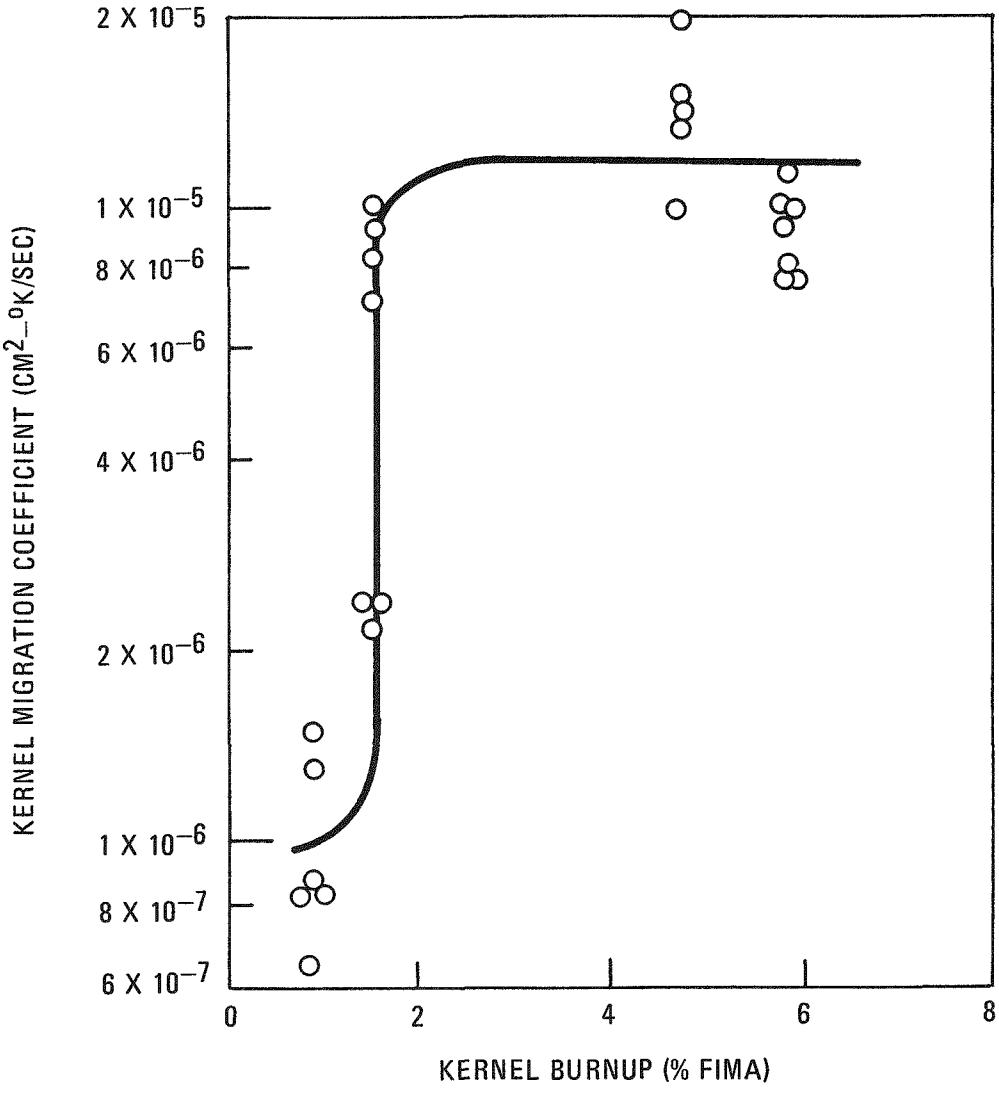

Fig. 9-18. Variation in KMC with kernel burnup for irradiated ThO_2 particles heated in a thermal gradient at 1510° to 1559°C

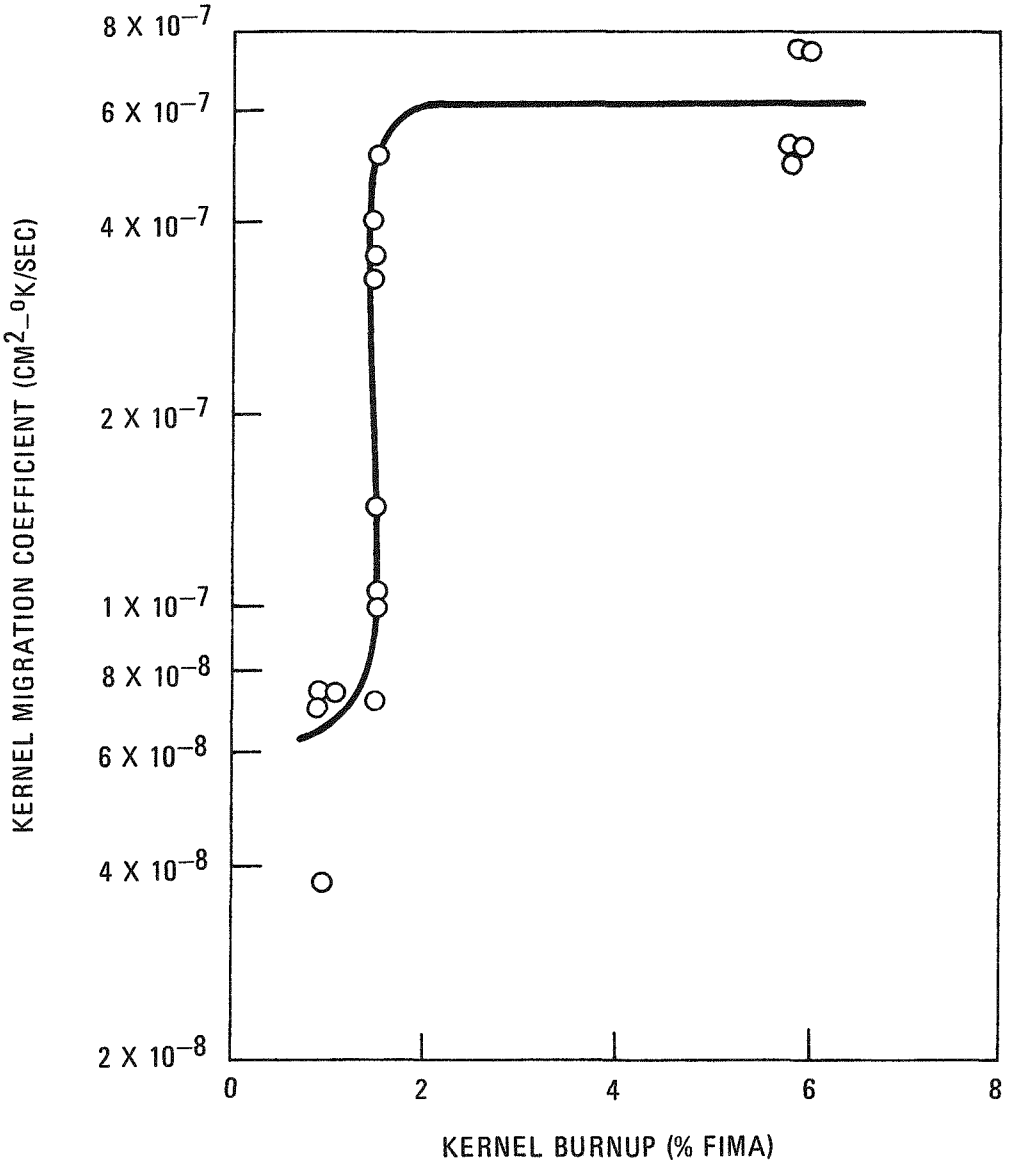

Fig. 9-19. Variation in KMC with kernel burnup for irradiated ThO_2 particles heated in a thermal gradient at 1319° to 1335°C

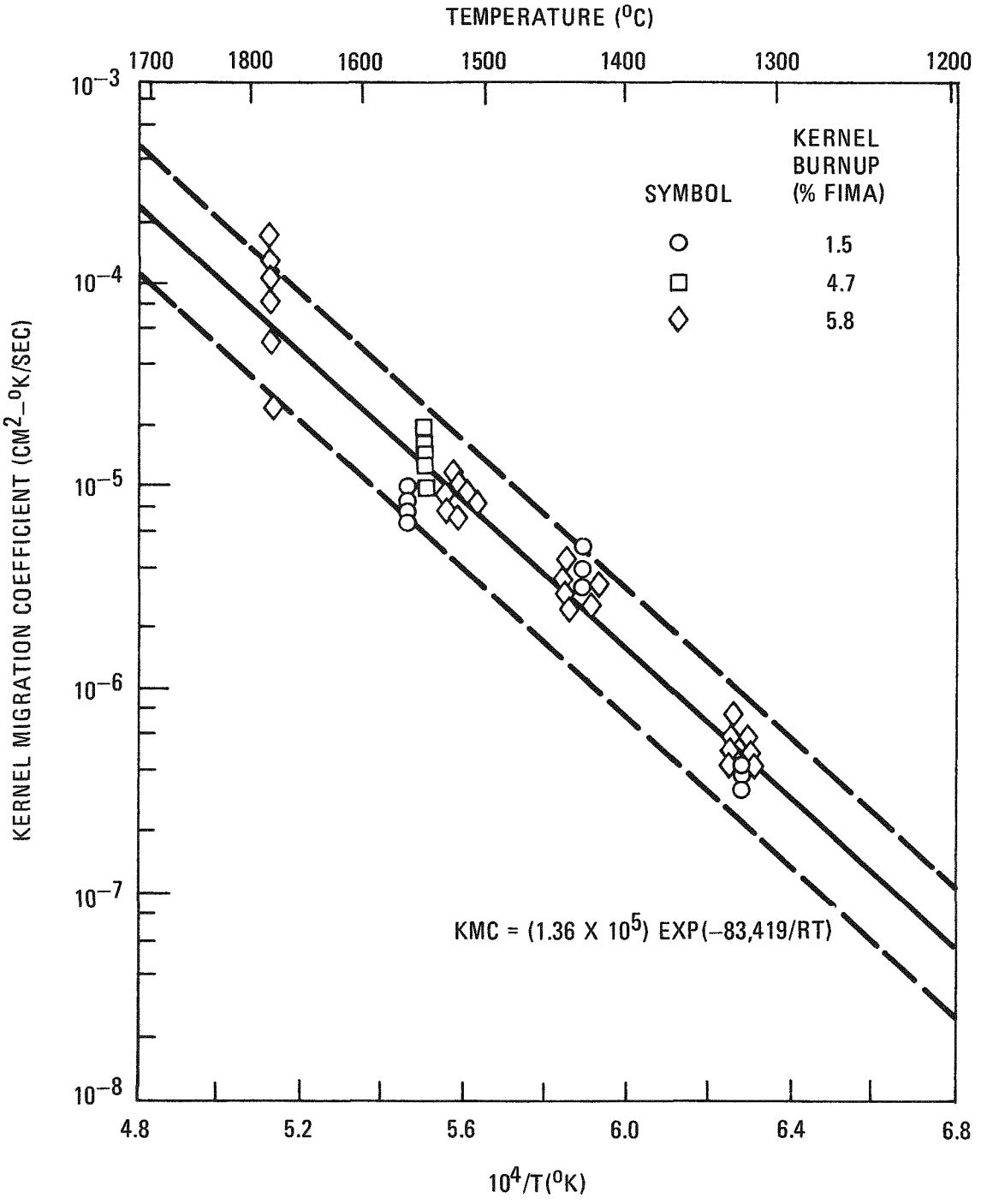

Fig. 9-20. Kernel migration coefficient versus inverse temperature for irradiated BISO coated ThO_2 fuel kernels

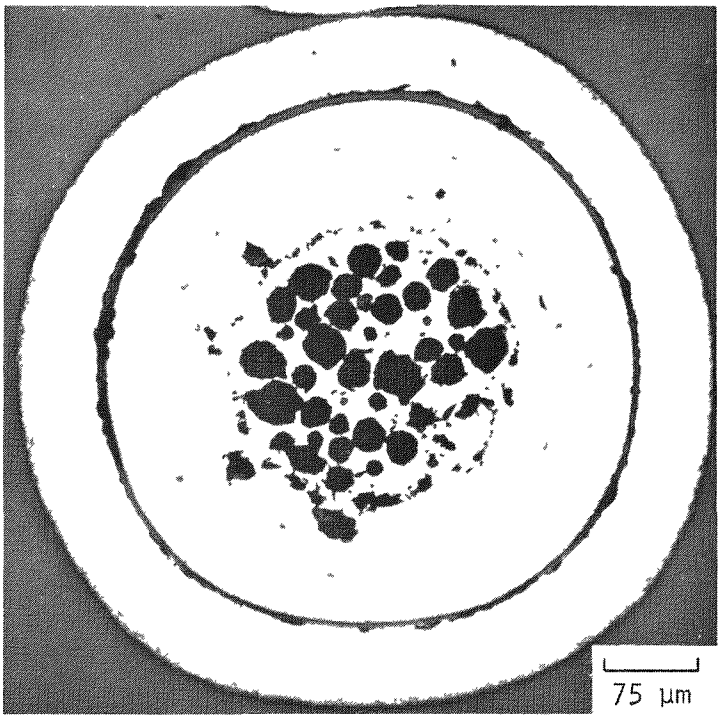

(a) R69118

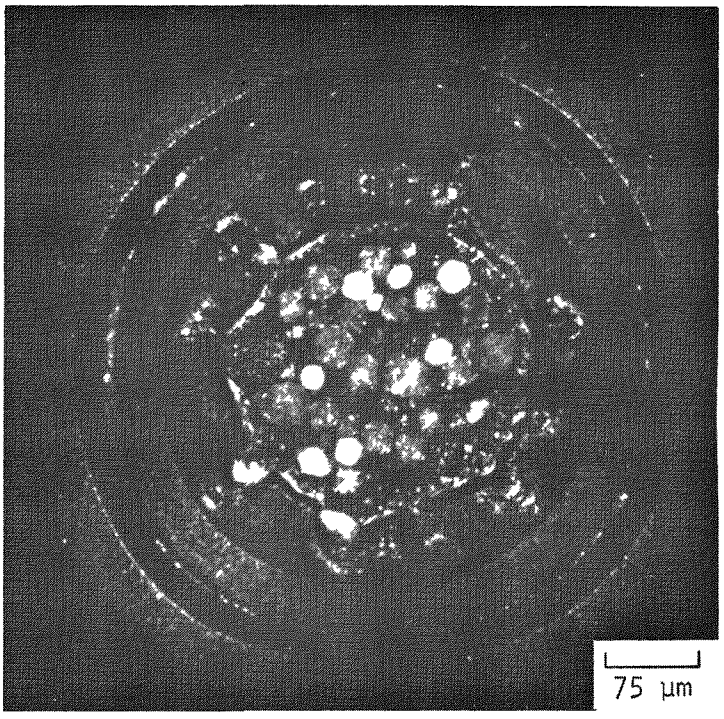

(b) R69119

Fig. 9-21. Representative photomicrographs of TRISO coated, dense melted UC_2 (batch 6151-00-0351-001) after low-temperature irradiation in capsule HB-1: (a) bright field and (b) polarized light

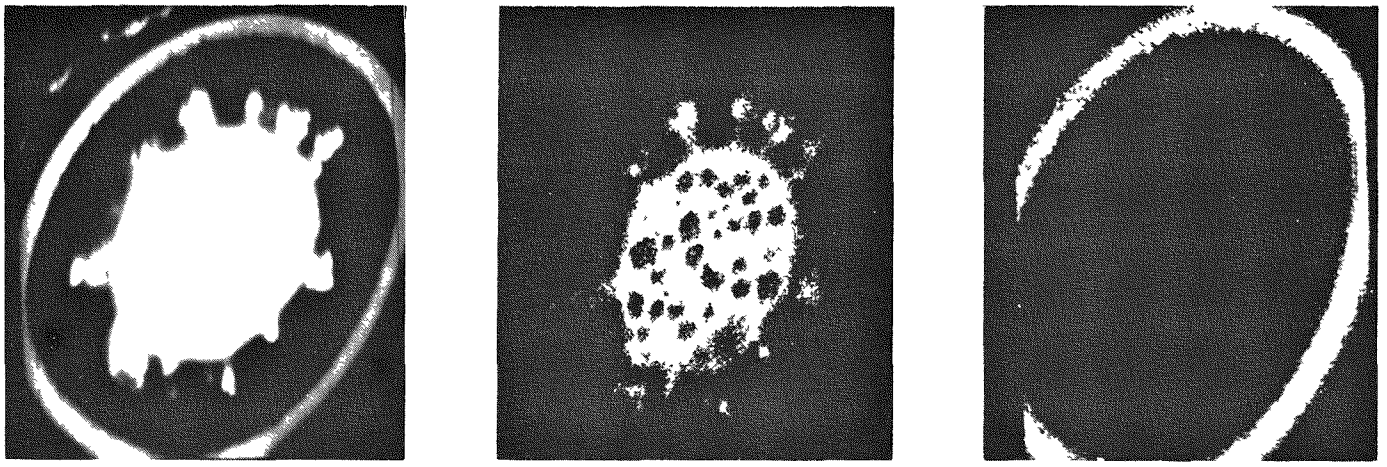

(a) EM-75002-1 (b) EM-75002-2 (c) EM75002-3

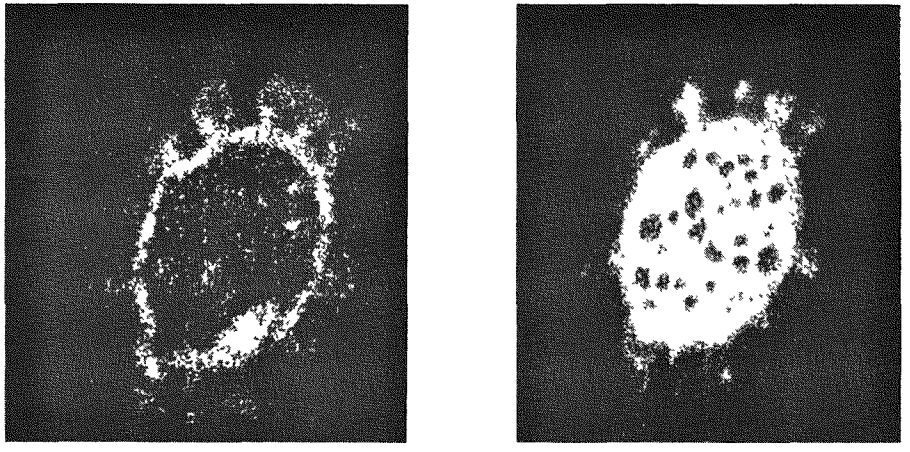

(d) EM-75002-6 (e) EM-75002-11

Fig. 9-22. Results of electron microprobe examination of TRISO coated UC_2 (batch 6151-00-0351-001) after irradiation to 63% FIMA and 2.1 x 10^{21} n/cm^2 (E $\geq$ 0.18 MeV)$_{HTGR}$ at less than 700°C: (a) specimen current, (b) uranium, (c) silicon, (d) cesium, and (e) neodynium

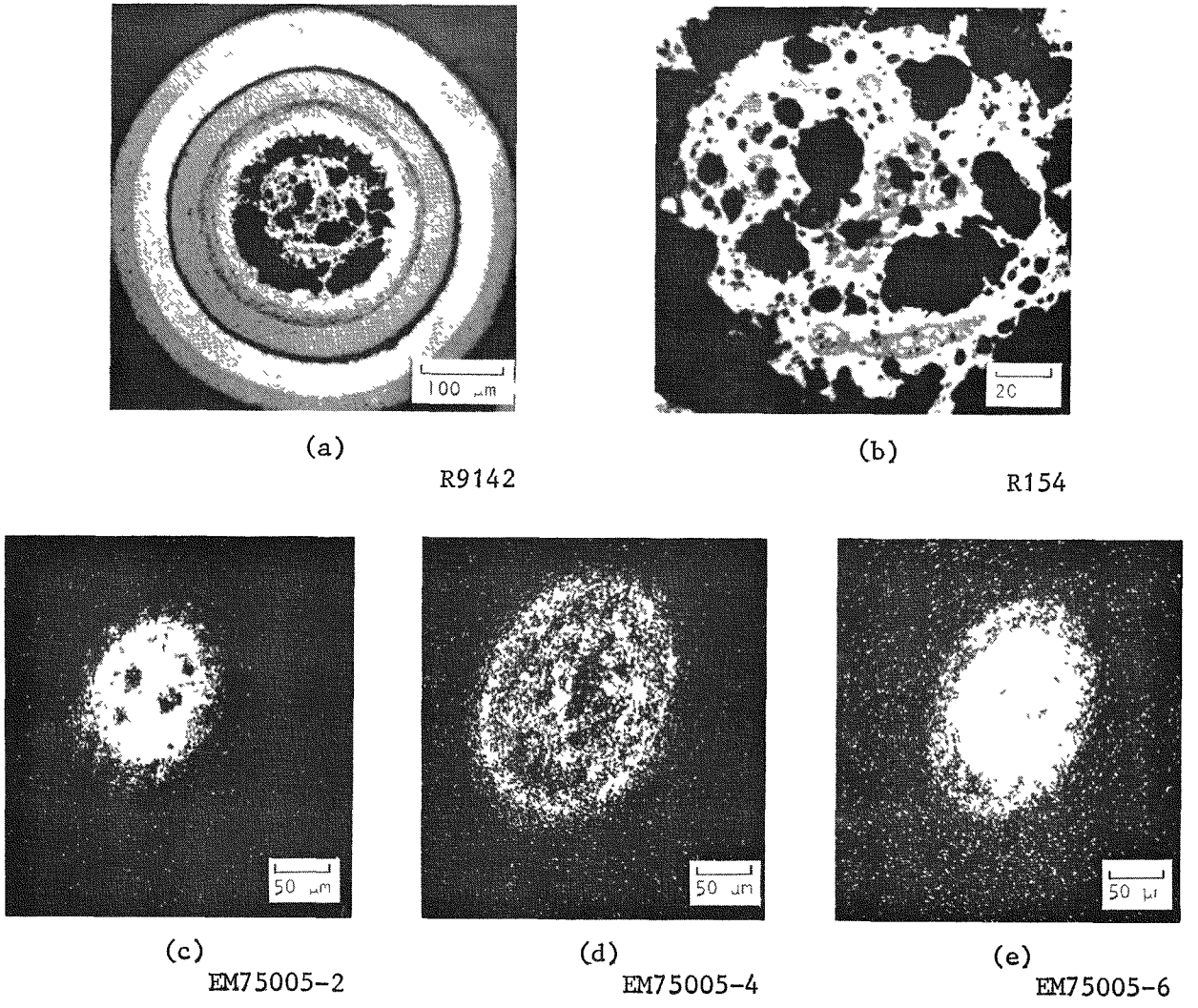

Fig. 9-23. TRISO coated $UC_{3.0}O_{0.7}$ (batch 6157-02-016) after irradiation to 63% FIMA and 2.1 x 10^{21} n/cm^2 $(E \geq 0.18\ MeV)_{HTGR}$ at temperatures less than 700°C: (a,b) representative photomicrographs; (c,d,e) results of electron microprobe examination of uranium, cesium, and neodynium, respectively

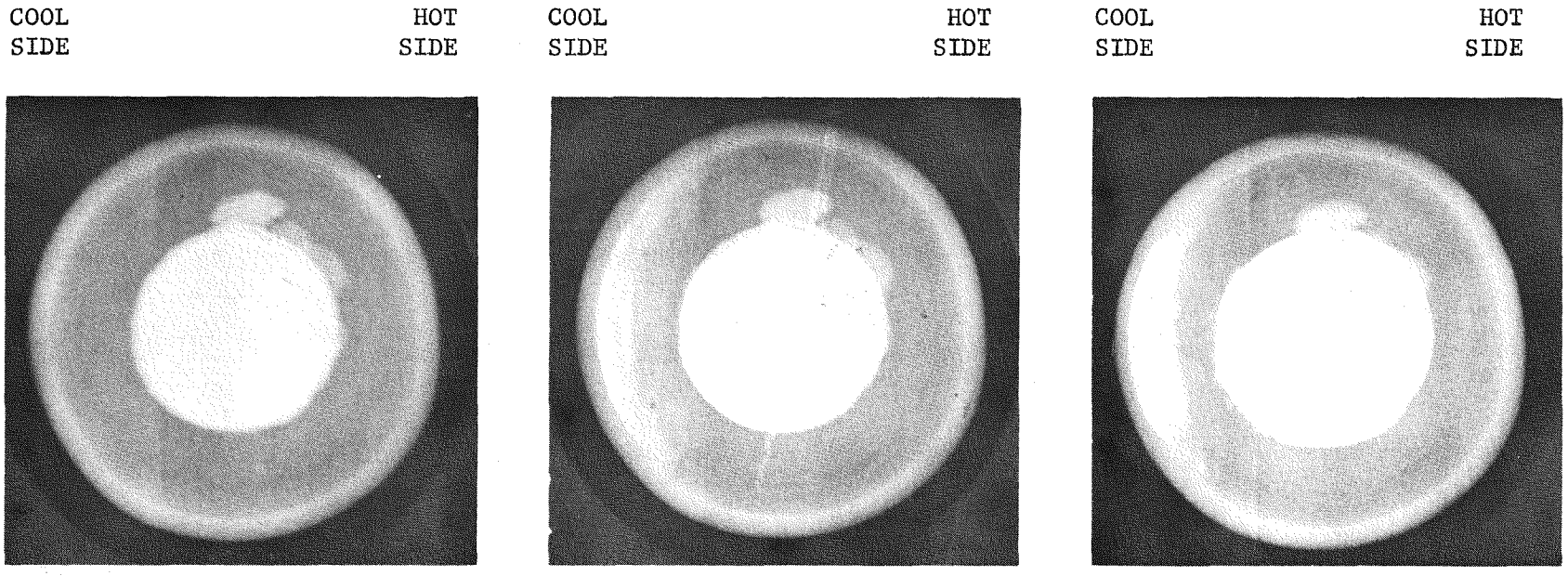

Fig. 9-24. Radiographs of a TRISO UC_2 fuel particle heated at 1552°C under a thermal gradient of 476°C/cm for: (a) 0 hr, (b) 93 hr, and (c) 476 hr after irradiation at 1000°C to 30% FIMA and 1.1×10^{21} n/cm^2 ($E \geq 0.18$ MeV)$_{HTGR}$

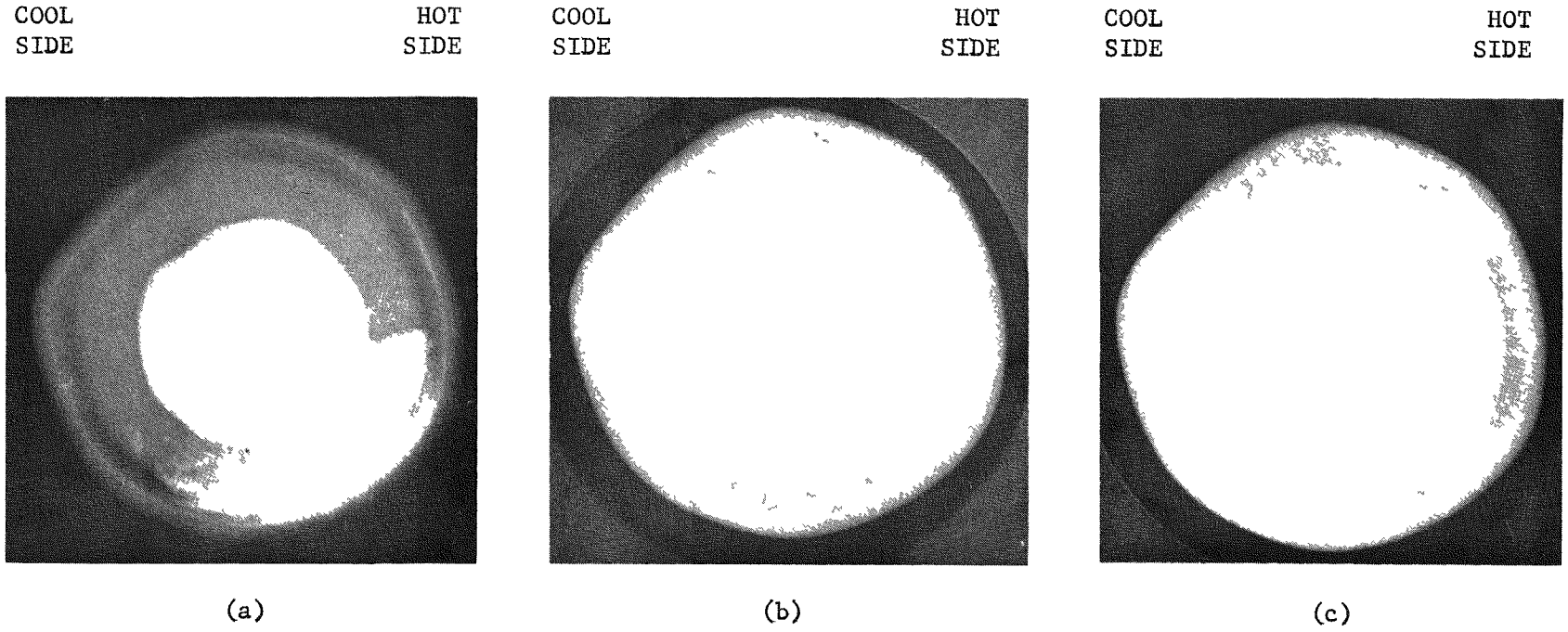

Fig. 9-25. Radiographs of a TRISO UC_2 fuel particle heated at 1523°C under a thermal gradient of 442°C/cm for: (a) 0 hr, (b) 93 hr, and (c) 476 hr after irradiation at 1350°C to 61% FIMA and 5.3×10^{21} n/cm^2 $(E \geq 0.18 \text{ MeV})_{HTGR}$

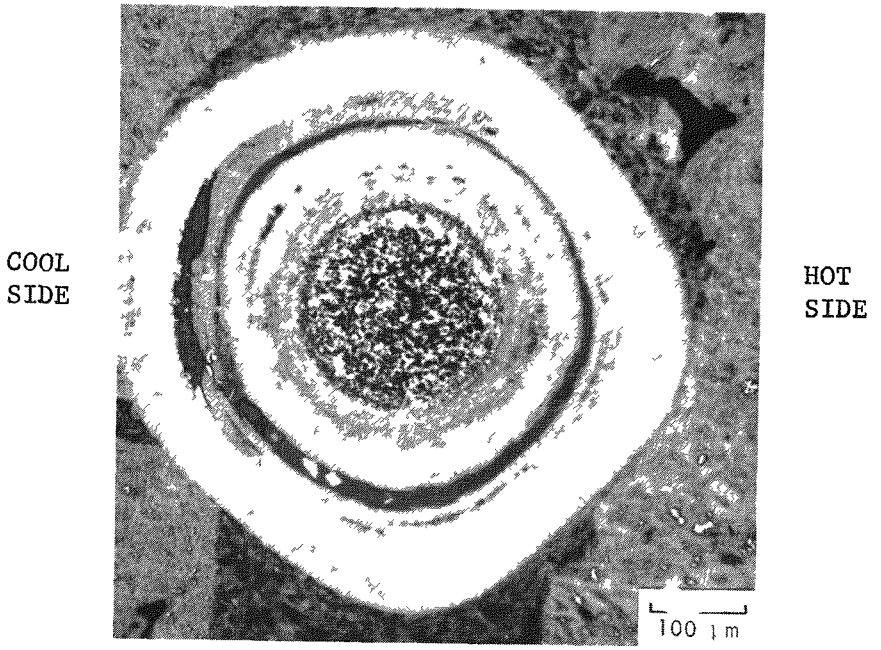

(a) R69182

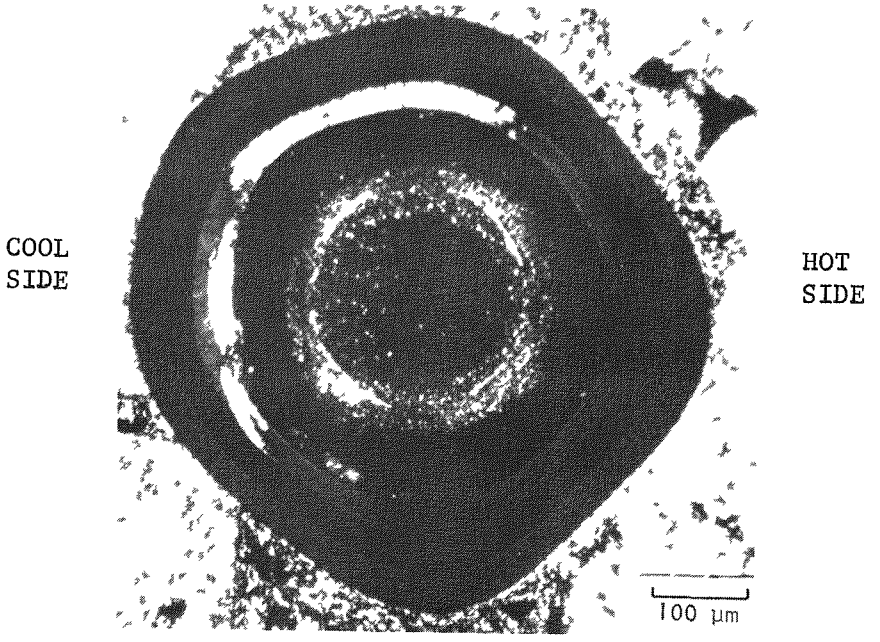

(b) R69183

Fig. 9-26. Photomicrographs of a TRISO coated, dense melted UC_2 particle heated for 188 hr at ∿1500°C under a thermal gradient of ∿430°C/cm after irradiation to 30% FIMA and 1.1 x 10^{21} n/cm^2 $(E \geq 0.18 \text{ MeV})_{HTGR}$ at ∿1000°C: (a) bright field and (b) polarized light

Fig. 9-27. SiC - fission product reaction zone on the cool side of a TRISO UC_2 particle heated for 188 hr at ∿1500°C under a thermal gradient of ∿450°C/cm after irradiation at 1000°C to 30% FIMA and 1.1 x 10^{21} n/cm^2 ($E \geq 0.18$ MeV)$_{HTGR}$

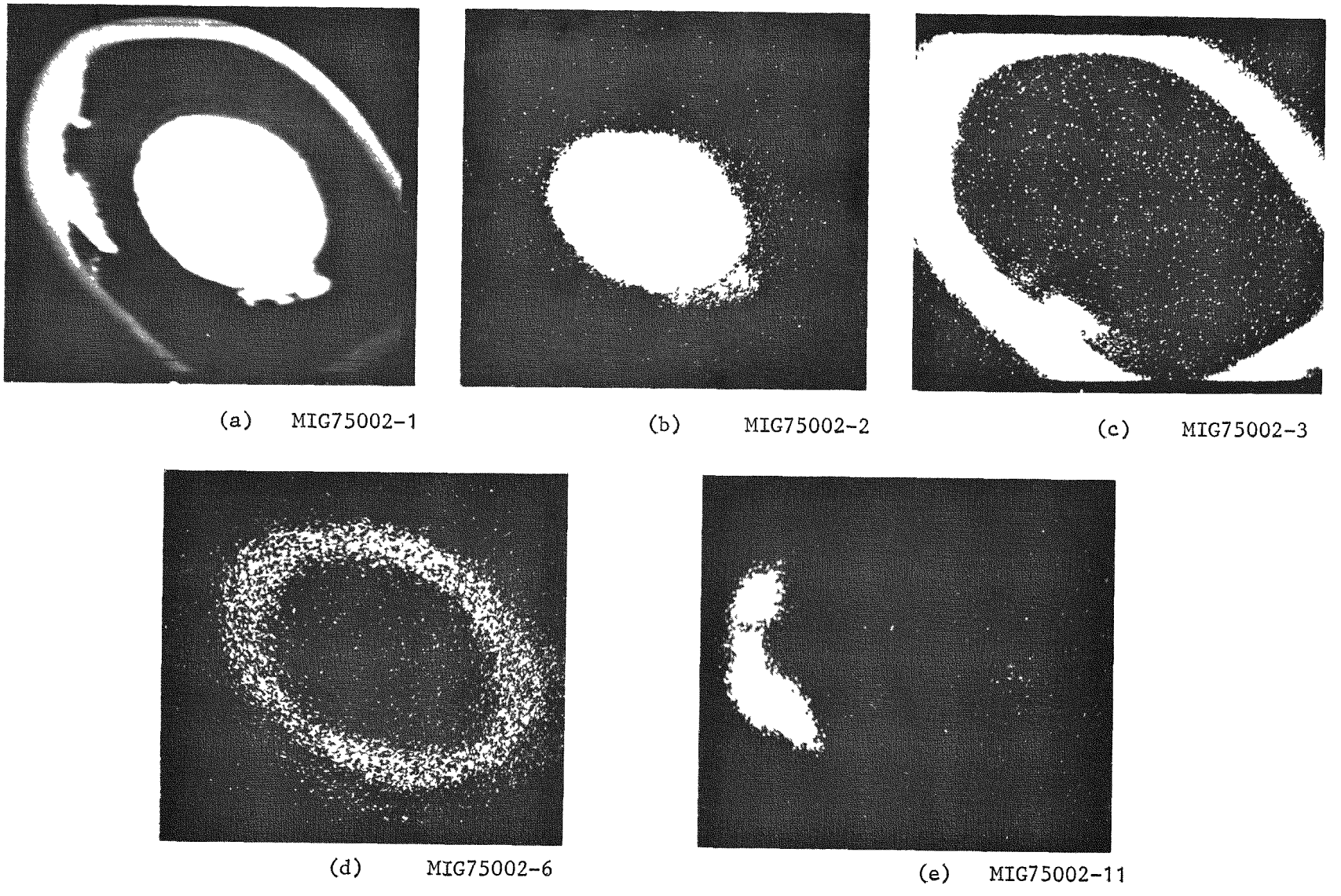

Fig. 9-28. Summary of electron microprobe examination of a TRISO UC_2 particle heated for 188 hr at ∿1500°C under a gradient of ∿450°C/cm after irradiation at 1000°C to 30% FIMA: (a) specimen current, (b) uranium, (c) silicon, (d) cesium, and (e) neodynium. (The cool side of the particle is the left hand side of each figure.)

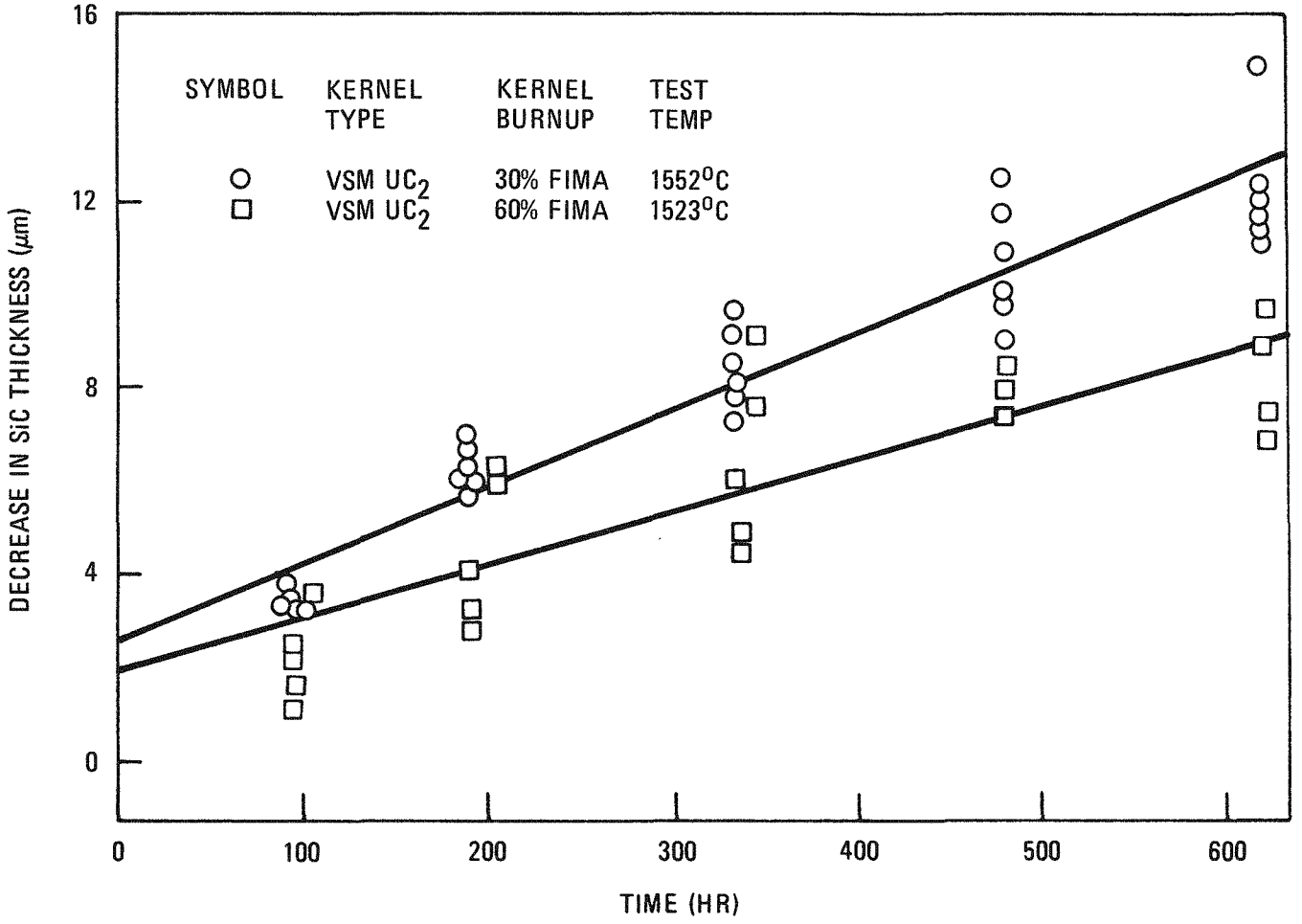

Fig. 9-29. Decrease in apparent SiC thickness with time during thermal gradient heating at 1523° or 1552°C for TRISO UC_2 samples irradiated to 30 or 60% FIMA

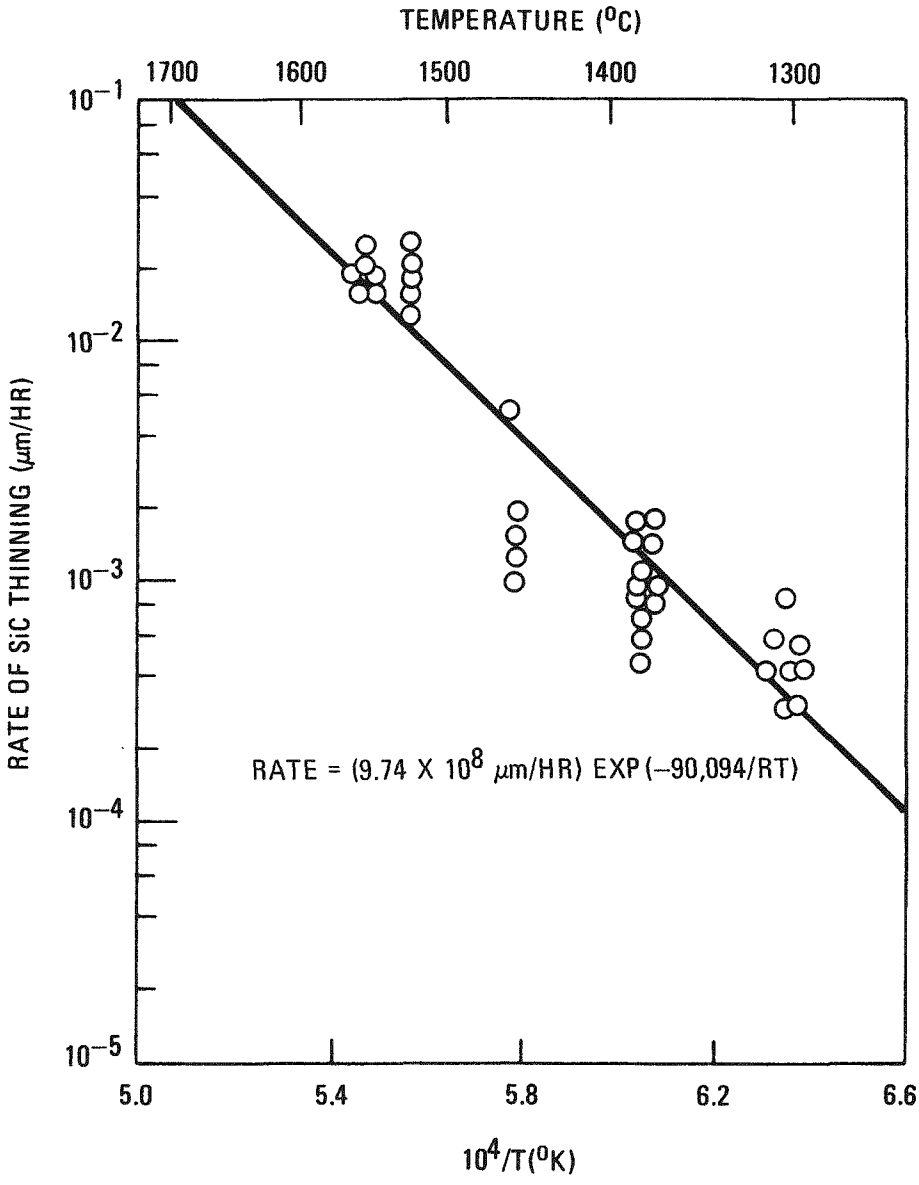

Fig. 9-30. Variation in rate of SiC thinning (μm/hr) observed during out-of-pile thermal gradient heating of irradiated TRISO UC_2 fuel with inverse temperature

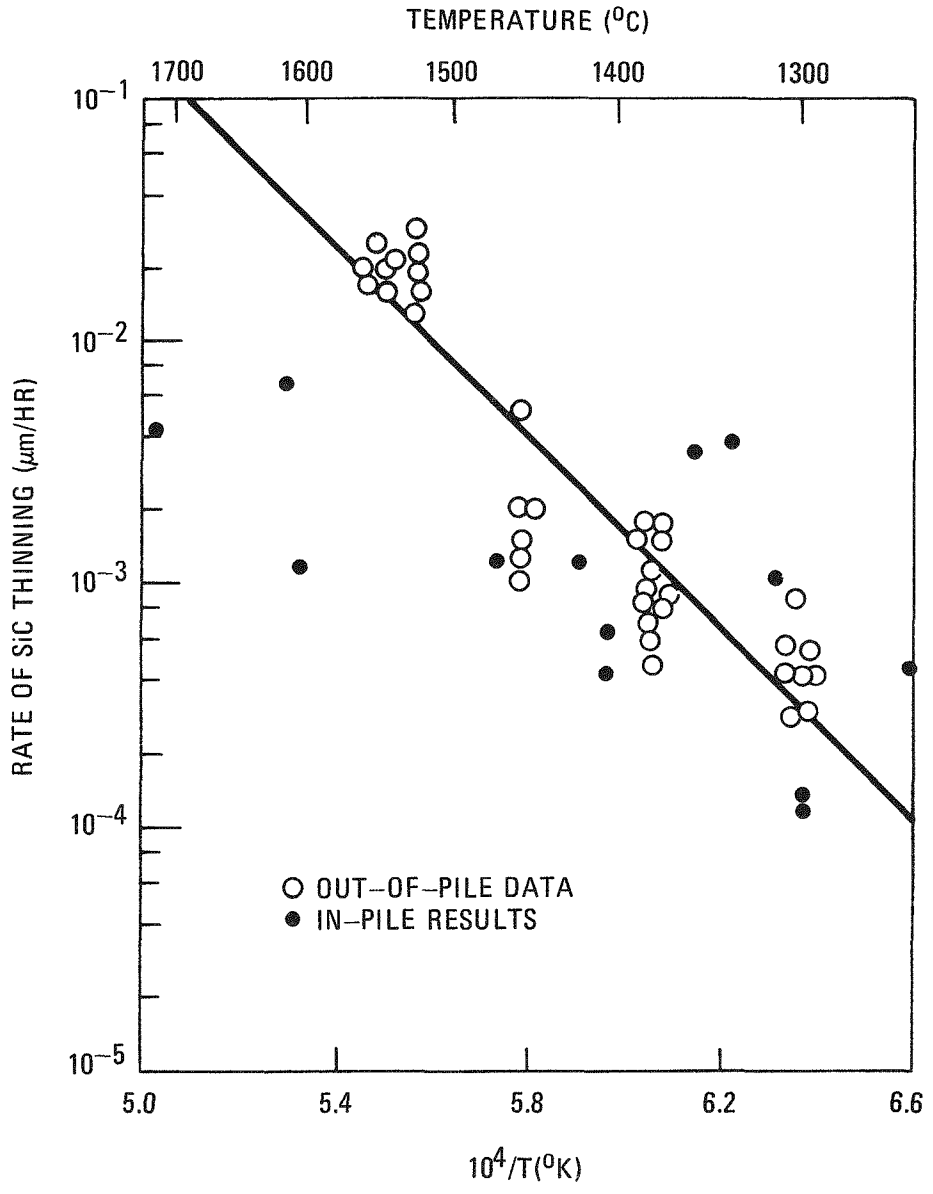

Fig. 9-31. Comparison of postirradiation heating results with in-pile SiC thinning rates observed during postirradiation examination

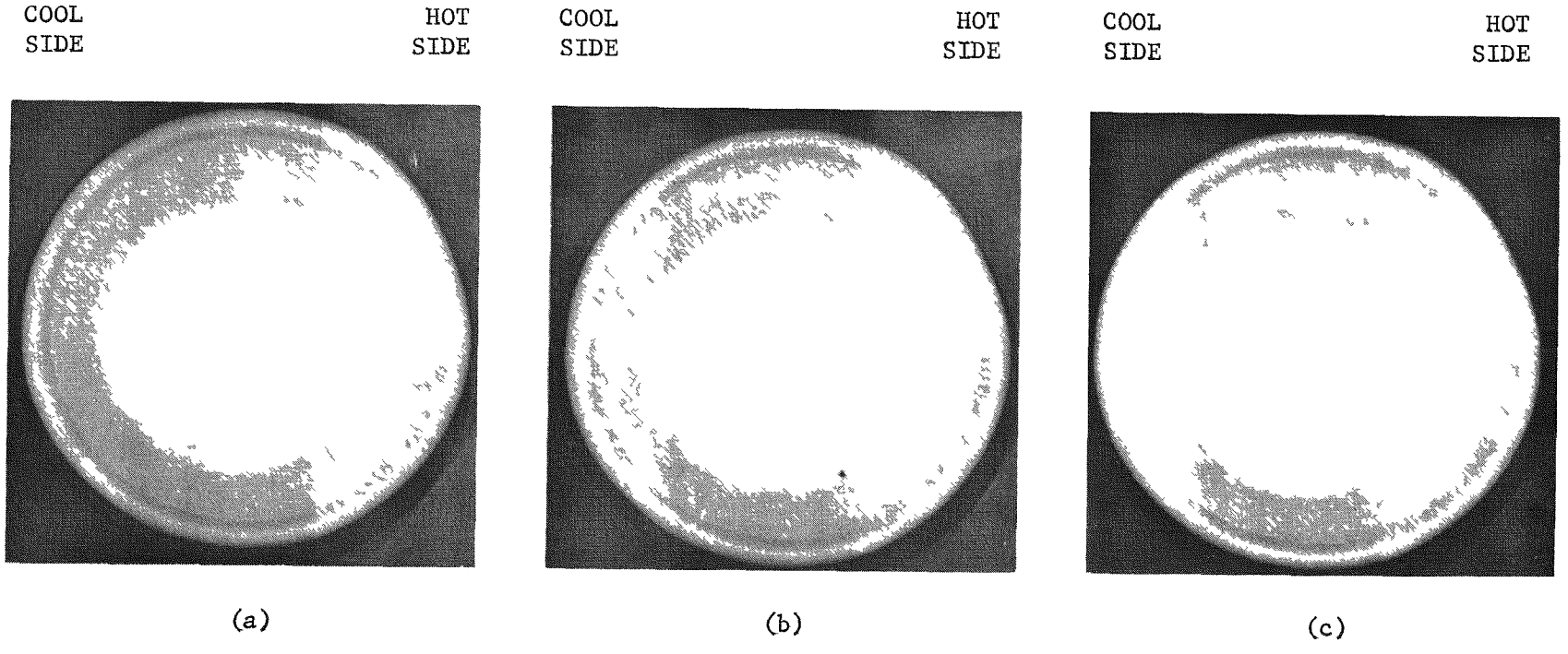

Fig. 9-32. Radiographs of a TRISO WAR $UC_{4.3}O_{1.3}$ particle heated at 1530°C under a thermal gradient of 515°C/cm for: (a) 0 hr, (b) 93 hr, and (c) 476 hr after irradiation at 1050°C to 60% FIMA and 5.8×10^{21} n/cm^2 $(E \geq 0.18 \text{ MeV})_{HTGR}$

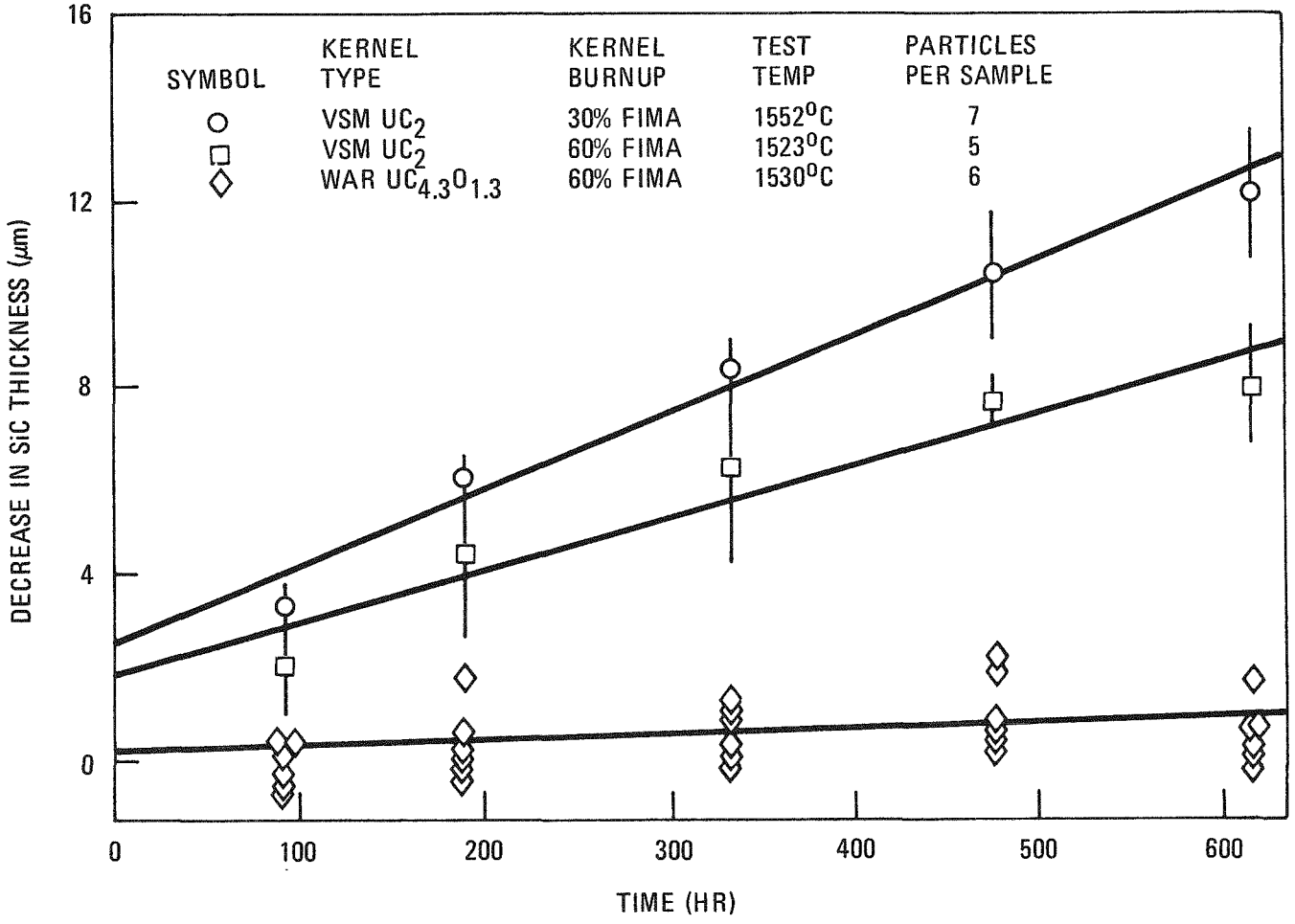

Fig. 9-33. Comparison of the change in SiC thickness with time measured on TRISO $UC_{4.3}O_{1.3}$ fuel particles irradiated to 60% FIMA and TRISO UC_2 fuel particles irradiated to 30 or 60% FIMA. Samples were heated at 1520° to 1550°C under a thermal gradient of 440° to 540°C/cm. Average values plus or minus 1 standard deviation are given for the UC_2 samples.

11. GRAPHITE DEVELOPMENT

189a NO. SU004

TASK 100: FABRICATION AND OPERATION OF IRRADIATION CAPSULES IN THE ORR

This task consists of the fabrication and operation of the irradiation capsules used to determine the irradiation behavior of the graphites.

Capsule OG-3

Capsule OG-3 was removed from the C-3 position of the Oak Ridge Reactor on December 9, 1975 after successful operation for 6 months. The capsule is now awaiting disassembly in the GA Hot Cell.

Capsule OG-4

Capsule OG-4 has been canceled.

Capsule OG-5

OG-5 is the successor capsule to OG-3 and will have identical thermal design. Capsule OG-5 is being prepared and will be inserted in the ORR in September 1976.

TASK 200: GRAPHITE SPECIMEN PREPARATION AND PROPERTY MEASUREMENTS FOR CAPSULE IRRADIATIONS

Capsule OG-2

The final report on the OG-2 graphite irradiation experiment, containing full data on the experimental measurements, was issued (Ref. 11-1).

Capsule OG-3

Postirradiation examination of specimens from OG-3 will begin in February 1976.

Capsule OG-5

A Test Plan for this experiment has been drafted and submitted to ERDA for Approval-In-Principle. Priority in the capsule experiment will be given to H-451 graphite. Samples from two pre-production lots (426 and 440) and from a production lot being made for Fort St. Vrain reload segment 9 will be tested. Other materials to be included in the experiment include specimens of TS-1240 graphite previously irradiated in capsules OG-2 and OG-3; subsize extrusions of SO-818 graphite containing various fractions of recycle graphite in the filler; and a few specimens of two candidate graphites for HTGR side reflector blocks, HLM and PGX.

TASK 300: CHARACTERIZATION OF CANDIDATE GRAPHITES FOR PROPERTIES AND PURITY

Characterization of Great Lakes Carbon Company (GLCC) grade H-451, Union Carbide Corporation (UCC) grade TS-1240, and AirCo Speer (AS) grade SO-818 is continuing.

The characterization work on H-451 (lot 426) and TS-1240 (lot 1) has been completed and a final topical report has been issued (Ref. 11-2).

Characterization of grade H-451 (lot 440) and grade SO-818 (lot 1) is 90% complete. Purity, density and tensile properties, and thermal expansivity data for grade H-451 (lot 440) are presented in Tables 11-1 through 11-8.* Additional density and tensile property data for grade SO-818 (lot 1) are presented in Table 11-9.

*Tables appear at the end of Section 11.

Lot 440 has higher mean densities than lot 426, but the mean strength values are lower. Completion of the strength measurements on lot 1 of SO-818 continued to show good mean strength values and a narrow distribution around the mean.

TASK 400: STATISTICAL STUDY OF GRAPHITE STRENGTH

Work under this task is continuing; there are no current results to report.

TASK 500: FATIGUE BEHAVIOR OF GRAPHITE

Uniaxial fatigue testing at room temperature is being conducted on axial specimens of H-451 graphite. The test method and data from a set of 1:1 tension:compression tests were reported in the previous quarterly report (Ref. 11-3).

A second set of tests using a 2:1 tension:compression loading has been completed. The data are tabulated in Table 11-10. The core numbers in the table correspond to locations shown in Fig. 11-1 of Ref. 11-3. Figure 11-1 shows the data plotted as peak stress versus log (cycles to failure). The open circles indicate specimens which survived 100,000 cycles without failure. Lines indicating 10, 50, and 90% failure probability are shown. The lines fall a little higher than those for the 1:1 tension:compression tests reported previously. The endurance limit for 100,000 cycles (50% survival) was 63% of the mean single-cycle tensile strength, compared with 59% for the 1:1 tension:compression tests.

Additional tests using 1:0 tension:zero and 2:1 tension:tension stressing modes are in progress. On completion of these tests, a Goodman constant-life fatigue diagram will be constructed.

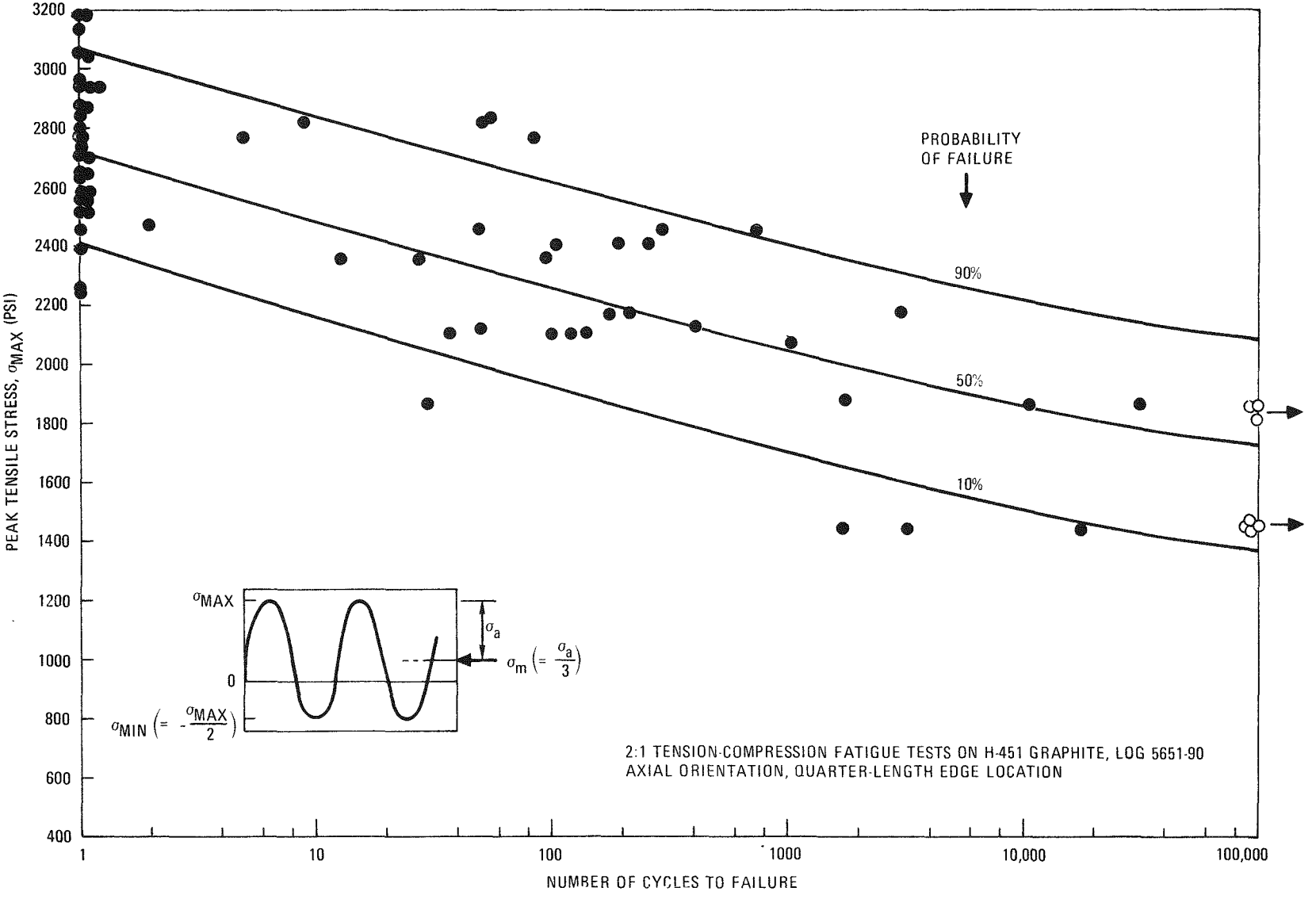

Fig. 11-1. Fatigue test data on axial H-451 graphite; cycles to failure versus peak tensile stress for uniaxial tests, 2:1 tension:compression

TASK 600: STRUCTURAL INTEGRITY OF GRAPHITE BLOCKS

A program plan titled "Graphite Structural Verification" was completed in December. It is included here and fulfills milestone A, Subtask 600 shown in the FY-76 Work Plan for Task 11.

Plan for Graphite Structural Verification

Objectives

The objectives of this task are:

1. To verify the accuracy of the structural design methods and the data used to predict deformation and stresses in fuel and reflector graphite.

2. To establish limiting stresses and stress distributions at which cracking occurs in graphite fuel and reflector elements.

3. To establish suitable design margins between stress and strength to assure structural reliability and safety.

Milestones for the program are given in Table 11-11.

Justification

This work is needed to prove that the methods, data, and stress limits used in HTGR structural design, if properly applied, are sufficiently accurate or conservative to preclude structural failure. This is needed to assure safety and reliability in the design and to meet design quality assurance and reactor licensing requirements.

Background

The final structural design verification of HTGR fuel elements is performed by constructing finite element models of the elements and performing calculations with two-dimensional finite element computer programs (Ref. 11-4). The programs use data describing the properties of graphite under irradiation that were obtained by evaluating the physical property data measured on small samples in other subtasks of this program. The irradiation strain, irradiation creep coefficient, thermal conductivity, thermal expansivity, and elastic modulus are defined as functions of temperature and fast neutron fluence. With the help of the computer programs and the materials data, the temperature and stress distributions in fuel elements are calculated from the power, coolant flow, and fast neutron flux distributions in the reactor core. The computer programs have been verified to be mathematically correct, but the validity of the models to combine the effects of dimensional changes, creep, and property changes measured on small samples has never been verified by comparison with experiments for large graphite structures.

Calculations performed with these programs have shown that thermal stresses are developed in the graphite elements when the reactor goes to power. Tension is developed in colder areas, e.g., near coolant holes, while compression develops in hotter areas, e.g., near fuel holes. Irradiation strain quickly alters the initial thermal stress distribution. Hotter areas of the element shrink more rapidly under irradiation than colder areas and soon go into tension. Tensile stresses in the hotter areas increase until creep rates, which are proportional to stress, become equal to the differences in the rate of irradiation strain within the structure. The maximum operating stresses are reached at approximately 1 year after the start of irradiation at a fast neutron fluence of about 2×10^{21} n/cm^2.

When an operating reactor is shut down, the temperature differences present during operation drop to negligible values, producing differential thermal shrinkage (reverse thermal stresses) within the element. The hotter areas of the element, which were already in tension because of the higher rate of irradiation shrinkage, also shrink more thermally, causing tensile stresses to increase above the operating levels. The peak shutdown stresses are found to be typically two to three times the peak operating stresses. These residual shutdown stresses are the most critical secondary stresses in the fuel elements. This is fortunate since residual stresses can be studied and measured more readily than can the operating stresses, which are present only while the element is being irradiated.

Strip Cutting. The most effective method of determining residual stress distributions in irradiated graphite bodies is to cut the bodies to allow deformation to occur to relieve the stresses. The location of the cuts must be carefully selected to provide for maximum deformation and to allow the largest residual stresses in the bodies to be estimated. The technique most widely used to date has been strip cutting, in which thin specimens are cut parallel to the axis of the graphite body as shown in Fig. 11-2. The location of the cuts is generally chosen to remove a strip that has residual tensile stress on one side and residual compressive stress on the other.* Following the cutting operation the strip bows to relieve the bending moment that had been present in the strip.

Strip cutting experiments to measure residual stresses in irradiated graphite bodies have been performed for many years. The first strip cutting experiments, begun at the Dragon project in 1967 on hollow rod elements FE-700, -701, and -703, were in good agreement (±20%) with calculations. Later work on tubular fuel elements (FE-923) (Ref. 11-5) showed general agreement between analysis and experiment within 20 to 40%.

*Any gradient in axial stress will cause bowing, but the largest, most easily measured bow is produced when the residual stress varies from a high value of tension to a high value of compression across the strip.

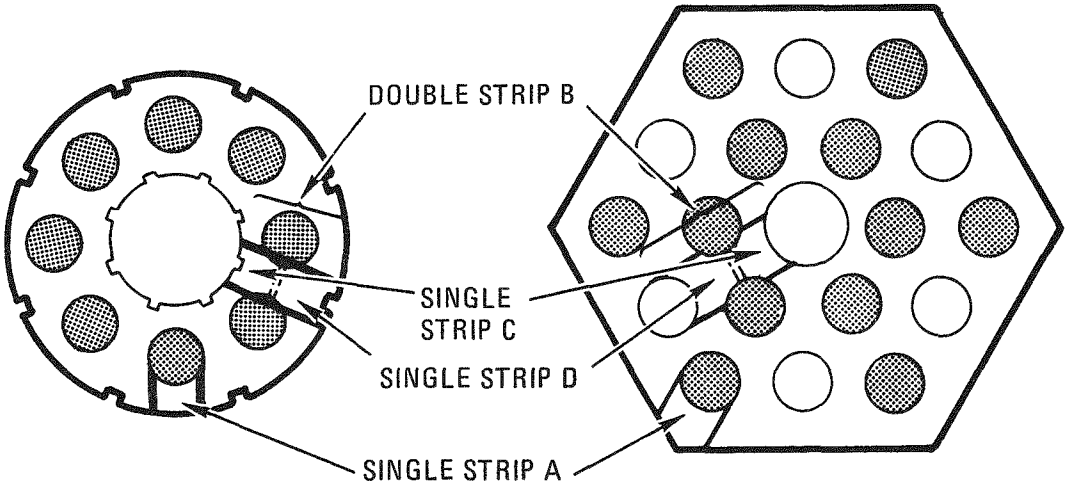

Fig. 11-2. Strip cutting to measure axial stresses

Teledial fuel elements FE-X-115, -135, and -155 have been examined at Dragon by strip cutting experiments. In these experiments, the agreement with predictions was not as good, with observed bowing of strips as much as 50% less than predicted (Ref. 11-6).

The deformation of strips is actually a measure of the residual elastic strain distribution rather than the residual stress distribution. The residual stress distribution can be determined by straightening the strips in a four point bend apparatus and measuring the curvature as a function of load. This test measures the effective elastic modulus of the irradiated strip, thereby verifying changes in the elastic modulus predicted from measurements of specimens irradiated under unstressed isothermal conditions in the OG-capsules. By extending the bend test to failure, the strength of irradiated material can be verified.

Strips cut from a web between fuel and coolant holes or between a fuel hole and the cooled surface of a teledial element verify axial stress and strain in fuel elements. Strips can be cut in the horizontal direction to measure in-plane stress and strain in locations where there is a sufficient uninterrupted length of graphite in the horizontal direction. Cases where this may be practical are from the sides or from the edges between sides and the top or bottom faces of fuel elements irradiated in the Fort St. Vrain reactor. The pattern of alternating fuel and coolant holes at the edge of a fuel element is expected to lead to in-plane bending stresses in this area. Bending stresses are also expected in the web between the control rod or reserve shutdown channel and the outside surface of control fuel elements. Strips cut from the top or bottom faces of the elements are expected to bow substantially due to axial temperature gradients between the fueled central portion of the element and the unfueled top and bottom faces.

Side reflector elements are expected to have large fluence gradients and strain gradients on the sides adjacent to the reactor core. Horizontal and vertical strips cut from these sides of the reflector elements are

expected to show some substantial bowing due to the relief of axial and in-plane stresses.

The configuration of teledial test elements and capsules allows residual in-plane strains to be measured by making a single cut as shown in Fig. 11-3. The distance between points on opposite sides of the cut is measured accurately as shown in Fig. 11-3 before and after the cut is made. The measured distance is predicted to be reduced by the cut, which relieves the in-plane bending moment in the specimens. The residual hoop tension along the inside diameter of the hollow cylinder and compression along the outside diameter are relieved as its radius of curvature is reduced.

As in the case of strip cutting, the deformation of cut rings is a measure of the residual strain, rather than stress. To measure the in-plane stress, bending moments can be applied to the cut ends of the ring to return it to the original shape before the cut was made. This also allows the effective elastic modulus of the ring in the in-plane direction to be determined.

Primary Loading Tests. Tests in which irradiated graphite bodies are loaded to failure by the application of primary stresses are required to provide a good simulation of the most severe operating condition in the reactor: the combination of primary loads due to a seismic event with secondary stresses caused by the prior history of temperature and irradiation. The chief limitation of these tests is that, should failure loads not be predicted accurately, it is difficult to identify the source of the discrepancy. These tests do, however, give the ultimate verification of our ability to predict design margins.

The simplest primary loading test is the four point bend test on a strip cut from an irradiated specimen, which may be continued to failure. The failure load and deformation at failure give a measure of the margin for primary bending stress and strain. A variation on this type of test

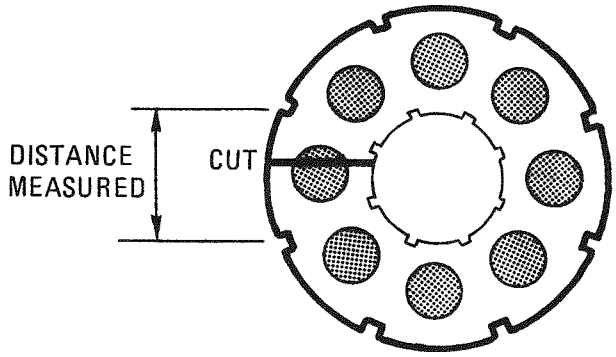

Fig. 11-3. Ring cutting to measure in-plane stresses

would be to apply a bending moment to the ends of a ring cut from a teledial test element to verify in-plane stresses. The bending moment would be increased until failure while the magnitude of the moment and the increase in the distance across the cut is measured.

Hydraulic pressurization of fuel holes is another fairly simple test, with which there is already some experience for both unirradiated specimens (Ref. 11-7) and irradiated specimens (Ref. 11-8). Since the peak residual stresses in the graphite are generally found at the surface of the fuel holes, this type of test has the advantage of adding the peak primary load in the same location where the peak secondary residual stress exists.

Where multihole fuel elements or test elements are available, tests more closely simulating seismic events are possible. The simplest of these is a compression test of a fuel element section or a test element that simulates a portion of a multihole block. A simulation of interelement collisions during a seismic event is obtained by performing impact tests on sections of multihole test elements or irradiated fuel elements from the HTGR surveillance program. Impact tests on full HTGR elements are also possible, although this will require a large hot cell and fairly elaborate test equipment.

Failure Criteria. Tensile tests on cylindrical specimens have been the principal method of characterizing the strength of graphite. Tensile specimens were taken from every graphite element used in the Fort St. Vrain reactor and tested to failure. In addition, logs of needle-coke and near-isotropic graphite have been sampled extensively to determine the effect of diameter on strength and thereby gain more insight into the statistical nature of failure in graphite.

Four point bend tests of graphite specimens have also been performed and the results compared with those of tensile tests. The modulus of rupture in bending has been shown to be 50 to 80% greater than the tensile strength. Pressure burst tests of thick-walled cylinders have also been

performed and have shown stresses at failure to be higher than the tensile strength, by factors varying from 20% at a diameter ratio (O.D. to I.D.) of 1.2 to 70% at a diameter ratio of 3 (Ref. 11-7). More recently thermal stress tests have been performed on thick-walled hollow cylinders heated by electromagnetic induction and cooled by water flow through the central hole. Preliminary results of these tests have indicated stresses at failure two or more times the tensile strength.

Tests of notched specimens of different geometries machined from isotropic graphite have shown that the observed stress concentration factors are always less than theoretical predictions for an elastic material of the same specimen geometry (Ref. 11-9). The observed stress concentration factors never exceeded 2.0, even with sharp V-notches with a tip radius less than 0.0254 mm (0.001 in.). The data indicated that the ratio of observed-to-theoretical stress intensity factor tended to zero as the notch radius approached zero. Stresses calculated by an elastic analysis to be many times the uniaxial tensile strength were shown to be sustainable without cracking if they were sufficiently localized.

The insensitivity of graphite to localized stress peaks is important to the design of graphite moderated reactors. It is particularly important to the design of HTGR fuel elements, which have many fuel and coolant holes and stresses that typically vary from peak tension to peak compression over a span of less than 10 mm.

For the designer to take advantage of the insensitivity of graphite to local stress peaks, a general model for the failure of graphite must be established. Many attempts have been made to apply theoretical models, such as the Weibull theory, but none has yet been successful in explaining the experimental results for specimens of many sizes and shapes (Ref. 11-10). While it may still be possible to develop a general theoretical model, the approach of developing an empirical model that may be limited to a particular class of specimen shapes appears more certain to lead to useful results. Such an empirical model could be developed by testing simple

specimens with stress distributions similar to those in fuel elements. It would have to be verified as applicable to fuel elements by testing specimens whose shapes and stress distributions are nearly the same as those in the regions of fuel elements where peak stresses are found.

Test Elements. A number of test elements were irradiated in the Peach Bottom reactor. All of these contained fuel rods inserted in holes in H-327 graphite bodies. They consisted of 8-hole and 6-hole teledial elements and a small hexagonal element representing a portion of a multihole block. The characteristics of these elements are given in Table 11-12. Each element consisted of three 762 mm (30-in.) long graphite bodies with a cross section as shown in Fig. 11-4. The teledial elements were cooled only externally, so that the graphite near the central hole was about 300°C hotter than the outside surface. The central hole in PTE-2 was not cooled, so that this element was also hotter in the center. As a result of these temperature gradients, fairly high residual axial and in-plane stresses are expected to be present within the irradiated graphite, as shown in Table 11-12. While these irradiated graphite bodies do not have all the characteristics one would have in specimens from an irradiation experiment designed specifically for verifying graphite structural methods and data (see final section under Task 600, "Stress Verification Experiment"), they have the advantage that they have already been irradiated and are presently available for examination.

In addition to the test elements, there are seven short [less than 203.2 mm (8 in.) long] graphite bodies from fuel test capsules P13Q and P13T. The cross section of these elements is shown in Fig. 11-4. While the stresses in these elements are expected to be much lower than the stresses in the test elements, these elements are of interest because they are the only irradiated H-451 graphite bodies presently available for examination.

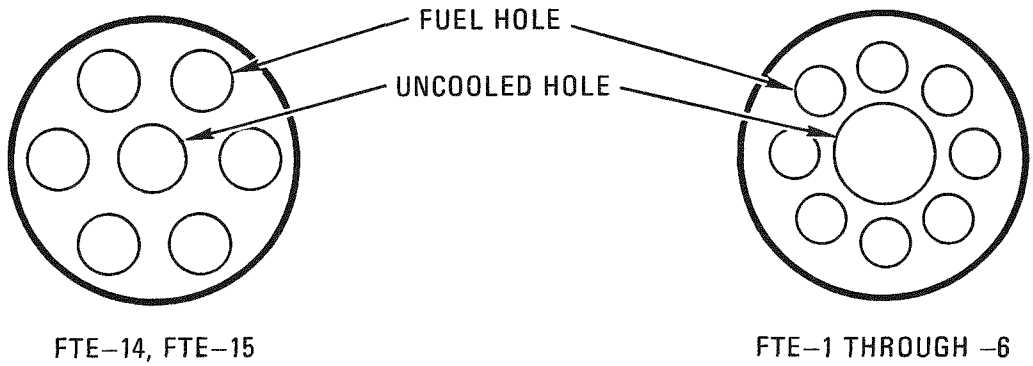

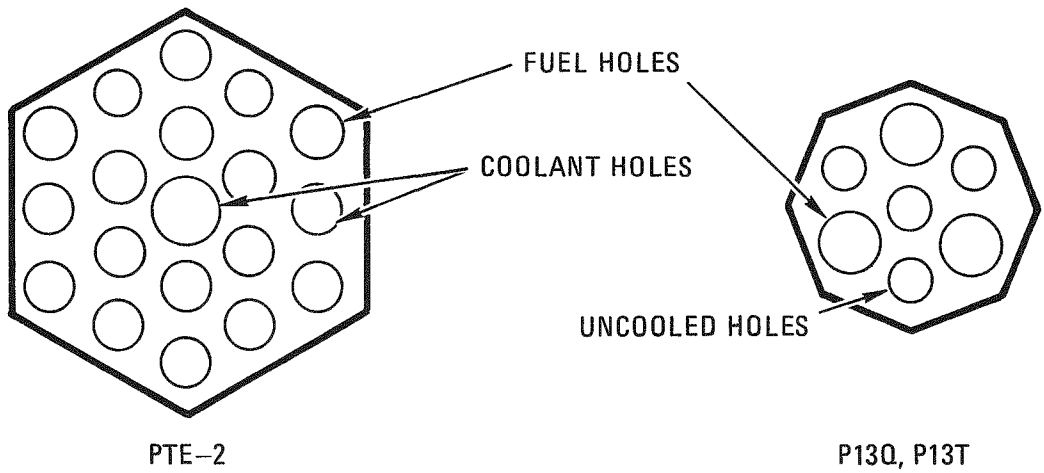

Fig. 11-4. Irradiated graphite for examination

Beginning in 1977, surveillance elements from Fort St. Vrain are expected to be available for postirradiation examination. These elements are made from H-327 graphite. Test elements of H-451 graphite are planned for insertion in the Fort St. Vrain reactor in late 1977 and may be removed after irradiation at the rate of one per year.

Work Scope

Residual Stress Analysis. Deformation and residual stresses in the graphite fuel test element and fuel capsules will be calculated using the finite element computer programs used for design of commercial HTGRs. The physical property data used will be that developed under other subtasks of Task 11. Measurements of burnup, neutron flux, and temperature made during and after the irradiation of each element will be used to obtain the most accurate analysis.

The contraction or extension and bowing to be expected when strips are cut from the irradiated graphite will be derived from the residual stress distribution by an elastic relaxation calculation. The elastic stress distribution from uniform pressurization of fuel holes or uniform loading of external faces will be calculated with a finite element model and added to the residual stress distribution to find the combined stress and to predict the location of cracks and the load at which they form.

A detailed experimental plan for each element will be constructed on the basis of the analytical predictions. This will include dimensions to be measured, accuracy and precision of measurements, location of cuts to be made in the graphite, and measurements to be made after cutting. Sections to be cut for pressure burst, compressive, or impact testing to failure will also be specified, along with the manner in which the load is to be applied.

Phase I of the residual stress analysis consists of the preliminary analyses on the Peach Bottom fuel test elements in the FTE series. The preliminary calculations will be made at various axial positions in each test element to identify the elements and the fuel bodies within the elements that are of most interest for strip cutting analysis and primary loading experiments. Complete time history calculations will be performed, considering the effects of changes in power and temperature distributions in the course of irradiation of the elements. Azimuthal asymmetry will be assumed in these preliminary calculations and the calculations will be performed only at a single axial position in any given fuel body. Alternatives in locations and shapes of strips to be cut and in locations of primary load application will be compared. The principal results of Phase I will be detailed plans for residual stress measurements and primary loading experiments for all of the Peach Bottom test elements. In addition, preliminary predictions will be made of the bow to be expected in strips and the primary load expected to cause failure. These preliminary predictions will be used to guide the development of experimental apparatus and techniques.

Phase II of the program consists of the detailed thermal and structural analysis of the graphite bodies from the Peach Bottom test elements selected for residual stress measurements and/or primary loading experiments. In these final calculations, azimuthal asymmetry in power and temperature will be treated explicitly. Calculations will also be performed at several axial positions in the elements examined to predict such effects as variation in curvature of a strip with position and variation in primary load at failure with specimen location. The multihole block element PTE-2 and the H-451 graphite bodies from fuel test capsules P13Q and P13T will also be analyzed in Phase II.

Sensitivity and uncertainty analysis will also be performed to assess the effects of uncertainties in graphite property data and in power, flux, or temperature distributions. This will provide a range in predicted behavior to be compared with the observed behavior and will help to identify the source of any discrepancies.

Phase III of the program consists of both preliminary and detailed calculations of stresses in Fort St. Vrain test and surveillance elements. Calculations for each element will be completed at about the time the element becomes available for postirradiation examination based on the calculated and measured irradiation conditions for the element. These calculations will identify which of the test and surveillance elements should be subjected to residual stress measurements or primary loading experiments and will define the locations and shapes of specimens and the locations of primary loading to be applied. Webs between fuel and coolant holes from which strips should be cut will be identified. Portions of the side, top, or bottom faces of the elements from which the plates or strips should be cut will also be identified. The suitability of pressure burst tests of individual fuel holes or groups of fuel holes will be evaluated, as will the suitability of loading horizontal sections of elements in compression on opposite sides.

Residual Stress Measurements. Residual stress measurements will be performed in the hot cell and, where radiation levels are low enough, in a glove box. Long sections [up to 600 mm (24.5 in.)] of the graphite bodies will be used to allow changes in curvature to be measured accurately. Equipment and procedures will be developed to permit measurements to be made accurately and quickly in the hot cell. Strips will be cut using a double-bladed saw already developed for graphite strip cutting.

Measurements will be made and strips will be cut according to detailed plans for each graphite body developed in the analysis subtask. Examples of strip shapes that may be specified are shown in Fig. 11-2. The length and curvature of each strip will be measured before and after cutting with all measurements made to surfaces or marks that are not destroyed or altered by the cutting operation. For strips such as A in Fig. 11-2, the measurements would be on the outside surfaces of the graphite body. For double strips such as B in Fig. 11-2, measurements will be made on both the inside and outside surfaces of the double strip before it is cut into the

single strips C and D. The distances between points on opposite sides of the first cut made into the center of a graphite body will be measured before and after the cut at several axial locations for comparison with in-plane stress calculations.

The strips will be tested in a four point bending apparatus equipped to measure the load-deflection curve. Metal strips will be used for calibration. The bend tests will be continued to failure.

Primary Loading Tests. Primary loading tests will be performed by pressurizing fuel holes or other holes in the irradiated graphite specimen or by applying a compressive load to the outside of the specimen, e.g., to opposite faces of a section from a hexagonal element or opposite sides of a ring cut from a teledial element. The pressurization apparatus will apply a uniform load with a hydraulic fluid acting through a rubber tube. The apparatus will be developed by adapting to hot cell use a pressure burst apparatus used previously for tests of unirradiated graphite performed in the laboratory. External compressive loads will be applied by a tensile/compressive test machine through appropriate fixtures. Both types of tests will be so instrumented that the load at failure can be determined accurately.

Thin [$\sim$25 mm (1 in.)] sections cut perpendicular to the axis of the element will be used for most primary loading tests so that several specimens can be taken from the same portion of an element, from a region where the stresses are predicted to show little change with axial position. This will allow the fracture results to be evaluated statistically. A few longer sections may be tested to assess the effect of axial stresses, which are largely eliminated by cutting into thin sections, or the in-plane stress at failure.

Graphite Failure Criteria. Failure criteria for H-451 graphite will be developed with the help of several experimental programs. The programs will investigate both crack initiation and crack propagation in zones of

varying stress distribution. The programs are directed toward determination of empirical models to be used for the particular type of stress distributions seen in the HTGR fuel element.

Simple primary loading tests such as four point bend and pressurized tube tests have demonstrated that in an uniaxial nonuniform stress distribution, the maximum tensile stress is an overly conservative failure criterion. Fuel element loadings are a combination of bending and uniform tension stresses and are expected to have a failure limit greater than the ultimate tensile strength. A program is proposed to investigate the available stress margin between that predicted from a maximum tensile stress criterion and that determined experimentally with various ratios of tensile stress to bending stress. Room temperature tests will be conducted to failure on unirradiated graphite specimens loaded in combined tension and bending with various ratios of tensile stress to bending stress.

Test specimens will be uniform beams with circular or rectangular cross sections. The specimens will be loaded in tension between the crossheads of an Instron testing machine with chain or gimball couplings, while a four point bending fixture incorporating its own load cell and drive motor will apply an additional bending moment to the beam. The bending fixture will be floating with respect to the test frame so that all stresses on the specimen will be determinate.

Specimens from one log of H-451 graphite will be tested in two modes:

1. Maintain a constant tensile load and increase bending moment until failure occurs.

2. Maintain a constant bending moment and increase tensile load to failure.

For each testing mode, four different ratios of tensile-to-bend stress will be used, and twenty replicates will be tested under each condition. A total of 160 specimens will be used for these tests.

The test data will be used to develop a failure criterion for uniaxial stresses whose magnitude varies across a load-bearing section of graphite.

Verification of Failure Stress for Fuel Elements. Determination of failure limits for simulated fuel element sections is proposed as a second phase to determine the peak failure stress as a function of stress distribution in simple specimen geometry. Test specimens representing the web between fuel and coolant holes will be loaded to failure with combined tension and bending loads to simulate fuel element stress distributions during normal operation and shutdown conditions.

The test specimens will be designed to be used in the test rig developed for study of combined bending and tension on simple specimens. They will be similar to rectangular beams with a necked-down central region. This central region will duplicate the geometry of a fuel element web. Twenty to thirty replicate specimens will be tested for four combinations of bending and tensile stress. The results of this test will allow extension of the failure criterion developed for simple geometries to the more complex geometry of the fuel element.

The results will be used to develop appropriate failure criteria for uniaxial stresses whose magnitude varies both along the directions of load application and across the load-bearing section.

Fracture Toughness of H-451 Graphite. Fracture mechanics is commonly used for predicting the brittle fracture of high-strength metals. A basic postulate of fracture mechanics is the existence of flaws in the material which raise the local stress level and produce fracture at a lower nominal stress level. Since graphite is a material which naturally contains many flaws, the fracture mechanics approach of predicting fracture should be applicable to graphite. Critical stress intensity factors and critical flaw sizes have previously been determined for graphites other than H-451.

A fracture mechanics approach will be investigated as to its applicability to H-451 graphite, values of the critical stress intensity factor will be determined, and a critical crack size will be related to the structure. Stresses determined necessary for propagation of a stable crack will be compared to those allowed by the present stress criteria. Determination of the critical size flaw will provide a basis for allowable crack growth from initially flawed areas.

Values of the critical stress intensity factor, K_{IC}, will be determined experimentally (at room temperature) for both unirradiated and irradiated H-451 graphite. Initial work on unirradiated material will compare results from notched beam, notched tensile, and double cantilever beam specimens with a range of notch depths to identify the technique which gives the best consistency in the results. Subsequent work will use this technique to measure K_{IC} for H-451 graphite as a function of fluence and orientation and location in the log. Groups of 20 to 30 replicate specimens will be used and mean values for K_{IC}, together with confidence limits, will be determined. A total of 500 specimens will be used during initial testing and determination of unirradiated K_{IC} values.

Irradiation of fracture toughness specimens will require an irradiation capsule. Specimens will be limited to one log location and will be irradiated at a temperature of 700° to 1000°C to a fluence of 2 to 4 x 10^{21} n/cm^2 ($E > 0.18$ MeV). Forty specimens will be used for determination of irradiated H-451 graphite K_{IC} values.

Crack Propagation. Due to a nonuniform distribution of flaws in the H-451 fuel element graphite log, stresses in localized element volumes could possibly exceed the local strength. This will not lead to structural failure if the crack formed is stable or its growth rate is sufficiently slow that it never reaches a critical crack size at which uncontrolled propagation occurs. In extending fracture mechanics principles to the prediction of structural performance under repetitive loading, it is

necessary to determine crack growth as a function of stress level experimentally. When allowable crack sizes are determined throughout the component and the crack growth is determined at each critical point from crack growth data, allowable load magnitudes and the number of loading cycles can be set to keep crack sizes below the critical size.

Experimental work will determine the increase of crack size as a function of the magnitude and number of applications of load for both specimens of simple shape and those simulating the HTGR fuel element. These tests will determine the importance of local cracking in small areas of the element and will be used to define the circumstances under which small cracks will propagate to cause failure of the fuel element.

The tests will be done on both unirradiated and irradiated H-451 graphite. Initial work will determine the optimum specimen type to study graphite crack propagation and to conform to irradiation capsule requirements. This initial study will be specifically directed toward compact tension and double cantilever specimens.

Approximately 30 replicate specimens will be used for each orientation during determination of unirradiated crack propagation rate, da/dn, as a function of stress intensity factor, K_I.

Approximately 40 specimens will be included in an irradiation capsule together with fracture toughness specimens for irradiation to 2 to 4 x 10^{21} n/cm^2 at 700° to 1000°C.

Multiaxial Failure Criteria. Currently several sources in the literature indicate that use of a maximum stress failure criterion may be nonconservative in a biaxial or multiaxial stress field. Therefore, it is appropriate at this time to define the biaxial failure surface of H-451 graphite and to evaluate the impact of this failure surface on the present failure criterion.

Published literature on biaxial and triaxial fracture tests on graphites will be reviewed in order to develop a failure criterion for multiaxial stress conditions. Room temperature tests will be performed on H-451 graphite specimens under one or two states of biaxial tension and tension-compression to confirm the applicability of the multiaxial failure criterion to H-451 graphite. Ten to twenty replicates will be tested for each stress state.

Stress Verification Experiment*

An experiment is described to verify residual stress distributions and margins between residual stress and strength in an irradiated graphite test element. The experiment is designed to verify the stress analysis methods and graphite data used in analysis of HTGR fuel elements. The experiment described is one that would be performed solely for the purpose of structural verification of the graphite rather than for the purpose of obtaining data on fuel particles or rods.

The test element would be a section of a multihole block having a fuel and coolant hole pattern identical to that in the reference HTGR fuel element. The test element would be as large as possible in horizontal dimensions to contain as many fuel and coolant holes as possible. As tested in the Dragon reactor, for example, the configuration would be that shown in the upper right-hand quadrant of Fig. 11-5. The test element would extend the full height of the core, although it could be fabricated in two or three sections to be stacked one above the other in the core if this were necessary to simplify fabrication. The test element is fueled with a loading of thorium and uranium designed to give a linear heating rate that varies with fast neutron fluence in about the same way that the linear heating rate varies with fluence in an HTGR fuel element at maximum power density.

---

*The program described here would be recommended if there were no other irradiation programs. The program proposed relies on graphite specimens irradiated in fuel test elements and capsules to reduce costs.

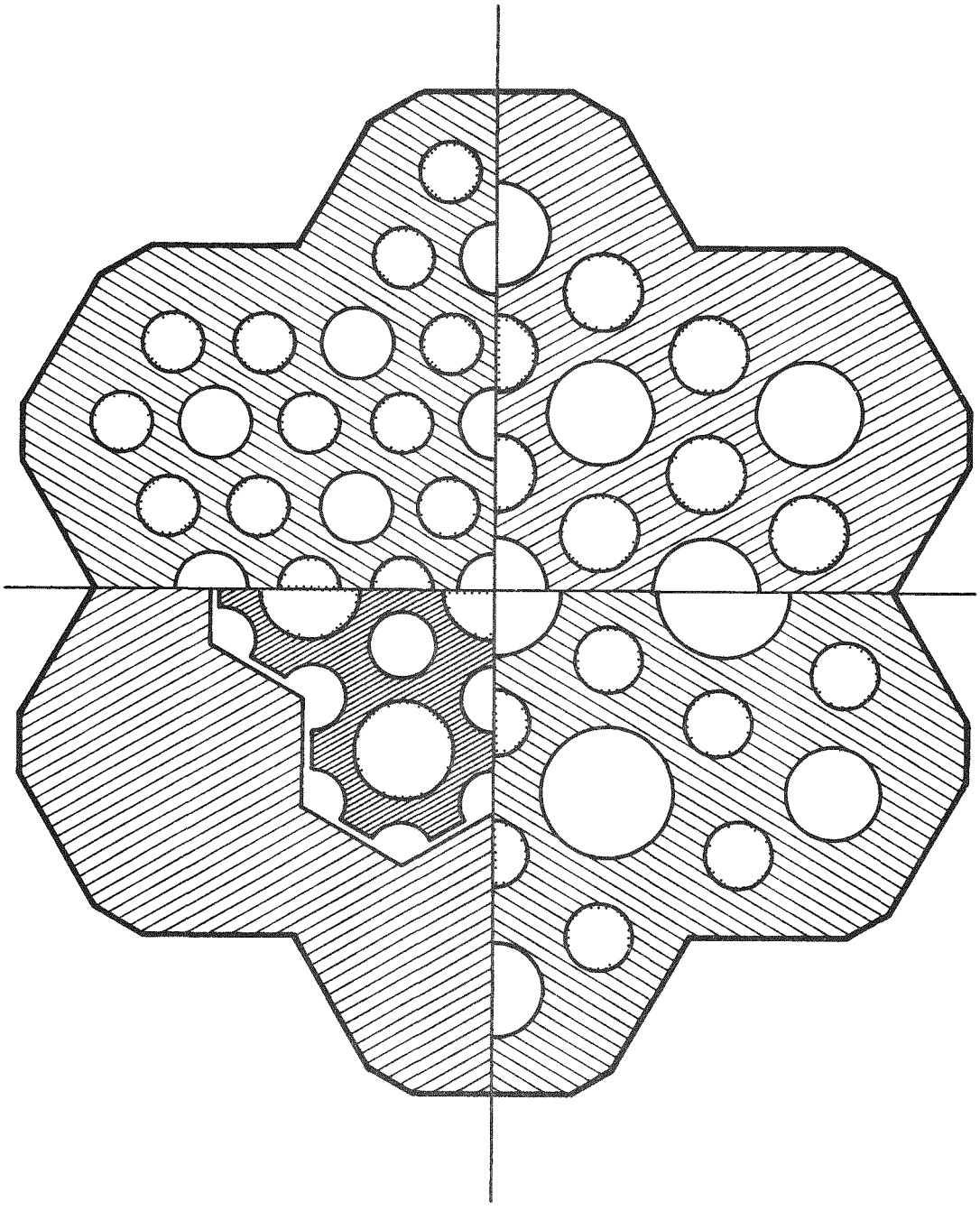

Fig. 11-5. Integral block test geometries in Dragon reactor

The test element would be cooled by the flow of coolant through the coolant holes, but with flow restrictions placed in the central coolant channel or channels to produce a symmetrical temperature gradient across the element. This gradient, with a hotter region in the center of the element, would be small at the end of the element where the coolant enters, but would increase to a maximum level at the core outlet end. The degree of flow maldistribution would be selected to produce appropriate peak shutdown stresses at the core outlet end of the element. These peak shutdown stresses are the largest ever expected to be reached in any element in any HTGR core. With this arrangement, the web stresses will be relatively constant at the level found in an element at high power density, while the stresses from gradients across the element will vary from zero to the maximum found anywhere in an HTGR. This spans the range of conditions expected in the reactor core.

The test element will be irradiated in a reactor position selected to provide uniform flux and, as nearly as possible, a circularly symmetric power and temperature distribution. The element will be well instrumented to allow the power, flux, and temperature distributions to be predicted accurately. The element will be irradiated to the point where the peak shutdown stresses are reached. As mentioned above, these peak shutdown stresses should be the largest that would be expected in an HTGR core.

Following irradiation, the fuel will be removed and the test element will be cut into sections for structural examination. The sections will consist of thin [less than 25 mm (1 in.)] slabs for compressive edge loading and pressure burst testing, and approximately 508 mm (20 in.) lengths to be used for dimensional measurements. Some slabs will be tested by pressurizing the central fuel holes with a hydraulic fluid inside a rubber bladder. Other slabs will be loaded in compression across opposite faces of the element to cause web cracking in the center of the slab. The detailed plan for the tests will be determined on the basis of the analysis to predict residual stresses in the irradiated elements. The apparatus and test methods will be calibrated in advance with tests on unirradiated

specimens of the same dimensions. The tests on slabs will superimpose a stress pattern due to primary loading on the residual stress pattern in the elements due to differences in thermal and irradiation strain. By measuring the load at failure and the curve of load versus deflection, the magnitude of the primary stress and the effective elastic modulus of the irradiated structure can be determined. While these experiments do not measure the residual stress directly, they do measure the margin to failure, that is, the difference between the irradiated strength and the residual stress.

To measure the residual stress distribution, the approximately 508 mm (20 in.) long sections of the test element will be used. A series of cuts will be made to section the element, with accurate measurements of key dimensions made before and after each cut. The cuts will be in the vertical direction, along the direction of coolant flow. The first cut will be made from the outside of the specimen toward the center. The distance between points on opposite sides of the first cut will be measured before and after cutting to determine the extent of residual in-plane bending moment, from which the residual in-plane strains and stresses can be inferred. Later cuts will allow individual strips to be removed. The lengths and curvature of these strips will be measured before and after they are cut away, with similar measurements made on the remainder of the specimen from which the strip is cut. From these measurements, the axial strain distribution can be inferred. The cut strips will then be tested in a four point bend test apparatus to measure the effective elastic modulus and residual stresses in the strips. These bend tests will be carried to failure to provide a measure of the margin to failure for axial stresses. The detailed plan for measurement and cutting of the specimens will be determined on the basis of the residual stress distribution predicted by the detailed structural analysis of the element under irradiation.

The results of all of the tests will be compared with predictions from the detailed stress analyses. If there are significant discrepancies, additional tests to determine the cause of the discrepancies will be defined.

TASK 700: PROGRAM PLAN

Work on the Program Plan has been suspended until future direction of the Base Program is determined.

REFERENCES

11-1. Price, R. J., and L. A. Beavan, "Final Report on Graphite Irradiation Test OG-2," ERDA Report GA-A13556, General Atomic Company, December 15, 1975.

11-2. Johnson, W. R., and G. B. Engle, "Properties of Unirradiated Fuel Element Graphites H-451 and TS-1240," ERDA Report GA-A13752, General Atomic Company, January 31, 1976.

11-3. "HTGR Fuels and Core Development Program Quarterly Progress Report for the Period Ending November 30, 1975," ERDA Report GA-A13737, General Atomic Company, December 31, 1975.

11-4. Smith, P. D., "Methods of Stress Analysis in Use at General Atomic for Core Design," General Atomic Report GA-A12870 (GA-LTR-12), May 1, 1974.

11-5. Everett, M. R., L. W. Graham, and F. Ridealgh, "Studies on the Behaviour of Graphite Structures Irradiated in the Dragon Reactor," Dragon Project Report 769, November 1971.

11-6. Kinkead, A. N., P. Barr, and M. R. Everett, "The Thermal and Mechanical Performance of HTR Fuel Elements," Dragon Project Report 847, September 1973.

11-7. Price, R. J., and H. R. W. Cobb, "Application of Weibull Statistical Theory to the Strength of Reactor Graphite," Gulf General Atomic Report GA-10257, August 6, 1970.

11-8. Everett, M. R., and E. Smith, Dragon Project, personal communication.

11-9. Brocklehurst, J. E., and R. G. Brown, "Fatigue, Notch Sensitivity and Work of Fracture Studies on Isotropic Graphite," UKAEA TRG Report 2513(S), December 5, 1973.

11-10. Brocklehurst, J. E., and M. I. Darby, Mater. Sci. Eng. 16, 91 (1974).

TABLE 11-1
IMPURITY CONTENT OF H-451 GRAPHITE, LOT 440[a]
(ppm)

(GA Log No./GLCC Log No.) GA Sample No.	Position in Log[b]	Ash	B	Fe	V	Ti	S	Al	Ca	Si	Na	Mg	Pb
(6484-54/GLCC 22)													
6484-54-3A-L016	MLC	50	<0.5	<1.0	<0.5	<1.0	<1.0	<1.0	<20.0	<10.0	<10.0	1.0	<6.0
-3B-L016	MLC	80										2.0	
-3A-L036	MLE	30										2.0	
-3B-L036	MLE	<20										4.0	
-1A-L016	EC	130										<0.5	
-1B-L016	EC	20										2.0	
-1A-L036	EE	50										1.0	
-1B-L036	EE	<20	<0.5	<1.0	<0.5	<1.0	<1.0	<1.0	<20.0	<10.0	<10.0	2.0	<6.0
Mean	Whole log	<50	<0.5	<1.0	<0.5	<1.0	<1.0	<1.0	<20.0	<10.0	<10.0	1.8	6.0
(6484-55/GLCC 27)													
6484-55-3B-L216B	MLC	60	<0.5	<1.0	<0.5	<1.0	<1.0	<1.0	<20.0	<10.0	<10.0	1.0	<6.0
-L274B	MLC	150										2.0	
-3A-L211B	MLE	110										4.0	
-L273B	MLE	100										2.0	
-1B-L016B	EC	20					4.0					2.0	
-L074B	EC	60					<1.0					2.0	
-1A-L011B	EE	60					8.6					2.0	
-L073B	EE	50	<0.5	<1.0	<0.5	<1.0	<1.0	<1.0	<20.0	<10.0	<10.0	<0.5	<6.0
Mean	Whole log	76	<0.5	<1.0	<0.5	<1.0	<2.3	<1.0	<20.0	<10.0	<10.0	<1.9	<6.0
(6484-56/GLCC 28)													
6484-56-3B-L216B	MLC	34	2.0	<1.0	<0.5	<1.0	<1.0	<1.0	<20.0	10.0	<10.0	2.0	<6.0
-L274B	MLC	166					<1.0			20.0		2.0	
-3A-L211B	MLE	87					22.5					2.0	
-L273B	MLE	70					<1.0					2.0	
-1B-L016B	EC	70	4.0				17.3					2.0	
-L074B	EC	118	2.0	40.0			<1.0					4.0	
-1A-L011B	EE	45	2.0	<1.0			37.9					4.0	
-L073B	EE	113	4.0	1.0	<0.5	<1.0	<1.0	<1.0	<20.0	20.0	<10.0	2.0	<6.0
Mean	Whole log	88	2.5	<5.9	<0.5	<1.0	<10.3	<1.0	<20.0	18.7	<10.0	2.5	<6.0

[a] Other elements present in all samples were Be, Zr, Ag, Ba, Lu <0.5 ppm; Li, Sc, Mn, Cu, Mo <1.0 ppm; Bi <2.0 ppm; Co, Ni, In, Tm, <4.0 ppm; Nb, Sn, Er <6.0 ppm; Sb <0.8 ppm; K, Cr, Cd, La, Eu, Gd, Ho, Yb <10.0 ppm; Zn, Hf, Tl, Dy <20.0 ppm; Rb, Sr, Ta, W, Tb <40.0 ppm; Ce <80.0 ppm; Sm, Pr, Cs, P <100.0 ppm; Nd <200.0 ppm.

[b] MLC = midlength center, MLE = midlength edge, EC = end center, EE = end edge.

TABLE 11-2

TENSILE PROPERTIES OF H-451 GRAPHITE, LOT 440

[Log 6484-54 (GLCC 22), whole log density = 1.78 g/cm^3 [a], 0.505-in.-diameter by 3.0-in.-long specimens]

Specimen No.	Location in Log and Orientation [b]	Bulk Density (g/cm^3)	Modulus of Elasticity x 10^{-6} on Second Loading (psi)	Permanent Set After First Loading (%)	Strain at Fracture (%)	Ultimate Strength (psi)
6484-54-3A-L002B	MLC, axial	1.772	1.500	0.009	0.231	2364
-L005B		1.768	1.500	0.014	0.262	2560
-L006B		1.765	1.406	0.010	0.219	2293
-L008B		1.779	1.406	0.008	0.174	(d)
-3B-L002B		1.784	1.406	0.014	0.250	2480
-L005B		1.782	1.406	0.012	0.249	2470
-L006B		1.778	1.406	0.011	0.236	2414
-L008B		1.764	1.343	0.011	0.219	2209
-3A-L002A						2348
-L005A						2295
-L006A						2423
-L008A						2566
-L003A						2468
-L009A						2370
-3B-L002A						2693
-L005A						2247
-L006A						2635
-L008A						2420
-L003A						2061
-L009A						2596
Mean		1.774	1.422	0.011	0.230	2416
Std. Dev.		0.008	0.053	0.002	0.027	157
6484-54-3A-L011	MLC, radial	1.770	(b)	(b)	(b)	883
-L013		1.772	1.216	0.020	0.138	1312
-L018		1.767	(d)	(d)	(d)	504
-L020		1.767	(d)	(d)	(d)	953
-3B-L011		1.764	1.216	0.014	0.226	1966
-L013		1.767	1.216	0.011	0.217	1936
-L018		1.789	(c)	(c)	(c)	1023
-L020		1.774	1.058	0.021	0.123	1023
-3A-L012						1815
-L014						1602
-L015						1516
-L017						1049
-L019						978
-L021						174
-3B-L012						1950
-L014						2150
-L015						1858
-L017						1047
-L019						1014
-L021						899
Mean		1.771	1.176	0.016	0.176	1283
Std. Dev.		0.008	0.079	0.005	0.053	539

TABLE 11-2 (Continued)

Specimen No.	Location in Log and Orientation[b]	Bulk Density (g/cm^3)	Modulus of Elasticity x 10^{-6} on Second Loading (psi)	Permanent Set After First Loading (%)	Strain at Fracture (%)	Ultimate Strength (psi)
6484-54-3A-L031B	MLE, axial	1.791	1.525	0.009	0.275	2902
-L034B		1.789	1.578	0.010	(c)	(c)
-L035B		1.794	1.475	0.013	0.268	2772
-L038B		1.791	1.475	0.010	0.281	2881
-3B-L031B		1.808	1.551	0.011	0.264	2869
-L034B		1.787	1.525	0.013	0.255	2665
-L035B		1.783	1.475	0.011	0.250	2643
-L038B		1.786	1.500	0.008	0.246	2544
-3A-L031A						2909
-L034A						2875
-L035A						(c)
-L038A						2622
-L039A						(c)
-L039B						(c)
-3B-L031A						(c)
-L034A						2561
-L035A						2761
-L038A						(c)
-L039A						389
-L039B						2541
Mean		1.791	1.513	0.011	0.263	2567
Std. Dev.		0.008	0.039	0.002	0.013	642
6484-54-3A-L041	MLE, radial	1.778	1.200	0.015	0.192	1707
-L043		1.780	1.216	0.018	0.187	1686
-L048		1.793	1.250	0.017	0.114	1148
-L050		1.793	1.267	0.017	0.186	1747
-3B-L041		1.794	1.200	0.018	0.110	1047
-L043		1.793	1.267	0.021	0.141	1367
-L048		1.780	1.184	0.017	0.174	1511
-L050		1.783	1.184	0.022	0.180	1546
-3A-L042						1623
-L044						1687
-L045						1293
-L047						1398
-L049						1722
-L051						1478
-3B-L042						1945
-L044						1699
-L045						1308
-L047						1149
-L049						1752
-L051						1288
Mean		1.787	1.221	0.018	0.160	1505
Std. Dev.		0.007	0.035	0.002	0.034	246

TABLE 11-2 (Continued)

Specimen No.	Location in Log and Orientation[b]	Bulk Density (g/cm^3)	Modulus of Elasticity x 10^{-6} on Second Loading (psi)	Permanent Set After First Loading (%)	Strain at Fracture (%)	Ultimate Strength (psi)
6484-54-1A-L002B	EC, axial	1.789	1.250	0.014	0.168	1633
-L005B		1.789				1948
-L006B		1.793	1.384	0.012	0.167	1748
-L008B		1.792	1.384	0.015	0.222	2206
-1B-L002B		1.791	1.384	0.010	0.205	2087
-L005B		1.789	1.363	0.014	0.211	2044
-L006B		1.790	1.343	0.012	0.217	2015
-L008B		1.790	1.304	0.015	0.201	1908
-1A-L002A						2049
-L005A						1541
-L006A						2106
-L008A						2300
-L003A						2101
-L009A						1959
-1B-L002A						2075
-L005A						1800
-L006A						2190
-L008A						1991
-L003A						2100
-L009A						1850
Mean		1.790	1.345	0.013	0.199	1983
Std. Dev.		0.002	0.051	0.002	0.022	191
6484-54-1A-L011	EC, radial	1.764	1.139	0.022	0.185	1520
-L013		1.775	1.323	0.030	0.170	1548
-L018		1.780	1.267	0.021	0.219	1937
-L020		1.782	1.184	0.016	0.129	1188
-1B-L011		1.782	1.216	0.019	0.221	1943
-L013		1.786	1.250	0.020	0.250	2197
-L018		1.774	1.168	0.021	0.212	1788
-L020		1.780	1.216	0.020	0.213	1890
-1A-L012						1339
-L014						1755
-L015						1380
-L017						1789
-L019						1709
-L021						1524
-1B-L012						1985
-L014						2005
-L015						2060
-L017						2065
-L019						1375
-L021						2110
Mean		1.778	1.220	0.021	0.200	1755
Std. Dev.		0.007	0.059	0.004	0.037	294

TABLE 11-2 (Continued)

Specimen No.	Location in Log and Orientation[b]	Bulk Density (g/cm^3)	Modulus of Elasticity x 10^{-6} on Second Loading (psi)	Permanent Set After First Loading (%)	Strain at Fracture (%)	Ultimate Strength (psi)
6484-54-1A-L031B	EE, axial	1.798	1.525	0.007	0.256	2718
-L034B		1.798	1.451	0.004	(d)	(d)
-L035B		1.794	1.475	0.010	0.260	2691
-L038B		1.788	1.451	0.012	0.234	2336
-1B-L031B		1.802	1.475	0.010	0.245	2591
-L034B		1.791	1.578	0.008	(c)	(c)
-L035B		1.785	1.451	0.009	0.254	2636
-L038B		1.778	1.304	0.011	0.156	1402
-1A-L031A						2874
-L034A						2540
-L035A						3100
-L038A						2510
-L039A						2515
-L039B						200
-1B-L031A						2857
-L034A						2473
-L035A						(c)
-L038A						1924
-L039A						2409
-L039B						2520
Mean		1.792	1.464	0.009	0.234	2370
Std. Dev.		0.008	0.078	0.003	0.039	676
6484-54-1A-L041	EE, radial	1.795	1.304	0.017	0.211	1939
-L043		1.792	1.232	0.018	0.274	2401
-L048		1.782	1.232	0.020	0.200	1796
-L050		1.789	1.250	0.010	0.205	1887
-1B-L041		1.785	1.267	0.015	0.210	1848
-L043		1.781	1.216	0.015	0.215	1932
-L048		1.787	1.216	0.012	0.159	1563
-L050		1.789	1.267	0.011	0.232	2058
-1A-L042						1938
-L044						2103
-L045						2572
-L047						1698
-L049						1703
-L051						2058
-1B-L042						1879
-L044						2074
-L045						2214
-L047						2184
-L049						1670
-L051						1898
Mean		1.787	1.248	0.015	0.213	1971
Std. Dev.		0.005	0.030	0.004	0.032	248

[a] Measured at GLCC.

[b] MLC = midlength center, MLE = midlength edge, EC = end center, EE = end edge. (Axial and radial) = parallel and perpendicular, respectively, to extrusion direction.

[c] Bond failure.

[d] Specimen failed on first loading.

TABLE 11-3
TENSILE PROPERTIES OF H-451 GRAPHITE

LOT NO. 440 SPEC. DIA. 0.505 IN.
LOG NO. 6484-57 SPEC. LENGTH 3.0 IN.
LOG DENSITY 1.77 G/CC(a)

SPECIMEN NUMBER		ORIENTATION(b)	LOCATION(b)	DENSITY (G/CC)	YOUNGS MODULUS E (10 PSI)	PERMANENT SET (PCT)	FRACTURE STRAIN (PCT)	TENSILE STRENGTH (PSI)
3A	L203A	AX	MLC	1.762	1.122	.017	.192	1616.
	L213A	AX	MLC	1.773	1.151	.007	.112	1127.
	L213B	AX	MLC	1.772	1.212	.014	.178	1579.
	L217B	AX	MLC	1.769	1.135	.011	.188	1679.
3B	L204A	AX	MLC	1.762	1.187	.010	.174	1579.
	L214A	AX	MLC	1.766	1.108	.009	.163	1535.
	L214B	AX	MLC	1.772	1.212	.014	.157	1485.
	L218B	AX	MLC	1.771	1.180	.014	.170	1539.
3A	L201B	AX	MLC					1548.
	L203B	AX	MLC					1354.
	L215A	AX	MLC					1502.
	L215B	AX	MLC					1236.
	L217A	AX	MLC					1755.
	L219B	AX	MLC					1285.
3B	L202B	AX	MLC					1494.
	L204B	AX	MLC					1619.
	L212A	AX	MLC					1726.
	L212B	AX	MLC					1993.
	L218A	AX	MLC					1157.
	L220A	AX	MLC					1647.
	MEAN			1.768	1.163	.012	.167	1523.
	STD. DEV.			.004	.040	.003	.025	210.
3A	L227	RAD	MLC	1.771	1.150	.020	.221	1759.
	L231	RAD	MLC	1.774	1.122	.023	.170	1496.
	L247	RAD	MLC	1.773	1.196	.013	.205	1834.
	L251	RAD	MLC	1.763	1.166	.009	.169	1501.
3B	L228	RAD	MLC	1.779	1.181	.016	.148	1760.
	L232	RAD	MLC	1.770	1.247	.013	.116	1187.
	L248	RAD	MLC	1.779	1.213	.014	.240	2095.
	L252	RAD	MLC	1.771				838.
3A	L225	RAD	MLC					1407.
	L229	RAD	MLC					878.
	L233	RAD	MLC					1272.
	L245	RAD	MLC					2050.
	L249	RAD	MLC					1512.
	L253	RAD	MLC					1033.
3B	L226	RAD	MLC					1746.
	L230	RAD	MLC					1766.
	L234	RAD	MLC					1726.
	L246	RAD	MLC					1601.
	L250	RAD	MLC					1172.
	L254	RAD	MLC					1994.
	MEAN			1.772	1.182	.015	.181	1531.
	STD. DEV.			.005	.041	.005	.043	372.

TABLE 11-3 (Continued)

SPECIMEN NUMBER		ORIENTATION[b]	LOCATION[b]	DENSITY (G/CC)	YOUNGS MODULUS E (10 PSI)	PERMANENT SET (PCT)	FRACTURE STRAIN (PCT)	TENSILE STRENGTH (PSI)
3A	L263A	AX	MLE	1.764	1.321	.014	.186	1841.
	L267B	AX	MLE	1.798	1.495	.009	.249	2561.
	L279A	AX	MLE	1.760	1.264	.009	.234	2124.
	L287B	AX	MLE	1.781	1.300	.013	.229	2188.
3B	L264A	AX	MLE	1.784	1.214	.017	.130	1293.
	L280A	AX	MLE	1.773	1.265	.011	.245	2245.
	L288B	AX	MLE	1.792	1.360	.011	.202	2039.
	L268B	AX	MLE	1.784	1.403	.011	.237	2354.
3A	L263B	AX	MLE					2170.
	L267A	AX	MLE					2436.
	L275A	AX	MLE					2108.
	L275B	AX	MLE					1820.
	L279B	AX	MLE					2075.
	L297A	AX	MLE					1937.
3B	L264B	AX	MLE					1761.
	L268A	AX	MLE					2240.
	L276A	AX	MLE					2362.
	L276B	AX	MLE					2163.
	L280B	AX	MLE					2432.
	L288A	AX	MLE					2047.
	MEAN			1.780	1.328	.012	.214	2110.
	STD. DEV.			.013	.090	.003	.040	288.
3A	L293	RAD	MLE	1.774	1.178	.019	.205	1791.
	L297	RAD	MLE	1.775	1.148	.016	.124	1194.
	L313	RAD	MLE	1.774	1.149	.014	.192	1658.
	L317	RAD	MLE	1.769	1.180	.011	.192	1674.
3B	L294	RAD	MLE	1.776	1.149	.020	.190	1638.
	L298	RAD	MLE	1.777	1.135	.020	.170	1420.
	L314	RAD	MLE	1.770				1618.
	L318	RAD	MLE	1.777	1.196	.017	.164	1455.
3A	L291	RAD	MLE					1600.
	L295	RAD	MLE					1382.
	L299	RAD	MLE					1839.
	L311	RAD	MLE					1800.
	L315	RAD	MLE					1686.
	L319	RAD	MLE					1645.
3B	L292	RAD	MLE					1779.
	L296	RAD	MLE					1631.
	L300	RAD	MLE					1890.
	L312	RAD	MLE					1296.
	L316	RAD	MLE					1621.
	L320	RAD	MLE					1491.
	MEAN			1.774	1.162	.017	.177	1605.
	STD. DEV.			.003	.022	.003	.027	189.

TABLE 11-3 (Continued)

SPECIMEN NUMBER		ORIENTATION[b]	LOCATION[b]	DENSITY (G/CC)	YOUNGS MODULUS 6 (10 PSI)	PERMANENT SET (PCT)	FRACTURE STRAIN (PCT)	TENSILE STRENGTH (PSI)
1A	L003A	AX	EC	1.769	1.081	.018	.144	1296.
	L013A	AX	EC	1.782	1.283	.012	.202	1966.
	L013B	AX	EC	1.787	1.381	.018	(c)	(c)
	L017B	AX	EC	1.785	1.320	.010	.253	2424.
1B	L004A	AX	EC	1.791	1.360	.010	.224	2169.
	L014A	AX	EC	1.784	1.301	.015	.220	2145.
	L014B	AX	EC	1.777	1.320	.010	.170	1750.
	L018B	AX	EC	1.784	1.301	.010	.173	1770.
1A	L001B	AX	EC					1916.
	L003B	AX	EC					1920.
	L015A	AX	EC					1797.
	L015B	AX	EC					1536.
	L017A	AX	EC					2067.
	L019B	AX	EC					2235.
1B	L002A	AX	EC					1761.
1B	L004B	AX	EC					1935.
	L012A	AX	EC					1742.
	L012B	AX	EC					1970.
	L018A	AX	EC					2227.
	L020B	AX	EC					1737.
	MEAN			1.783	1.293	.013	.198	1914.
	STD. DEV.			.007	.092	.004	.038	267.
1A	L027	RAD	EC	1.778	1.165	.008	.192	1739.
	L031	RAD	EC	1.773	1.137	.011	.139	1208.
	L047	RAD	EC	1.785	1.182	.012	.172	1597.
	L051	RAD	EC	1.773	1.136	.011	.177	1566.
1B	L028	RAD	EC	1.782	1.198	.012	.188	1786.
	L032	RAD	EC	1.780	1.167	.014	.180	1632.
	L048	RAD	EC	1.783	1.197	.016	.181	1646.
	L052	RAD	EC	1.778	1.197	.015	.146	1741.
1A	L025	RAD	EC					1463.
	L029	RAD	EC					1462.
	L033	RAD	EC					1107.
	L045	RAD	EC					1458.
	L049	RAD	EC					1357.
	L053	RAD	EC					689.
1B	L026	RAD	EC					1637.
1B	L030	RAD	EC					1597.
	L034	RAD	EC					1821.
	L046	RAD	EC					2054.
	L050	RAD	EC					749.
	L054	RAD	EC					1756.
	MEAN			1.779	1.173	.012	.172	1503.
	STD. DEV.			.004	.026	.003	.019	343.

TABLE 11-3 (Continued)

SPECIMEN NUMBER		ORIENTATION[b]	LOCATION[b]	DENSITY (G/CC)	YOUNGS MODULUS (10 PSI)	PERMANENT SET (PCT)	FRACTURE STRAIN (PCT)	TENSILE STRENGTH (PSI)
1A	L063A	AX	EE	1.780	1.341	.012	.231	2236.
	L067B	AX	EE	1.796	1.403	.015	.296	2904.
	L079A	AX	EE	1.772	1.199	.013	.172	1568.
	L087A	AX	EE	1.783	1.248	.012	.218	1966.
1B	L064A	AX	EE	1.773	1.214	.013	.191	2760.
	L068B	AX	EE	1.792	1.470	.005	.270	1729.
	L080A	AX	EE	1.784	1.341	.010	.247	2436.
	L088B	AX	EE	1.795	1.426	.010	.239	2406.
1A	L063B	AX	EE					2667.
	L067A	AX	EE					2055.
	L075A	AX	EE					2236.
	L075B	AX	EE					2199.
	L079B	AX	EE					2400.
	L087B	AX	EE					2251.
1B	L064B	AX	EE					1745.
	L063A	AX	EE					2598.
	L076A	AX	EE					1973.
	L076B	AX	EE					2195.
	L080B	AX	EE					2470.
	L088A	AX	EE					1993.
	MEAN			1.784	1.330	.011	.233	2239.
	STD. DEV.			.009	.101	.003	.040	353.
1A	L093	RAD	EE	1.781	1.180	.015	.194	1834.
	L097	RAD	EE	1.782	(d)	(d)	(d)	(d)
	L113	RAD	EE	1.776	1.229	.010	.133	1883.
	L117	RAD	EE	1.783	1.196	.014	.237	2048.
1B	L094	RAD	EE	1.781	1.264	.015	.225	2044.
	L098	RAD	EE	1.780	1.212	.014	.271	1944.
	L114	RAD	EE	1.775	1.165	.014	.241	2079.
	L118	RAD	EE	1.783	1.213	.015	.242	2094.
1A	L091	RAD	EE					1848.
	L095	RAD	EE					1771.
	L099	RAD	EE					1494.
	L111	RAD	EE					1469.
	L115	RAD	EE					1455.
	L119	RAD	EE					1610.
1B	L092	RAD	EE					2269.
	L096	RAD	EE					2069.
	L100	RAD	EE					1805.
	L112	RAD	EE					2343.
	L116	RAD	EE					2048.
	L120	RAD	EE					1819.
	MEAN			1.780	1.208	.014	.220	1891.
	STD. DEV.			.003	.032	.002	.045	255.

(a) Measured at GLCC.

(b) MLC = midlength center, MLE = midlength edge, EC = end center, EE = end edge; AX = axial, RAD = radial.

(c) Bond failure

(d) Specimen broke prior to testing.

TABLE 11-4

TENSILE PROPERTIES OF H-451 GRAPHITE

LOT NO. 440 SPEC. DIA. 0.505 IN.
LOG NO. 6484-55 SPEC. LENGTH 3.0 IN.
LOG DENSITY 1.76 G/CC[a]

SPECIMEN NUMBER	ORIENTATION[b]	LOCATION[b]	DENSITY (G/CC)	YOUNGS MODULUS 10^6 (PSI)	PERMANENT SET (PCT)	FRACTURE STRAIN (PCT)	TENSILE STRENGTH (PSI)
3A L203A	AX	MLC	1.750	1.268	.011	.224	1916.
L213A	AX	MLC	1.745	1.169	.015	.202	1750.
L213B	AX	MLC	1.738	1.125	.016	.236	1889.
L217B	AX	MLC	1.757	1.363	.019	.203	1880.
3B L204A	AX	MLC	1.749	1.185	.014	.166	1476.
L214A	AX	MLC	1.758	1.198	.014	.239	1947.
L214B	AX	MLC	1.757	1.200	.011	.194	1800.
L218B	AX	MLC	1.753	1.199	.017	.195	1748.
3A L201B	AX	MLC					1992.
L203B	AX	MLC					1814.
L215A	AX	MLC					1560.
L215B	AX	MLC					1668.
L217A	AX	MLC					1662.
3A L219B	AX	MLC					1568.
3B L202B	AX	MLC					1783.
L204B	AX	MLC					1769.
L212A	AX	MLC					1774.
L212B	AX	MLC					1568.
L218A	AX	MLC					1863.
L220A	AX	MLC					1759.
MEAN			1.751	1.213	.015	.207	1759.
STD. DEV.			.007	.073	.003	.024	140.
3A L227	RAD	MLC	1.767	1.136	.015	.190	1646.
L231	RAD	MLC	1.769	1.083	.017	.214	1648.
L247	RAD	MLC	1.767	1.153	.018	.190	1643.
L251	RAD	MLC	1.761	1.182	.015	.212	1796.
3B L228	RAD	MLC	1.755	1.073	.015	.175	1423.
3B L232	RAD	MLC	1.751	1.070	.018	.185	1538.
L248	RAD	MLC	1.742	1.144	.014	.234	1963.
L252	RAD	MLC	1.761	1.214	.017	.232	1991.
3A L225	RAD	MLC					1396.
L229	RAD	MLC					1637.
L233	RAD	MLC					1511.
L245	RAD	MLC					1601.
L249	RAD	MLC					1796.
L253	RAD	MLC					1457.
3B L226	RAD	MLC					1636.
L230	RAD	MLC					1488.
L234	RAD	MLC					1469.
L246	RAD	MLC					1448.
L250	RAD	MLC					1896.
L254	RAD	MLC					2064.
MEAN			1.759	1.132	.016	.205	1652.
STD. DEV.			.009	.053	.002	.022	202.

TABLE 11-4 (Continued)

SPECIMEN NUMBER		ORIENTATION[b]	LOCATION[b]	DENSITY (G/CC)	YOUNGS MODULUS 6 (10 PSI)	PERMANENT SET (PCT)	FRACTURE STRAIN (PCT)	TENSILE STRENGTH (PSI)
3A	L263A	AX	MLE	1.756	1.267	.012	(c)	(c)
	L267B	AX	MLE	1.764	1.322	.012	.286	2697.
	L279A	AX	MLF	1.755	1.231	.011	.204	1907.
	L287B	AX	MLE	1.751	1.284	.015	.239	2241.
3P	L264A	AX	MLE	1.765	1.323	.010	.255	2458.
	L264B	AX	MLE	1.772	1.303	.014	.262	2398.
	L280A	AX	MLF	1.796	1.449	.010	.211	2257.
	L288B	AX	MLE	1.762	1.302	.011	.251	2340.
3A	L263B	AX	MLF		1.322	.006	(c)	(c)
	L267A	AX	MLF					2644.
	L275A	AX	MLF					2173.
	L275B	AX	MLE					1768.
	L279B	AX	MLF					2120.
	L287A	AX	MLE					1938.
3B	L268B	AX	MLF					2544.
3B	L268A	AX	MLF					2698.
	L276A	AX	MLE					2296.
	L276B	AX	MLE					2234.
	L280B	AX	MLE					2434.
	L288A	AX	MLE					2511.
		MEAN		1.765	1.311	.011	.244	2314.
		STD. DEV.		.014	.060	.003	.029	268.
3A	L293	RAD	MLF	1.764	1.241	.015	.117	1258.
	L297	RAD	MLF	1.762	1.182	.019	.218	1802.
	L313	RAD	MLE	1.771	1.138	.016	.135	1224.
	L317	RAD	MLE	1.773	1.215	.018	.139	1318.
3B	L294	RAD	MLF	1.762	1.214	.015	.251	2101.
	L298	RAD	MLF	1.766	1.138	.014	.206	1753.
	L314	RAD	MLF	1.755	1.182	.015	.234	1981.
3B	L318	RAD	MLE	1.757	1.265	.014	.191	1747.
3A	L291	RAD	MLF					1725.
	L295	RAD	MLE					1707.
	L299	RAD	MLE					1537.
	L311	RAD	MLE					1198.
	L315	RAD	MLF					1348.
	L319	RAD	MLE					1183.
3B	L292	RAD	MLF					1848.
	L296	RAD	MLE					1787.
	L300	RAD	MLE					1826.
	L312	RAD	MLE					1242.
	L316	RAD	MLE					1596.
	L320	RAD	MLE					1766.
		MEAN		1.764	1.209	.016	.186	1597.
		STD. DEV.		.006	.068	.002	.050	286.

TABLE 11-4 (Continued)

SPECIMEN NUMBER		ORIENTATION[b]	LOCATION[b]	DENSITY (G/CC)	YOUNGS MODULUS 6 (10 PSI)	PERMANENT SET (PCT)	FRACTURE STRAIN (PCT)	TENSILE STRENGTH (PSI)
1A	L003A	AX	EC	1.770	1.285	.016	.205	1903.
	L013A	AX	EC	1.753	1.168	.012	.240	1983.
	L013B	AX	EC	1.767	1.198	.018	.182	1628.
	L017B	AX	EC	1.760	1.247	.015	.181	1711.
1B	L004A	AX	EC	1.678	1.342	.012	.194	1914.
	L014A	AX	EC	1.761	1.285	.011	.186	1839.
	L014B	AX	EC	1.765	1.283	.010	.225	2155.
	L018B	AX	EC	1.771	1.247	.012	.179	1811.
1A	L001B	AX	EC					1765.
	L003B	AX	EC					1936.
	L015A	AX	EC					2019.
	L015B	AX	EC					1896.
	L017A	AX	EC					1644.
	L019B	AX	EC					1881.
1B	L002B	AX	EC					1417.
	L004B	AX	EC					1875.
	L012A	AX	EC					1988.
1B	L012B	AX	EC					2045.
	L018A	AX	EC					2083.
	L020B	AX	EC					2004.
		MEAN		1.753	1.257	.013	.199	1875.
		STD. DEV.		.031	.055	.003	.023	176.
1A	L027	RAD	EC	1.766	1.215	.013	.223	1978.
	L031	RAD	EC	1.767	1.167	.017	.209	1748.
	L047	RAD	EC	1.765	1.153	.014	.209	1749.
	L051	RAD	EC	1.762	1.111	.015	.222	1799.
1B	L028	RAD	EC	1.773	1.153	.015	.193	1698.
	L032	RAD	EC	1.767	1.137	.016	.252	2036.
	L048	RAD	EC	1.768	1.123	.023	.210	1697.
	L052	RAD	EC	1.763	1.138	.012	.211	1783.
1A	L025	RAD	EC					2297.
1A	L029	RAD	EC					2078.
	L033	RAD	EC					1649.
	L045	RAD	EC					1649.
	L049	RAD	EC					1549.
	L053	RAD	EC					1484.
1B	L026	RAD	EC					2013.
	L030	RAD	EC					1912.
	L034	RAD	EC					1562.
	L046	RAD	EC					1764.
	L050	RAD	EC					1722.
	L054	RAD	EC					1673.
		MEAN		1.766	1.150	.016	.216	1792.
		STD. DEV.		.003	.032	.003	.017	203.

TABLE 11-4 (Continued)

SPECIMEN NUMBER	ORIENTATION[b]	LOCATION[b]	DENSITY (G/CC)	YOUNGS MODULUS 6 (10 PSI)	PERMANENT SET (PCT)	FRACTURE STRAIN (PCT)	TENSILE STRENGTH (PSI)
1A L063A	AX	EE	1.768	1.303	.013	.217	2038.
L067B	AX	EE	1.775	1.360	.010	.233	2294.
L079A	AX	EE	1.764	1.137	.011	.210	1817.
L087B	AX	EE	1.777	1.247	.013	.149	1486.
1B L064A	AX	EE	1.788	1.303	.011	.220	2153.
L068B	AX	EE	1.788	1.425	.010	(c)	(c)
L080A	AX	EE	1.771	1.361	.010	.246	2366.
L088B	AX	EE	1.667	1.263	.013	.230	2130.
1A L063B	AX	EE					2110.
L067A	AX	EE					2596.
L075A	AX	EE					1886.
L075B	AX	EE					1860.
L079B	AX	EE					2085.
L087A	AX	EE					1947.
1B L064B	AX	EE					1997.
L068A	AX	EE		1.427	.010	.321	3131.
L076A	AX	EE					2182.
L076B	AX	EE					2256.
L080B	AX	EE					2245.
1B L088A	AX	EE					2287.
MEAN			1.762	1.316	.011	.228	2151.
STD. DEV.			.039	.091	.001	.047	338.
1A L093	RAD	EE	1.761	1.183	.013	.270	2287.
L097	RAD	EE	1.757	1.182	.012	.256	2186.
L113	RAD	EE	1.771	1.231	.017	.291	2431.
L117	RAD	EE	1.768	1.198	.017	.254	2182.
1B L094	RAD	EE	1.768	1.083	.016	.167	1418.
L098	RAD	EE	1.765	1.123	.014	.194	1698.
L114	RAD	EE	1.763	1.153	.017	.258	2123.
L118	RAD	EE	1.764	1.167	.010	.186	1683.
1A L091	RAD	EE					2407.
L095	RAD	EE					2072.
L099	RAD	EE					1887.
1A L111	RAD	EE					2248.
L115	RAD	EE					2287.
L119	RAD	EE					2112.
1B L092	RAD	EE					1673.
L096	RAD	EE					1603.
L100	RAD	EE					1728.
L112	RAD	EE					2094.
L116	RAD	EE					2168.
L120	RAD	EE					1683.
MEAN			1.765	1.165	.014	.234	1998.
STD. DEV.			.005	.046	.003	.045	299.

(a) Measured at GLCC.

(b) MLC = midlength center, MLE = midlength edge, EC = end center, EE = end edge; AX = axial, RAD = redial.

(c) Bond failure.

TABLE 11-5

TENSILE PROPERTIES OF H-451 GRAPHITE

LOT NO. 440 SPEC. DIA. 0.505 IN.
LOG NO. 6484-56 SPEC. LENGTH 3.0 IN.
LOG DENSITY 1.77 G/CC[a]

SPECIMEN NUMBER		ORIENTATION[b]	LOCATION[b]	DENSITY (G/CC)	YOUNGS MODULUS $(10^6$ PSI)	PERMANENT SET (PCT)	FRACTURE STRAIN (PCT)	TENSILE STRENGTH (PSI)
3A	L203A	AX	MLC	1.752	1.137	.015	.197	1657.
	L203A	AX	MLC	1.756	1.230	.013	.218	1901.
	L213B	AX	MLC	1.745	1.096	.017	.224	1762.
	L217B	AX	MLC	1.742	1.198	.014	.200	1768.
3B	L204A	AX	MLC	1.759	1.246	.009	.220	1963.
	L214A	AX	MLC	1.772	1.248	.017	.187	1697.
	L214B	AX	MLC	1.784	1.248	.017	.181	1647.
	L218B	AX	MLC	1.755	1.213	.021	.224	1806.
3A	L201B	AX	MLC					1611.
	L203B	AX	MLC					1812.
	L215A	AX	MLC					(c)
	L215B	AX	MLC					1897.
	L217A	AX	MLC					1606.
3A	L219B	AX	MLC					1628.
3B	L202B	AX	MLC					1700.
	L204B	AX	MLC					1839.
	L212A	AX	MLC					2028.
	L212B	AX	MLC					1844.
	L218A	AX	MLC					1902.
	L220A	AX	MLC					1715.
	MEAN			1.758	1.202	.015	.206	1776.
	STD. DEV.			.014	.057	.004	.017	124.
3A	L227	RAD	MLC	1.760	1.153	.020	.214	1749.
	L231	RAD	MLC	1.761	1.153	.014	.195	1638.
	L247	RAD	MLC	1.749	1.020	.025	.166	1257.
	L251	RAD	MLC	1.756	.999	.023	.204	1433.
3B	L228	RAD	MLC	1.757	1.150	.018	.207	1744.
	L232	RAD	MLC	1.757	1.151	.019	.225	1825.
	L248	RAD	MLC	1.753	1.124	.022	.207	1648.
	L252	RAD	MLC	1.755	1.021	.020	.158	1223.
3A	L225	RAD	MLC					2049.
	L229	RAD	MLC					2058.
	L233	RAD	MLC					1508.
	L245	RAD	MLC					1488.
	L249	RAD	MLC					1673.
	L253	RAD	MLC					1393.
3B	L226	RAD	MLC					1585.
	L230	RAD	MLC					1784.
	L234	RAD	MLC					1865.
	L246	RAD	MLC					1558.
	L250	RAD	MLC					1627.
	L254	RAD	MLC					1713.
	MEAN			1.756	1.096	.020	.197	1641.
	STD. DEV.			.004	.070	.003	.023	224.

TABLE 11-5 (Continued)

SPECIMEN NUMBER		ORIENTATION[b]	LOCATION[b]	DENSITY (G/CC)	YOUNGS MODULUS 6 (10 PSI)	PERMANENT SET (PCT)	FRACTURE STRAIN (PCT)	TENSILE STRENGTH (PSI)
3A	L263A	AX	MLF	1.761	1.185	.006	.209	1986.
	L267B	AX	MLF	1.788	1.345	.019	.247	2303.
	L279A	AX	MLF	1.782	1.344	.011	.252	2441.
	L287B	AX	MLF	1.783	1.325	.014	.242	2263.
3B	L264A	AX	MLF	1.784	1.267	.014	.244	2129.
	L264B	AX	MLE	1.781	1.232	.012	.257	2294.
	L280A	AX	MLF	1.782	1.429	.010	.303	2946.
	L288B	AX	MLE	1.782	1.430	.013	.237	2403.
3A	L263B	AX	MLF					1992.
	L267A	AX	MLE					1371.
	L275A	AX	MLF					2112.
	L275B	AX	MLE					1790.
	L279B	AX	MLE					2488.
	L287A	AX	MLF					2197.
3B	L268A	AX	MLF					2447.
3B	L268B	AX	MLE					2387.
	L276A	AX	MLF					2311.
	L276B	AX	MLF					2423.
	L280B	AX	MLF					3022.
	L288A	AX	MLF					2411.
		MEAN		1.780	1.320	.012	.249	2286.
		STD. DEV.		.018	.088	.004	.026	359.
3A	L293	RAD	MLF	1.769	1.138	.010	.150	1338.
	L297	RAD	MLF	1.771	1.137	.016	.221	1851.
	L313	RAD	MLE	1.759	1.011	.020	.192	1419.
	L317	RAD	MLF	1.760	.999	.030	.195	1588.
3B	L294	RAD	MLF	1.764	1.163	.015	.191	1627.
	L298	RAD	MLF	1.772	1.225	.016	.185	1698.
3B	L314	RAD	MLF	1.661	1.082	.017	.154	1278.
	L318	RAD	MLF	1.766	1.083	.014	.189	1573.
3A	L291	RAD	MLF	1.770				1196.
	L295	RAD	MLF					1890.
	L299	RAD	MLF					1965.
	L311	RAD	MLF					1347.
	L315	RAD	MLE					1348.
	L319	RAD	MLE					1378.
3B	L292	RAD	MLF					1396.
	L296	RAD	MLE					1637.
	L300	RAD	MLF					1403.
	L312	RAD	MLF					1496.
	L316	RAD	MLE					1497.
	L320	RAD	MLE					1672.
		MEAN		1.755	1.105	.017	.185	1530.
		STD. DEV.		.035	.077	.006	.023	211.

TABLE 11-5 (Continued)

SPECIMEN NUMBER		ORIENTATION[b]	LOCATION[b]	DENSITY (G/CC)	YOUNGS MODULUS 6 (10 PSI)	PERMANENT SET (PCT)	FRACTURE STRAIN (PCT)	TENSILE STRENGTH (PSI)
1A	L003A	AX	EC	1.762				1772.
	L013A	AX	EC	1.758				2114.
	L013B	AX	EC	1.762				1391.
	L017B	AX	EC	1.776				1576.
1B	L004A	AX	EC	1.765				2043.
	L014A	AX	EC	1.769				2050.
	L014B	AX	EC	1.777				2133.
	L018B	AX	EC	1.773				1899.
1A	L001B	AX	EC					1913.
	L003B	AX	EC					1986.
	L015A	AX	EC					2056.
	L015B	AX	EC					1647.
	L017A	AX	EC					2003.
	L019B	AX	EC					1537.
1B	L002B	AX	EC					1803.
	L004B	AX	EC					2113.
	L012A	AX	EC					1832.
1B	L012B	AX	EC					2136.
	L018A	AX	EC					2203.
	L020B	AX	EC					1784.
		MEAN		1.768				1900.
		STD. DEV.		.007				227.
1A	L027	RAD	EC	1.764	1.058	.015	.205	1649.
	L031	RAD	EC	1.762	1.046	.021	.171	1349.
	L047	RAD	EC	1.767	1.058	.020	.185	1474.
	L051	RAD	EC	1.768	1.111	.016	.186	1559.
1B	L028	RAD	EC	1.757	1.110	.016	.215	1757.
	L032	RAD	EC	1.759	1.070	.024	.196	1537.
	L048	RAD	EC	1.772	1.124	.008	.192	1679.
	L052	RAD	EC	1.763	1.124	.014	.186	1609.
1A	L025	RAD	EC					1759.
	L029	RAD	EC					1739.
	L033	RAD	EC					1703.
	L045	RAD	EC					1534.
	L049	RAD	EC					1454.
	L053	RAD	EC					1598.
1B	L026	RAD	EC					1794.
	L030	RAD	EC					1862.
	L034	RAD	EC					1588.
	L046	RAD	EC					1675.
	L050	RAD	EC					1549.
	L054	RAD	EC					1793.
		MEAN		1.764	1.088	.017	.192	1633.
		STD. DEV.		.005	.033	.005	.014	132.

TABLE 11-5 (Continued)

SPECIMEN NUMBER		ORIENTATION[b]	LOCATION[b]	DENSITY (G/CC)	YOUNGS MODULUS 6 (10 PSI)	PERMANENT SET (PCT)	FRACTURE STRAIN (PCT)	TENSILE STRENGTH (PSI)
1A	L063A	AX	EE	1.764	1.271	.013	.238	2135.
	L067B	AX	EE	1.771	1.236	.013	.201	1905.
	L079A	AX	EE	1.783	1.363	.008	.294	2824.
	L087B	AX	EE	1.770	1.270	.010	.250	2359.
1B	L064A	AX	EE	1.798	1.249	.012	.206	1834.
	L068B	AX	EE	1.747	1.112	.018	.209	1671.
	L080A	AX	EE	1.808	1.526	.015	[c]	
	L088B	AX	EE	1.781	1.40[illegible]	.011	.263	2595.
1A	L063B	AX	EE					2602.
	L067A	AX	EE					1462.
	L075A	AX	EE					1850.
	L075B	AX	EE					1898.
	L079B	AX	EE					2388.
	L087A	AX	EE					2416.
1B	L064B	AX	EE					1751.
	L068A	AX	EE					1750.
	L076A	AX	EE					2499.
	L076B	AX	EE					256[illegible].
	L080B	AX	EE		1.454	.012	.283	2800.
1B	L088A	AX	EE					2487.
		MEAN		1.778	1.321	.012	.243	2200.
		STD. DEV.		.019	.128	.003	.036	418.
1A	L093	RAD	EE	1.775	1.215	.017	.222	1918.
	L097	RAD	EE	1.771	1.110	.019	.253	2034.
	L113	RAD	EE	1.753	1.168	.013	.226	1949.
	L117	RAD	EE	1.753	1.138	.012	.239	1993.
1B	L094	RAD	EE	1.770	1.199	.017	.233	2039.
	L098	RAD	EE	1.769	1.199	.018	.203	1769.
	L114	RAD	EE	1.764	1.322	.007	.182	1774.
	L118	RAD	EE	1.766	1.304	.014	.289	2359.
1A	L091	RAD	EE	1.779				2050.
	L095	RAD	EE					1544.
1A	L099	RAD	EE					1894.
	L111	RAD	EE					2018.
	L115	RAD	EE					2147.
	L119	RAD	EE					1999.
1B	L092	RAD	EE					2201.
	L096	RAD	EE					1994.
	L100	RAD	EE					1789.
	L112	RAD	EE					1469.
	L116	RAD	EE					2297.
	L120	RAD	EE					2100.
		MEAN		1.767	1.207	.015	.231	1967.
		STD. DEV.		.009	.074	.004	.032	221.

[a] Measured at GLCC.

[b] MLC = midlength center, MLE = midlength edge, EC = end center, EE = end edge; AX = axial, RAD = radial.

[c] Bond failure.

TABLE 11-6
THERMAL EXPANSIVITY OF H-451 GRAPHITE, LOT 440
Log 6484-54 (GLCC 22), whole log density = 1.78 g/cm^3[a]

Specimen No.	Location in Log and Orientation[b]	Mean Coefficient of Thermal Expansion, $\alpha \times 10^6$ °C^{-1} (22°-500°C)
6484-54-3A-004A	MLC, axial	3.93
-004B		4.18
-014A		3.91
-014B		3.99
-3B-004A		4.04
-004B		3.90
-014A		4.03
-014B		4.04
Mean		4.00
Std. Dev.		0.09
6484-54-3A-031A	MLC, radial	4.48
-031B		4.47
-044A		4.60
-044B		4.70
-3B-031A		4.77
-031B		4.77
-044A		4.55
-044B		4.54
Mean		4.61
Std. Dev.		0.12
6484-54-3A-053A	MLE, axial	3.99
-053B		4.08
-058A		4.01
-058B		4.16
-3B-053A		3.92
-053B		4.22
-058A		4.09
-058B		3.96
Mean		4.05
Std. Dev.		0.10
6484-54-3A-071A	MLE, radial	4.68
-071B		4.51
-084A		4.72
-084B		4.04
-3B-071A		4.65
-071B		4.78
-084A		4.68
-084B		4.63
Mean		4.59
Std. Dev.		0.23

TABLE 11-6 (Continued)

Specimen No.	Location in Log and Orientation[b]	Mean Coefficient of Thermal Expansion, $\alpha \times 10^6$ °C^{-1} (22°-500°C)
6484-54-1A-004A	EC, axial	4.04
-004B		3.78
-014A		3.94
-014B		4.15
-1B-004A		4.04
-004B		4.13
-014A		4.05
-014B		3.96
Mean		4.01
Std. Dev.		0.12
6484-54-1A-031A	EC, radial	4.61
-031B		4.78
-044A		4.37
-044B		4.67
-1B-031A		4.50
-031B		4.54
-044A		4.48
-044B		4.51
Mean		4.56
Std. Dev.		0.13
6484-54-1A-053A	EE, axial	3.96
-053B		3.98
-058A		4.03
-058B		3.84
-1B-053A		4.03
-053B		4.14
-058A		4.07
-058B		4.01
Mean		4.01
Std. Dev.		0.09
6484-54-1A-071A	EE, radial	4.55
-071B		4.60
-084A		4.77
-084B		4.74
-1B-071A		4.67
-071B		4.66
-084A		4.76
-084B		4.73
Mean		4.68
Std. Dev.		0.08

[a] Measured at GLCC.

[b] MLC = midlength center, MLE = midlength edge, EC = end center, EE = end edge. Axial and radial = parallel and perpendicular, respectively, to extrusion direction.

TABLE 11-7
THERMAL EXPANSIVITY OF H-451 GRAPHITE, LOT 440
Log 6484-55 (GLCC 27), whole log density = 1.76 g/cm^3 (a)

Specimen No.	Location in Log and Orientation (b)	Mean Coefficient of Thermal Expansion, $\alpha \times 10^6$ °C^{-1} (22°-500°C)
6484-55-3A-201A	MLC, axial	4.38
-201B		4.51
-217A		4.17
-217B		4.73
-3B-202A		4.51
-202B		4.57
-218A		4.20
-218B		4.53
Mean		4.45
Std. Dev.		0.19
6484-55-3A-243C	MLC, radial	4.91
-243D		4.86
-261B		4.78
-261C		4.92
-3B-244C		4.95
-244D		4.92
-262B		4.78
-262C		4.74
Mean		4.86
Std. Dev.		0.08
6484-55-1A-001A	MLE, axial	4.26
-001B		4.25
-017A		4.43
-017B		4.40
-1B-002A		4.53
-002B		4.43
-018A		4.40
-018B		4.33
Mean		4.38
Std. Dev.		0.09
6484-55-1A-043C	MLE, radial	4.91
-043D		4.58
-061B		4.94
-061C		4.88
-1B-044C		4.95
-044D		4.63
-062B		4.84
-062C		4.94
Mean		4.83
Std. Dev.		0.15

TABLE 11-7 (Continued)

Specimen No.	Location in Log and Orientation[b]	Mean Coefficient of Thermal Expansion, $\alpha \times 10^{-6}$ °C^{-1} (22°-500°C)
6484-55-3A-271A	EC, axial	4.49
-271B		4.35
-281A		4.34
-281B		4.20
-3B-272A		4.16
-272B		4.30
-282A		4.12
-282B		4.33
Mean		4.29
Std. Dev.		0.12
6484-55-3A-303B	EC, radial	4.88
-303C		4.89
-321B		4.92
-321C		4.82
-3B-304B		5.00
-304C		4.56
-322B		4.71
-322C		4.76
Mean		4.82
Std. Dev.		0.14
6484-55-1A-071A	EE, axial	4.23
-071B		4.06
-081A		4.31
-081B		4.30
-1B-072A		4.29
-072B		4.44
-082A		4.38
-082B		4.30
Mean		4.29
Std. Dev.		0.11
6484-55-1A-103B	EE, radial	4.99
-103C		4.86
-121B		4.87
-121C		4.73
-1B-104B		5.00
-104C		4.81
-122B		4.75
-122C		4.75
Mean		4.84
Std. Dev.		0.11

[a] Measured at GLCC.

[b] MLC = midlength center, MLE = midlength edge, EC = end center, EE = end edge. Axial and radial = parallel and perpendicular, respectively, to extrusion direction.

TABLE 11-8
THERMAL EXPANSIVITY OF H-451 GRAPHITE, LOT 440
Log 6484-56 (GLCC 28), whole log density = 1.77 g/cm^3 (a)

Specimen No.	Location in Log and Orientation (b)	Mean Coefficient of Thermal Expansion, $\alpha \times 10^6$ °C^{-1} (22°-500°C)
6484-56-3A-201A	MLC, axial	4.65
-201B		4.54
-217A		4.85
-217B		4.64
-3B-202A		4.51
-202B		4.58
-218A		4.59
-218B		4.45
Mean		4.60
Std. Dev.		0.12
6484-56-3A-243C	MLC, radial	4.98
-243D		4.69
-261B		4.91
-261C		5.06
-3B-244C		5.20
-244D		5.26
-262B		4.82
-262C		5.16
Mean		5.01
Std. Dev.		0.20
6484-56-1A-001A	MLE, axial	4.36 (4.30) (c)
-001B		4.31
-017A		4.41
-017B		4.46
-1B-002A		4.39
-002B		4.18
-018A		4.16
-018B		4.39
Mean		4.33
Std. Dev.		0.11
6484-56-1A-043C	MLE, radial	5.15
-043D		5.30
-061B		5.39 (5.36)
-061C		5.61 (5.27)
-1B-044C		5.12
-044D		5.15
-062B		5.27 (5.17)
-062C		5.51 (5.15)
Mean		5.31
Std. Dev.		0.18

TABLE 11-8 (Continued)

Specimen No.	Location in Log and Orientation[b]	Mean Coefficient of Thermal Expansion, $\alpha \times 10^6$ °C^{-1} (22°-500°C)
6484-56-3A-271A	EC, axial	4.66
-271B		4.71
-281A		4.70
-281B		4.65
-3B-272A		4.59
-272B		4.63
-282A		4.57
-282B		4.65
Mean		4.64
Std. Dev.		0.05
6484-56-3A-303B	EC, radial	5.30
-303C		5.27
-321B		5.10
-321C		5.08
-3B-304B		5.14
-304C		5.15
-322B		5.09
-322C		5.26
Mean		5.17
Std. Dev.		0.09
6484-56-1A-071A	EE, axial	4.20
-071B		4.27
-081A		4.34
-081B		4.25
-1B-072A		4.06
-072B		4.45
-082A		4.52
-082B		4.81
Mean		4.36
Std. Dev.		0.23
6484-56-1A-103B	EE, radial	5.19
-103C		5.05
-121B		5.34
-121C		5.23
-1B-104B		5.09
-104C		5.25
-122B		5.11
-122C		5.42
Mean		5.21
Std. Dev.		0.13

[a] Measured at GLCC.

[b] MLC = midlength center, MLE = midlength edge, EC = end center, EE - end edge. Axial and radial = parallel and perpendicular, respectively, to extrusion direction.

[c] Values in parenthesis are repeat measurements.

TABLE 11-9
TENSILE PROPERTIES OF SO-818 GRAPHITE, LOT 1
[Log 6484-19 (AS 13), whole log density = 1.74 g/cm^3 (a)
0.505-in.-diameter by 3.00-in.-long samples]

GA Specimen No.	Location in Log and Orientation (b)	Bulk Density (g/cm^3)	Modulus of Elasticity x 10^{-6} on Second Loading (c) (psi)	Permanent Set After First Loading (%)	Strain at Fracture (%)	Ultimate Strength (psi)
6484-19-3A-L002B	MLC, axial					1888
-L005B						1663
-L006B						1634
-L008B						1829
-3B-L002B						1997
-L005B						2009
-L006B						1893
-L008B						2000
-3A-L002A		1.739	1.034	0.025	0.274	1910
-L005A		1.684	0.873	0.009	0.247	1677
-L006A		1.684	0.882	0.025	0.245	1594
-L008A		1.699	0.927	0.019	0.274	1798
-L003B						1981
-L009B						1819
-3B-L002A		1.734	1.084	0.043	0.275	1867
-L005A		1.744	1.058	0.026	0.279	1995
-L006A		1.743	1.071	0.016	0.245	1903
-L008A		1.742	1.046	0.024	0.282	1950
-L003B						2023
-L009B						1913
Mean		1.721	0.997	0.023	0.265	1867
Std. Dev.		0.027	0.088	0.010	0.016	133
6484-19-3A-L011	MLC, radial	1.699	0.891	0.021	0.243	1598
-L013		1.708	0.909	0.029	0.283	1753
-L018		1.725	1.034	0.028	0.285	1948
-L020		1.727	1.034	0.028	0.290	1910
-3B-L011		1.739	0.947	0.023	0.279	1826
-L013		1.742	0.967	0.011	0.215	1612
-L018		1.741	0.978	0.016	0.253	1836
-L020		1.737	1.011	0.024	0.268	1862
-3A-L012						1762
-L014						1730
-L015						1513
-L017						1749
-L019						1887
-L021						1913
-3B-L012						1794
-L014						1910
-L015						1671
-L017						1942
-L019						1737
-L021						1807
Mean		1.727	0.971	0.022	0.264	1788
Std. Dev.		0.016	0.054	0.006	0.026	121

TABLE 11-9 (Continued)

GA Specimen No.	Location in Log and Orientation[b]	Bulk Density (g/cm^3)	Modulus of Elasticity x 10^{-6} on Second Loading[c] (psi)	Permanent Set After First Loading (%)	Strain at Fracture (%)	Ultimate Strength (psi)
6484-19-3A-L031B	MLE, axial	1.722	1.232	0.013	0.258	2190
-L034B		1.695	0.947	0.044	0.270	1766
-L035B		1.745	1.125	0.031	0.296	2208
-L038B		1.665	0.927	0.020	0.275	1754
-3B-L031B		1.754	1.428	0.013	0.309	2594
-L034B		1.752	1.323	0.011	0.274	2350
-L035B		1.764	1.184	0.016	0.316	2589
-L038B		1.757	1.111	0.012	0.267	2132
-3A-L031A						2281
-L034A						1841
-L035A						2098
-L038A						1662
-L039A						2237
-L039B						2257
-3B-L031A						2599
-L034A						2171
-L035A						2346
-L038A						2174
-L039A						2315
-L039B						2547
Mean		1.732	1.160	0.020	0.283	2205
Std. Dev.		0.035	0.172	0.012	0.021	279
6484-19-3A-L041	MLE, radial	1.662	0.967	0.021	0.210	1488
-L043		1.665	0.882	0.022	0.256	1602
-L048		1.721	0.918	0.025	0.256	1652
-L050		1.725	0.927	0.021	0.245	1646
-3B-L041		1.756	1.011	0.019	0.243	1770
-L043		1.749	1.343	0.016	0.211	1747
-L048		1.748	1.058	0.025	0.271	1899
-L050		1.746	1.097	0.022	0.247	1817
-3A-L042						1487
-L044						1511
-L045						1550
-L047						1726
-L049						1506
-L051						1829
-3B-L042						1747
-L044						1741
-L045						1870
-L047						1897
-L049						1940
-L051						1895
Mean		1.721	1.025	0.021	0.242	1716
Std. Dev.		0.038	0.147	0.003	0.021	152

TABLE 11-9 (Continued)

GA Specimen No.	Location in Log and Orientation[b]	Bulk Density (g/cm^3)	Modulus of Elasticity x 10^{-6} on Second Loading[c] (psi)	Permanent Set After First Loading (%)	Strain at Fracture (%)	Ultimate Strength (psi)
6484-19-1A-L002B	EC, axial	1.734	1.084	0.006	0.259	2020
-L005B		1.734	1.084	0.016	0.247	1905
-L006B		1.741	1.084	0.016	0.271	2065
-L008B		1.745	1.139	0.011	0.285	2254
-1B-L002B		1.731	1.058	0.017	0.242	1865
-L005B		1.733	1.168	0.016	0.256	2080
-L006B		1.733	1.084	0.014	0.254	1945
-L008B		1.762	1.111	0.015	0.253	1995
-1A-L002A						2071
-L005A						2096
-L006A						1895
-L008A						1998
-L003A						2050
-L009A						2005
-1B-L002A						2224
-L005A						2056
-L006A						2056
-L008A						1940
-L003A						1896
-L009A						2020
Mean		1.739	1.101	0.014	0:258	2022
Std. Dev.		0.010	0.036		0.014	101
6484-19-1A-L011	EC, radial	1.733	1.000	0.017	0.239	1814
-L013		1.737	1.084	0.019	0.243	1834
-L018		1.737	1.071	0.016	0.291	2120
-L020		1.736	1.058	0.018	0.254	1894
-1B-L011		1.730	0.989	0.014	0.243	1766
-L013		1.731	1.000	0.024	0.269	1827
-L018		1.734	1.084	0.012	0.262	1998
-L020		1.734	1.046	0.015	0.240	1794
-1A-L012						2010
-L014						1895
-L015						2021
-L017						2116
-L019						2081
-L021						2095
-1B-L012						1578
-L014						1897
-L015						1663
-L017						1988
-L019						1923
-L021						1700
Mean		1.734	1.041	0.017	0.255	1851
Std. Dev.		0.003	0.039	0.004	0.018	288

TABLE 11-9 (Continued)

GA Specimen No.	Location in Log and Orientation[b]	Bulk Density (g/cm^3)	Modulus of Elasticity x 10^{-6} on Second Loading[c] (psi)	Permanent Set After First Loading (%)	Strain at Fracture (%)	Ultimate Strength (psi)
6484-19-1A-L031B	EE, axial					2009
-L034B						1697
-L035B						2343
-L038B						1867
-1B-L031B						2290
-L034B						1856
-L035B						2191
-L038B						2224
-1A-L031A		1.751	1.232	0.014	0.254	2207
-L034A		1.725	1.084	0.019	0.265	1965
-L035A		1.748	1.216	0.012	0.254	2185
-L038A		1.738	1.084	0.016	(d)	(d)
-L039A						2060
-L039B						2280
-1B-L031A		1.750	1.153	0.018	(d)	(d)
-L034A		1.744	1.168	0.019	(d)	(d)
-L035A		1.750	1.200	0.013	0.253	2121
-L038A		1.729	1.139	0.019	(d)	(d)
-L039A						2250
-L039B						1756
Mean		1.742	1.159	0.016	0.256	2081
Std. Dev.		0.010	0.056	0.003	0.006	202
6484-19-1A-L041	EE, radial	1.737	0.989	0.025	(d)	(d)
-L043		1.739	1.046	0.017	0.272	1963
-L048		1.735	1.034	0.016	0.226	1693
-L050		1.734	1.011	0.026	0.232	1640
-1B-L041		1.736	1.034	0.018	0.219	1629
-L043		1.735	1.000	0.019	(d)	(d)
-L048		1.739	0.937	0.020	(d)	(d)
-L050		1.741	1.034	0.017	(d)	(d)
-1A-L042						1595
-L044						1874
-L045						1965
-L047						1934
-L049						1994
-L051						1933
-1B-L042						1680
-L044						1789
-L045						1535
-L047						1922
-L049						1834
-L051						1830
Mean		1.737	1.010	0.018	0.237	1801
Std. Dev.		0.002	0.036	0.006	0.024	151

[a] Measured at AS.

[b] Position in parent extrusion (∿18-in. diameter by ∿68 in. long): MLC = midlength center, MLE = midlength edge, EC = end center, EE = end edge. Axial and radial = parallel and perpendicular, respectively, to extrusion direction.

[c] Specimens were loaded to 1000 psi, unloaded to zero stress, and reloaded to failure while recording the stress-strain curve. Elastic modulus = chord modulus between 100 and 1000 psi on second loading.

[d] Bond failure.

TABLE 11-10
UNIAXIAL FATIGUE TESTS ON AXIAL H-451 GRAPHITE
(2:1 TENSION:COMPRESSION)

Core No.	Sample No.	Diameter (in.)	Stress Range (psi)		No. of Cycles to Failure
			Max.	Min.	
4	C	0.49979	2079	-1145	1,033
5	C	0.49979	2109	-1084	139
6	C	0.50015	2106	-1083	122
7	C	0.50005	2125	-1023	50
8	C	0.50011	2136	-1023	412
9	C	0.50017	2106	-1023	100
10	C	0.49951	2111	-1025	37
11	C	0.50003	2408	-1264	193
12	C	0.50006	2468	-1204	302
13	C	0.49979	2410	-1265	105
14	C	0.49992	2469	-1204	49
15	C	0.49989	2469	-1205	1
16	C	0.50017	2466	-1203	748
17	C	0.49997	2408	-1264	258
18	C	0.50008	2828	-1384	51
19	C	0.49896	2841	-1390	55
20	C	0.50019	2767	-1444	85
21	C	0.50002	2829	-1384	9
22	C	0.50009	2768	-1384	≤1 [a]
23	C	0.50000	2589	-1385	<1 [a]
25	C	0.49993	2770	-1445	5
26	C	0.49938	1871	-966	31,500
27	C	0.49920	1872	-966	10,800
28	C	0.49920	1872	-966	30
29	C	0.49854	1877	-969	1,756
30	C	0.49945	1870	-965	100,000 [b]
31	C	0.49908	1813	-1027	114,000 [b]
34	C	0.49900	1874	-967	194,300 [b]
35	C	0.49900	1451	-786	3,100
36	C	0.49872	1452	-787	102,000 [b]
37	C	0.49900	1451	-786	186,500 [b]
38	C	0.49908	1450	-785	16,900
39	C	0.49875	1452	-787	194,000 [b]
41	C	0.49878	1452	-786	1,700
42	C	0.49876	1452	-786	100,000 [b]
43	C	0.49950	2171	-1025	176
44	C	0.49925	2174	-1026	210
45	C	0.49901	2176	-1027	3,000
46	C	0.49920	2355	-1208	28
47	C	0.49932	2354	-1207	13
48	C	0.49952	2352	-1206	96

[a] First cycle failure.

[b] No failure.

TABLE 11-11
MILESTONES FOR GRAPHITE STRUCTURAL VERIFICATION

Preliminary analyses and test plans for Peach Bottom test elements	6/76
Development and qualification of pressure burst apparatus	1/77
Final report on Peach Bottom test elements	10/77
Test plan for first FSV surveillance elements	8/77
Final report on first FSV surveillance elements	3/78
Test plan for first FSV test element	8/78
Final report on first FSV test element	3/79
Final report on last FSV test element	3/85
Final report on verification of failure criteria for HTGR fuel elements	3/79
Final report on fracture toughness of H-451	9/81
Final report on crack propagation	9/82
Recommend multiaxial failure criteria	9/79

TABLE 11-12
TEST ELEMENTS FOR EXAMINATION

Element	Configuration	Graphite	Fast Fluence (10^{21} n/cm^2)	In-Plane Temperature Differences (°C)	Temperature Range (°C)	Maximum Stress Axial/In-Plane
FTE-3	8-hole teledial	H-327	0.6	300	650 - 950	1500/500
FTE-4	8-hole teledial	H-327	1.9	300	860 - 1150	1500/500
FTE-5	8-hole teledial	H-327	4.5	300	900 - 1200	1500/500
FTE-6	8-hole teledial	H-327	3.2	300	900 - 1200	1500/500
FTE-14	6-hole teledial	H-327	1.5	300	1040 - 1380	1600/700
FTE-15	6-hole teledial	H-327	2.6	300	1040 - 1380	1600/700
PTE-2	MHB section	H-327	1.9	110[a]	820 - 950	900/370

[a] Across web.

APPENDIX

PROJECT REPORTS PUBLISHED DURING THE QUARTER

Price, R. J., and L. A. Beavan, "Final Report on Graphite Irradiation Test OG-2," ERDA Report GA-A13556, General Atomic Company, December 15, 1975.

Wattier, J. B., "Final Test Operations Report - Caplule P13N," ERDA Report GA-A13578, General Atomic Company, December 17, 1975.

Johnson, W. R., and G. B. Engle,"Properties of Unirradiated Fuel Element Graphites H-451 and TS-1240," ERDA Report GA-A13752, General Atomic Company, January 31, 1976.